

# New Approaches in Porous Silicon Based Optical Immunosensors

---

*Andrew Oliver Jane*



**Flinders**  
UNIVERSITY

*School of Chemical and Physical Sciences*

*Supervised by*

**Professor Joseph Shapter** (Flinders University)

**Dr Roman Dronov** (Flinders University)

**Professor Nicolas Voelcker** (University of South Australia)

**Dr Alastair Hodges** (Universal Biosensors Inc.)

*Submitted on the 25<sup>th</sup> of March 2014  
in fulfilment for the degree of Doctor of Philosophy (PhD)  
Accepted on the 28<sup>th</sup> of August 2014*



# Table of Contents

<b>Abstract</b> .....	<b>i</b>
<b>Declaration</b> .....	<b>iii</b>
<b>Acknowledgements</b> .....	<b>iv</b>
<b>List of Figures</b> .....	<b>vi</b>
<b>List of Tables</b> .....	<b>xvi</b>
<b>List of Equations</b> .....	<b>xviii</b>
<b>List of Abbreviations</b> .....	<b>xix</b>
<b>List of Units</b> .....	<b>xxiii</b>
<b>Peer Reviewed Publications</b> .....	<b>xxv</b>
<b>1 Introduction</b> .....	<b>1</b>
1.1 Immunoassays and Immunosensing Principles .....	2
1.1.1 Antibody Structure and Principles of Immunoassays .....	2
1.1.2 Immunosensors .....	3
1.1.3 Optical Immunosensing.....	5
1.1.4 Immunosensing Summary .....	13
1.2 Porous Silicon in Biosensor Applications .....	14
1.2.1 Etching Techniques .....	15
1.2.2 Types of pSi .....	18
1.2.3 Surface Functionalisation .....	20
1.2.4 pSi Based Transducers .....	23
1.2.5 Photoluminescence Based Transducers.....	47
1.2.6 Chemiluminescence-Based pSi Transducers.....	49
1.2.7 Infrared-Based pSi Transducers .....	50
1.2.8 Electrochemical Transduction on pSi.....	51
1.2.9 pSi Summary .....	54
1.3 S-Layer Proteins - A Versatile Receptor Platform .....	55
1.3.1 Introduction .....	55
1.3.2 S-Layer Structure .....	57
1.3.3 Self-Assembly .....	59
1.3.4 Applications of native S-layer proteins .....	61
1.3.5 Genetic Modification of S-layers .....	61
1.3.6 S-layer Summary .....	66
1.4 Conclusions .....	67

<b>2</b>	<b>Materials and General Methods .....</b>	<b>69</b>
2.1	Materials.....	70
2.1.1	Chemicals and Reagents.....	70
2.2	General Methods .....	79
2.2.1	pSi Etching Procedure .....	79
2.2.2	Surface Modification and Functionalisation .....	80
2.2.3	Spectroscopy Techniques .....	83
<b>3</b>	<b>Porous Silicon Optical Transducer Design .....</b>	<b>87</b>
3.1	Abstract .....	88
3.2	Introduction .....	89
3.3	Experimental .....	91
3.3.1	Preparation of Porous Silicon.....	91
3.3.2	Surface Functionalisation and Characterisation .....	91
3.4	Results .....	93
3.4.1	pSi Fabrication Technique.....	93
3.4.2	N-type and P-type pSi Comparison.....	94
3.4.3	Effect of Current Density on Pore Diameter .....	96
3.4.4	Effect of Current Density on Porosity .....	96
3.4.5	N-type pSi Etching Rate.....	98
3.4.6	Current Density – Sensitivity to Refractive Index Change .....	98
3.5	Conclusion.....	100
<b>4</b>	<b>Detection of Human IgG on Porous Silicon via Enzyme Catalysed Precipitation of BCIP/NBT.....</b>	<b>101</b>
4.1	Abstract .....	102
4.2	Introduction .....	103
4.3	Experimental Method.....	106
4.3.1	Preparation of Porous Silicon.....	106
4.3.2	Formation of the Immunosensing Platform and Functionalisation of Porous Silicon.....	106
4.3.3	Immobilisation of Alkaline Phosphatase.....	107
4.3.4	Immobilisation of $\alpha$ -Human IgG Conjugated to Alkaline Phosphatase .....	107
4.3.5	Functionalisation of Flat Silicon with Alkaline Phosphatase .....	108
4.3.6	Enzyme Substrate Optimisation .....	108
4.3.7	Human IgG pSi Immunosensing .....	109
4.3.8	Cross-Reactivity/Specificity of the pSi Immunosensor.....	111
4.3.9	Fabrication of Immunoassay Patterned pSi for FTIR Mapping .....	111

4.3.10	Refractive Index Measurements .....	113
4.4	Results and Discussion .....	114
4.4.1	Surface Characterisation .....	114
4.4.2	Enzyme Substrate Optimisation .....	119
4.4.3	Signal Processing Optimisation .....	125
4.4.4	Intensity Response to BCIP/NBT Precipitation on pSi and Flat Silicon....	131
4.4.5	Human IgG Immunosensing .....	133
4.4.6	Surface Characterisation Following Immunosensing.....	142
4.5	Conclusions and Future Directions .....	149
<b>5</b>	<b>S-layer Fusion Protein as a Promoter for pSi Immunosensors.....</b>	<b>151</b>
5.1	Abstract .....	152
5.2	Introduction .....	153
5.3	Experimental Method.....	156
5.3.1	Cell Culture - <i>Lysinibacillus sphaericus</i> ATCC 4525.....	156
5.3.2	Extraction and Purification of Native S-layer Protein SbpA.....	156
5.3.3	Genetic Modification of S-layer Protein .....	157
5.3.4	<i>E. Coli</i> Cell Culture and Expression of rSbpA <sub>31-1068</sub> /ZZ .....	157
5.3.5	Extraction and Purification of rSbpA <sub>31-1068</sub> /ZZ S-layer Fusion Protein.....	158
5.3.6	Growth Measurements .....	160
5.3.7	Solid Substrate Preparation .....	160
5.3.8	Static Contact Angle Analysis.....	162
5.3.9	In vitro Recrystallisation of S-layers on Solid Supports .....	162
5.3.10	Atomic Force Microscopy.....	163
5.3.11	S-layer Based ELISA .....	163
5.3.12	pSi Preparation .....	165
5.3.13	pSi Functionalisation.....	165
5.3.14	Capture Antibody Immobilisation on SbpA-ZZ modified pSi and Human IgG Immunosensing. ....	166
5.4	Results and Discussion.....	169
5.4.1	Expression and Extraction of SbpA S-layer Protein from <i>L. Sphaericus</i> ATCC 4525 .....	169
5.4.2	Optimisation of S-layer Recrystallisation on Silicon .....	170
5.4.3	Expression and Purification of the S-layer Fusion protein SbpA-ZZ .....	179
5.4.4	Recrystallisation of SbpA-ZZ Fusion Protein on Solid Supports .....	181
5.4.5	Accessibility of Fused ZZ Domains - Human IgG Assay .....	185

5.4.6	Assessment of SbpA-ZZ performance (ELISA Studies).....	186
5.4.7	S-layer Integration into pSi Immunosensor Architecture.....	192
5.5	Conclusions and Future Directions .....	198
<b>6</b>	<b>Enzyme Mediated Signal Enhancement by Silver Reduction on Gold Modified pSi: Towards a New Optical Immunosensor Detection Strategy.....</b>	<b>201</b>
6.1	Abstract .....	202
6.2	Introduction .....	203
6.3	Experimental .....	206
6.3.1	Preparation of porous silicon.....	206
6.3.2	Surface Functionalisation .....	206
6.3.3	Surface Characterisation.....	209
6.3.4	Silver Enhancement of Gold .....	209
6.3.5	Organic Synthesis of Hydroquinone Diphosphate .....	211
6.3.6	Detection of Human IgG by Enzyme Mediated Silver Contrast Enhancement of Gold.....	211
6.4	Results .....	214
6.4.1	Silver Contrast Enhancement on Gold Nanoparticle (AuNP) Modified pSi 214	
6.4.2	Enzyme Mediated Silver Deposition on Gold Coated pSi .....	220
6.4.3	Detection of Human IgG by Silver Contrast Enhancement on Gold Plated pSi.....	234
6.5	Conclusions and Future Directions .....	236
<b>7</b>	<b>Conclusions and Future Perspectives .....</b>	<b>239</b>
	<b>References.....</b>	<b>244</b>

## Abstract

The rapid and reliable detection of diseases and pathogens is essential to modern healthcare systems. Development of new and more efficient sensing techniques is continuously being undertaken to meet this requirement with a large focus on immuno- and biosensing devices. The work conducted in this thesis seeks to address these needs via the development of new detection mechanisms and receptor immobilisation techniques for porous silicon (pSi) based optical immunosensors.

Initial investigations focused on the fabrication of an appropriate pSi optical sensor platform via changes in the electrochemical etching parameters. Higher current density applied during the etching cycle resulted in increased pore size, porosity and etching rate of n-type pSi. Monolayer pSi containing higher levels of porosity were demonstrated to be more sensitive to changes in refractive index through interferometric reflectance spectroscopy (IRS). Optimisation of these parameters yielded a sensitive and flexible sensor platform.

Development of a new absorbance based pSi optical biosensor was then undertaken. Detection of a human IgG analyte was achieved via a cascade of immunological reactions at the pore walls to form a sandwich assay. The detection strategy involved an alkaline phosphatase (AP) labelled secondary antibody and precipitation of the enzyme substrate 5-bromo-4-chloro-3-indoyl phosphate (BCIP)/nitro blue tetrazolium (NBT) within the porous matrix. The intense colour change and strong absorbance of the biocatalysed BCIP/NBT compounds at 600 nm provided a measurable response on the intensity of the reflected optical profile of the porous layer. This approach yielded a limit of detection of 2.14 ng/mL, well within the working range required for analysis of clinical samples.

Following development of the new pSi sensor, a special protein based IgG affinity coating was investigated as a new method of receptor immobilisation on optical sensors. Adaptation of a previously reported genetically modified bacterial surface layer (S-layer) protein from *Lysinibacillus sphaericus* containing twin IgG binding domains (SbpA<sub>31-1064</sub>/ZZ) provided a route to the formation of a self-

assembling protein layer capable of immobilising receptor IgG molecules with defined orientation. In vitro self-assembly of purified recombinant rSbpA<sub>31-1068</sub>/ZZ fusion protein was demonstrated by the formation of crystalline protein layers on various surface chemistries. IgG binding capacity was shown on rSbpA<sub>31-1068</sub>/ZZ coated ELISA microtiter plates via the immobilisation of IgG capture antibodies and detection of human IgG and human Interleukin-6 analytes. Integration of this coating into the previously developed pSi biosensor yielded a general improvement in sensor performance compared to covalent attachment of capture antibodies indicating that this new approach resulted in less receptor inhibition and greater numbers of viable binding sites.

Finally, the development of a new pSi optical interferometric biosensor based on metallic deposition was investigated. Chemical reduction of silver and deposition within gold treated pSi was found to result in a significant decrease to the EOT of the material due to a refractive index change. This refractive index ‘contrast’ enhancement was demonstrated on both gold nanoparticle decorated pSi and gold plated pSi and optimised to provide maximum signal change. An enzyme mediated silver deposition system was then developed using alkaline phosphatase and a synthesised enzyme substrate, hydroquinone diphosphate. Enzyme mediated silver deposition on gold plated pSi was demonstrated and optimised. Finally, adaptation of this system to a pSi optical immunosensor was demonstrated via the detection of human IgG.

The new organic and metallic enhancement immunosensors developed in this thesis demonstrate strong sensor platforms and with further investigation may be viable as future diagnostic techniques. In addition, the S-layer affinity coating has vast potential for use in a variety of immunosensors and a swath of other applications including patterned microarrays, biomimetics and drug delivery.

## Declaration

‘I certify that this thesis does not incorporate without acknowledgment any material previously submitted for a degree or diploma in any university; and that to the best of my knowledge and belief it does not contain any material previously published or written by another person except where due reference is made in the text. I also certify that the entirety of the experimental work represented herein was conducted solely by the author unless otherwise stated.’

Andrew Oliver Jane

# Acknowledgements

I would like to express my very great appreciation to Dr Roman Dronov who initially worked on this project as a colleague and eventually became my supervisor and friend. His support, both academic and financial, was essential in finishing this work. I would also like to thank Professor Nico Voelcker who encouraged me to undertake a PhD and was instrumental in the project's conception and direction. His willingness to take an active role and generously give his time has been very much appreciated and is recognized by all of his students. To my other supervisors, Dr Alastair Hodges and Professor Joe Shapter go my eternal thanks for their expansive knowledge and advice on the practicalities of biosensing; and especially to Joe for taking me under his wing when circumstances left me without a supervisor.

My great friend Chris Williams has shared this journey with me from the beginning of undergraduate studies and I would like to offer heartfelt thanks for keeping my spirits up and understanding the many trials and tribulations associated with a PhD when many others wouldn't. To the members of the cockpit, Marty and Steve, I thank you for your camaraderie and support. The office may be long gone but our friendship remains.

I am particularly grateful for the assistance given by Dr Endre Szili who taught me everything I know about porous silicon biosensing and provided financial support when things became difficult. To Dr Anthony Quinn and Lastek, you are the best employer anyone could ask for. Your ongoing flexibility and active support of my studies has allowed me the time and space needed to finish research work and write this thesis.

I wish to acknowledge my parents for their loving support and encouraging my education. They made me who I am today and instilled a passion for knowledge and logic, without their guidance I would never have made it so far. To my son Noah, your arrival into this world was a bright ray of light. I thank you for the happiness and laughter that you bring to my life.

Finally, and most importantly, I would like to thank my beautiful, loving and supportive wife, Megan. She has my deepest gratitude for her encouragement during the rough times and for single handedly running the household and a business so I could concentrate on my studies. You are my rock and have my undying thanks.

# List of Figures

Figure 1.1: IgG antibody structure. Top: 3D representation of IgG determined via X-ray crystallography. Bottom: Schematic of the IgG structure and important regions [7].	3
Figure 1.2: Immunosensor design principles. (a) Schematic of general immunosensor design. Adapted from [1]. (b) Common forms of labelled immunoassays utilised in immunosensing.	4
Figure 1.3: Alkaline phosphatase catalysed hydrolysis of a phosphate ester to an alcohol and orthophosphate.	7
Figure 1.4: Enhanced detection of the breast cancer marker, CA15-3, with modified AuNP's [27]. The nanoparticles acted as carriers for the secondary antibody in a sandwich assay, resulting in increased numbers of enzyme labels per analyte. This led to an improvement in the sensitivity of the approach (red trace) compared with traditional ELISA methods (blue trace).	9
Figure 1.5: Detection limit of the test strip developed by Yang <i>et al.</i> [29]. Abrin-a standard solutions at concentrations of 0, 0.1, 1.0, 10, 100 and 1000 ng/mL were assayed. (a) The result of the immunochromatographic assay using gold labelled antibodies. (b) Amplified assay signal by gold promoted silver deposition (silver enhancement).	10
Figure 1.6: SPR sensorgram detailing formation of the sensing element and detection of <i>Autographa californica</i> multiple nuclear polyhedrosis virus (AcMNPV) via direct immunosensing [30]. The sensor signal is formed by changes in the angle of the light reflected from the underside of the metal film upon alterations to the refractive index on the sensor surface.	11
Figure 1.7: TIRF optical fibre sensor traces for various MC-LR concentrations. The sensorgrams represent an increase in fluorescence as labelled antibodies bind to the sensor surface. All analyte samples were pre-treated with 0.28 µg/mL MC-LR-MAb and regeneration of the sensor probe was achieved by addition of 2 mg/mL pepsin solution (pH 1.9) [31].	12
Figure 1.8: Electrochemical formation of pSi. The application of an electrical current draws positive holes ( $h^+$ ) towards the surface of the semiconductor, weakening Si-H bonds and facilitating the dissolution of silicon [44].	16
Figure 1.9: Top view and cross sectional SEM micrographs of a variety of pSi architectures. (a – g) depicts mesoporous through to macroporous silicon structures [47]. (i & j) SEM micrographs of pSi after exposure to blood. Size exclusion due to pSi is clearly evident, depicting filtered erythrocytes on the surface of the porous layer [48].	18
Figure 1.10: Respective reflectance spectra, schematic and cross sectional micrograph of (a) a pSi single layer, (b) a pSi double layer [57], (c) multilayered pSi [58] and (d) a pSi microcavity [59].	20
Figure 1.11: Schematic of pSi optical detection due to pore loading. Addition of an analyte to the porous matrix results in the displacement of the aqueous phase at the pSi/medium interface and an increase in the refractive index. This causes a finite shift in the fringe pattern reflectance spectra, allowing quantification of an analyte [86].	24
Figure 1.12: A) Detection of DNA hybridisation via a shift in the reflected Fabry-Perot fringe pattern; and B) Subsequent control experiment indicating no signal upon exposure of the surface to non-complementary DNA [84].	26
Figure 1.13: (a) Effect of functionalisation techniques on the stability of pSi in 10% (v/v) EtOH in PBS. The reduction in normalised EOT ( $n_{\text{eff}} l / (n_{\text{eff}} l_0)$ ) over time decreases	

with increased functionalisation. (□) hydride terminated pSi, (■) ozone oxidised pSi, (○) thermally oxidised pSi (400°C 1 hr), (●) ozone oxidised pSi functionalised with (2-pyridyldithiopropionamidobutyl)dimethyl-methoxysilane. (b) Effect of biotin – streptavidin binding on the EOT of a pSi substrate. (A) Control, introduction of a solution containing pre-reacted biotin – streptavidin; (B) addition of 10 μM streptavidin and subsequent binding to biotin; (C) washing steps with buffer; (D) introduction of dithiothreitol reduced the disulphide bonds and cleaved the protein complex from the surface [66]. .....27

Figure 1.14: EOT sensorgram showing reversibility of IgG binding to a Protein A modified surface [88]. Biotin functionalised pSi was introduced to PBS and a baseline established. 1 mg/mL of streptavidin was then introduced followed by a PBS wash. The surface was then exposed to 2.5 mg/mL of biotinylated Protein A before being rinsed with PBS. 2.5 mg/mL of Human IgG was then introduced before being washed with 0.1 M acetic acid. Human IgG was then re-introduced at the same concentration before once again being rinsed with acetic acid. ....28

Figure 1.15: EOT real-time experiment showing detection of DNA hybridisation via corrosion of the pSi surface [91]. (A) Addition of non-complementary DNA, (B) Addition of cDNA and subsequent degradation in 100 mM phosphate buffer, pH 7.0. (○) Represents p<sup>++</sup>, while (●) represents p<sup>+</sup> pSi.....30

Figure 1.16: (A) Effect of streptavidin detection on the EOT of a biotin-functionalised pSi surface in PBS [92]. a) Introduction of 1 mM of avidin. b) Washing step with buffer. c) Addition of 1 mM of ammonium persulfate, (NH<sub>2</sub>)<sub>2</sub>S<sub>2</sub>O<sub>8</sub>. d) Washing step with buffer. e) Introduction of 100 mM of biotin-Ni<sup>2+</sup>cyclam. f) Washing step with buffer. g) Addition of 1 mM of (NH<sub>2</sub>)<sub>2</sub>S<sub>2</sub>O<sub>8</sub>. (B) Reflectance spectra of the biotin functionalised pSi. The black line represents the chip prior to addition of avidin, while the red line represents the surface after 20min incubation with 1 mM of avidin. The blue trace depicts the surface after incubation with 100 mM of biotin-Ni<sup>2+</sup>cyclam and 1 mM of (NH<sub>2</sub>)<sub>2</sub>S<sub>2</sub>O<sub>8</sub>. .....32

Figure 1.17: Effect on the effective optical thickness of a La protein functionalised pSi surface upon detection of anti-La antibodies. A) Baseline in PBS. B) Introduction of a 200 ng/mL anti-La solution. C) Addition of IgG-HRP (1:500) and D) Introduction of OPD solution (4 mg/mL). The sensor surface is represented as a solid line, while the control (no anti-La) is shown as a dashed line. ....33

Figure 1.18: Real-time detection of *E. coli* on pSi. (a) EOT vs. time, (b) Reflected intensity vs. time, (c) & (d) SEM micrographs of *E. coli* within the porous silicon matrix following a sensing experiment [93]. .....34

Figure 1.19: (a) Schematic of a double-layered pSi film and sensor signal readout [57]. The schematic identifies the layers associated with this sensor and highlights how the interaction of light with each layer produces a unique reflectance effect. The combination of layers 1 and 2 gives rise to layer 3 which is utilised in the detection mechanism. (b) The plot represents the introduction of sucrose and BSA to the double-layered pSi film. The real-time trace of the EOT of layer 3 (a combination of layers 1&2) and layer 2 are depicted, allowing the calculation of a difference trace. The smaller pores of layer 2 do not allow entry of the large BSA and as such only respond to the smaller sucrose molecule, while layer 1 responds to both. This enables the selective detection of BSA by layer 1 even in the presence of large amounts of sucrose. (All data acquired in Buffer pH 4). .....36

Figure 1.20: (a) Pepsin deposited onto zein modified pSi at various pmol levels, (b) Subsequent red shift of a pSi rugate filter reflectance peak due to increasing concentrations of the protease, pepsin [95]. .....37

Figure 1.21: Optical response of a peptide modified pSi multilayer sample upon exposure to the protease, subtilisin ( $(\Delta\lambda_{\text{protease}} - \Delta\lambda_{\text{control}} / \Delta\lambda_{\text{peptide}}) \times 100$ ). The low value observed at 37 $\mu\text{M}$ can be attributed to enzyme denaturation and adsorption to the pores, reducing the blue shift [96].	38
Figure 1.22: Intensity of scattered light from a pSi surface as a function of bacterial cell concentration (CFU/mL) [97].	39
Figure 1.23: Light scattering of a pSi resonance peak due to morphological changes in primary rat hepatocytes upon cell death from the toxin $\text{Cd}^{2+}$ . (a) The right axis depicts the relative intensity of light from the pSi surface and the left axis shows the percent viability from MTT stain with respect to time after the introduction of 50 $\mu\text{M}$ $\text{Cd}^{2+}$ to rat hepatocytes. The solid blue trace represents the change in intensity of light scattering. The red trace represents a control contain no $\text{Cd}^{2+}$ , while (●) denotes a corresponding MTT stain viability assay on a typical petri dish. (b) The pSi spectra clearly depicts an increase in the intensity of scattered light over 10 hrs [98].	41
Figure 1.24: Reduction in reflected light intensity upon functionalisation of pSi with 3-aminopropyltriethoxysilane and immobilisation of a polyclonal mouse antibody [99].	42
Figure 1.25: SEM cross-section of a microcavity displaying the confined defect layer [100].	42
Figure 1.26: Photoluminescence spectra of a Gram-negative biosensor. Blue plot: Prior to addition of bacteria, Red plot: after incubation with bacteria, and Green plot: difference between the spectra before and after addition of bacteria. The spectrum on the left depicts the addition of Gram-positive bacteria and subsequent lack of a difference signal. The spectra on the right represents the addition of Gram-negative bacteria and displays a large wavelength shift and difference signal due to the specific interaction with the surface [101].	43
Figure 1.27: Microcavity sensor calibration curve for rabbit IgG. Extent of resonance wavelength shift upon binding of increasing concentrations of rabbit IgG [48].	44
Figure 1.28: (a) & (b) Cross-section SEM images of the silicon microcavity used to detect the Intimin-ECD protein. (c) Top view of the same pSi sample. (d) Reflection spectrum of the microcavity structure with an indicative absorption dip at $\sim 830$ nm [103].	46
Figure 1.29: Detection of DNA hybridisation via an increase in photoluminescence intensity. (a) Functionalisation of pSi with trimethoxy-3-bromoacetamidopropylsilane, (b) immobilisation of the single stranded probe DNA, (c) hybridisation of the probe and cDNA; and (d) exposure to non-cDNA. (I – prior to attachment, II – after attachment) [109].	48
Figure 1.30: Chemiluminescence signals upon <i>E. coli</i> sensing on pSi and planar silicon against a pSi control. The increased surface area associated with pSi led to 3x the light emission of a planar silicon surface (RLU – Relative Light Units/sec) [110].	49
Figure 1.31: Cross-sectional SEM images of a pSi microarray well in two different magnifications [111].	51
Figure 1.32: Liver disease biosensor array, (a) Cross-sectional schematic of PDMS microfluidic system on top of a silicon substrate, (b) photograph of the device [112].	52
Figure 1.33: (a) Schematic of the pSi capacitance sensor for DNA. (b) Impedance ( $Z$ ) and (c) phase angle ( $\Theta$ ) of the pSi device. The introduction of the probe DNA (pDNA1) and complementary DNA (cDNA1) result in a large change to both properties. The recovery of the signal to baseline is attributed to the drying of the sample prior to introduction of cDNA1 [115].	54

Figure 1.34: Schematic depicting the cell wall architecture of the major types of bacterial cells covered by S-layers. (a) Most archaea: S-Layer proteins are the only cell wall component external to the cytoplasmic membrane. (b) Gram-positive eubacteria and archaea. (c) Gram-negative eubacteria and cyanobacteria: S-layers are bound to the outer membrane (adapted from [119]).	55
Figure 1.35: Schematic identifying the known S-layer lattice patterns. Each lattice unit is formed from the symmetric array of identical mono-, di-, tri-, tetra-, or hexamer subunits. Graphic adapted from [119].	58
Figure 1.36: S-layer lattice on the surface of a bacterial cell and after extraction and recrystallisation. (a) Electron micrograph of S-layer lattice on the wall of a <i>Desulfotomaculum nigrificans</i> NCIB 8706 bacterial cell [118]. The lattice displays a square pattern (p4 symmetry). Scale bar 100 nm. (b) Liquid AFM image of isolated S-layer protein recrystallised on a silicon wafer. Protein was extracted from <i>Lysinibacillus sphaericus</i> CCM 2177 and also displays p4 symmetry. Image parameters: 0.5 $\mu\text{m} \times 0.5 \mu\text{m}$ , Z-range 2 nm [134].	59
Figure 1.37: Schematic of the role of calcium in the self-assembly of S-layer subunits into a complete morphological unit [135].	60
Figure 1.38: (a) SEM micrograph of cellulose microbeads coated with the rSbpA <sub>31-1068</sub> /ZZ fusion protein. (b) Schematic depicting the surface of the microbeads and the capture of Human IgG via the S-layer fusion protein [148].	64
Figure 1.39: SPR Sensorgram showing association (—) and dissociation (- - -) between PSA and an rSbpA <sub>31-1068</sub> /cAb-PSA-N7 coated gold chip. The retention of PSA after washing indicated specific binding of PSA to the S-layer fusion protein [153].	64
Figure 2.1: Schematic of the Teflon electrochemical etching cell used to fabricate pSi	80
Figure 2.2: pSi biological reaction vessel. (a) Assembled vessel and (b) the disassembled components.	82
Figure 2.3: Interferometric Reflectance Spectroscopy. (a) Schematic of the IRS components and operation. (b) IRS flow cell used for pSi studies.	84
Figure 3.1: SEM analysis of the 2-step n-type template etching protocol. (a) Templated silicon surface after exposure to 275 mA/cm <sup>2</sup> for 1.82 seconds. (b) Final porous layer after the application of a second, lower current density, 40 mA/cm <sup>2</sup> for 100 seconds. All scale bars represent 200 nm.	94
Figure 3.2: Comparison between a templated and non-templated etches on n- and p-type pSi. (a & b) N-type pSi etched at 275 mA/cm <sup>2</sup> for 1.82 seconds followed by 40 mA/cm <sup>2</sup> for 100 seconds. (c & d) P-type pSi etched at 450 mA/cm <sup>2</sup> for 10 seconds. All scale bars depict 1 $\mu\text{m}$ . Both the cross-sectional and surfaces micrographs were analysed to extract pore size and pore to pore distributions which are included next to each image.	95
Figure 3.3: Dependence of pore diameter of n-type pSi on current density.	96
Figure 3.4: The relationship between current density and porosity for n-type pSi.	97
Figure 3.5: The relationship between current density and the rate of the electrochemical etching process for n-type pSi.	98
Figure 3.6: Relationship between current density and the sensitivity of the material to refractive index change as assessed by optical interferometry. (a) Response of a 50 mA/cm <sup>2</sup> pSi sample to: i – milliQ water (n = 1.3334), ii – ethanol (n = 1.3611), iii – isopropanol (n = 1.3776), iv – milliQ water. (b) Combined EOT responses for different current densities normalised to 1 refractive index unit.	99
Figure 4.1: Reaction pathway of BCIP/NBT precipitation [165].	104
Figure 4.2: Surface functionalisation procedure showing oxidation, silanisation and biomolecule immobilisation.	107

Figure 4.3: Schematic and experimental timeline of the alkaline phosphatase, BCIP/NBT based pSi immunosensor. (a) Schematic detailing the major steps of the immunosensor procedure, Step 1: human IgG (yellow protein) capture. Step 2: binding of the secondary antibody and formation of a sandwich immunoassay. Step 3: precipitation of the substrate BCIP/NBT by alkaline phosphatase. (b) Experimental timeline indicating the sensor sequence. ....	110
Figure 4.4: Schematic detailing the formation of immunoassay patterned pSi. (1) Capture antibody pSi was masked with a PDMS film and exposed to human IgG analyte (yellow protein). (2) The human IgG patterned pSi was unmasked and exposed to the secondary antibody conjugated to alkaline phosphatase. (3) Incubation with BCIP/NBT caused precipitation to only occur in the unmasked region. ....	112
Figure 4.5: SEM micrographs of 0.008-0.02 $\Omega$ .cm n-type pSi etched following a two step process – surface templating: 275 mA/cm <sup>2</sup> for 1.82 seconds, pore propagation: 50 mA/cm <sup>2</sup> for 45 seconds. (a) Top down view of the pSi surface. (b) Cross-sectional perspective. (c) Pore size distribution histogram. ....	115
Figure 4.6: IR spectra of sequential pSi surface modifications resulting in the immobilisation of $\alpha$ -human IgG capture antibody. (a) Freshly etched, thermally oxidised, isocyanate silanised and capture antibody immobilised pSi. (b) Expanded view of the isocyanate silane and capture antibody spectra to highlight the urea vibrations more clearly. ....	118
Figure 4.7: Response from de-phosphorylation of BCIP by alkaline phosphatase on pSi. (a) Active and control n-type pSi surfaces. (b) Active and control p-type pSi surfaces. ....	120
Figure 4.8: Response from precipitation of BCIP/NBT by alkaline phosphatase on n-type pSi as a result of oxidation protocol and pH. ....	123
Figure 4.9: Response from precipitation of BCIP/NBT by alkaline phosphatase on n-type pSi as a result of reduced exposure times. (a) Active pSi surfaces containing covalently immobilised alkaline phosphatase. (b) Control pSi surfaces containing no enzyme. (c) Change in EOT experienced by both active and control surfaces. (d) Signal ratio, active:control, for each exposure time investigated. ....	125
Figure 4.10: Effect of biocatalysed BCIP/NBT precipitation on the fringe pattern of pSi. (a) Active surface containing the alkaline phosphatase enzyme. (b) Control surface containing no enzyme. ....	128
Figure 4.11: Comparison of 3 signal processing techniques. Goat $\alpha$ -human IgG antibody conjugated to alkaline phosphatase was covalently immobilised pSi at dilutions of 0:1, 1:5000 and 1:2000 antibody:Tris buffer. The modified surfaces were then exposed to BCIP/NBT and the response monitored. (a) Percentage change of EOT. (b) Percentage change of wavelength shift. (c) Percentage change in intensity at 600 nm. (d) Combined data from a, b and c comparing the signal strength from the three approaches. ....	130
Figure 4.12: Effect on the reflected optical profiles of pSi and flat silicon in response to precipitation of BCIP/NBT. (a) & (b) Active and control pSi surfaces. (c) & (d) Active and control flat silicon surfaces. ....	132
Figure 4.13: Comparison of the change in intensity experienced by pSi and flat silicon upon precipitation of BCIP/NBT. (a) Change in intensity over time experienced by pSi and flat silicon surfaces upon exposure to BCIP/NBT (Active – alkaline phosphatase, Control – no enzyme). (b) Comparison of the total signal response experienced by pSi and flat silicon. ....	133
Figure 4.14: Combined porous silicon reflection spectra and corresponding change in intensity at 600 nm for the detection of 500 ng/mL human IgG. (a) Compiled fringe patterns from 0 to 92 minutes depicting a sharp decrease in the intensity of the reflected light upon detection of the human IgG, this effect is particularly strong	

	over the region 500 nm – 750 nm. (b) Change in reflected light intensity over time at 600 nm, the absorbance wavelength of NBT [166].	134
Figure 4.15:	Human IgG detection on pSi via alkaline phosphatase catalysed precipitation of BCIP/NBT. (a) Sensorgrams representing the change in reflected intensity at 600 nm for the detection of human IgG. Analyte concentration was varied between 0 ng/mL, and 2000 ng/mL. The detection event occurred at 70 minutes, while the signal step at 80 minutes was a result of a final rinsing step. (b) Background corrected standard curve of human IgG detection on pSi via alkaline phosphatase – BCIP/NBT precipitation.	136
Figure 4.16:	Replicate intensity measurements for a pSi immunoassay sensor exposed to (a) 0 ng/mL human IgG analyte; and (b) 10 ng/mL human IgG analyte. The black trace represents intensity measurements; the blue dotted line represents the average value, while the red dashed line represents the limit of detection.	137
Figure 4.17:	Precision profile of the alkaline phosphatase - BCIP/NBT based human IgG pSi immunosensor. The dashed line represents the threshold of the working range of the assay.	140
Figure 4.18:	Sensorgrams representing cross-reactivity to alternate biomarkers on the alkaline phosphatase - BCIP/NBT based human IgG pSi immunosensor. (a) Positive and negative cross-reactivity controls using Rabbit IgG. (b) Positive and negative cross-reactivity controls using BSA. Note: the negative control for both species was spiked with 25 ng/mL human IgG.	141
Figure 4.19:	Cross-sectional and top down SEM images of pSi following a human IgG immunosensor experiment. (a), (b) & (c) Control pSi surface exposed to 0 ng/mL human IgG (scale bar = 1 $\mu\text{m}$ unless otherwise identified). (d), (e) & (f) Active pSi surface exposed to 1000 ng/mL human IgG. (g) Schematic of the flow cell configuration and the location of the strong colour change on active pSi. (h) EDAX analysis of the active pSi surface in (f).	144
Figure 4.20:	IR characterisation of pSi surfaces following a human IgG immunosensor experiment. (a) IR spectra displaying covalently immobilised capture antibody pSi prior to immunosensing, and masked and unmasked patterned pSi following a immunosensor experiment. (b) An expanded section of the IR spectra displaying labelled stretching vibrations of precipitated BCIP/NBT more clearly. (c) IR correlation intensity map of IR spectra matching that of the catalysed BCIP/NBT peak at 1320 $\text{cm}^{-1}$ . (d) Schematic of the patterned pSi and the resulting immunoassay configuration following the immunosensor experiment. The IR map was obtained from the interface between the PDMS masked and unmasked regions.	148
Figure 5.1:	Schematic of common receptor immobilisation techniques on biosensing platforms. Binding bio-receptors via (a) adsorption and (b) covalent approaches can lead to the miss-alignment and steric hindrance of molecules such as capture antibodies.	153
Figure 5.2:	Schematic of the genetically modified SbpA-ZZ fusion protein. The N-terminal contains a binding domain for the SCWP while the C-terminal has been modified to contain two Z domains capable of binding the Fc chain of IgG antibodies. The protein architecture aligns the IgG such that the antibodies active sites point away from the solid support. Adapted from [119].	154
Figure 5.3:	SDS-polyacrylamide gel electrophoresis of whole cell extract and purification of SbpA from <i>L. sphaericus</i> ATCC 4525. Lanes: M = Protein marker; C = Pellet of <i>L. sphaericus</i> bacterial culture; S1–S4 & P1–P4 = Supernatant and pellet fractions following cell lysis and subsequent centrifugation and washing steps; GnHCl = S-layer unfolding step with guanidine hydrochloride; P5 & S5 = Pellet and supernatant	

fractions following dialysis and centrifugation. The single band in the S5 lane has a molecular weight of approximately 130 kDa. ....	170
Figure 5.4: SEM micrographs of n-type pSi scaffolds for S-layer recrystallisation. (a) Cross-sectional micrograph of an initial template etch demonstrating the roughness of the surface. Scale bar 200 nm. The porous silicon matrix is propagated from this surface template. (b) Top-down micrograph of pSi surface following pore propagation. Scale bar 1 $\mu\text{m}$ . ....	171
Figure 5.5: Digital photograph of a static water contact angle measurement performed on freshly ozone treated silicon. ....	172
Figure 5.6: Liquid AFM images of recrystallised SbpA protein on various surface chemistries. Images are ranked in order of increasing surface hydrophobicity. The left column shows 10 $\mu\text{m}^2$ height images and the scale bars correspond to 2 $\mu\text{m}$ . The right column shows 400 $\text{nm}^2$ height images and the scale bars correspond to 100 nm. ....	175
Figure 5.7: AFM analysis of recrystallised SbpA protein on ozone treated silicon. (a) AFM height image indicating the average centre-to-centre distance (CtC) between monomeric protein subunits. Scale bar 25 nm, Z-range 1.2 nm (b) 3D representation of the SbpA protein layer (c) AFM height image indicating the sectional height analysis of a SbpA protein layer on ozone treated silicon. The protein layer was removed from the underlying silicon surface through increased tip force. Scale bar 100 nm, Z-range 30 nm. (d) Line profile showing the height of the SbpA layer formed. (e) Schematic representation of SbpA protein structures formed on hydrophobic and hydrophilic surface chemistries. Adapted from [134, 139]. ....	178
Figure 5.8: SDS-polyacrylamide gel electrophoresis detailing the purification of the fusion protein rSbpA31-1068/ZZ (SbpA-ZZ) from <i>E. coli</i> BL21DE3. Lanes: (a), (g) & (q) Protein marker – these lanes are highlighted by a blue line; (b) <i>E. coli</i> pre-culture; (c) <i>E. coli</i> culture prior to induction; (d) <i>E. coli</i> culture after induction and expression of SbpA-ZZ; (e)&(f) <i>E. coli</i> culture 2 and 4 hours after induction; (h) Cell lysis supernatant; (i) Cell lysis pellet; (j) IgG column – Flow through 1; (k) IgG column – IgG micro bead matrix; (l) IgG column – Flow through 2; (m) IgG column – wash 1; (n) IgG column – wash 2; (o) IgG column – elutant; (p) IgG column – IgG matrix; (r) IgG column – wash 4; (s) IgG elutant following dialysis containing purified SbpA-ZZ; (t) Precipitate formed during dialysis. ....	180
Figure 5.9: Liquid AFM images of recrystallised SbpA-ZZ protein on ozone oxidised silicon and polystyrene. (a)&(c) Height image of a 10 $\mu\text{m}^2$ area, scale bar 2 $\mu\text{m}$ . (b)&(d) Height image of a 400 $\text{nm}^2$ area, scale bar 100 nm. ....	182
Figure 5.10: AFM analysis of recrystallised SbpA-ZZ protein on ozone treated silicon. (a) AFM height image indicating the average CtC distance between monomeric protein subunits. Scale bar 50 nm, Z-range 1.5 nm. (b) 3D representation of the SbpA-ZZ protein layer (c) AFM height image indicating the sectional height analysis of a SbpA-ZZ protein layer on oxidised silicon. Scale bar 100 nm, Z-range 10 nm. (d) Line profile showing the height of the SbpA-ZZ layer. ....	184
Figure 5.11: Assessment of the binding affinity of SbpA-ZZ to IgG antibodies via sandwich immunoassay to human IgG on a 96-well untreated polystyrene plate. Recrystallised SbpA-ZZ and SbpA surfaces were exposed to sheep $\alpha$ -human IgG which selectively bound to the Z domains on SbpA-ZZ. Exposure to 250 ng/mL of the target analyte, human IgG, and formation of an immunocomplex containing a goat $\alpha$ -human IgG secondary antibody conjugated to alkaline phosphatase caused a colour change upon de-phosphorylation of the enzyme substrate BCIP/NBT which was monitored at 530 nm. ....	186

Figure 5.12: Human IL-6 sandwich ELISA standard curves performed on High Bind, Medium Bind, Tissue Culture, SbpA-ZZ and SbpA surfaces. Native SbpA and SbpA-ZZ fusion protein were recrystallised on each type of 96-well microtiter plate and the response compared against untreated wells. (a) ELISA response on Costar 9018 High Binding 96-well microtiter plate. (b) Response on Costar 9017 Medium Binding 96-well microtiter plate. (c) Response on Costar 3596 Tissue Culture Treated 96-well microtiter plate (d) Comparison of the ELISA signal observed on the tested surfaces for an analyte concentration of 200 pg/mL Human IL-6.....	189
Figure 5.13: Cross-sectional SEM micrograph of n-type pSi used as a scaffold for SbpA-ZZ recrystallisation and sensing experiments. Scale bar 1 $\mu\text{m}$ . For the relevant SEM top-down perspective, refer to Figure 5.4 .....	192
Figure 5.14: EOT sensorgram as a function of time of SbpA-ZZ recrystallisation on pSi. The fusion protein was added at a concentration of 0.1 mg/mL.....	194
Figure 5.15: Background corrected human IgG standard curve on a SbpA-ZZ modified pSi optical immunosensor platform.....	195
Figure 5.16: Comparison of the human IgG pSi immunosensor prepared using covalent and SbpA-ZZ functionalisation methods. (a) Standard curves for human IgG detection. (b) Precision profiles of the two sensors. The dashed line represents the threshold of the working range of the assay. ....	197
Figure 6.1: Silver enhancement of immunogold. Gold labelled biomolecules target specific analytes and the reduction of silver ions to bulk silver by hydroquinone results in the coating and growth of the gold nanoparticles. In this manner the detection event is amplified improving the sensitivity compared to the use of gold alone. ....	203
Figure 6.2: Proposed silver enhancement of gold transduction on pSi.....	204
Figure 6.3: Reaction scheme for the covalent attachment of AuNP's on pSi. Oxidised pSi is first silanised with APTES and the sample then exposed to AuNP's and cross-linked to the surface via addition of EDC/NHS. ....	207
Figure 6.4: Immobilisation of biomolecules to gold plated pSi. Gold deposits are first treated with MUA to form a carboxylic acid terminated SAM. The surface is then activated with EDC/NHS to facilitate covalent immobilisation of enzymes and antibodies. ....	208
Figure 6.5: SEM micrographs of covalently immobilised gold nanoparticles on pSi. (a),(b)&(c) Solution immobilisation approach (Method 1). Respective scale bars 25 $\mu\text{m}$ , 500 nm, 250 nm. (d),(e)&(f) Drying immobilisation approach (Method 2). Respective scale bars 2 $\mu\text{m}$ , 200 nm and 500 nm. The sample in (f) was not indicative of the normal porous structure and was etched at 35 mA/cm <sup>2</sup> . Its presence is merely to demonstrate propagation of AuNP's within the pores. (g) Schematic representation of method 1 protocol and (h) method 2.....	215
Figure 6.6: Silver enhancement of AuNP pSi prepared under method 1 (M1) and method 2 (M2) using commercial reagents. (a) pSi baselined in milliQ water. (b) Sample shielded from light and "Nanoprobes LI" silver enhancement solution injected into the flow cell. (c) MilliQ water rinse and reacquisition of the sample.....	217
Figure 6.7: SEM micrographs of silver contrast enhancement on gold nanoparticle decorated pSi. (a)&(b) AuNP's immobilised via method 1. Respective scale bars 1 $\mu\text{m}$ and 250 nm. (c)&(d) AuNP's immobilised via method 2. Scale bars both represent 500 nm. ....	218
Figure 6.8: Silver enhancement of AuNP's on pSi with 6 mM silver acetate and 22 mM hydroquinone in citrate buffer, pH 3.8. (a) EOT sensorgram of silver enhancement on AuNP modified pSi and APTES pSi. (i) AuNP modified pSi baselined in citrate buffer, pH 3.8. (ii) Sample shielded from light and silver enhancement solution injected into the flow cell. (iii) Surface rinse and reacquisition of the sample. (b)	

Effect of the silver contrast enhancing solution exposure time on the EOT response of AuNP modified pSi.....	219
Figure 6.9: Electroless deposition of gold reaction scheme. The electroless deposition process described in Chapter 6 section 6.3.2.3 first involves the sensitisation of the porous silicon surface with tin cations through electrostatic interactions. The sensitised porous layer is then ‘activated’ with silver nitrate which causes a redox reaction in which Sn <sup>2+</sup> is oxidised to Sn <sup>4+</sup> and aqueous Ag <sup>+</sup> ions are reduced to bulk silver, coating the porous surface with silver particles. Gold deposition then occurs in solution through the galvanic replacement of the silver particles by the more noble metal and growth of these particles into a coating or film is achieved by the concurrent reduction of Au <sup>+</sup> to bulk gold by formaldehyde. Variation to the deposition time is used to achieve gold coatings of different coverage and thickness [238, 242, 243]. .....	222
Figure 6.10: SEM micrographs detailing the extent of gold deposition within the porous matrix as a function of exposure time to Au bath (beta). The left column represents a top down perspective of the porous surface, while the right column displays the corresponding cross-sectional view. All surfaces were exposed to Au bath (Alpha) for 2 hours before immersion in Au bath (beta) for: (a)&(b) 0 hours, (c)&(d) 30 minutes, (e)&(f) 5 hours and (g)&(h) 17 hours. All scale bars represent 500 nm. ....	223
Figure 6.11: Effect of electroless deposition of gold on the optical properties of pSi. (a) Change experienced by the reflected fringe pattern as a function of deposition time. (b) Change to the calculated EOT of the porous layer as a function of deposition time.....	224
Figure 6.12: Silver contrast enhancement of electrolessly deposited gold on pSi with silver acetate and hydroquinone. (a) EOT sensorgram of silver contrast enhancement on pSi subjected to varying degrees of gold deposition. (i) Gold plated pSi baselined in citrate buffer, pH 3.8. (ii) Sample shielded from light and silver contrast enhancement solution injected into the flow cell. (iii) Surface rinse with citrate buffer and reacquisition of the sample. (iv) Final point in the acquisition. (b) Effect of silver contrast enhancement of gold on the reflected fringe pattern of pSi.....	226
Figure 6.13: (a) Organic synthesis of hydroquinone diphosphate (HQDP). HQ – Hydroquinone; HQDC – bis(phosphorodichloridate); HQDP – Hydroquinone diphosphate; C(HQDP) – Cyclohexylamine salt; Na(HQDP) – Sodium salt. (b) Hypodiphosphoric acid sodium salt bi-product. (c) Electropray Mass Spectroscopy spectrum of aqueous Na(HQDP) solution. The major peaks at 269 and 291 m/z relate to the HQDP compound, while the other major peak at 159 m/z represents the presence of a bi-product. ....	228
Figure 6.14: Schematic and scheme of the proposed reaction pathway for enzyme mediated reduction of silver on gold plated pSi.....	229
Figure 6.15: Reactivity of hydroquinone diphosphate (HQDP) to silver acetate (SA) and the reduction of SA by alkaline phosphatase (AP) mediated hydrolysis of HQDP to hydroquinone in solution.....	230
Figure 6.16: Alkaline phosphatase mediated silver contrast enhancement of electrolessly gold plated pSi. (a) EOT sensorgram of silver contrast enhancement in citrate buffer, pH 7.0. The plot represents both enzyme based (6 mM SA, 22 mM HQDP) and SA/HQ (6 mM SA, 22 mM HQ) enhancement. i – Citrate buffer, pH 7.0, ii – Enzyme silver contrast enhancing solution, iii – Citrate buffer, pH 7.0. (b) Combined sensor responses for the optimisation of the enzyme based system and relevant controls. ....	231
Figure 6.17: Detection of 10 µg/mL human IgG via alkaline phosphatase mediated silver contrast enhancement of gold on pSi. (a) Electrolessly gold plated pSi containing	

immobilised sheep  $\alpha$ -human IgG antibody in PBS, pH 7.4. (b) 10  $\mu$ g/mL human IgG in immunosensing buffer (Control, 0  $\mu$ g/mL). (c) Washing step and baseline in Tris buffer, pH 7.4. (d) 1:250 goat  $\alpha$ -human IgG secondary antibody conjugated to alkaline phosphatase in immunosensing buffer. (e) Washing step and baseline in citrate buffer, pH 7.0. (f) Enzyme silver contrast enhancement solution – the flow cell was shielded from light to prevent non-specific reduction of silver. (g) Wash with citrate buffer, pH 7.0. ....235

# List of Tables

Table 1.1: Common approaches to optical immunosensing. Adapted from [8].....	6
Table 1.2: Common alkaline phosphatase substrates used in optical immunosensing and immunostaining.....	8
Table 1.3: Overview of functional domains fused to S-layer proteins and their application. Adapted from [155].....	65
Table 2.1: Chemicals and biological substances used for pSi functionalisation, immunosensing and cell culture.....	73
Table 2.2: Proteins and commercial biological kits used in immunosensing and protein purification.....	74
Table 2.3: Cell lines and suppliers that were used for S-layer protein expression and extraction.....	74
Table 2.4: Custom made buffers and solutions used for pSi preparation, immunosensing, cell culture and protein purification.....	77
Table 2.5: Media used for the cell culture of <i>L. sphaericus</i> and <i>E. coli</i> .....	78
Table 2.6: 96 well microtiter plates used in ELISA and protein recrystallisation studies.....	78
Table 2.7: Silicon wafer, dopant type and resistivity used for pSi fabrication.....	79
Table 2.8: Typical conditions and electrolyte composition used for the electrochemical etching of Si.....	80
Table 2.9: Experimental timeline for human IgG immunosensing on pSi.....	85
Table 3.1: Electrochemical etching conditions used in the optimisation of the pSi optical immunosensor platform.....	91
Table 4.1: The absorbance wavelengths of the biocatalysed alkaline phosphatase substrates, BCIP & NBT.....	104
Table 4.2: Experimental timeline of the alkaline phosphatase BCIP/NBT based pSi sensor experiment.....	111
Table 4.3: Refractive indices of solutions used in the biocatalysation of BCIP/NBT by alkaline phosphatase.....	126
Table 4.4: Intra-assay precision of the alkaline phosphatase - BCIP/NBT based human IgG pSi immunosensor. The pools listed above correspond to the following concentrations of human IgG analyte, Low – 10 ng/mL, Medium – 250 ng/mL, High – 1000 ng/mL.....	140
Table 4.5: Cross-Reactivity of the alkaline phosphatase - BCIP/NBT based human IgG pSi immunosensor to biomolecules from other animal species.....	142
Table 5.1: Experimental timeline of the SbpA-ZZ-pSi human IgG immunosensor experiment.....	168
Table 5.2: Static water contact angle measurements as a function of surface chemistry.....	173
Table 5.3: SbpA lattice properties extracted from AFM analysis of in vitro protein recrystallisation on hydrophilic and hydrophobic surfaces. CtC – Centre-to-Centre distance between morphological units; SbpA D – S-layer thickness; Domain Ø – Diameter of S-layer crystalline domains; Mass – Theoretical mass of recrystallised protein on the surface.....	176
Table 5.4: SbpA-ZZ lattice properties extracted from AFM analysis of in vitro protein recrystallisation. CtC – Centre-to-Centre distance between morphological units; SbpA-ZZ D – S-layer Thickness; Domain Ø – Diameter of S-layer Crystalline domains; Mass – Theoretical mass of recrystallised protein on the surface.....	182

Table 5.5: Limits of detection of Human Interleukin-6 on commercial and SbpA-ZZ treated 96 well plate surfaces. SbpA treated surfaces exhibited a low background signal and were not included in this comparison.....	191
Table 5.6: Comparison of human IgG pSi immunosensor parameters as a function of surface functionalisation. The table contains sensitivity (LOD) and precision (CV) data for human IgG pSi immunosensors prepared using covalent and SbpA-ZZ functionalisation methods. The limit of detection was calculated using the $3\sigma$ technique and the intra-assay pools correspond to the following concentrations of human IgG analyte, Low – 10 ng/mL, Medium – 250 ng/mL, High – Covalent: 1000 ng/mL, SbpA-ZZ: 500 ng/mL. ....	197
Table 6.1: Experimental timeline for the detection of human IgG by enzyme mediated contrast enhancement of gold plated pSi.....	213
Table 6.2: Effect of surface and silver contrast enhancement conditions on the signal to noise ratio of the pSi platform. S/N was calculated from $\Delta EOT/EOT_0$ values for active and control surfaces from each study. ED = 1hour Electroless Deposition of gold on pSi, SA = 6 mM silver acetate, HQ = 22 mM hydroquinone, AP = 10 U/mL covalently immobilised alkaline phosphatase. ....	233

# List of Equations

Equation 1.1: Fabry-Perot fringe pattern. ....	23
Equation 1.2: Bruggeman effective medium approximation. ....	24
Equation 2.1: Gravimetric determination of porosity. ....	82
Equation 4.1: Effective Optical Thickness of a porous film. ....	126
Equation 4.2: Refractive index of mixed solutions. ....	127
Equation 4.3: Limit of detection (Absorbance) [188]. ....	137
Equation 4.4: Limit of Detection (Concentration) [188]. ....	138
Equation 4.5: Intra-assay precision [21]. ....	139

## List of Abbreviations

---

Abbreviation	Full Name
Ab	Antibody
ABS	Antigen Binding Site
ADH	Alcohol dehydrogenase
AFM	Atomic Force Microscopy
AP	Alkaline Phosphatase
APTES	3-aminopropyl triethoxysilane
Atg	Antigen
ATR	Attenuated total reflectance
AuNP	Gold nanoparticle
BCIP	5-bromo-4-chloro-3-indoyl phosphate
BCIP-indigowhite	5,5-dibromo-4,4-dichloro-indigowhite
BSA	Bovine serum albumin
CCD	Charge-Coupled Device
CtC	Centre-to-centre distance
CV	Coefficient of variation
DCM	Dichloromethane
DMSO	Dimethyl sulfoxide
DNA	Deoxyribonucleic acid
<i>E. Coli</i>	Escherichia Coli
EDAX	Energy Dispersive X-ray Analysis
ED	Electroless Deposition
EDC	1-ethyl-3-(3-dimethylaminopropyl) carbodiimide
ELISA	Enzyme-Linked Immunosorbent Assay
EOT	Effective Optical Thickness
etc	et cetera
EtOH	Ethanol
FFT	Fast Fourier Transform
FTIR	Fourier Transformed Infrared Spectroscopy

---

---

GnHCl	Guanidine hydrochloride
HAc	Acetic acid
HF	Hydrofluoric acid
HQ	Hydroquinone
HQDP	Hydroquinone diphosphate
HRP	Horseradish peroxidase
IgA	Immunoglobulin A
IgG	Immunoglobulin G
IgM	Immunoglobulin M
IL-6	Interleukin-6
IPTES	3-isocyanatopropyl triethoxysilane
IPTG	Isopropyl $\beta$ -D-1-thiogalactopyranoside
IR	Infrared
IRS	Interferometric Reflectance Spectroscopy
<i>L. sphaericus</i>	<i>Lysinibacillus sphaericus</i>
LB	Lysogeny Broth
LOD	Limit of Detection
Method 1	Solution based immobilisation of AuNP's on pSi
Method 2	Drying based immobilisation of AuNP's on pSi
milliQ	Ultrapure water, resistivity 18.2 M $\Omega$ .cm
MS	Mass spectroscopy
MUA	11-Mercaptoundecanoic acid
$m\lambda$	Spectral order of the Fabry-Pérot fringe (m) times wavelength of the incident light striking the surface at an incident angle of 0° ( $\lambda$ )
Na(HQDP)	Sodium Salt of hydroquinone diphosphate
NB	Nutrient Broth
NBT	Nitro Blue Tetrazolium
nd	Average refractive index of a porous silicon layer (n) times porous silicon layer thickness (d)
NHS	N-Hydroxysuccinimide
NMR	Nuclear Magnetic Resonance spectroscopy
n-type	Phosphorous doped silicon

---

---

OD	Optical Density
OPD	O-Phenylenediamine dihydrochloride
Ozone Silicon	Ozone oxidised silicon, treated with mild thermal oxidation
PBS	Phosphate Buffer Saline
PBS-T	PBS-Tween® 20
PDMS	Polydimethylsiloxane
PEG	Polyethylene Glycol
PEG Silane	n-(triethoxysilylpropyl)-o-polyethylene oxide urethane
PFCS	Pentafluorophenyl dimethylchlorosilane
pSi	Porous silicon
PSS	Polystyrene sulfonate
Pty Ltd	Proprietary Limited
p-type	Boron doped silicon
QCM	Quartz Crystal Microbalance
RIA	Radio-immunoassay
RMS	Root mean squared
S/N	Signal to noise ratio
SA	Silver acetate
SbpA	S-Layer protein from <i>L. sphaericus</i>
SbpA-ZZ	Recombinant S-layer fusion protein, rSbpA <sub>31-1068</sub> /ZZ
SCWP	Secondary Cell Wall Polymer
SDS-PAGE	Sodium Dodecyl Sulfate - Polyacrylamide Gel Electrophoresis
SEM	Scanning Electron Microscopy
S-layer	Surface layer protein
SPR	Surface Plasmon Resonance
Sulfo-NHS	N-Hydroxysulfosuccinimide
TDFCS	Tridecafluoro-1,1,2,2-tetrahydrooctyl-dimethylchlorosilane
TIR	Total Internal Reflectance
TIRF	Total Internal Reflectance Fluorescence
TM	Trademark
TMB	3,3',5,5'-Tetramethylbenzidine

---

---

Tris	Trizma base
Tris-HCl	Trizma HCl
Tris-T	Tris buffer-Tween® 20
™	Trade Mark
UV-Vis	Ultraviolet-Visible
Z	Synthetic IgG binding domain
$\alpha$	Anti
$\lambda$	Wavelength
®	Registered

---

## List of Units

Unit Abbreviation	Full Name
%	Percentage
~	Approximately
<	Less than
>	Greater than
≤	Less than or equal to
≥	Greater than or equal to
°	Degrees
°C	Degrees Celsius
<sup>1</sup> H	Proton
A	Ampere
au	Arbitrary units
avg	Average
C	Coulomb
cm	Centimetre
cm <sup>-1</sup>	Reciprocal centimetres (wavenumbers)
d	Porous layer thickness
eV	Electronvolt
g	Grams
hr	Hour
J	Coupling constant (Hz).
kDa	Kilo Daltons
kV	Kilovolt
M	Molar
m/z	Mass to charge ratio
mA	Milliamps
min	Minute
mL	Millilitre
mM	Millimolar

---

mmol	Millimoles
n	Refractive index
ng	Nanogram
nm	Nanometre
∅	Diameter
pH	Potential of hydrogen
pKa	Acid dissociation constant
S	Singlet
sec	Seconds
v/v	Volume per volume
W	Watts
w/v	Weight per volume
ε	Molar extinction coefficient
μg	Microgram
μL	Microlitre
μm	Micrometre
μM	Micromolar
Ω	Ohms

---

## Peer Reviewed Publications

Szili, E.J., Jane, A., Low, S.P., Sweetman, M., Macardle, P., Kumar, S., Smart, R.St.C., Voelcker, N.H., 'Interferometric porous silicon transducers using an enzymatically amplified optical signal', *Sensors and Actuators B*, 160 (2011), 341-348.

Dronov, R., Jane, A., Shapter, J.G., Hodges, A., Voelcker, N.H., 'Nanoporous Alumina-based Interferometric Transducers Ennobled', *Nanoscale*, 3 (2011), 3109 - 3114.

Jane, A., Dronov, R., Hodges, A., Voelcker, N.H., 'Porous Silicon Biosensors on the Advance', *Trends in Biotechnology*, 27 (2009), 230-239.

Jane, A.O., Szili, E.J., Reed, J.H., Gordon, T.P., Voelcker, N.H., 'Porous Silicon Biosensor for the Detection of Autoimmune Diseases', *Proceedings of SPIE 6799* (2007), 6799081-11



# Chapter 1

---

## 1 Introduction

## **1.1 Immunoassays and Immunosensing Principles**

The ability to quickly and efficiently detect pathogens and disease markers is essential in today's healthcare industry. There exist many different methods to achieve this goal, however, one of the most convenient and widely used tools in clinical diagnostics is the immunoassay [1, 2]. The history of the immunoassay first began in the 1950's with the development of a radioisotope labelled immunoassay (RIA) by Yalow and Berson for the detection of insulin levels in blood [3, 4]. These early studies led to the rapid development of immunochemical methods for clinical use and in 1971 another landmark advancement was made with the introduction of enzymes as immunoassay labels, removing the hazards associated with radioactive isotopes. Since that time, the use of immunoassays has increased dramatically, forming the basis of many clinical diagnostic laboratories. The appeal of immunoassays over other analytical techniques lies in their many advantages, including low limits of detection, high analyte specificity, and a wide range of detectable analytes [2, 5]. They have been incorporated into a plethora of technologies and applications, including devices to detect viruses, disease markers, illicit drugs, pesticides and even industrial chemicals. From early beginnings, the unique flexibility of this immunoassay system continues to drive intensive research and herald exciting new sensing technologies.

### **1.1.1 Antibody Structure and Principles of Immunoassays**

The structure of Immunoglobulin G (IgG), the most widely used antibody in immunoassays, is well characterised and consists of a Y shape comprising of three equal-sized portions, loosely connected by a flexible tether (Figure 1.1) [6]. The antibody is comprised of two heavy and two light polypeptide chains that are linked together by disulphide bonds. The Fc stem of the protein is made from the heavy chains and determines the isotype of the antibody. The V structure contains both heavy and light chains with variable regions, constituting the antigen binding site (ABS). The sequence of these regions provides specificity to certain antigens with high affinity and specificity.

An immunoassay is an analytical technique which uses antibodies for quantitative detection of specific analytes. They are based on the interaction between an

epitope on the antigen (Atg) and the ABS of a selective antibody (Ab) to give a quantifiable product (Atg–Ab).

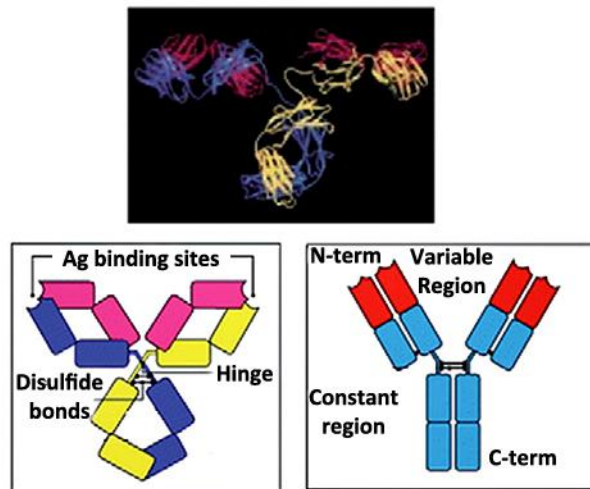


Figure 1.1: IgG antibody structure. Top: 3D representation of IgG determined via X-ray crystallography. Bottom: Schematic of the IgG structure and important regions [7].

### 1.1.2 Immunosensors

Immunosensors are affinity based biosensors that incorporate immunochemical reactions similar to immunoassays, to a transducer. Antigens or antibodies are immobilised to a transducer to form a sensing or recognition element for specific analytes. Binding of target molecules to form an immunocomplex is transformed into a measurable signal by the transducer. Detection of analytes based on this ‘immunoassay’ principle has been demonstrated since the 1960’s and continues to dominate clinical diagnostic techniques due to the strong selectivity and specificity associated with antibody-analyte binding, even in highly complex samples such as blood and urine [2]. Immunosensors have been developed using a number of transduction technologies and can generally be classified into three main groups: optical (intrinsic and extrinsic), microgravimetric and electrochemical [1]. The method of transduction is primarily related to the signal generation process caused upon interaction between antibodies and antigen. This signal can originate from physical changes to the mass or refractive index on the transducer induced by the binding of an antigen and antibody and formation of an immunocomplex. Such techniques are often referred to as direct immunoassays

and are restricted to highly sensitive techniques such as Surface Plasmon Resonance (SPR) or Quartz Crystal Microbalance (QCM).

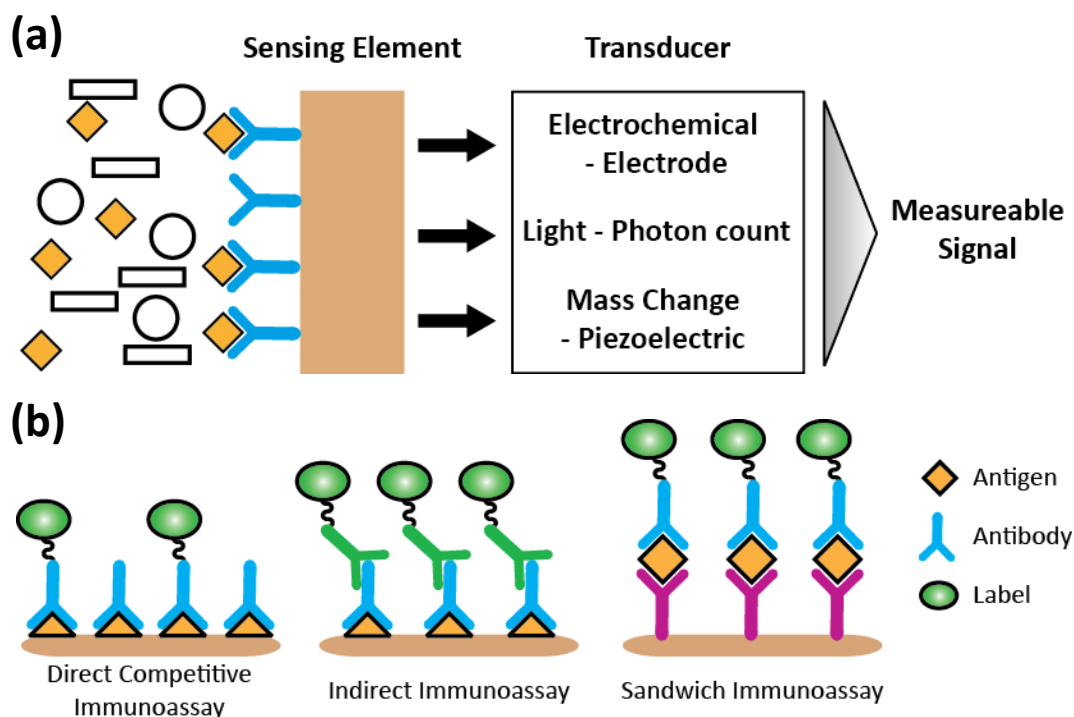


Figure 1.2: Immunosensor design principles. (a) Schematic of general immunosensor design. Adapted from [1]. (b) Common forms of labelled immunoassays utilised in immunosensing.

Another more common and sensitive approach involves the use of a unique label, such as an enzyme, nanoparticle or some other marker which is covalently attached to the analyte or antibody. The nature of these labels can provide changes to a range of properties including fluorescence, colour and resistivity to amplify the presence of a target molecule. Such techniques can be used in direct competitive, indirect and sandwich assay configurations (Figure 1.2 (b)). Competitive direct immunoassays involve the immobilisation of an antigen to the sensor surface and exposure to a medium containing the analyte and an artificially labelled analyte. The two compete with one another to bind to the immobilised receptor and the ratio of bound analyte is measured. Indirect assays are similar to the direct method; however a secondary, labelled antibody specific to the primary antibody is used. Sandwich assays are amongst the most popular due to their

sensitivity and robustness and employ immobilised antibodies to capture antigen after which a secondary, labelled antibody binds to the immunocomplex ‘sandwiching’ the antigen between the two antibodies. The incorporation of a label in all of these assays provides a pathway to register the binding event thus enhancing the sensitivity of immunosensors.

### ***1.1.3 Optical Immunosensing***

Due to the vast amount of literature and many forms of immunosensors, optical immunosensors will be the focus of subsequent discussion due to their relevance to the work in this thesis. This section will provide a general overview of major optical immunosensing techniques in addition to specific components vital to the development of the sensing devices reported in this thesis. Optical immunosensors currently dominate clinical diagnostics and form the largest group of immunosensing transducers [1, 8]. This type of immunosensor relies on changes to the optical properties of the antibody/antigen/sensor surface to provide a measure of the analyte present in a sample. The use of visible radiation as a transduction method offers a simple, sensitive, affordable, rapid and non-destructive approach to immunosensing. Monitoring changes in absorption, fluorescence, luminescence, light scattering or refractive index using photodiodes or photomultipliers, forms the basis of many optical immunosensing techniques. Table 1.1 contains the corresponding transduction techniques used in conjunction with these optical signals to form a functional immunosensor.

Optical Signal	Transduction Technique
Absorbance	Light intensity measurement
Reflectance	Light intensity measurement
Fluorescence	Light intensity measurement Total internal reflection fluorescence (TIRF)
Refractive index	Interferometry Surface plasmon resonance (SPR) Total internal reflection
Optical path	Interferometry

Table 1.1: Common approaches to optical immunosensing. Adapted from [8]

To accommodate such a large range of signals and transduction techniques, many different materials have been adapted for use as optical transducers, including planar optical waveguides [9], optical fibres [10, 11], polymers [2, 12, 13], glass [14], metalized diffraction gratings [15] and porous surfaces [16, 17].

### 1.1.3.1 Enzyme Labelled Immunosensors

Due to the broad range of optical transduction techniques, many different labels have been developed for use with optical indirect immunosensors, including fluorescent molecules, and nanoparticles and the most predominant label, enzymes [18]. Integration of enzymes allows a high degree of versatility by providing many detection routes and transduction options. Commonly used enzymes include alkaline phosphatase (AP), horseradish peroxidase (HRP),  $\beta$ -galactosidase, and luciferase which are capable of promoting a measurable colour or luminescence change at certain wavelengths [18]. Through the catalytic nature of enzymes, the original binding signal is amplified with colour production directly relating to the concentration of bound analyte.

#### 1.1.3.1.1 Enzyme-Linked Immunosorbent Assay (ELISA)

One of the most successful and widely used sensing techniques ever developed is based on an enzyme immunoassay. Since the development of the Enzyme-Linked Immunosorbent Assay (ELISA) in 1971 by Engvall *et al.* and van

Weemen *et al.*, this technique has become the backbone of the clinical diagnostics industry due to its sensitivity, high throughput, versatility and robustness [19, 20]. The generalised technique utilises an array of clear plastic wells to which an antibody or antigen is adsorbed. Formation of an immunocomplex containing an enzyme labelled secondary antibody is reported by adding a substrate that changes colour upon reaction with the enzyme. The absorbance or intensity of the resulting colour is proportional to the amount of enzyme bound to the well and thus the amount of antibody. In this manner the ELISA is used to quantitatively detect analytes. Most forms of immunoassays can be performed via this technique, including direct competitive, indirect and most commonly sandwich assays.

#### 1.1.3.1.2 *Alkaline Phosphatase*

Alkaline phosphatase (AP) has been used as an immunosensor label since the invention of ELISA in 1971, when it was used to quantify IgG in rabbit serum by Engvall *et al.* [19]. Since that time, AP has continued as a primary label for ELISA and now has a variety of commercially available substrates to suit a range of transduction techniques. The enzyme's name originates from its ability to catalyse the hydrolysis of an orthophosphoric monoester to provide an alcohol and an orthophosphate in alkaline conditions as shown in Figure 1.3.

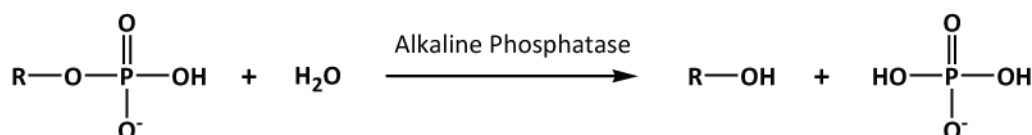


Figure 1.3: Alkaline phosphatase catalysed hydrolysis of a phosphate ester to an alcohol and orthophosphate.

Alkaline phosphatase optical sensor substrates normally consist of dyes or fluorescent molecules that have been phosphorylated rendering the compound colourless. Hydrolysis and 'dephosphorylation' of the substrate by AP then results in a measurable coloured product. Common substrates and their properties are listed in Table 1.2 [21]. Alkaline Phosphatase detection systems have been developed beyond ELISA and now appear in a wide range of technologies

including microfluidic [22], magnetic microbeads [23], paper ELISA's [24] and nanoparticle enhancement [25] optical sensors.

Substrate	Coloured Hydrolysis Product
p-Nitrophenyl phosphate	Yellow
4-Methylumbelliferyl phosphate	488 nm Fluorescence
5-bromo-4-chloro-3-indoxyl phosphate (BCIP)	Blue
Naphthol Phosphate	Reaction with secondary chromogens to produce red or blue coloured products.

Table 1.2: Common alkaline phosphatase substrates used in optical immunosensing and immunostaining.

### 1.1.3.2 Gold Nanoparticle Labelled Immunosensors

Advances in nanotechnology have resulted in a more recent form of labelling involving the conjugation of nanoparticles to secondary antibodies. The unique optical properties and tunability of many nanoparticles such as quantum dots and gold nanoparticles has led to their successful use in immunosensing applications. One of the simplest forms of nanoparticle based detection relies on a colour shift due to particle aggregation [7]. Gold nanoparticles (AuNP) are often used in such applications due to their plasmonic properties and subsequent high extinction coefficient. The optical properties of these nanoparticles are related to inter-particle separation and aggregation of AuNP's upon the formation of immunocomplexes can result in a shift in the extinction spectrum and a colour change.

Mirkin *et al.* first reported this phenomenon as a sensing mechanism in 1996, where AuNP tethered single stranded DNA caused aggregation of AuNP's and a colour shift upon DNA hybridisation [26]. Since then, AuNP's have been used as a label for many different sensing applications. More recently, Ambrosi *et al.* reported a colourimetric ELISA utilising AuNP's for the detection of the breast cancer biomarker, CA15-3. In this approach AuNP's acted as enzyme coated enhancers, increasing the number of enzymes per antibody, improving the

sensitivity and speed of the technique compared to traditional ELISA (Figure 1.4) [27].

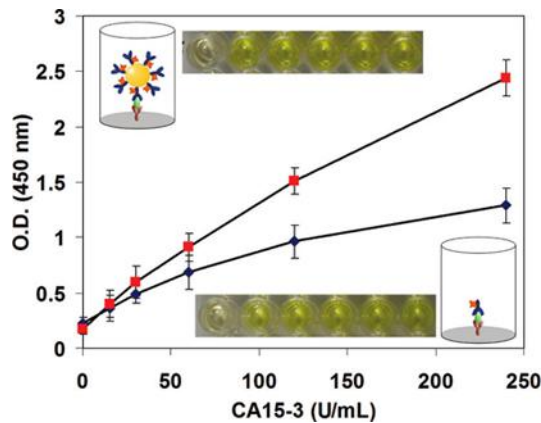


Figure 1.4: Enhanced detection of the breast cancer marker, CA15-3, with modified AuNP's [27]. The nanoparticles acted as carriers for the secondary antibody in a sandwich assay, resulting in increased numbers of enzyme labels per analyte. This led to an improvement in the sensitivity of the approach (red trace) compared with traditional ELISA methods (blue trace).

Another form of common immunosensor that utilises AuNP labelled antibodies is the lateral flow immunoassay or immunochromatographic assay. The most successful form of this sensor is the household urine pregnancy test that utilises aggregation of analyte bound AuNP labelled antibodies to form red lines over immobilised capture antibody or analyte to denote a positive or negative result [28]. Recently this form of qualitative sensor has been adapted to provide a highly sensitive quantitative platform. Yang *et al.* developed an immunochromatographic sensor utilising colloid gold antibody probes to detect the protein abrin-a [29]. The sensor strip reported good sensitivity, achieving a limit of detection of 10 ng/mL, however, the author was then able to increase the sensitivity 100-fold via a secondary amplification step. Following normal sensing, the size of the AuNP's was increased by a process known as silver enhancement. The reduction of silver nitrate in the presence of the reducing agent hydroquinone led to the catalysed deposition of silver metal on the AuNP's and the growth of the particles. The increase in particle size improved the detection signal by darkening the test line and allowing visualisation of abrin-a down to 0.1 ng/mL.

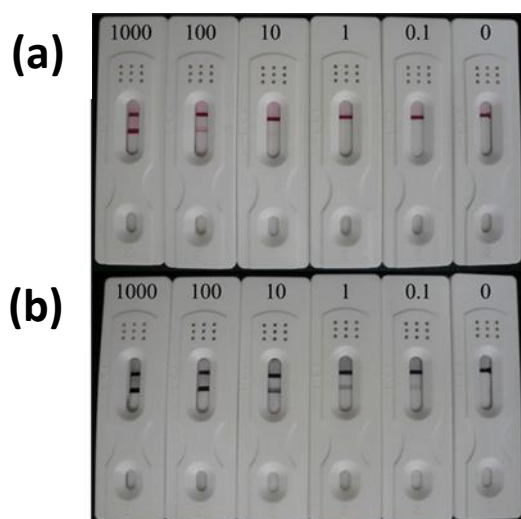


Figure 1.5: Detection limit of the test strip developed by Yang *et al.* [29]. Abrin-a standard solutions at concentrations of 0, 0.1, 1.0, 10, 100 and 1000 ng/mL were assayed. (a) The result of the immunochromatographic assay using gold labelled antibodies. (b) Amplified assay signal by gold promoted silver deposition (silver enhancement).

### 1.1.3.3 Surface Plasmon Resonance Immunosensing

Another main optical immunosensor technology is SPR. In a SPR immunosensor, the formation of an immunocomplex on the surface of a thin layer of metal alters the refractive index of the surface. This change in surface conditions alters the properties of light reflected off the metal surface and can be used to reveal information about the antibody/antigen binding. This technique is highly sensitive and can be used for unlabelled, direct immunosensing between an antibody and antigen. One such example is shown in Figure 1.6 which depicts a sensorgram for the detection of *Autographa californica* multiple nuclear polyhedrosis virus (AcMNPV) via direct immunosensing [30]. Baac *et al.* formed a sensing element on a SPR chip with three distinct layers; the first consisted of an amine-reactive crosslinker with a disulfide bond (DTSSP) which chemisorbed to the gold surface. IgG specific protein A was then covalently immobilised to the cross-linker to form the second layer and the third layer consisted of a mouse IgG monoclonal antibody against the AcMNPV pathogen (AcV1). Introduction of a negative control tobacco mosaic virus (TMV) did not illicit a response from the sensor, however introduction and specific binding of

the target AcMNPV yielded a shift in the angle of the reflected light, denoting successful detection.

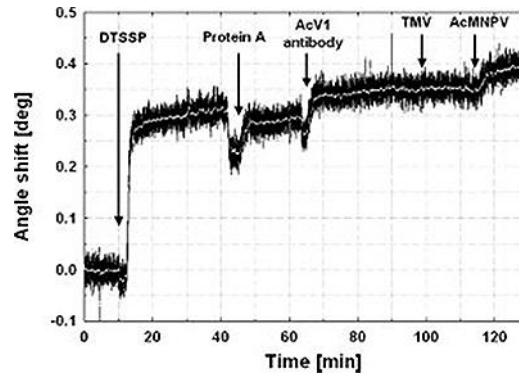


Figure 1.6: SPR sensorgram detailing formation of the sensing element and detection of *Autographa californica* multiple nuclear polyhedrosis virus (AcMNPV) via direct immunosensing [30]. The sensor signal is formed by changes in the angle of the light reflected from the underside of the metal film upon alterations to the refractive index on the sensor surface.

#### 1.1.3.4 Total Internal Reflectance (TIR) Immunosensing

Total Internal Reflectance (TIR) involves the use of two transparent media of different refractive indices. Light is introduced into the material of greater refractive index (i.e. an optical fibre) and is reflected off the interface between this material and the medium of lower refractive index (i.e. water). Upon reflection at the dielectric interface, some light is lost and enters the lower refractive index medium resulting in changes to the intensity of the reflected component. The intensity of the penetrating light decreases exponentially over distance from the interface and is dissipated over a distance equating to the wavelength of the light [8, 9]. This electromagnetic field in this region is known as the evanescent field and its thin penetration properties make it suitable to act as a transduction technology. Fluorescently labelled antibodies bound by immunological interaction to the dielectric interface will fluoresce within this field, while unbound antibodies still in solution will not participate in the signal. This methodology allows for sensitive immunosensing, similar to an ELISA, without the need for washing steps as the detection signal originates only from specifically bound secondary antibodies. This same property also allows the analysis of turbid and absorbing solutions which interfere with many other optical

immunosensors [8]. Transduction can be performed via monitoring the intensity of the evanescent field initiated fluorescence or through direct changes to the intensity of the reflected light [9]. An example of an optical fibre based Total Internal Reflectance Fluorescence (TIRF) immunosensor was reported by Long *et al.* [31]. This sensor was based on an indirect competitive immunoassay for the detection of microcystin-LR (MC-LR), a toxic product from freshwater cyanobacteria. The sensing element consisted of immobilised MC-LR on the fibre surface and sensing involved introduction of pre-incubated samples containing free MC-LR with a MC-LR specific monoclonal antibody conjugated to the fluorescent probe, Cy5.5, (MC-LR-MAb). Depending on the concentration of the analyte, antibodies left with free binding sites were able to bind to the antigen immobilized onto the probe and fluoresce in the evanescent field. As shown in Figure 1.7, increasing concentration of the analyte reduced the fluorescence signal because the free MC-LR inhibited the binding of antibodies to the sensing element.

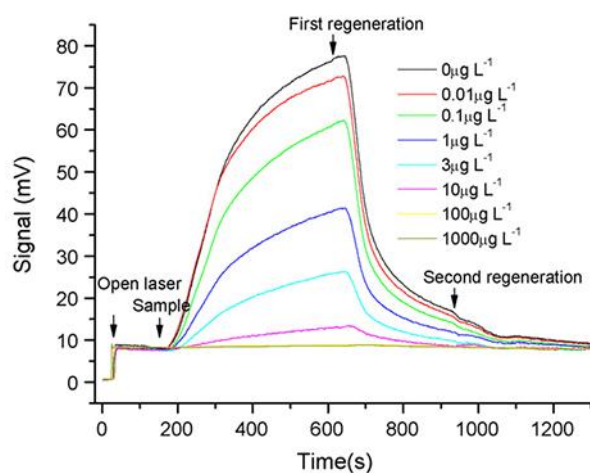


Figure 1.7: TIRF optical fibre sensor traces for various MC-LR concentrations. The sensorgrams represent an increase in fluorescence as labelled antibodies bind to the sensor surface. All analyte samples were pre-treated with 0.28 µg/mL MC-LR-MAb and regeneration of the sensor probe was achieved by addition of 2 mg/mL pepsin solution (pH 1.9) [31].

#### ***1.1.4 Immunosensing Summary***

The diverse application and nearly limitless analyte possibilities, highlights immunosensing as an important field moving forward. While classical immunosensor techniques still constitute a great majority of commercial design, new generations of immunosensors started to appear right from the very invention of the technique. These methods included the use of enzyme labels, nanoparticles and signal enhancement strategies with silver reduction. A variety of transduction mechanisms have been adapted for use in immunosensing further improving flexibility of the technique. It continues to be an area of intensive research and innovation and incorporation of new materials and techniques is driving the optical immunosensor towards faster, smaller, more sensitive and powerful forms. The work in this thesis builds upon the reported immunodetection approaches in combination with porous silicon and another form of optical transduction, interferometric reflectance spectroscopy.

## **1.2 Porous Silicon in Biosensor Applications**

The growing need for small, fast, efficient and mobile sensors for the detection of biological materials has led to a large amount of research into suitable sensing platforms. As technology has progressed, new materials with desirable properties have been adapted in an attempt to advance biosensor performance. One of the most important materials of the last 50 years has been semiconducting silicon. Its use in the development of micro-electronics revolutionised the industry and allowed the miniaturisation of computers and other electrical devices.

Investigation into the use of silicon as a sensing platform has also been occurring since the 1960's [32], and many optical, temperature, pressure and chemical sensors were developed [33-36]. With the advent of the biosensor, silicon was once again adapted to this field, producing many early biosensors [37-39]. However it was the discovery of visible light emission from porous silicon (pSi) that intensified biosensor research into this material [40]. While pSi was initially discovered more than 50 years ago by Uhlir [41], it was not investigated in depth until Canham discovered the material's photoluminescence at room temperature in the early 90's [40, 42]. Since that time there has been a concerted effort from researchers around the world to investigate the capabilities of this unique material. The properties of porous silicon, such as a large surface area, ease of production, tuneable optical properties and non-toxicity have allowed it to be used in a variety of applications including biomimetic surfaces, chemical sensing, drug release and biological implants. One of the most successful uses of pSi is as a detection platform for biomolecules. The large surface area provides the opportunity for large amounts of interaction between biomolecules over a small working area, offering a route for the miniaturisation of biosensing devices. Coupled with unique methods of optical and electrochemical transduction, pSi has quickly become a widely used material in biosensor design.

### **1.2.1 Etching Techniques**

Porous silicon (pSi) is a porous material produced when a silicon surface is dissolved in a chemical etching solution, often under an anodising current. The etching solution consists of hydrofluoric acid (HF), which acts as the electrolyte, dissolved in a surfactant. The surfactant, generally ethanol, acts as a wetting agent, lowering the surface tension of the hydrophobic silicon surface, permitting access to the HF. Other organic solvents can also be used such as dimethylformamide and acetonitrile to achieve different etches. Silicon semiconductors are often doped with impurities to alter the material's electrical properties. P-type silicon typically contains boron, an element that contributes 3 valence electrons, within the crystal structure. This results in the formation of positive holes, or a lack of electrons in the crystal lattice [43]. To convert this material into a porous structure it is anodised in the presence of HF. Application of an anodising current draws the positive holes ( $h^+$ ) to the surface, weakening the surface bonds, allowing attacks from the fluoride ions and subsequent dissolution of the silicon surface [44] (Figure 1.8). Pore propagation occurs due to a number of factors, the most important one being the availability of holes being higher at the bottom of a pore compared with the top surface of the material. To identify the concentration of dopant within the crystal structure a classification system has been developed. For example, for p-type silicon, additional positive signs signify a decrease in the resistivity of the material, i.e. p,  $p^+$ ,  $p^{++}$ . The inherent ease (simple galvanostatic setup) and speed (fabrication time of seconds to minutes) associated with the production of p-type pSi has provided a simple route for the production of a high surface area material with potential use in biosensor platforms.

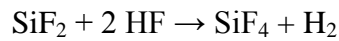
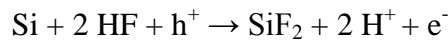
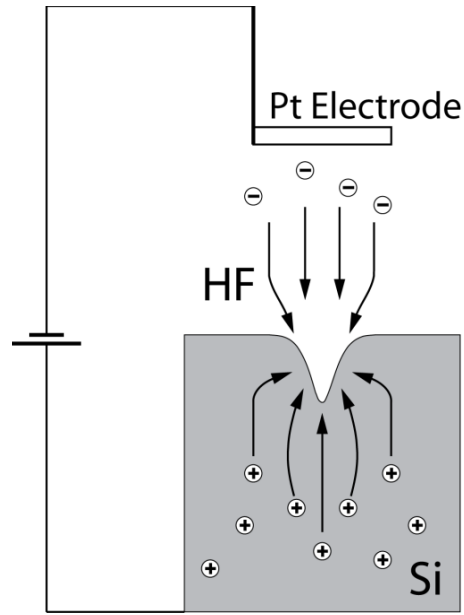


Figure 1.8: Electrochemical formation of pSi. The application of an electrical current draws positive holes ( $\text{h}^+$ ) towards the surface of the semiconductor, weakening Si-H bonds and facilitating the dissolution of silicon [44].

N-type silicon requires a slightly different method of etching, involving the application of light to drive the dissolution mechanism. The negative holes within n-type silicon are caused by the presence of group V elements antimony, arsenic or phosphorus, which impart an excess of electrons within the crystal structure [43]. To generate a porous matrix, the silicon wafer is introduced to HF and illuminated with white light. The illumination generates electron-hole pairs under depletion, which then initiates a dissolution mechanism proceeding in the same manner as the p-type silicon [45]. The etching process associated with n-type silicon provides extensive control over pore uniformity and allows for patterning of the surface via the use of photomasks to restrict light exposure to specific regions.

While the above methods are the most common ones, pSi can also be produced via stain etching. This process is the simpler and involves the use of HF, water and nitric acid to chemically etch the silicon [41]. Pore propagation is proportional to the concentration of the nitric acid, and is independent of the material's resistivity [46]. This method of pSi formation has been studied for over fifty years, however problems such as the lack of uniform pores and the slow reaction rate limited to producing thin porous layers ( $\sim 10^2$  nm) have restricted the development of this material despite the ease of production [45]. It has mostly been used in the investigation of p-n junctions prior to the discovery of visible light emission from electrochemically etched pSi [45].

### *1.2.1.1 Pore Geometry*

Varying etching parameters such as, crystal alignment, current density, etching time or the composition of the etching solution, it is possible to produce pSi of different pore geometry, size and depth [45]. Pores ranging from micropores (<2 nm) to mesopores (2-50 nm) and macropores (>50 nm) afford a wide range of pore size dependent material properties (Figure 1.9 (a – h)). This is relevant to biological applications where one desires to interface the porous layer with biological materials that also span a similar size range. Pore geometry can also be used to exclude certain species from entering the sensing part of the porous layer, reducing sensor interference (Figure 1.9 (i & j)).

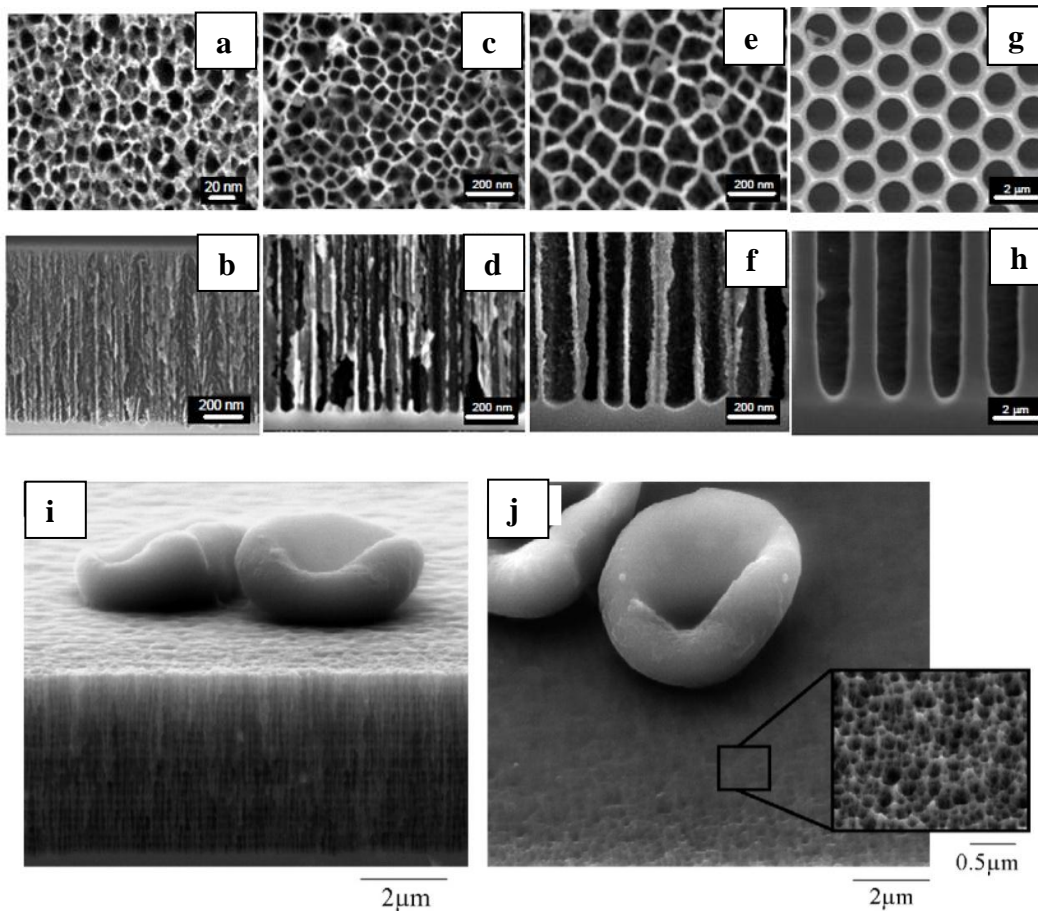


Figure 1.9: Top view and cross sectional SEM micrographs of a variety of pSi architectures. (a – g) depicts mesoporous through to macroporous silicon structures [47]. (i & j) SEM micrographs of pSi after exposure to blood. Size exclusion due to pSi is clearly evident, depicting filtered erythrocytes on the surface of the porous layer [48].

## 1.2.2 Types of pSi

### 1.2.2.1 Single Layer pSi

The etching of pSi at a set current results in the formation of a single layer consisting of ordered pores with uniform depth. Impinging light is reflected off the pSi/air interface, and pSi/crystalline Si interface resulting in an interference effect (This effect is discussed further in Chapter 1, section 1.2.4.1). Changes to the resulting fringe pattern (Figure 1.10 (a)) by addition of mass or variation in refractive index can be used to monitor changes on the surface of the material, thus providing an effective biological and chemical transduction mechanism.

### *1.2.2.2 One-Dimensional Photonic Crystal Structures*

Variations to the etching procedure are used to produce diverse types of pSi, which can be utilised in different ways to detect biomolecules. As discussed in the previous section, pSi is often etched as a single uniform layer. However, by varying the current density during etching, double or multilayered pSi can also be produced [49]. By periodically changing the current density, 1D photonic crystals can be produced. Alternating between two distinct currents in a stepwise fashion has been shown to result in Bragg reflectors [50, 51]. Alternatively, sinusoidal variation of the etching current will result in the formation of rugate filters [52, 53]. In both cases a series of layers are produced that exhibit different porosities and thus different refractive indexes. At the layer interfaces, reflection of a certain wavelength band occurs, while the remaining spectrum is absorbed by the material. By modifying the thickness and refractive index contrast of the layers, the resulting spectra can be tailored for sensing purposes in a similar fashion to single layer pSi.

### *1.2.2.3 Microcavities*

Another form of multilayered pSi is the microcavity. Microcavities were first produced by Pavesi and involve the positioning of a defect or active layer between two optical resonators such as pSi Bragg mirrors [50, 54]. This results in the formation of an optical ‘trap’, whereby photons with the same wavelength as the Fabry-Perot resonance are absorbed by the material, while the remaining spectrum is mostly reflected. Changes to the specific wavelength of this material can be used as a transduction mechanism for the detection of biomolecules.

### *1.2.2.4 Particles (Smart Dust)*

Soon after the discovery of pSi photoluminescence, it was demonstrated that exposure of pSi films to ultrasonic waves resulted in the formation of luminescent particles [55]. Building upon this work, the Sailor group recently developed what has been named ‘smart dust’. Consisting of micron sized pSi particles and containing a specific optical signature, they are generally produced from pSi Bragg or rugate filters and incorporate specific regions of high reflectivity. By altering the etching parameters such as overlaying several sinusoidal waveforms, it is possible to generate multiple reflectance peaks producing millions of unique optical signatures. The unique optical signature of the particles can effectively be used as a barcode, identifying captured molecules or immunocomplexes from the

reflectance peak of the particle that they are attached to [56]. This form of pSi has therefore been termed ‘Smart Dust’.

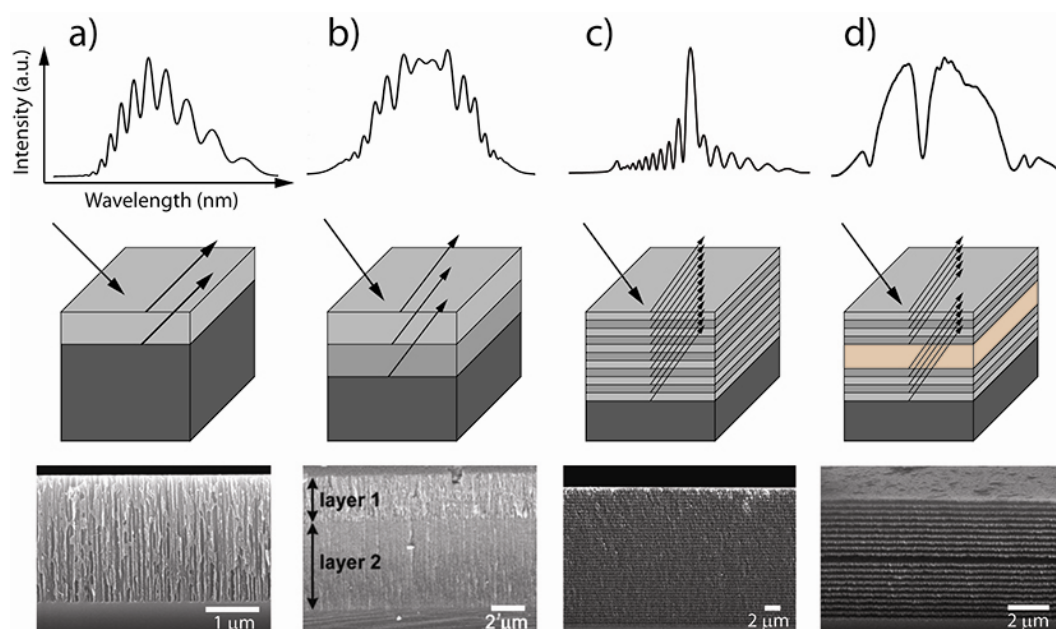


Figure 1.10: Respective reflectance spectra, schematic and cross sectional micrograph of (a) a pSi single layer, (b) a pSi double layer [57], (c) multilayered pSi [58] and (d) a pSi microcavity [59].

### 1.2.3 Surface Functionalisation

Freshly etched pSi is hydrophobic yet unstable in aqueous medium due to nucleophilic attacks on the silicon hydride terminated surface by water molecules [60]. Biosensing experiments are generally conducted in aqueous environments and a biosensor platform must therefore be able to withstand such environments. In order to serve as a viable biosensor, the surface must be stabilised and functionalised with appropriate biological recognition elements.

#### 1.2.3.1 Oxidation

One of the simplest routes to stabilisation is oxidation. Oxidation makes the material more hydrophilic and provides locations for the attachment of linker molecules. Lengthy exposure to normal atmosphere results in oxidation of the surface, however this process is slow and provides poor distribution of oxide

groups [45]. Alternatively it can be achieved through various other routes, which most commonly involves exposure to ozone gas, or thermal oxidation due to the simple nature of these processes.

Thermal oxidation can be used to provide a surface of high stability, as heating the pSi sample to high temperatures promotes backbond oxidation and the formation of Si-OH (silanol) groups on the surface, thus inhibiting nucleophilic attacks [61, 62]. The extent of oxidation depends upon the temperature, exposure time and atmospheric conditions [61, 63-65]. For example, introduction to 300°C for 1 hour in dry O<sub>2</sub> provides partial oxidation, exposure to 800 – 1100°C for 1 - 2 hours in wet O<sub>2</sub> results in the complete oxidation of the porous structure, while 1100 – 1150°C for 6 hours in dry O<sub>2</sub> results in the removal of the porous structure due to silica viscous flow [45]. While this process is effective at oxidising pSi, other methods have been developed that require less time and can result in higher silanol density. Processes such as chemical oxidation can be used as an alternative to provide a thinner layer of oxidation on the surface, offering a path for gradual dissolution, which can be used for drug release or biosensing. Ozonolysis of the sample leads to the formation of SiO<sub>2</sub> and Si-OH groups on the surface [66]. Alternatively reaction of freshly etched pSi with iodine, bromine or chloride vapour results in the formation of a halide terminated surface and subsequent exposure to air results in the hydrolysis of the halide bonds and the formation of oxide groups at the surface [67, 68]. The Si-OH surface can then be capped with linker molecules, such as silanes in order to stabilise and attach biomolecules to the pSi for biosensing purposes.

### *1.2.3.2 Silanisation*

Silanisation is popular technique to further stabilise pSi and immobilise biomolecules [69]. This is due to the ease of which oxidised pSi can be functionalised with the alkoxy- or chlorosilanes, allowing the introduction of a range of functional groups on the surface. In many cases, after silanisation with one of the commercially available silanes, chemical modification is performed to change the functional group for later coupling reactions with biomolecules. Trifunctional silanes exhibit the ability to strongly adhere to the surface thus protecting it from nucleophilic attack from aqueous medium [69, 70]. The

disadvantage of the trifunctional silanes is the tendency to form poorly aligned monolayers, reducing the amount of possible binding sites. Monofunctional silanes have been trialled and found to form extremely uniform self-assembled monolayers, however they result in a less stable surface coverage. As such trifunctional silanes are generally used in sensing devices due to the ability to increase a sensor's lifetime [70].

### 1.2.3.3 Si-C Bond Forming Reactions

Another common approach uses hydride terminated pSi to attach linker molecules directly. The surface can be functionalised with a number of compounds, including unsaturated hydrocarbons [71] (hydrosilation), Grignard and alkyl lithium reagents. These reactions lead to the formation of silicon carbon bonds that provide high sample stability. One of the pioneering groups in this area, Buriak *et al.*, developed various approaches to Si-C bond formation such as, Lewis acid mediated hydrosilation, white light hydrosilation or cathodic electrografting [72-78]. An alternate method employed by Salonen *et al.* to achieve a Si-C surface chemistry is thermal carbonisation. This process involves the thermal decomposition of acetylene on freshly etched pSi to achieve a thin silicon carbide-like layer [79-81]. The subsequent lack of Si-H and Si-OH groups on hydrosilated and thermally carbonised samples prevents the dissolution mechanism from occurring, thus providing stability even in aggressive aqueous media such as boiling aqueous sodium hydroxide.

### 1.2.3.4 Self-Assembling Protein Monolayers

A more recent functionalisation technique pioneered by De Stefano *et al.* involves coating pSi with a self-assembling biofilm. De Stefano *et al.* coated pSi with hydrophobins, a family of small fungal proteins which possess the ability to self-assemble into thin membranes at hydrophilic/hydrophobic interfaces [82, 83]. Hydrophobin membranes can form on freshly etched hydrophobic hydride terminated pSi or on more hydrophilic oxidised pSi. Once formed, the protein biofilm acts as a barrier, protecting the underlying silicon from exposure to aqueous media and imparting a high degree of stability without the need for

chemical modification of the substrate. Hydrophobins also have the capacity to control the wettability of a substrate, converting hydrophobic surfaces into hydrophilic and vice versa, an essential factor in many sensing and drug delivery applications [82].

### **1.2.4 pSi Based Transducers**

#### **1.2.4.1 Optical Transduction**

The unique optical properties associated with pSi allow detection of target molecules via changes to the material's optical signature. White light illumination of a pSi sample results in the reflection of light from the pSi/medium interface and the pSi/crystalline Si interface, producing a constructive and destructive interference effect called a Fabry-Perot fringe pattern [84] (Figure 1.11). This fringe pattern can be detected by a CCD spectrometer and can be used to extract information about the pSi such as the refractive index of the porous layer and its dielectric constant. The maxima in the fringe pattern occur at  $\lambda_m$  and are related to the physical properties of the pSi via:

$$m = \frac{2nd}{\lambda_m}$$

Equation 1.1: Fabry-Perot fringe pattern.

where  $m$  refers to the fringe order,  $d$  the film thickness and  $n$  the average refractive index of the layer at wavelength  $\lambda_m$ . Plotted as a function of wavelength ( $1/\lambda$ ), the maxima are equally spaced, since the refractive index is independent of the wavelength. Further analysis in the form of Fourier-Transformation (FT) of the intensity vs. frequency ( $\text{nm}^{-1}$ ) provides a peak proportional to the effective optical thickness (EOT) of the film ( $\text{EOT} = nd$ ) [85]. Due to this relationship, a change to the refractive index or thickness of the material will manifest itself as a change in the fringe pattern and EOT, constituting the basis for the transduction mechanism utilised by many pSi optical biosensors. Figure 1.11 depicts a shift in the reflectance spectra upon detection of an analyte. The change to the refractive index upon the displacement of water

(1.33) within the pores by biomolecules such as antibodies (~1.44), results in a shift in the reflected spectra.

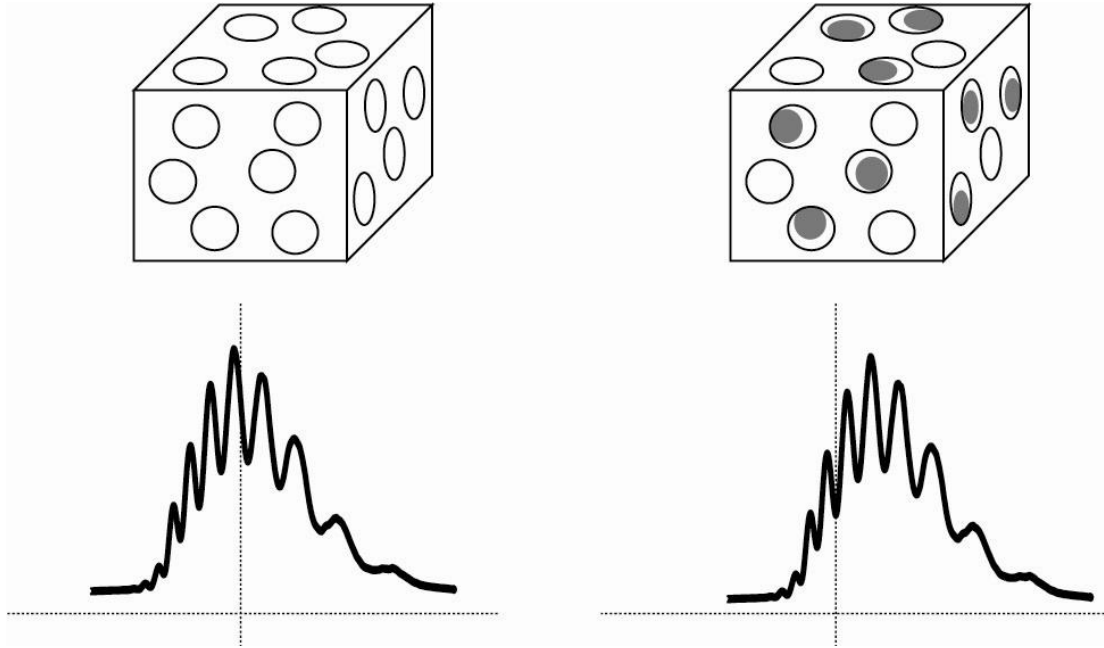


Figure 1.11: Schematic of pSi optical detection due to pore loading. Addition of an analyte to the porous matrix results in the displacement of the aqueous phase at the pSi/medium interface and an increase in the refractive index. This causes a finite shift in the fringe pattern reflectance spectra, allowing quantification of an analyte [86].

Changes in to the refractive index upon the binding of biomolecules can be explained using the Bruggeman effective medium approximation (Equation 1.2) which relates the effective dielectric constant of a pSi layer to its porosity [87]:

$$(1 - P) \frac{n_{Si}^2 - n_{pSi}^2}{n_{Si}^2 - 2n_{pSi}^2} + P \frac{n_{void}^2 - n_{pSi}^2}{n_{void}^2 - 2n_{pSi}^2} = 0$$

Equation 1.2: Bruggeman effective medium approximation.

P denotes porosity,  $n_{pSi}$  is the refractive index of porous silicon,  $n_{Si}$  represents the refractive index of silicon, and  $n_{void}$  is the refractive index of the medium within the pores.

This model illustrates how the effective refractive index of pSi ( $n_{pSi}$ ) increases as the porosity decreases and/or the  $n_{void}$  increases. This can be directly applied to

sensing applications where the  $n_{\text{void}}$  increases upon binding of target molecules within the porous structure. This results in a subsequent increase in the refractive index of the pSi ( $n_{\text{pSi}}$ ) causing a red-shift in the optical reflectance of the pSi, enabling label-free detection of biomolecules and greatly simplifying sensor design [66].

### 1.2.4.2 Single Layer pSi Transducers

Lin *et al.* were the first to utilise this phenomena to detect small organic molecules (biotin and digoxigenin), 16-nucleotide DNA oligomers, and proteins (streptavidin and antibodies) via comparison of the fringe pattern before and after the recognition event [84]. The pSi platform was shown to be highly sensitive, detecting levels down to the femtomolar and picomolar levels. The bioelements were immobilised onto the surface via silanisation and a solution containing the analytes was introduced. Interestingly the binding event induced a shift in the fringe pattern towards the blue. The reason for the blue shift will be explained later. It was shown that the extent of the shift correlated with the concentration of the target analyte. Hybridisation of DNA was detectable to levels of  $9 \text{ fg/mm}^2$  (Figure 1.12 (a) & (b)), which provided far higher sensitivity compared with typical techniques such as grating couplers and SPR. Fringe shifting was also achieved for a cascade of binding events involving biotin, streptavidin, primary and secondary antibodies and digoxigenin. Upon addition of each of the components a blue shift was registered and the layer experienced a corresponding decrease in EOT. Again, detection of extremely small concentrations ( $10^{-12} \text{ M}$ ) was achieved via this sensing mechanism.

This system helped identify pSi as a sensitive platform for the detection of biomolecules. In subsequent years, various research groups worldwide have built on those initial studies.

## Introduction

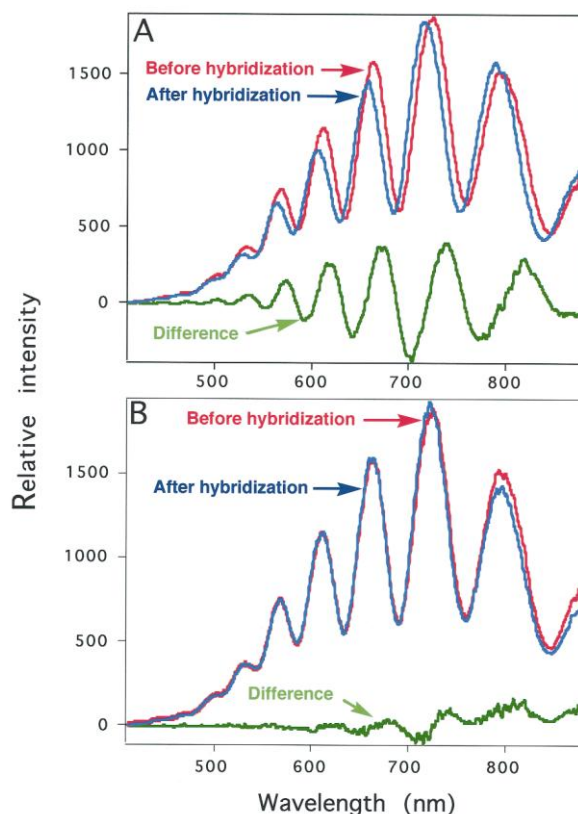


Figure 1.12: A) Detection of DNA hybridisation via a shift in the reflected Fabry-Perot fringe pattern; and B) Subsequent control experiment indicating no signal upon exposure of the surface to non-complementary DNA [84].

Janshoff *et al.* also investigated the effect of biotin – streptavidin binding on pSi surfaces [66]. pSi was ozone oxidised before being functionalised with (2-pyridyldithiopropionamiobutyl) dimethylmethoxysilane. Through a series of subsequent reactions biotin was then covalently linked to the silane via disulfide bonds. This functionalised surface was found to greatly increase stability in aqueous environments by limiting access to the underlying pSi surface (Figure 1.13 (a)). Exposure of the biotinylated surface to streptavidin triggered a large red shift due to the change in the refractive index upon binding of the protein with its ligand. Figure 1.13 (b) shows the effect on EOT as a large increase is seen upon binding. It should also be noted that ensuing washing steps failed to alter the EOT, demonstrating the signal stability. Dithiothreitol was then introduced to reduce the disulphide bonds, and release the protein-ligand complex from the surface. This resulted in a return of EOT to baseline levels, indicating that the

initial increase in EOT was solely due to the recognition event between biotin and streptavidin. The theoretical change in EOT was calculated using the Bruggeman approximation to be 32 nm which was comparable with the experimentally determined thickness of 23 nm. The device was found to be quite sensitive, able to achieve detection of 1 – 10 ng of protein.

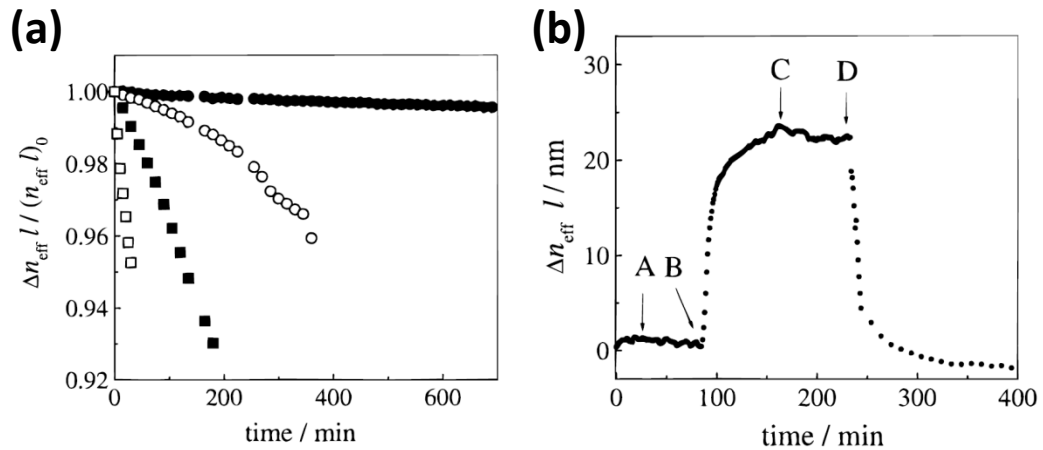


Figure 1.13: (a) Effect of functionalisation techniques on the stability of pSi in 10% (v/v) EtOH in PBS. The reduction in normalised EOT ( $n_{\text{eff}} l / (n_{\text{eff}} l)_0$ ) over time decreases with increased functionalisation. ( $\square$ ) hydride terminated pSi, ( $\blacksquare$ ) ozone oxidised pSi, ( $\circ$ ) thermally oxidised pSi (400°C 1 hr), ( $\bullet$ ) ozone oxidised pSi functionalised with (2-pyridyldithiopropionamidobutyl)dimethylmethoxysilane. (b) Effect of biotin – streptavidin binding on the EOT of a pSi substrate. (A) Control, introduction of a solution containing pre-reacted biotin – streptavidin; (B) addition of 10  $\mu\text{M}$  streptavidin and subsequent binding to biotin; (C) washing steps with buffer; (D) introduction of dithiothreitol reduced the disulphide bonds and cleaved the protein complex from the surface [66].

Dancil *et al.* studied the reversibility of IgG binding to Protein A modified pSi [88]. In this study, special attention was paid to the issue of non-specific binding. A large protein bovine serum albumin (BSA) conjugated to biotin was incorporated into the linking molecule's structure to help protect the surface from non-specific adsorption. Protein A was then covalently immobilised. Exposure of the protein A modified surface to human IgG gave a red shift in the fringe pattern and a large increase in the EOT of the material due to the mass of the antibody within the pore. It was shown that IgG binding could be reversed by

## Introduction

simply decreasing the pH and that the sensor could achieve a number of on/off IgG binding cycles with minimal signal loss. Importantly, this study also provided evidence that the increase in EOT upon binding is proportional to the mass of the analyte bound, providing a means for the quantitative detection of biomolecules.

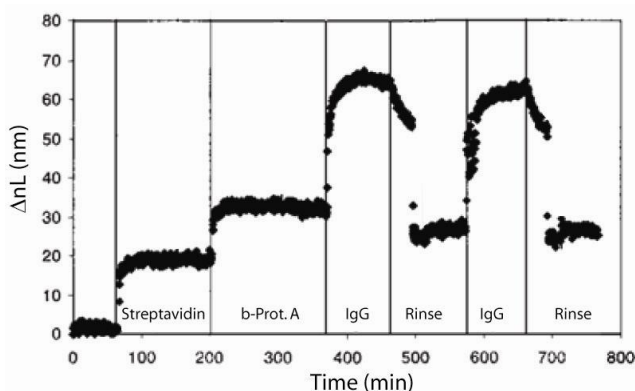


Figure 1.14: EOT sensorgram showing reversibility of IgG binding to a Protein A modified surface [88]. Biotin functionalised pSi was introduced to PBS and a baseline established. 1 mg/mL of streptavidin was then introduced followed by a PBS wash. The surface was then exposed to 2.5 mg/mL of biotinylated Protein A before being rinsed with PBS. 2.5 mg/mL of Human IgG was then introduced before being washed with 0.1 M acetic acid. Human IgG was then re-introduced at the same concentration before once again being rinsed with acetic acid.

This effect was further investigated by Schwartz *et al.* who analysed antibody binding affinity [85]. Instead of covalently linking protein A to the surface, it was adsorbed to thermally oxidised pSi. The surface was then exposed to IgG from various species and the binding affinity was measured via the relative change in EOT. The largest increase in EOT was seen upon addition of human IgG, indicating that far more IgG had bound compared with other species, thus causing a larger change in the effective optical thickness of the material. This result was consistent with those previously reported on IgG affinity in the literature [89, 90]. The surface was shown to be reusable since it produced a signal over multiple cycles. However, the strength of the signal was seen to

## Introduction

diminish over time. Significantly, Schwartz demonstrated that exposure of the protein A surface to BSA resulted in no signal change, effectively demonstrating that non-specific adsorption was successfully prevented and that a dedicated low-fouling synthetic molecule such as poly(ethyleneglycol) was not required.

Detection of biomolecules has also been achieved via the degradation of the pSi layer upon recognition of the target molecule. The degradation of the layer results in a change to the pore thickness and thus manifests itself as a shift in the fringe pattern and decrease in EOT. Steinem *et al.* has shown that recognition of complementary DNA (cDNA) on the surface of oxidised pSi can result in a corrosive effect on p-type pSi [91]. Steinem postulated that the corrosion of the pores was the result of enhanced oxidation of the pSi in the presence of negatively charged double-stranded DNA. The change in the electrostatic field upon hybridisation is believed to draw positive holes to the surface of the pSi facilitating nucleophilic attack from the water molecules and subsequent oxidation and dissolution of silicon. Importantly, the corrosion effect was absent upon addition of  $Mg^{2+}$  cations or charge neutral peptide nucleic acids (PNA), confirming that the corrosion is indeed caused by the DNA's negative charge. The corrosive effect induced a reduction in the EOT of the material due to a blue shift in the fringe pattern. This mechanism can also be used to explain the same effect depicted by Lin's sensor discussed previously. This corrosive effect results in the amplified detection of hybridisation via a dramatic decrease in the EOT, thus improving the sensitivity of the sensor. This amplifying effect allowed the device to detect concentrations of cDNA down to  $0.1 \text{ amol/mm}^2$ , emphasizing the high sensitivity achievable by pSi based devices.

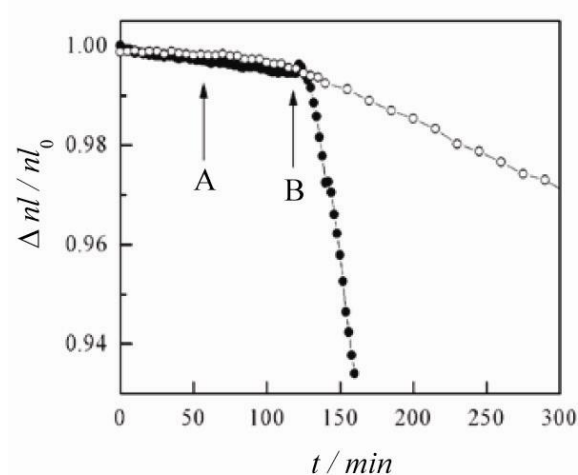


Figure 1.15: EOT real-time experiment showing detection of DNA hybridisation via corrosion of the pSi surface [91]. (A) Addition of non-complementary DNA, (B) Addition of cDNA and subsequent degradation in 100 mM phosphate buffer, pH 7.0. (○) Represents  $p^{++}$ , while (●) represents  $p^+$  pSi

Building upon this work Voelcker *et al.* investigated the detection of DNA hybridisation and ligand-receptor interactions via transition metal complexes [92]. The author adapted the well known ability of transition metal complexes to oxidise certain materials as a detection mechanism. Preliminary studies indicated that the metal complexes were able to corrode ozone oxidised pSi due to an oxidative pathway. Several metal complexes were then trialled in order to identify the most effective and it was found that  $Ni^{2+}$  cyclam resulted in the greatest change in the EOT of the material. The Ni complex required the presence of ammonium persulfate,  $(NH_2)_2S_2O_8$ , to achieve oxidation of the surface, in much the same way that an enzyme requires a substrate to produce a measurable response in an ELISA. Once it had been established that a transitional metal complex could produce a measurable optical response, it was adapted as a biosensor detection mechanism. It was trialled on both DNA hybridisation and protein-ligand interaction. In both cases the surface was

## *Introduction*

modified with [3-(2-bromoacetamido)propyl] dimethylmethoxysilane to immobilise the capture molecules. A single strand 16-mer DNA probe was immobilised onto the surface and exposed to 1  $\mu\text{M}$  of complimentary DNA conjugated to  $\text{Ni}^{2+}$  cyclam. This had no effect on the EOT slope of the material, however introduction of  $(\text{NH}_2)_2\text{S}_2\text{O}_8$  resulted in a decrease in the EOT,  $\sim 8$  nm, and a shift in the fringe pattern. The detection of biotin-streptavidin binding was then examined. A pSi surface was coated with biotin, exposed to 1  $\mu\text{M}$  streptavidin before the introduction of 100  $\mu\text{M}$   $\text{Ni}^{2+}$  cyclam conjugated biotin. The optical properties of the material experienced a sharp decrease in the EOT slope upon introduction of  $(\text{NH}_2)_2\text{S}_2\text{O}_8$ . Control experiments including unconjugated cDNA and biotin resulted in no change to the EOT slope. The transition metal complex resulted in the EOT slope decreasing by a factor of 30 upon detection of DNA and a factor of 48 upon detection of the biotin-streptavidin binding. This is far greater than the slope change exhibited solely due to DNA hybridisation as reported by Steinem (20 fold decrease). The ability to graft this complex onto various molecules provides a versatile system which could be used to detect a large number of analytes.

## Introduction

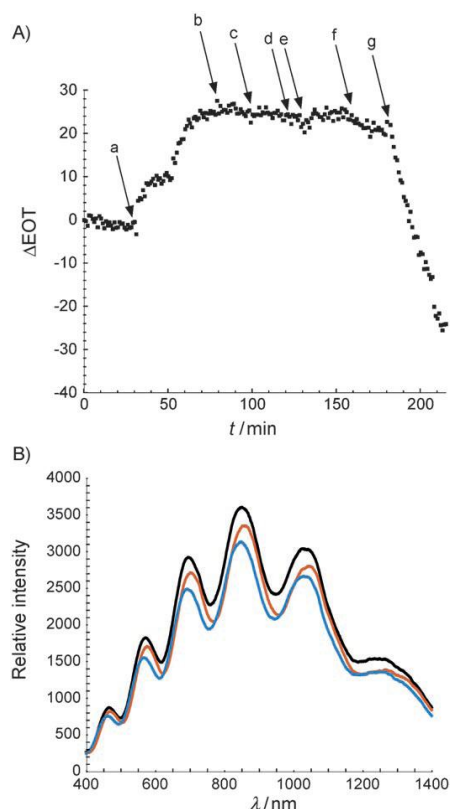


Figure 1.16: (A) Effect of streptavidin detection on the EOT of a biotin-functionalised pSi surface in PBS [92]. a) Introduction of 1 mM of avidin. b) Washing step with buffer. c) Addition of 1 mM of ammonium persulfate,  $(\text{NH}_2)_2\text{S}_2\text{O}_8$ . d) Washing step with buffer. e) Introduction of 100 mM of biotin- $\text{Ni}^{2+}$ cyclam. f) Washing step with buffer. g) Addition of 1 mM of  $(\text{NH}_2)_2\text{S}_2\text{O}_8$ . (B) Reflectance spectra of the biotin functionalised pSi. The black line represents the chip prior to addition of avidin, while the red line represents the surface after 20min incubation with 1 mM of avidin. The blue trace depicts the surface after incubation with 100 mM of biotin- $\text{Ni}^{2+}$ cyclam and 1 mM of  $(\text{NH}_2)_2\text{S}_2\text{O}_8$ .

Detection via corrosive amplification has also been achieved via enzyme catalysed oxidation. A typical immunoassay used in such techniques as an enzyme linked immunosorbent assay (ELISA) has been adapted for use with pSi. Typically an ELISA involves immobilisation of a primary antibody to the pSi surface which is used to capture a specific analyte. Detection of the analyte is then achieved by introduction of an enzyme conjugated to a secondary antibody specific to the analyte. The enzyme is then able to turn over a chromatic, fluorescent or electrochemical substrate to generate a detectable signal. Jane *et*

*al.* recently investigated this phenomenon in the detection of the autoimmune diseases systemic lupus and Sjogren's syndrome [16]. The La protein was immobilised using 3-isocyanatopropyl triethoxysilane creating a receptor coated surface. The analyte, an antibody against the La protein, was then introduced, followed by exposure to a secondary antibody conjugated to the enzyme horse radish peroxidase (HRP). Introduction of the enzymatic substrate, o-phenylenediamine (OPD), resulted in the formation of an oxidised radical species that enhanced pSi corrosion. The degradation of the pSi layer manifested itself as a decrease in the EOT of the material (Figure 1.17) facilitating detection of antibody levels of down to 125 ng/mL, which could potentially be improved with further research. Importantly this device significantly reduced the detection time of these diseases to ~80 min compared to a minimum of 5 hours required for a typical ELISA. As with Voelcker's metal complex detection mechanism, this system also has the potential to be adapted to a wide range of biological systems, providing a highly versatile biosensor platform.

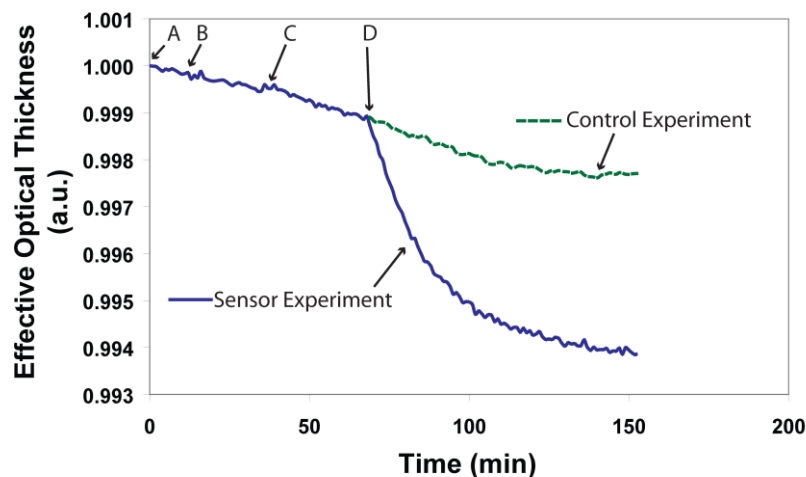


Figure 1.17: Effect on the effective optical thickness of a La protein functionalised pSi surface upon detection of anti-La antibodies. A) Baseline in PBS. B) Introduction of a 200 ng/mL anti-La solution. C) Addition of IgG-HRP (1:500) and D) Introduction of OPD solution (4 mg/mL). The sensor surface is represented as a solid line, while the control (no anti-La) is shown as a dashed line.

## Introduction

More recently the detection of large microorganisms such as bacteria has been achieved on single layer pSi. The interaction of bacteria with pSi can elicit a measurable change in the optical profile of the material, thus providing a detection pathway. Segal *et al.* demonstrated selective bacteria capture and detection on macroporous silicon via changes to the intensity of the Fabry Perot interference pattern and/or the EOT of the porous layer [93, 94]. Adsorption of *E. coli* within the macropores resulted in a change to the refractive index of the material which could be measured by monitoring the EOT of the porous layer (Figure 1.18). This process affords a flexible, label-free sensing platform for real-time detection and bacterial growth monitoring. Tailoring the surface chemistry of this material with specific recognition elements has great potential to provide a targeted sensor of large objects such as bacteria, fungi and viruses, thus broadening the potential of pSi further.

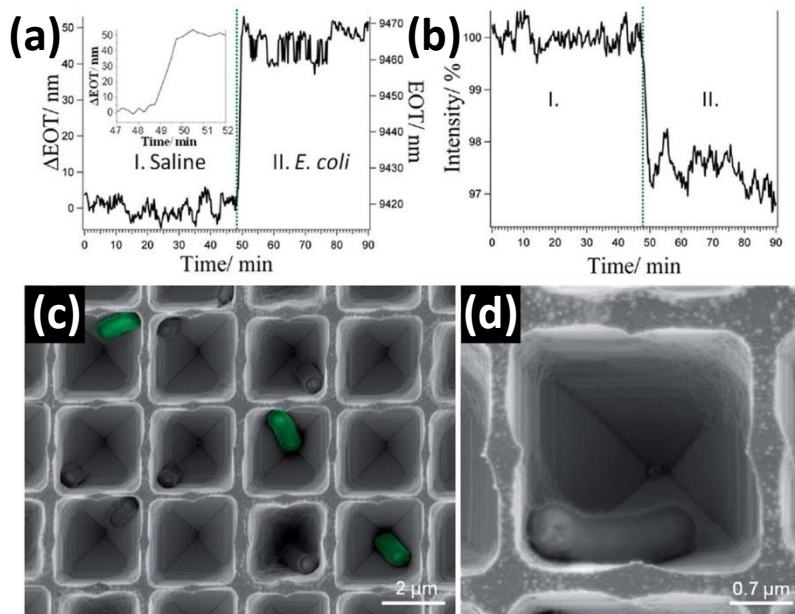


Figure 1.18: Real-time detection of *E. coli* on pSi. (a) EOT vs. time, (b) Reflected intensity vs. time, (c) & (d) SEM micrographs of *E. coli* within the porous silicon matrix following a sensing experiment [93].

### 1.2.4.3 Double Layer pSi Transducers

It has recently been shown that the simultaneous sensing of multiple analytes can be achieved by stacking pSi to form a double layer [57]. The formation of a double layer containing larger pores on the outer layer and smaller pores on the inner layer allows the separation and detection of biomolecules by size exclusion effects (Figure 1.19). The structure results in unique optical fringes that can be used to distinguish between events occurring in each layer. By using the smaller porous layer as a reference, the potentially interfering effect of the small molecules in the larger layer can be compensated for, thus allowing the detection of large molecules in the presence of high concentrations of small molecules. This structure provides the foundation for simple incorporation of a reference layer into a sensing platform, thus simplifying and miniaturising sensor design. Pacholski *et al.* fabricated a double-layered pSi film that allows large molecules (BSA) only into the top layer featuring larger pores 50 – 100 nm, while permitting smaller molecules (sucrose) into both layers, even the small pore layer, <20 nm. The resulting fringe pattern was Fourier-transformed to determine the EOT for both layers. In this manner, it was possible to distinguish between adsorption of the two different molecules. Notably, the device was able to detect 1 mg/mL BSA in solutions containing 100-fold excess of sucrose. While the detection level is not very impressive, the ability to remove interference from contaminants highlights the capability of this device.

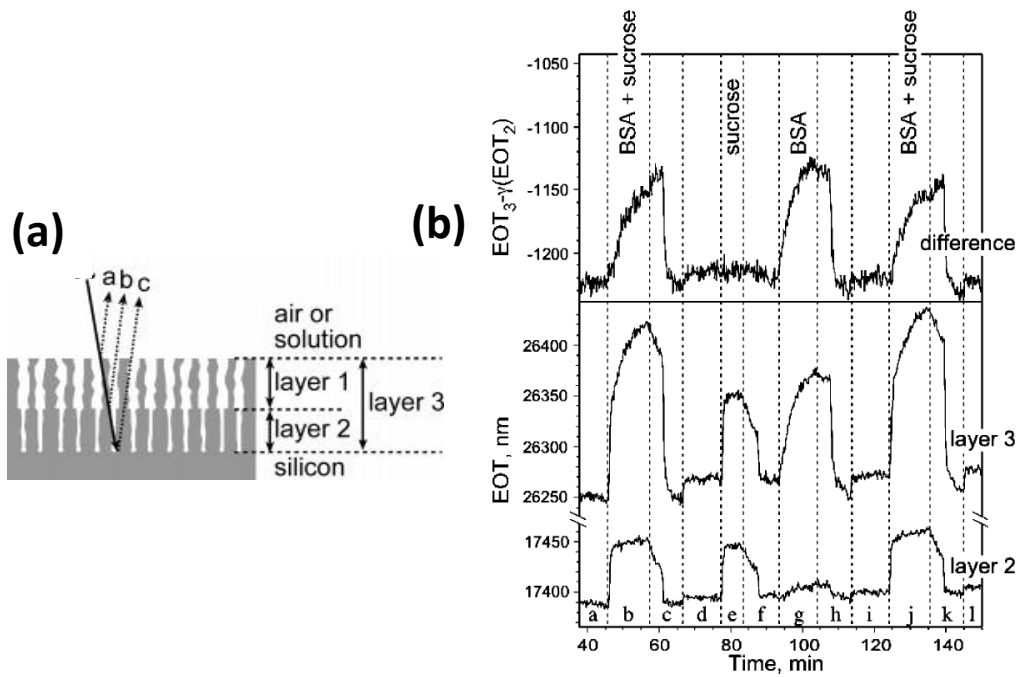


Figure 1.19: (a) Schematic of a double-layered pSi film and sensor signal readout [57]. The schematic identifies the layers associated with this sensor and highlights how the interaction of light with each layer produces a unique reflectance effect. The combination of layers 1 and 2 gives rise to layer 3 which is utilised in the detection mechanism. (b) The plot represents the introduction of sucrose and BSA to the double-layered pSi film. The real-time trace of the EOT of layer 3 (a combination of layers 1&2) and layer 2 are depicted, allowing the calculation of a difference trace. The smaller pores of layer 2 do not allow entry of the large BSA and as such only respond to the smaller sucrose molecule, while layer 1 responds to both. This enables the selective detection of BSA by layer 1 even in the presence of large amounts of sucrose. (All data acquired in Buffer pH 4).

#### 1.2.4.4 Multilayered pSi Transducers

The resonance peak produced from a pSi Bragg reflector or rugate mirror can act as an effective transduction signal. Orosco *et al.* recently reported the fabrication of a pSi rugate sensor aimed at the detection of protease activity [95]. Rugate pSi was methylated followed by spin-coating of the surface with the protein zein. The size of the pores (10 nm) restricts the entry of the protein, causing the formation of a protein coating on the porous matrix that does not affect the

reflectance spectrum. The protease, pepsin, was spotted onto the surface at various concentrations (Figure 1.20), and resulted in the digestion of zein and the infiltration of the pores by the peptide digest. The loading caused an increase in the refractive index of the pSi layer which in turn induced a measurable change to the reflectance band. The reaction produced a second resonance peak red-shifted from the original, which can be used to quantify the amount of pepsin. The original peak remained at  $\sim 550$  nm because the illuminated area included pSi that was not spotted with pepsin. The sensor achieved high sensitivity, displaying a detection limit of  $\sim 7$   $\mu\text{M}$  of protein.

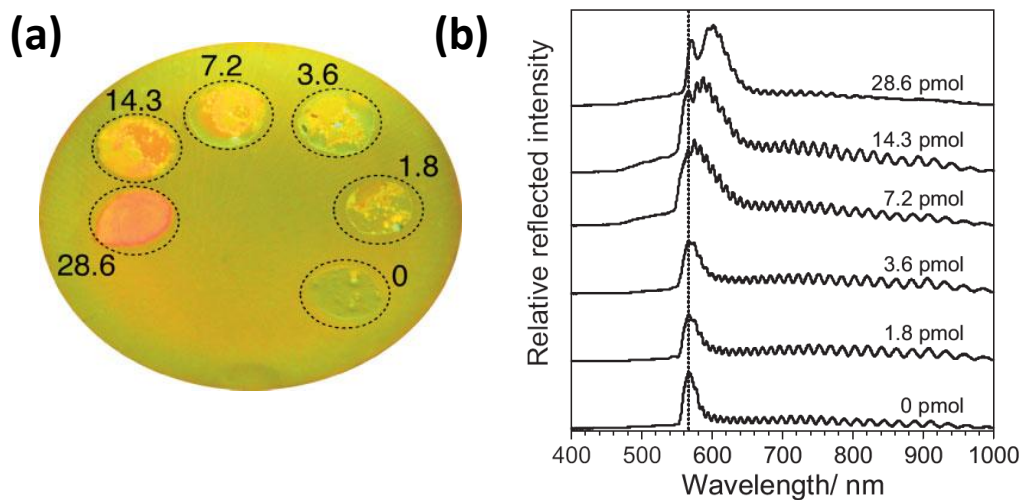


Figure 1.20: (a) Pepsin deposited onto zein modified pSi at various pmol levels, (b) Subsequent red shift of a pSi rugate filter reflectance peak due to increasing concentrations of the protease, pepsin [95].

Another multilayer sensor utilising a shift in the resonant peak of pSi was developed to detect protease activity. Kilian *et al.* utilised a narrow-line-width rugate filter to detect the protease, subtilisin, in solution [96]. The prepared pSi surface was functionalised via hydrosilylation to attach a linker molecule containing 1-amino-hexa(ethylene glycol) ( $\text{EG}_6$ ) to reduce non-specific adsorption of proteins and terminated with a carboxylic acid. Peptides were then immobilised onto the surface to complete the biofunctionalisation process. Cleavage of the peptides upon introduction of the protease resulted in a change in

## Introduction

the refractive index and subsequent blue shift of the resonance peak. The resulting shift ( $\Delta\lambda_{\text{protease}}$ ) was normalised against a control containing no enzyme ( $\Delta\lambda_{\text{control}}$ ) and the initial peptide ( $\Delta\lambda_{\text{peptide}}$ ) reflectivity shifts:  $(\Delta\lambda_{\text{protease}} - \Delta\lambda_{\text{control}} / \Delta\lambda_{\text{peptide}}) \times 100$ . The blue shift experienced in this sensor occurred from the cleavage and diffusion of immobilised peptides from the pores, whereas the red shift exhibited in the previous protease sensor arose from peptide fragments entering the pores. This sensor also proved to be highly sensitive, down to the low nanomolar level. The detection range exhibited by this sensor is comparable with other interferometry based detection platforms, while also providing certain advantages. The closely packed pSi layers combined with the non-fouling surface provided increased sensitivity and reduced interference from oxidation and non-specific interactions. While the two protease sensors reported here possess different detection mechanisms, the sensitivity of this device, 37 nM protein, was directly comparable to that achieved by Orosco's sensor, indicating that both approaches are capable of achieving high sensitivity.

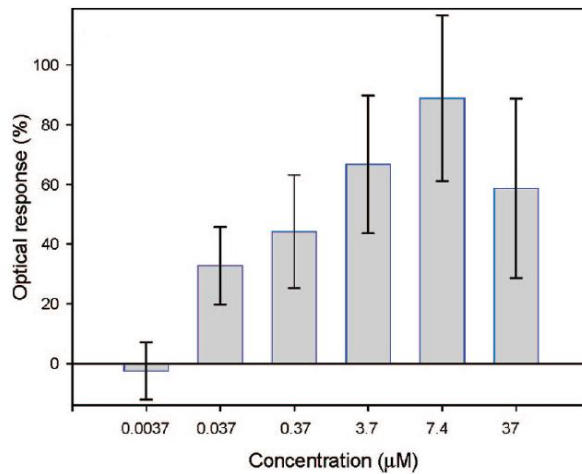


Figure 1.21: Optical response of a peptide modified pSi multilayer sample upon exposure to the protease, subtilisin ( $(\Delta\lambda_{\text{protease}} - \Delta\lambda_{\text{control}} / \Delta\lambda_{\text{peptide}}) \times 100$ ). The low value observed at 37  $\mu\text{M}$  can be attributed to enzyme denaturation and adsorption to the pores, reducing the blue shift [96].

## Introduction

A new transduction mechanism utilising multilayer pSi has been recently produced by Alvarez *et al.* for the monitoring of viral infection and lysis of bacteria [97]. This device provides a platform for the real-time study of cell growth and lysis, negating the need for time consuming procedures such as plating. This is achieved through a setup whereby the intensity of scattered light from a bacterial cell culture growing on an undecylenic acid coated rugate pSi. The surface was illuminated with white light at an oblique angle, while the CCD spectrometer was positioned perpendicular to the surface. Introduction of a scattering centre on the surface, such as a bacterial cell resulted in the scattering of light from the surface to the extent that the CCD spectrometer was able to detect a signal. Alvarez introduced bacteria, *Pseudomonas syringae*, to the pSi at a variety of different concentrations. The sensor exhibited a linear relationship between the concentration of the bacteria in colony forming units (CFU/mL) and the light intensity at the photonic resonance. The detection limit of this device was shown to be approximately  $1 \times 10^7$  CFU/mL (Figure 1.22), which is comparable to current spectrometer-based turbidity systems. Analysis of bacterial cell lysis due to viral infection was also analysed as a function of light intensity over time. Cells were seeded onto the pSi and infected at a ratio of 13:1 (bacteria:virus) with a phage virus specific to *P. syringae*,  $\Phi 6$ . A dramatic decrease in light intensity from the surface was seen at  $\sim 5.6$  hrs, which agreed with previously reported lysis studies, thus affording a pSi sensor capable of sensing cell infection and death.

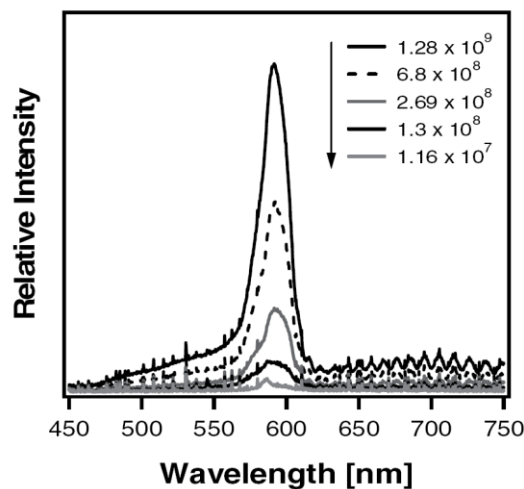


Figure 1.22: Intensity of scattered light from a pSi surface as a function of bacterial cell concentration (CFU/mL) [97].

## *Introduction*

This so called Smart petri dish concept was also applied to studies of apoptosis monitoring in primary rat hepatocytes [98]. This device was based upon the scattering of light due to the presence of eukaryote cells on the surface of the pSi. In this case rugate pSi was coated with polystyrene before being ozone oxidised to produce a hydrophilic surface that promoted cell adhesion similar to conventional petri dishes. The device also utilised the same angled illumination technique applied by Alvarez to detect light scattering due to cells. However this sensor differed from Alvarez's as cell death resulted in an increase in the amount of light scattering and light captured by the CCD spectrometer. This effect was attributed to changes in mitochondrial composition and lipid function upon death.

Hepatocytes seeded onto the surface were exposed to the toxins such as cadmium chloride to induce cell death. Cell death caused a morphological change that manifested itself as an increase in detected light intensity (Figure 1.23). The study revealed that the device readily showed an increase in light scattering within ~ 2 hrs of the addition of 50  $\mu\text{M}$   $\text{Cd}^{2+}$ . This result is impressive, as the scattering effect occurs ~2 hrs prior to detection by conventional cell viability techniques such as a MTT (methylthiazolyldiphenyl-tetrazolium bromide) stain. Interestingly Schwartz also utilised the material's ability to reflect certain colours (wavelength regions) to identify cell death. A pSi surface was prepared that reflected green light and was seeded with rat hepatocytes. Upon introduction of toxin and cell death, the increased light scattering highlighted the affected cells as green regions when analysed with an optical microscope. Coding different areas with discrete colours should allow the analysis of various drugs or toxins simultaneously. This method of cell observation is highly suitable, as the sampling of cells or use of dyes is not required and the cells can remain undisturbed and continue to be incubated providing great potential for adaptation into high-throughput applications.

## Introduction

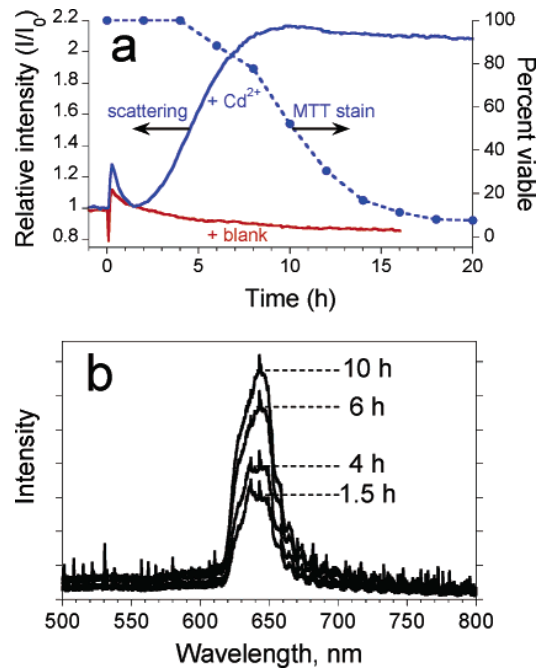


Figure 1.23: Light scattering of a pSi resonance peak due to morphological changes in primary rat hepatocytes upon cell death from the toxin  $\text{Cd}^{2+}$ . (a) The right axis depicts the relative intensity of light from the pSi surface and the left axis shows the percent viability from MTT stain with respect to time after the introduction of  $50 \mu\text{M Cd}^{2+}$  to rat hepatocytes. The solid blue trace represents the change in intensity of light scattering. The red trace represents a control contain no  $\text{Cd}^{2+}$ , while (●) denotes a corresponding MTT stain viability assay on a typical petri dish. (b) The pSi spectra clearly depicts an increase in the intensity of scattered light over 10 hrs [98].

Martin-Palma *et al.* have described a potential multilayer pSi platform for the detection of proteins through a reduction in reflected light intensity [99]. Studies into the functionalisation of rugate pSi revealed a marked decrease in the reflected light from the surface upon attachment of silane molecules. Subsequent immobilisation of a polyclonal mouse antibody onto the functionalised surface resulted in a further reduction in intensity. This was a preliminary report that did not provide detection levels or mechanisms behind the phenomena. It was however suggested by the author that this mechanism may be applicable to the detection of such biological systems as receptor-ligand interactions, although this

preliminary research needs to be further researched in order to provide more credible data.

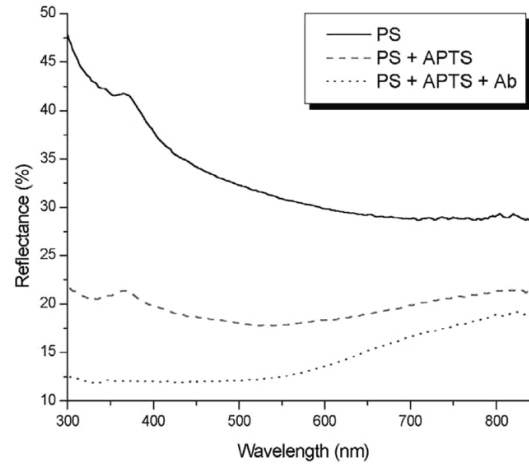


Figure 1.24: Reduction in reflected light intensity upon functionalisation of pSi with 3-aminopropyltriethoxysilane and immobilisation of a polyclonal mouse antibody [99].

#### 1.2.4.5 Microcavity-Based pSi Transducer

The optical properties of microcavities provide a simple route to the production of ultrasensitive biosensors. The narrow resonance peak/s generated through the confinement of a central layer by two Bragg reflectors is highly sensitive to changes to the refractive index. Interaction of biomolecules results in changes to the resonant peaks and thus provides a straightforward path for analyte detection.

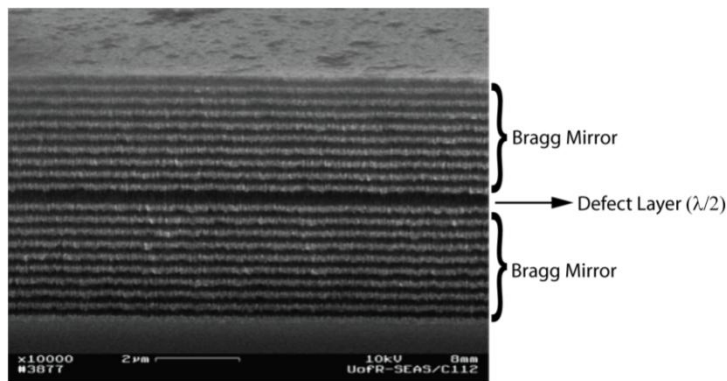


Figure 1.25: SEM cross-section of a microcavity displaying the confined defect layer [100].

## Introduction

Chan *et al.* fabricated a sensor capable of differentiating between Gram-negative and Gram-positive bacteria via changes to the resonance peaks of a pSi microcavity [101]. The microcavity was fabricated containing a photoluminescent defect layer. It was then functionalised with a silane onto which the organic receptor, *ter*-cyclo pentane (TWTCP), to ‘Lipid A’ was immobilised, which is a component of lipopolysaccharide (LPS) which is specific to Gram-negative bacteria. Excitation of the photoluminescent layer and exposure of the TWTCP decorated surface to purified lipid A resulted in a red shift of the resonance peaks by 8 nm. The sensor responded to Gram-negative bacteria by a red shift of 4 nm, while Gram-positive showed no response, demonstrating the potential for the sensor to replace the Gram stain test. The device has yet to be optimised, however current results indicate that a detection level of  $\sim 1.7$   $\mu\text{g/mL}$  could be achievable. Comparison with other Gram detection methods is difficult as the detection limit is typically reported as CFU/mL rather than as a mass, however the ability of pSi sensors to detect small molecules such as proteins indicate that this sensor has the potential to be highly sensitive

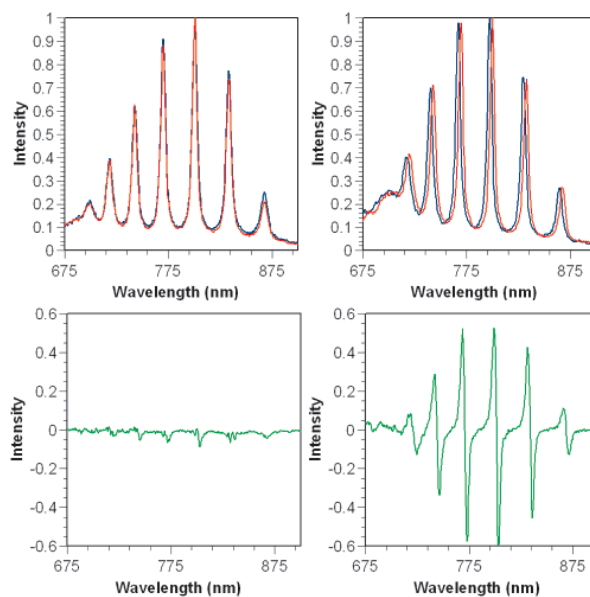


Figure 1.26: Photoluminescence spectra of a Gram-negative biosensor. Blue plot: Prior to addition of bacteria, Red plot: after incubation with bacteria, and Green plot: difference between the spectra before and after addition of bacteria. The spectrum on the left depicts the addition of Gram-positive bacteria and subsequent lack of a difference signal. The spectra on the right represents the addition of Gram-negative bacteria and displays a large wavelength shift and difference signal due to the specific interaction with the surface [101].

## Introduction

Bonanno *et al.* recently reported the fabrication of a label-free optical biosensor for the detection of IgG in whole blood using a pSi microcavity [48]. Pore morphology played an important role in the formation of this sensor, as it was used as a filtering mechanism, excluding the larger components of blood such as, blood cells and very large proteins, from entering the pores and interfering with the immobilised receptors (Figure 1.9 i&j).

Biotinylated anti-rabbit IgG was immobilised onto a streptavidin modified surface in order to detect IgG within a blood sample from a rabbit. Non-specific binding of small proteins was minimised by blocking the surface with bovine serum albumin (BSA) prior to sensing. Upon IgG binding, a red shift in the resonance peak upon occurred which scaled with IgG concentration. Target binding specificity was investigated by introducing the functionalised surface to serums and blood from different animals and the wavelength shift only manifested itself in samples containing the rabbit IgG. Cross-reactivity studies also found minimal signal change indicating that the sensor was specific to the target antibody.

Analytical studies carried out on rabbits produced comparable results to that of an ELISA over the sensor's detection range of 2-10 mg/mL. The poor detection level displayed by the sensor when compared to ELISA and surface plasmon resonance (SPR) are offset by its ability to analyse undiluted serum or more directly, the blood of patients, in a far shorter time.

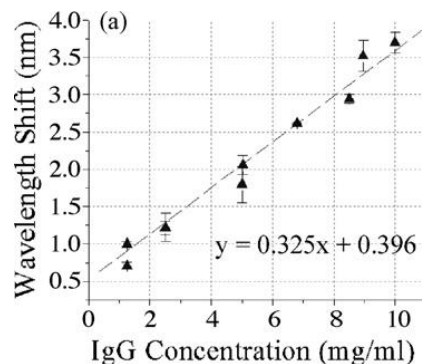


Figure 1.27: Microcavity sensor calibration curve for rabbit IgG. Extent of resonance wavelength shift upon binding of increasing concentrations of rabbit IgG [48].

Another label-free pSi sensor has been developed by Ouyang *et al.* utilising the microcavity structure [102]. The sensor operated via analysis of the red-shift in the resonance peak induced through the binding of an analyte to an immobilised probe molecule. The device was targeted at the detection of Intimin-ECB (extracellular domain of Intimin); a protein associated with the pathogenicity of enteropathogenic *Escherichia coli*. The probe molecule Tir-IBD (translocated Intimin receptor - Intimin binding domain) was immobilised onto the surface via an aminopropyltriethoxysilane/glutaraldehyde linker. To help prevent non-specific adsorption, the surface was saturated with Tir-IBD. The sensor was then calibrated with known concentrations of Intimin-ECD and the micromolar dissociation constant ( $K_d$ ) investigated.  $K_d$  was found to increase from  $0.3 \times 10^{-6}$  M in solution to  $1 \times 10^{-4}$  M for immobilised Tir-IBD. This indicated a weaker association between the probe and receptor and was attributed to steric issues and/or kinetic effects due to pH or concentration gradient within the pores. The sensor and control surface (did not contain Tir-IBD) were exposed to cell lysate (supernatants) from the BL21 *E. coli* cell line (expresses Intimin-ECD) and JM109 *E. coli* cell line (does not express Intimin-ECD). A 5 nm red-shift occurred upon introduction of the BL21 lysate indicating the presence of Intimin-ECD. Subsequent analysis determined that 15  $\mu$ M of the Intimin-ECD was present in the sample. Exposure to the JM109 lysate resulted in a 1 nm red-shift that was attributed to non-specific binding and exposure of both cell line lysates to the control surface resulted in no shift in the resonant peak. Analysis of the BL21 lysate by SDS-PAGE gel electrophoresis found the Intimin-ECD concentration to be 14  $\mu$ M which corresponded to that determined via the optical microcavity sensor. This indicated that the sensor could selectively and quantifiably detect a protein from a large mixture of supernatants. While the sensor was less sensitive than ELISA and other traditional techniques, the ease of production and operation must be taken into account. These factors make this sensor ideal for application in rapid high-throughput screening devices for point-of-care diagnostics, where ultra sensitive analysis is not required.

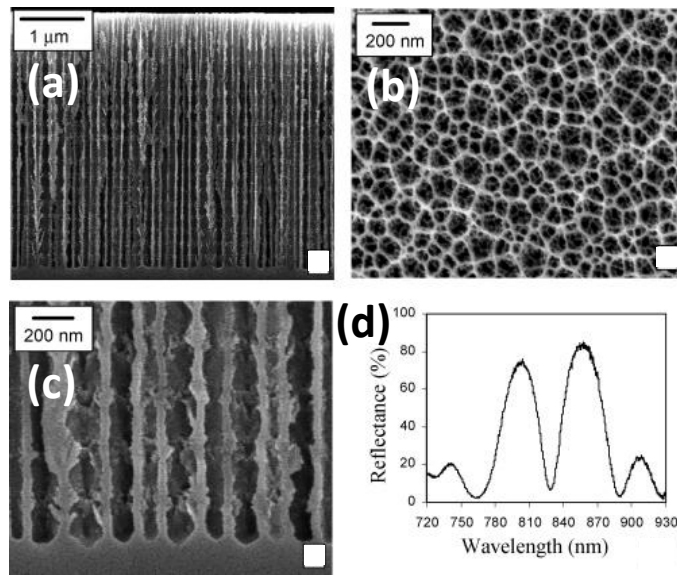


Figure 1.28: (a) & (b) Cross-section SEM images of the silicon microcavity used to detect the Intimin-ECD protein. (c) Top view of the same pSi sample. (d) Reflection spectrum of the microcavity structure with an indicative absorption dip at ~830 nm [103].

#### 1.2.4.6 Smart Dust pSi Sensors

Utilising encoded smart dust particles, Cunin *et al.* devised a procedure whereby rat albumin could be isolated from a solution containing bovine serum albumin [104]. Two variants of the particles were produced from rugate pSi, the first was encoded with a reflectance band at 750 nm and bovine serum albumin was adsorbed on the surface as a control. The second was encoded at 540 nm and coated with rat albumin before being exposed to rabbit anti-rat albumin antibody solution. The two particles were mixed together and exposed to fluorescently labelled anti-rabbit IgG. Upon analysis, fluorescence was found to only occur on the rat albumin particles encoded at 540 nm. This procedure highlights how easily the properties of pSi can be adapted to various roles. The ease with which the pSi particles can be encoded and manufactured, coupled with the material's biocompatibility and degradability [105] provide advantages over other coding systems such as the potentially toxic CdSe nanoparticles [106].

### 1.2.5 Photoluminescence Based Transducers

The discovery of room temperature photoluminescence, led to the development of one of the earliest pSi biosensors. Starodub *et al.* adapted the material's luminescence as a transduction mechanism for the detection of antigen-antibody interactions [107]. The effect of the interaction between rabbit IgG and sheep anti-rabbit IgG on photoluminescence was studied. Adsorption of the rabbit IgG on the stain etched pSi did not change the photoluminescence profile of the material, however, exposure of the treated pSi to a sheep anti-rabbit IgG solution resulted in a dramatic reduction in the intensity of photoluminescence from the surface. The change in intensity was found to be related to the exposure time and antibody concentration. Starodub postulated that the formation of the immunocomplex resulted in the dehydrogenisation of the pSi surface allowing a non-radiative pathway of recombination of the exposed Si bonds. Impressively, it was proposed that the sensor potentially has the ability to detect anti-rabbit IgG down to levels of ~10 ng/mL. This early biosensor highlighted the capability of devices manufactured from pSi to compete with traditional analytical techniques such as ELISA.

Starodub built upon this initial work with the formation of a sensor for the detection of the heart disease marker myoglobin [108]. An anti-human mouse monoclonal antibody specific to myoglobin was adsorbed onto the pSi surface and used to capture myoglobin present in buffers and human serum. The pSi's photoluminescence decreased upon myoglobin binding due to the removal of hydrogen from the surface. Calibration of the sensor revealed that it could also achieve detection at very low levels in serum, down to 10 ng/mL. In addition to achieving equivalent detection levels as ELISA, the response time of this sensing platform was remarkably shorter, requiring 15-30 min compared with the hours of incubation associated with ELISA. Operational stability of the sensor was also analysed and it was found that photoluminescence of the pSi recovered to approximately 50% after the initial measurement cycle, indicating that the sensor would be best adapted to a single use disposable system.

## Introduction

More recently label-free detection of DNA has been demonstrated using photoluminescent pSi [109]. Functionalisation of the surface with a bromo-acetamidopropylsilane linker resulted in a large reduction in photoluminescence believed to be due to the same pathway previously cited by Starodub. It was postulated that the presence of the active bromine group on the silanes further enhanced this effect, leading to the large decrease in photoluminescence depicted in Figure 1.29. Attachment of phosphothioate terminated probe DNA yielded a large increase in the photoluminescence intensity, which was attributed to the removal of the bromo groups from the silane and passivation of the surface. Introduction of cDNA resulted in further stabilisation of the surface and the subsequent increase in photoluminescence, while exposure of the probe DNA to non-complementary DNA did not change photoluminescence intensity. This sensor affords label-free DNA detection with salient features such as simple device manufacture and operation.

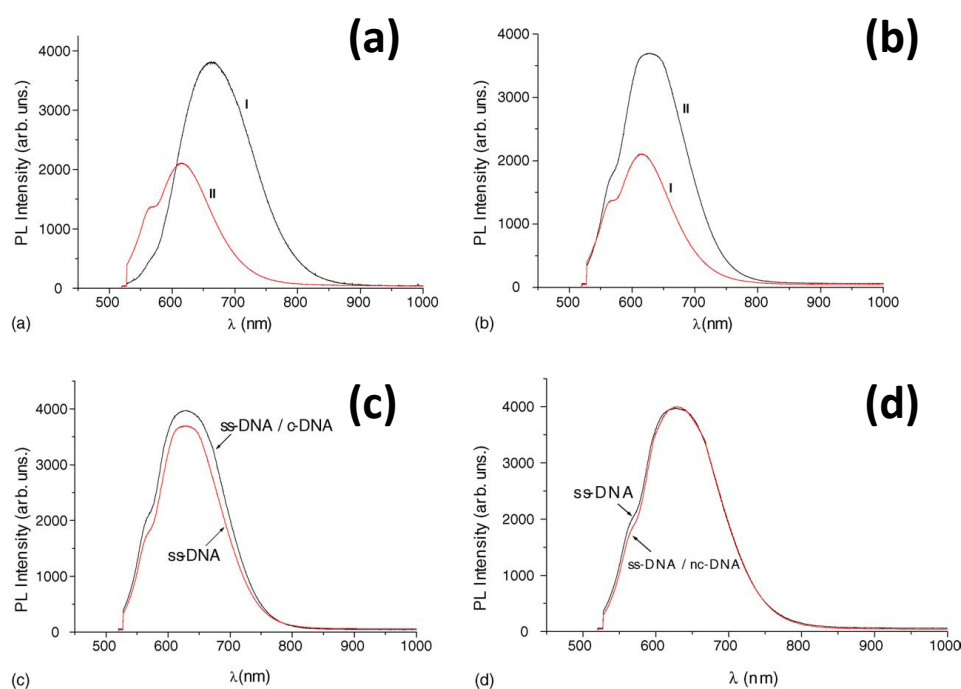


Figure 1.29: Detection of DNA hybridisation via an increase in photoluminescence intensity. (a) Functionalisation of pSi with trimethoxy-3-bromo-acetamidopropylsilane, (b) immobilisation of the single stranded probe DNA, (c) hybridisation of the probe and cDNA; and (d) exposure to non-cDNA. (I – prior to attachment, II – after attachment) [109].

### 1.2.6 Chemiluminescence-Based pSi Transducers

The generation of chemiluminescence on pSi has been used to detect pathogens, namely *E. coli*, for application in food and environmental testing [110]. pSi was functionalised with a dioxetane-polymyxin B (cell wall permeabiliser) that reacts with the  $\beta$ -galactosidase enzyme from *E. coli*. The enzyme is involved in the bacteria's metabolism and as the bacterial cells grows on the pSi, the bacterial enzymes turn over the dioxetane substrate to generate chemiluminescence at 530nm. In this fashion, a sensor was fabricated that imparted a 3x increase in light production compared to planar silicon due to the increased surface area. The increased surface area also resulted in a lower detection limit of  $10^1$  and  $10^2$  cells compared to  $10^3$  cells for previous single-tube chemiluminescence assays. Given its sensitivity, combined with a rapid detection time of 30 – 40 min, compared to the 48 hrs required for traditional techniques this sensor is a potent platform for pathogen detection.

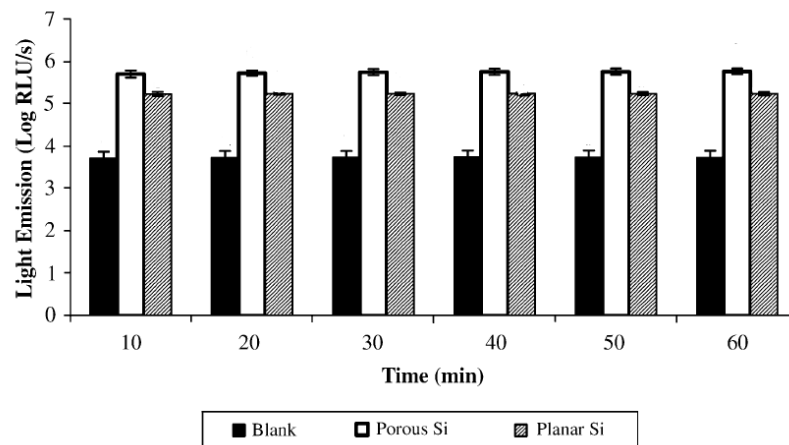


Figure 1.30: Chemiluminescence signals upon *E. coli* sensing on pSi and planar silicon against a pSi control. The increased surface area associated with pSi led to 3x the light emission of a planar silicon surface (RLU – Relative Light Units/sec) [110].

### 1.2.7 Infrared-Based pSi Transducers

Yamaguchi *et al.* recently developed a pSi microarray for the detection of DNA hybridisation based on infrared microspectroscopy [111]. DNA bases have specific vibration modes (C=O, C-N, and C=C stretching modes) that are highly sensitive to base pairing and can subsequently be used to detect hybridisation. To produce the microarray structure, n-type silicon was thermally oxidised and patterned using photolithography before being anisotropically etched to produce a series of ordered wells (Figure 1.31). Removal of the oxide layer and electrochemical etching in HF then resulted in the formation of pSi membranes at the bottom of each well. Immobilisation of a 20-base thymine oligonucleotide ( $dT_{20}$ ) was achieved via the formation of disulfide bonds with a mercapto silane monolayer. DNA was prepared in  $D_2O$ , to prevent interference from the scissoring vibration of  $H_2O$ .

Hybridisation with the target DNA was then detected via changes in the IR spectra.  $dT_{20}$  treated pSi was used as an IR reference (background) and introduced to a  $D_2O$  solution containing a complementary adenine oligonucleotide,  $dA_{20}$ , and NaCl. NaCl was used to neutralise the negative charge of the DNA and stabilise the double helix structure. Fourier Transform Infrared (FTIR) analysis of the pSi treated with  $dA_{20}$  displayed a strong absorption peak at  $1645\text{ cm}^{-1}$  due to the deformation mode of the purine ring of adenine. Subsequent washes of up to 12 hrs failed to remove the peak from the spectrum, indicating that hybridisation had occurred. Introduction of a non-specific oligonucleotide,  $dC_{20}$ , on the other hand produced no IR absorption profile after washing due to the removal of the non-specific DNA. Device sensitivity was not commented upon, and the requirement that samples be diluted in  $D_2O$  is a fundamental drawback, as traditional mediums such as PBS cannot be directly applied to the device, limiting its application.

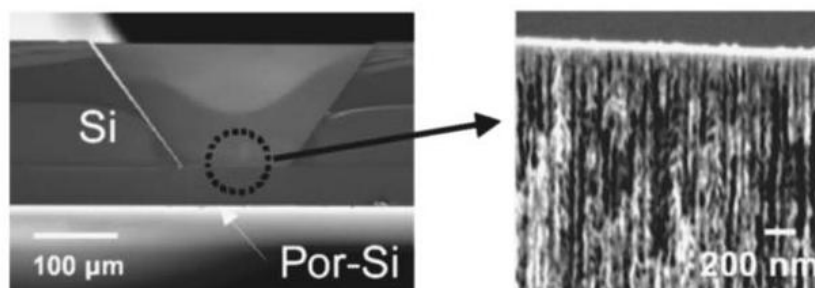


Figure 1.31: Cross-sectional SEM images of a pSi microarray well in two different magnifications [111].

### 1.2.8 Electrochemical Transduction on pSi

Exploitation of pSi's semiconductor properties has also produced biosensors capable of electrochemical transduction. Traditionally, electrochemical detection involves the conversion/production of an electro-active substance in the presence of the target analyte. The incorporation of pSi into such devices offers the advantage of larger sensing areas and inherent biocompatibility, thus improving sensor capabilities.

Song *et al.* utilised pSi adhered to a platinum working electrode to greatly increase the effective surface area, achieving high sensitivity for liver disease markers such as cholesterol, bilirubin and glutamate (aminotransferases) [112]. The biosensor, consisting of an enzyme array, was shown to be capable of detecting these markers in parallel. A series of wells within a PDMS microfluidic structure separated 4 pSi working electrodes and minimised cross-interference effects. Each well contained a separate pSi electrode coated with a different oxidase enzyme. The enzymes produced  $H_2O_2$  upon conversion of their respective analytes, which then underwent oxidation resulting in generation of two electrons which were detectable by the electrode [113].

The device was able to function over typical analyte concentrations, exhibiting detection levels of 1 mM for cholesterol, 0.002 mM for bilirubin, and 1.3 U/l for alanine aminotransferase and aspartate aminotransferase. Impressively, the

## Introduction

sensor was able to achieve a response time of 20 seconds with a sample size of  $\sim 40 \mu\text{L}$ . This was largely due to the incorporation of pSi into the working electrode which provided improved sensitivity, response time and miniaturisation compared with other previous array-based biosensors.

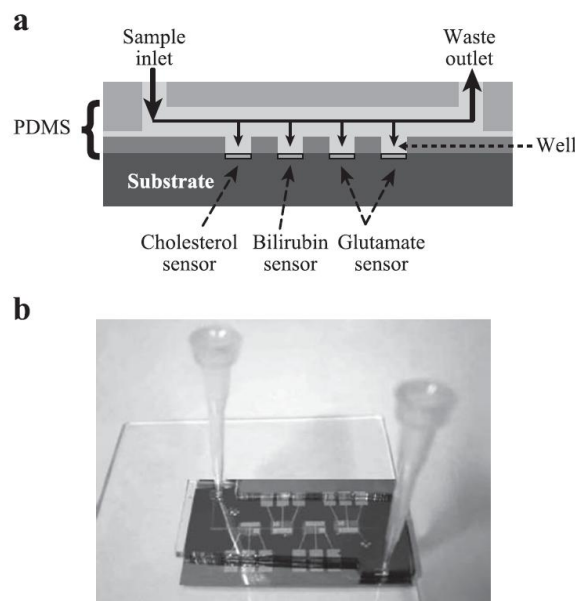


Figure 1.32: Liver disease biosensor array, (a) Cross-sectional schematic of PDMS microfluidic system on top of a silicon substrate, (b) photograph of the device [112].

Another system that has recently been reported involves the fabrication of a highly stable sensor for the detection of triglycerides [114]. Lipase sensors are important devices due to their ability to be applied to a variety of different applications including biomedical and food analysis. Setzu *et al.* immobilised the lipase enzyme onto the pSi surface through physisorption. A triglyceride, tributyrin, was then introduced and subsequent hydrolysis via the lipase produced a pH change resulting in a strong open circuit potential (OCP). This device exhibited high stability, providing reproducible data for up to 17 hours if used within 2 months of manufacture, offering important advantages over traditional

## *Introduction*

unstable triglyceride sensors. Significantly, this study also found that enzyme activity was not affected by diffusion into the porous structure, allowing the formation of accurate enzymatic pSi sensors.

Detection of charged molecules has also been achieved by monitoring the capacitance of the silicon substrate. Archer *et al.* produced a sensor capable of detecting the conjugation of complementary DNA strands via changes to the impedance of the pSi [115]. Electrodes were attached to the base of a macroporous silicon substrate, allowing unhindered access to the pSi. The surface was functionalised with poly-L-lysine and probe DNA was immobilised via electrostatic interactions [113] and then introduced to a solution containing complementary DNA. Binding of the cDNA resulted in a decrease in impedance and a shift in the phase angle. Archer proposed that this effect arose from the change in the dielectric constant within the porous matrix and the space-charge region in the crystalline silicon structure. The absence of a signal upon addition of an uncharged analogue of DNA, PNA, supported this argument. The sensor operated with nanomolar limit of detection, which compares well with modern hybridisation sensing devices.

## Introduction

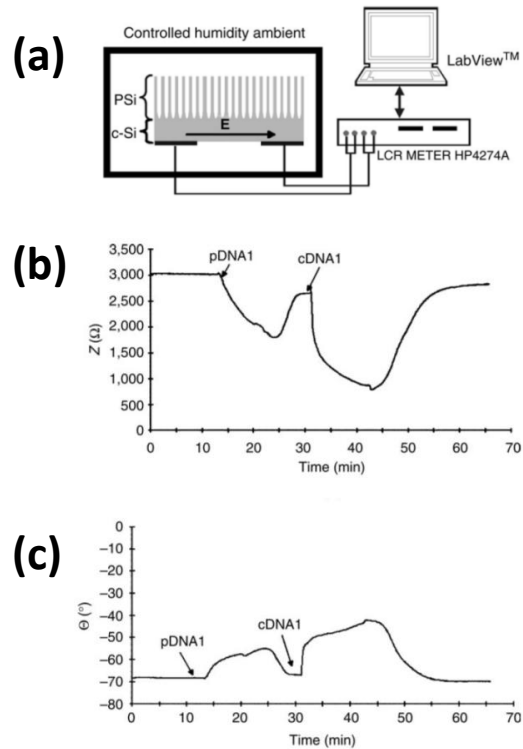


Figure 1.33: (a) Schematic of the pSi capacitance sensor for DNA. (b) Impedance ( $Z$ ) and (c) phase angle ( $\Theta$ ) of the pSi device. The introduction of the probe DNA (pDNA1) and complementary DNA (cDNA1) result in a large change to both properties. The recovery of the signal to baseline is attributed to the drying of the sample prior to introduction of cDNA1 [115].

### 1.2.9 pSi Summary

The application of pSi as a transducer material in biosensors has engendered many high impact discoveries in this field. In particular, the use of pSi has provided a whole new family of devices not limited to one transduction method featuring reduced detection times and increased sensitivity.

The unique structural, optical and electrical properties of pSi are poised to be applied in a range of future advanced sensing devices. The further capability for patterning and miniaturisation provides a path to the development of small, mobile and highly parallel biochip arrays for the simultaneous detection of a variety of antigens, where the transducer material can easily be integrated with electronics using established microfabrication technology. Most importantly, biocompatibility of pSi may allow integration of the material into implantable biosensors, able to monitor biological systems in real-time.

### 1.3 S-Layer Proteins - A Versatile Receptor Platform

#### 1.3.1 Introduction

The cell wall is an essential structural part of all organisms and is important in many facets of their life. In particular, the outer-most layer of many prokaryotic cell wall structures has evolved to cope with varying ecological and environmental conditions. With the exception of specialised prokaryotes that exist in unique ecological conditions, a large class of bacteria and archaea contain an ordered, crystalline, biological supramolecular layered cell-wall structure outside the cytoplasmic membrane [116]. In combination with the cytoplasmic membrane, this structure forms a regulatory barrier allowing molecular exchange between the cell and its environment. Such ordered outer layer cell wall structures have been termed surface layers (S-layers) [116]. Since the initial discovery of S-layer structures in 1953 by Houwink [117], such proteins have been found in all major groups of bacteria, including Gram-positive and Gram-negative eubacteria and archaea [118]. Regardless of the species, the S-layer normally forms the outer-most layer, acting as a protective sheath (Figure 1.34).

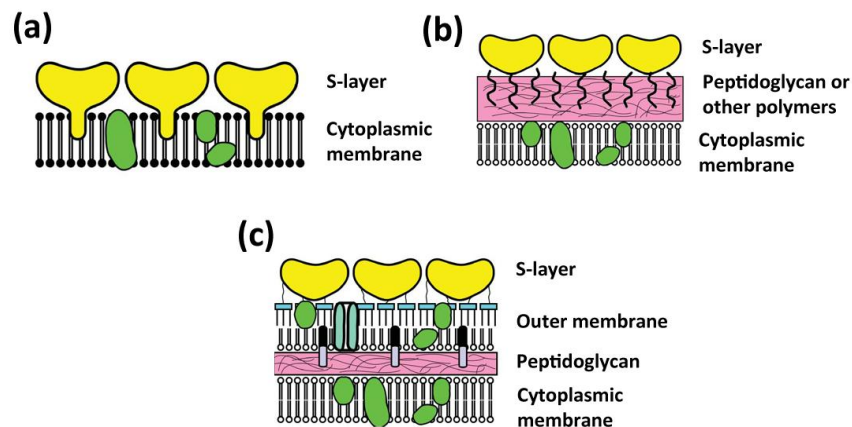


Figure 1.34: Schematic depicting the cell wall architecture of the major types of bacterial cells covered by S-layers. (a) Most archaea: S-Layer proteins are the only cell wall component external to the cytoplasmic membrane. (b) Gram-positive eubacteria and archaea. (c) Gram-negative eubacteria and cyanobacteria: S-layers are bound to the outer membrane (adapted from [119]).

## *Introduction*

S-layers consist of a monomolecular layer formed from proteins or glycoproteins and have the ability to assemble into closed, highly porous frameworks on the cell wall. The molecular weight of S-layer proteins can range from 40 – 200 kDa depending on the species. Furthermore, it has been demonstrated that S-layer proteins can contribute up to 15% of the total protein of a bacterial cell [120]. The abundance of such proteins combined with their unique properties has prompted extensive investigation into extracting S-layer proteins, replicating these effects *in vitro* and application in functional molecular arrangements. Research into S-layers over the past four decades has revealed much about the genes, transcription, proteins and principles involved in forming such structures. S-layer proteins can now be readily isolated from bacterial cultures and reassembled, via self-assembly, into regular arrays [121]. The formation of flat sheets, open-ended cylinders or closed vesicles can be achieved in solution [122, 123], while the self-assembly of large, structured, S-layer protein monolayers have been observed on solid supports, such as semiconductors, noble metals, glass, carbon, synthetic polymers and on lipid films and liposomes [116, 123-127].

These properties make S-layer lattices attractive for many applications in the fields of medicine, nanobiotechnology and biomimetics [116, 121]. Properties of the S-layer structures commonly exploited include:

S-layer subunits extracted from many prokaryotes can be re-crystallised as a self assembled monolayer on solid supports such as silicon, mica, lipid films and liposomes [128, 129].

The assembled S-layers contain pores of uniform size and shape useful for size exclusion applications.

The chemical structure of S-layer subunits has been extensively investigated, identifying precise locations on each the S-layer module where functional molecules can be attached.

Genetic manipulation of S-layer proteins has also expanded the versatility and functionality boundaries of the natural biomolecules. Modification of the protein structure and the fusing of S-layer sub-units with foreign functional protein

sequences have resulted in self-assembling arrays of uniform structure and functionality.

The capacity to self-assemble ordered monolayer structures of defined chemical structure and functionality has already led to the use of S-layers in many fields, from biotechnology and medicine to nanotechnology. Ultimately, there is much potential for adaptation in biological sensing, where it could improve sensitivity and give rise to a qualitatively new fabrication and immobilisation approaches.

### ***1.3.2 S-Layer Structure***

S-layers are formed by two-dimensional crystalline arrays of identical proteinaceous subunits which are organised in oligomeric unit cells of a given lattice symmetry [118]. S-layers commonly consist of a single protein or glycoprotein species and thus exhibit one of three 2-D lattice types, oblique (p1 or p2 symmetry), square (p4 symmetry) or hexagonal (p3 or p6 symmetry) (Figure 1.35). Depending on the lattice type, each unit consists of one, two, four, three or six identical subunits respectively and exhibit centre-to-centre spacing of approximately 2.5 to 35 nm [130]. The layer can range from 5 to 25 nm in thickness and generally exhibit a smooth outer surface and rougher inner surface. Chemical analysis of S-layer proteins from micro-organisms of dissimilar phylogenetic groups identified similarities in their composition with the majority of S-layer proteins exhibiting high levels of acidic and hydrophobic amino acids [130]. The main amino acid in many S-layer proteins is lysine, while levels of arginine, histidine, and methionine are generally low and cysteine has only been identified in a few cases [130].

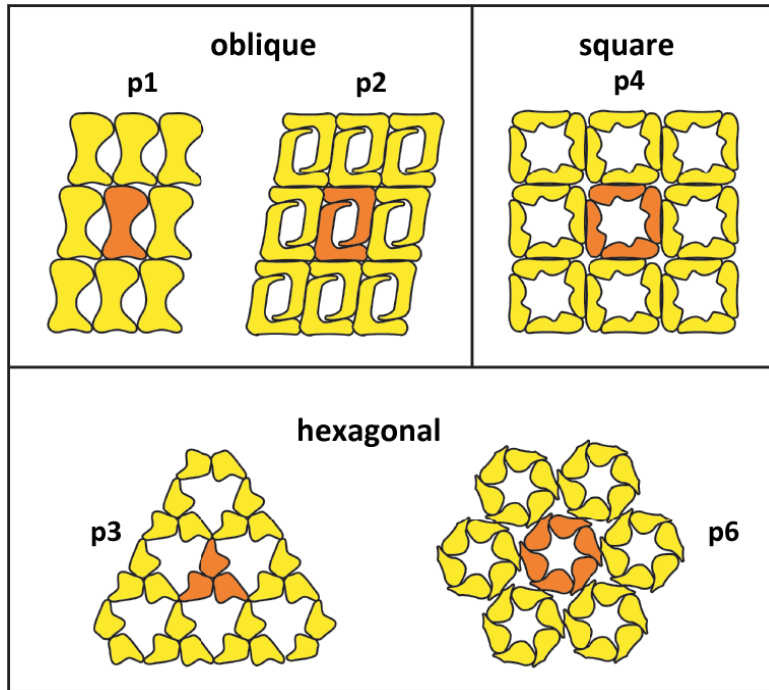


Figure 1.35: Schematic identifying the known S-layer lattice patterns. Each lattice unit is formed from the symmetric array of identical mono-, di-, tri-, tetra-, or hexamer subunits. Graphic adapted from [119].

Traditionally it has only been possible to visualise S-layer structures using electron microscopy. This involved killing the host organism by freeze-etching of pellets of unwashed cells in media (Figure 1.36 (a)) [131, 132]. However in recent years, liquid atomic force microscopy has been utilised due to the ability to record high-resolution images of extracted S-layer proteins and/or alive cells in their native environment (Figure 1.36 (b)) [116, 133].

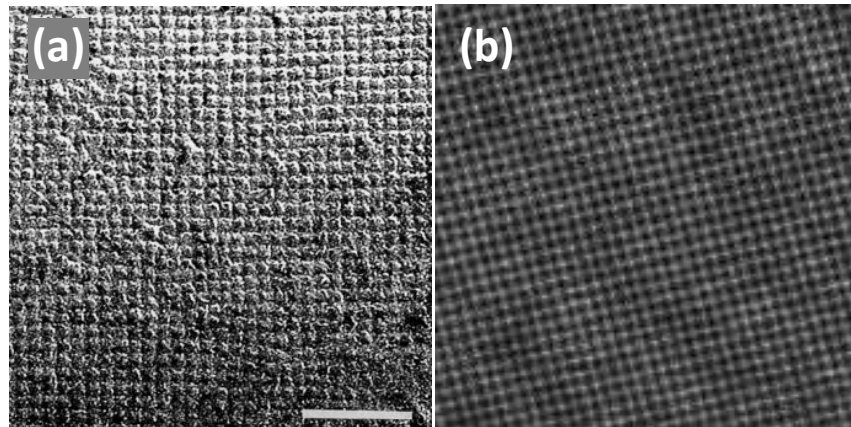


Figure 1.36: S-layer lattice on the surface of a bacterial cell and after extraction and recrystallisation. (a) Electron micrograph of S-layer lattice on the wall of a *Desulfotomaculum nigrificans* NCIB 8706 bacterial cell [118]. The lattice displays a square pattern (p4 symmetry). Scale bar 100 nm. (b) Liquid AFM image of isolated S-layer protein recrystallised on a silicon wafer. Protein was extracted from *Lysinibacillus sphaericus* CCM 2177 and also displays p4 symmetry. Image parameters:  $0.5 \mu\text{m} \times 0.5 \mu\text{m}$ , Z-range 2 nm [134].

### 1.3.3 Self-Assembly

The self-assembly of sub units into a complete morphological unit depends on a number of factors including the surface charge and inner and outer hydrophobicity of the proteins, relevant binding domains to the supporting platform and defined inter-subunit binding properties. All of these factors impact on the orientation and incorporation of S-layer subunits on cell surfaces [130]. More recently it has been theorised that the self-assembly of monomeric S-layer subunits is entropically driven and the formation of the S-layer lattice results in a favourable loss of hydrophobic surfaces [135]. This study and others have demonstrated that self-assembled recrystallisation of extracted S-layer protein is also dependent on protein concentration, temperature and other environmental conditions such as the presence of calcium, ionic strength and pH of the solution [116, 136].

The presence of calcium or other divalent cations is vitally important for most S-layer protein – protein interactions and the attachment of proteins to the surface via protein – surface interactions [134]. Studies have shown that calcium ions are

## Introduction

necessary for the self-assembly of S-layer proteins and that the concentration of this ion impacts the shape and size of the recrystallised lattices [135, 137]. It is proposed that calcium ions might be involved in the self-assembly mechanism via one or more of the following routes [135]:

The binding of calcium to a specific site on the protein may modify the structure, exposing certain domains required for the assembly process.

There may exist calcium mediated interactions between protein subunits.

Calcium may neutralise negative charges at specific binding domains, facilitating the self-assembly process.

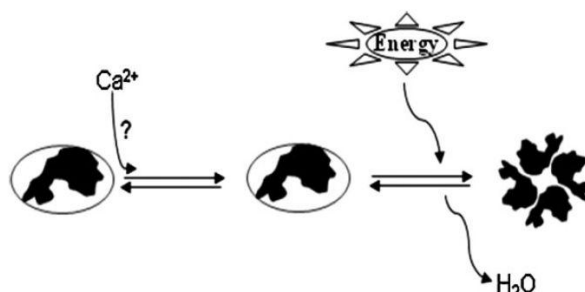


Figure 1.37: Schematic of the role of calcium in the self-assembly of S-layer subunits into a complete morphological unit [135].

Due to the S-layer subunits interacting with each other and the cell membrane through weak forces such as ionic bonding, hydrophobic interactions, hydrogen-bonding or salt-bridging interactions, disruption of these forces can provide a route to isolation and extraction of the protein. High concentrations of chaotropic agents such as urea and guanidine hydrochloride are commonly used to isolate the protein, while metal chelating chemicals such as ethylenediaminetetraacetic acid (EDTA) and ethylenebis(oxyethylenitrilo)tetraacetic acid (EGTA) or changes to the pH of the environment can also be used [131, 136]. Removal of these disrupting agents via dialysis can allow recrystallisation of the protein in vitro. Recrystallised S-layer lattices can be fragile due to the same weak binding forces that allow the use of relatively mild extraction procedures. Thus, maintaining favourable environmental conditions will preserve lattice coherence. Arrays can also be cross-linked together using glutaraldehyde (GA),

bis(sulfosuccinimidyl)suberat (BS<sup>3</sup>) or 1-ethyl-3-(3-dimethylaminopropyl)-carbodiimide (EDC) to improve the strength and durability of the structure [134].

#### ***1.3.4 Applications of native S-layer proteins***

The unique properties of S-layer proteins have potential for adaptation to many different applications such as biosensing, ultrafiltration, vaccine development and drug delivery [123]. It has been demonstrated that S-layer composites can be utilised in ELISA's to improve the sensor's response. In this study, Human IgG was covalently bound to S-layer coated cup-shaped microparticles and used as an analyte in sandwich immunoassays [138]. An increase in surface area and analyte levels lead to a corresponding increase in signal intensity. Drug delivery could also be achieved through the crystallization of S-layers on micro or nanocapsules as demonstrated by Toca-Herrera and Mader [139, 140]. Coating capsules, such as liposomes, with S-layer arrays provides an easy route for surface functionalisation with receptor molecules. In this fashion drug loaded capsules could be selectively bound to specific targets for payload release. Another broad application involves the recrystallisation of extracted S-layer protein onto membranes and liposomes [116, 126, 141-143] to mimic the cell wall structure of the organism the protein was isolated from. As such, these re-assembled lattices can be used in diagnostics, as vaccines, for drug targeting or delivery and for gene therapy [116, 130, 144-146]. Another technique with potential for lab-on-a-chip technologies or microarrays applications involves the microlithographic patterning of recrystallised S-layer arrays on solid supports such as silicon wafers [116, 126, 147].

This brief overview of the use of native S-layer applications has demonstrated the flexibility and value of the protein. The ability of extracted S-layer protein to self-assemble into large coherent crystalline lattices has allowed its use in diverse roles and has potential for further adaptation in the future.

#### ***1.3.5 Genetic Modification of S-layers***

While the native S-layer proteins have been successfully utilised for patterning and other applications, genetic engineering can incorporate specific functional

## Introduction

domains within S-layer proteins without impacting on the ability to self-assemble. Through alterations to their natural properties, S-layer proteins can be tailored to perform specific functions. Via this approach, genetically modified S-layers have now been incorporated in affinity structures, microcarriers, enzyme membranes, diagnostic devices, biosensors, vaccines and drug delivery devices [121]. To successfully modify the S-layer protein it must retain its original properties in addition to incorporating a new functionality. This requirement has been eloquently defined by Ilk *et al.* who stated, “S-layer proteins must be capable of tolerating insertions or fusions with foreign proteins or domains, remaining able to assemble into geometrically well-defined layers, and of incorporating a segment that has never participated in lattice formation” [121]. The production of S-layer fusion proteins used in the afore mentioned applications has generally followed two main approaches, homologous expression (expression of the modified protein within the same organism) and secretion by the cells or heterologous expression and production within a host cell, mostly *Escherichia coli* (*E. coli*) [121].

Genetically engineering S-layer fusion proteins provide the ability to form self-assembled, ordered arrays with defined nanometre periodicity of functionality. Potentially, S-layer proteins can be fused with a very large number of other functional proteins creating a flexible platform that could be incorporated a vast array of fields and applications. The most extensive research into S-layer fusion proteins has focused on protein from several bacterial strains including *Lysinibacillus sphaericus* CCM 2177 (previously known as *Bacillus sphaericus*). The properties of S-layer protein from *L. sphaericus* (commonly referred to as SbpA) have been broadly characterised, including the sequence of the protein, recrystallisation factors, lattice properties and the location of charged domains within the protein structure. SbpA has a molecular weight of 120 KDa, contains a total of 1268 amino acids, includes a N-terminal binding domain to a secondary cell wall polymer (SCWP) and forms a square lattice of p4 symmetry with a centre to centre spacing of 13.1 nm between individual units [137, 148]. Studies into the structure-function relationship of SbpA revealed that the C-terminal could be truncated by deleting 200 C-terminal amino acids without impacting on the self-assembly properties or the formation of the lattice structure. Importantly,

the new C-terminal, amino acid position 1068, was found to be located on the outer S-layer surface [148]. This has allowed the exploitation of C-terminally truncated SbpA<sub>31-1068</sub> to be used as the base partner for the construction of various S-layer fusion proteins discussed in the next section. N-terminally truncated forms of the native SbpA protein have also been generated and successfully integrated as a fusion partner in the formation of chimaeric S-layer fusion proteins [127, 147, 149].

### 1.3.5.1 S-layer Fusion Protein Based Sensors and other applications

The intrinsic ability to form self-assembled monolayers in conjunction with defined periodic functionality makes this protein highly attractive for integration into detection and diagnosis devices. The flexibility to change the functionality or binding domain of the fusion protein could provide the basis of a detection system for such analytes as DNA, various proteins and antibodies and could form a suitable platform for label-free sensors.

Of particular interest to the work in this thesis was the formation of an S-layer fusion protein for the binding of antibodies. The truncated rSbpA<sub>31-1068</sub> S-layer protein discussed earlier was combined with two copies of a 58 amino acid long Z domain to form the fusion protein rSbpA<sub>31-1068</sub>/ZZ [148]. The Z domain is a synthetic analogue of the IgG-binding domain of protein A from *Staphylococcus aureus* and is capable of binding the Fc component of all IgG's. Vollenkle *et al.* demonstrated the expression and recrystallisation of this fusion protein on microbeads for the extraction of antibodies from the blood of patients suffering from autoimmune diseases [148].

## Introduction

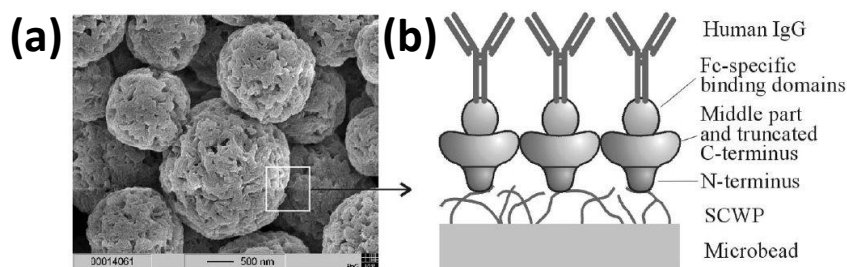


Figure 1.38: (a) SEM micrograph of cellulose microbeads coated with the rSbpA<sub>31-1068</sub>/ZZ fusion protein. (b) Schematic depicting the surface of the microbeads and the capture of Human IgG via the S-layer fusion protein [148].

S-layer fusion proteins have also been developed which incorporate streptavidin at either the N-terminal or C-terminal to serve as a universal affinity matrix. Labelling of analytes with biotin can facilitate surface patterning, extraction and/or detection [150-152]. In addition to these examples, label-free detection of analytes can be achieved through the formation of S-layer fusion proteins containing antibody domains specific to a certain analyte. This has been demonstrated via the incorporation of a camel antibody sequence recognising the prostate specific antigen (PSA) with SbpA to form the chimaeric protein rSbpA<sub>31-1068</sub>/cAb-PSA [153, 154]. Recrystallisation of this protein on gold chips allowed the label free detection of PSA via surface plasmon resonance (SPR).

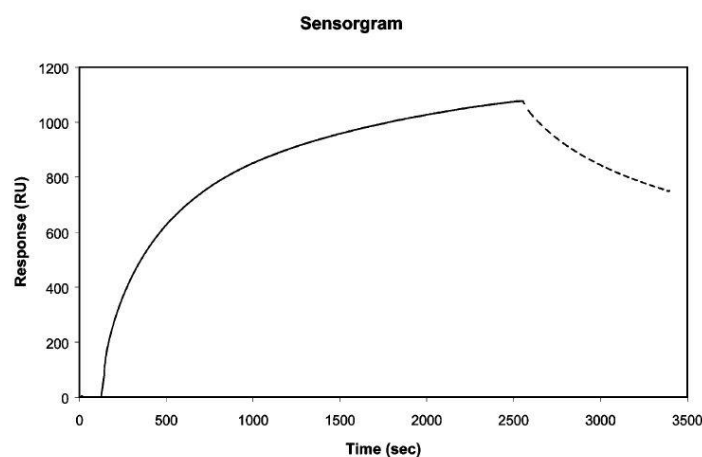


Figure 1.39: SPR Sensorgram showing association (—) and dissociation (- - -) between PSA and an rSbpA<sub>31-1068</sub>/cAb-PSA-N7 coated gold chip. The retention of PSA after washing indicated specific binding of PSA to the S-layer fusion protein [153].

## Introduction

In addition to the examples discussed here, many other chimaeric S-layer proteins have been prepared with a large range of functionality and application. Table 1.3 has been adapted from [155] and contains a current overview of functional domains fused to S-layer proteins and their application.

Functionality	Application
Core streptavidin	Binding biotinylated ligands (DNA, protein), Biochip development
Major birch pollen allergen (Bet v1)	Vaccines, treatment of type 1 allergy
Strep-tag II, Affinity tag for streptavidin	Biochip development
ZZ, IgG-binding domain of Protein A	Extracorporeal blood purification
Enhanced green fluorescent protein (EGFP)	Liposomes, Drug and delivery systems
cAb, Heavy chain camel antibody	Diagnostic systems and sensing layer for label-free detection systems
Hyperthermophilic enzyme laminarinase (LamA)	Immobilized biocatalysts
Cysteine mutants	Building of nanoparticle arrays
Mimotope of an Epstein-Barr virus (EBV) epitope (F1)	Vaccine development
M. tuberculosis antigen (mpt64)	Vaccine development
IgG-Binding domain of Protein G	Downstream processing
Glucose-1-phosphate thymidyltransferase (RmlA)	Immobilized biocatalysts
Enhanced cyan (ECFP), green (EGFP), yellow (YFP), monomeric red (RFP1) fluorescent protein	pH biosensors in vivo or in vitro, fluor. Markers for drug delivery systems
Metal, silica and titania precipitating peptides	Material sciences

Table 1.3: Overview of functional domains fused to S-layer proteins and their application. Adapted from [155].

### **1.3.6 S-layer Summary**

S-layer proteins form the simplest biological membrane developed during evolution and are one of the most abundant biopolymers on Earth [155]. Data obtained in studies on the structure, genetics, chemistry, morphogenesis and function of S-layer proteins has created an extensive knowledge base, from which the protein has been exploited. Reassembly of extracted S-layer proteins in solution or on solid supports has been shown to form lattices with perfect long range order. Their structure and physicochemical repetitive uniformity down to the sub-nanometer scale make an ideal material for use in many biomimetic, biotechnology and medical applications [121]. The inherent capacity to self-assemble coupled with the ability to genetically tailor the natural properties of S-layer proteins has expanded the potential of these biomolecules further. Incorporation of single or multifunctional domains from other proteins within the S-layer structure has been used to form chimaeric fusion proteins of defined functionality. Self-assembly of these fusion proteins has been shown to provide large ordered lattices of defined uniform functionality [122]. Such proteins could form the basis of a molecular construction kit utilising all forms of biomolecules. These properties make S-layer proteins highly attractive for applications in sensor technology, diagnostics, nanobiotechnology, electronic or optical devices, and high-throughput screening for drug discovery [121].

The adaptation of S-layers and chimaeric S-layers to such a diverse number of applications provides strong evidence of the value of such biomolecules. Integration of these protein arrays within a pSi matrix could act as self-assembled receptor coating for various analytes. Such biomimetic coatings could be used to improve the fabrication and sensitivity of pre-existing pSi sensors or to improve the biocompatibility of pSi particles and provide convenient surface labels for targeted drug delivery.

#### **1.4 Conclusions**

The discovery of new transducer materials, such as porous silicon, continues to rapidly advance the development of innovative immunosensing techniques. By combining the highly versatile transduction strategies achieved in pSi biosensor research with immunoassays, there is a huge potential for the development of new, cheap and very sensitive immunosensing technologies. The ability of immunoassay based systems to quantify an almost limitless number of analytes, coupled with an ever increasing range of labelled secondary antibodies, imparts a great deal of flexibility on pSi based immunosensors. Incorporation of genetically modified, self-assembling monolayers of S-layer fusion proteins to act as receptors for specific analytes, has the potential to greatly simplify sensor design and fabrication, while improving signal response and sensitivity.

pSi is a highly desirable immunosensing transduction platform and continued research into its unique properties may provide the basis of the next generation of sensing devices.



# Chapter 2

---

## 2 Materials and General Methods

## 2.1 Materials

### 2.1.1 Chemicals and Reagents

All chemicals used for pSi etching and functionalisation, immunosensing and cell culture are listed in Table 2.1. High purity solvents used for pSi modification were purified via distillation from commercial solvents [156]

#### 2.1.1.1 Chemicals

Chemical	Supplier	Grade
11-Mercaptoundecanoic Acid (MUA)	Sigma-Aldrich	98%
16 nm MUA functionalised gold nanoparticles (AuNP)	Donated by Professor Paul Mulvaney, University of Melbourne	-
3-Aminopropyl triethoxysilane (APTES)	Sigma-Aldrich	99%
3-Isocyanatopropyl triethoxysilane (IPTES)	Sigma Aldrich	95%
5-Bromo-4-chloro-3-indolyl phosphate disodium salt (BCIP)	Sigma-Aldrich	≥ 98%
Acetic acid, glacial	Chem Supply	≥ 99.7%
Acetone	Ajax Finechem	Analytic grade
Acrylamide	Bio-Rad	99.90%
Agar	Sigma-Aldrich	Molecular biology grade
Ammonium acetate (NH <sub>4</sub> C <sub>2</sub> H <sub>3</sub> O <sub>2</sub> )	Sigma-Aldrich	≥ 98%
Ampicillin	Sigma-Aldrich	Molecular biology grade
BCIP/NBT Liquid Substrate System	Sigma-Aldrich	Ready to Use
Beef extract	Sigma-Aldrich	Molecular biology grade
Bromophenol blue	Bio-Rad	Electrophoresis purity
BSA	Sigma-Aldrich	≥ 98 %
Calcium chloride dihydrate (CaCl <sub>2</sub> .2H <sub>2</sub> O)	Chem Supply	≥ 99%

*Materials and General Methods*

Citric acid monohydrate (C <sub>6</sub> H <sub>8</sub> O <sub>7</sub> ·H <sub>2</sub> O)	Chem Supply	≥ 99.5%
Coomassie Brilliant Blue R-250	Bio-Rad	-
D <sub>2</sub> O	Sigma-Aldrich	99.9%
Dichloromethane (DCM)	Biolab	Analytic grade
Dimethyl sulfoxide (DMSO)	Chem Supply	≥ 99%
1-ethyl-3-(3-dimethylaminopropyl) carbodiimide (EDC)	Sigma-Aldrich	98%
Ethanol	Chem Supply	Analytic grade
Ethanolamine hydrochloride	Sigma-Aldrich	99%
Ethidium bromide (EB)	Invitrogen	Ultrapure™
Ethylendiamine-tetraacetic acid (EDTA)	Sigma-Aldrich	≥ 99.4%
Formaldehyde	Sigma-Aldrich	Analytic grade
Glucose	Sigma-Aldrich	≥ 99%
Glycerol	Sigma-Aldrich	99%
Glycine	Merk	Molecular biology grade
Guanidine HCl	Sigma-Aldrich	≥ 99%
Hydrogen peroxide (H <sub>2</sub> O <sub>2</sub> (aq))	Chem Supply	29 – 32 %
Hydrochloric acid (HCl)	Sigma-Aldrich	Reagent grade
Hexane	Southern Cross	Commercial grade
Hydrofluoric acid (HF)	Merk	Analytic grade
Hydroquinone	Sigma-Aldrich	≥ 99%
Hydroquinone diphosphate	Synthesised by Author	-
Isopropyl alcohol	Sigma-Aldrich	Analytic grade
LI Silver enhancement kit	Nanoprobes	-
Magnesium acetate (Mg(CH <sub>3</sub> COO) <sub>2</sub> )	Ajax Finechem	≥ 99.5%
Magnesium chloride anhydrous (MgCl <sub>2</sub> )	Sigma-Aldrich	≥ 98%
Magnesium sulphate anhydrous (MgSO <sub>4</sub> ·7H <sub>2</sub> O)	Sigma-Aldrich	Reagent grade

*Materials and General Methods*

Methanol	Chem Supply	Analytic grade
n,n,n',n'-tetramethylethylenediamine (TEMED)	Bio-Rad	Electrophoresis purity
N-hydroxysuccinimide (NHS)	Sigma-Aldrich	98%
NCW-1001 Non-ionic surfactant	Wako	-
Nitric acid	Chem Supply	60%
Oromerse SO Part B (Na <sub>3</sub> Au(SO <sub>3</sub> ) <sub>2</sub> )	Technic Inc.	-
n-(triethoxysilylpropyl)-o-polyethylene oxide urethane (PEG Silane)	Fluorochem	Reagent grade
Pentafluorophenyl dimethylchlorosilane (PFCS)	Sigma-Aldrich	≥ 95%
Peptone	Sigma-Aldrich	Molecular biology grade
Phosphorus oxychloride (POCl <sub>3</sub> )	Sigma-Aldrich	≥ 99%
Poly(sodium 4-styrene sulfonate) (PSS)	Sigma-Aldrich	M <sub>wt</sub> 70,000
Potassium acetate (CH <sub>3</sub> COOK)	Sigma-Aldrich	≥ 99%
Potassium chloride (KCl)	Chem Supply	≥ 99%
Potassium dihydrogen phosphate (KH <sub>2</sub> PO <sub>4</sub> )	Sigma-Aldrich	≥ 98%
Silver acetate (CH <sub>3</sub> COOAg)	Sigma-Aldrich	99%
Silver nitrate	Proscitech	≥ 99%
Sodium (Na)	Riedel-de Haën	-
Sodium azide (NaN <sub>3</sub> )	Chem Supply	≥ 99%
Sodium bicarbonate (NaHCO <sub>3</sub> )	Sigma-Aldrich	≥ 99.7%
Sodium carbonate (Na <sub>2</sub> CO <sub>3</sub> )	Chem Supply	≥ 99.5%
Sodium chloride (NaCl)	Chem Supply	99%
Sodium dodecyl sulphate (SDS)	Bio-Rad	Electrophoresis purity
Sodium hydroxide (NaOH)	Ajax Finechem	Analytic grade
Sodium methoxide (CH <sub>3</sub> NaO)	Sigma-Aldrich	95%
Sodium phosphate dibasic (Na <sub>2</sub> HPO <sub>4</sub> )	Sigma-Aldrich	≥ 99%

Sodium phosphate monobasic dihydrate (NaHPO <sub>4</sub> .H <sub>2</sub> O)	Sigma-Aldrich	≥ 99%
Sodium sulfite (Na <sub>2</sub> SO <sub>3</sub> )	Sigma-Aldrich	≥ 98%
Sulphuric acid (H <sub>2</sub> SO <sub>4</sub> )	Chem Supply	98%
Sylgard 184 Silicone Elastomer Kit	Dow Corning	-
Tin chloride (SnCl <sub>2</sub> .2H <sub>2</sub> O)	Sigma-Aldrich	98%
Toluene	Ajax Finechem	95.5%
Tridecafluoro-1,1,2,2-tetrahydrooctyl-dimethylchlorosilane (TDFCS)	Gelest	-
Trifluoroacetic acid	Sigma-Aldrich	99%
Tris(hydroxymethyl)aminomethane base (Tris)	Sigma-Aldrich	≥ 99.8%
Tris(hydroxymethyl)aminomethane hydrochloride (Tris-HCl)	Sigma-Aldrich	≥ 99%
Trisodium citrate dihydrate (Na <sub>3</sub> C <sub>6</sub> H <sub>5</sub> O <sub>7</sub> .2H <sub>2</sub> O)	Sigma-Aldrich	≥ 99%
Triton X-100	Sigma-Aldrich	Laboratory grade
Tryptone	Sigma-Aldrich	Molecular biology grade
Tween 20	Sigma-Aldrich	Laboratory grade
Yeast extract	Sigma-Aldrich	Molecular biology grade
β-mercaptoethanol	Sigma-Aldrich	≥ 99%

Table 2.1: Chemicals and biological substances used for pSi functionalisation, immunosensing and cell culture.

#### 2.1.1.2 Antibodies, Enzymes and Protein Kits

Antibodies, Enzymes and Kits	Supplier
Alkaline phosphatase, from bovine intestinal mucosa	Sigma-Aldrich
Dc Protein Assay	Bio-Rad
Goat anti-human IgG, alkaline phosphatase conjugate	Millipore

Human Interleukin-6 Ready-SET-Go! ELISA Kit	eBioscience
IgG Sepharose 6 Fast Flow	GE Healthcare
IntraGAM (human IgG Solution)	Donated by Dr. Peter MacArdle, Flinders University
Precision Plus Protein Dual Colour Standards #161-0374,	Bio-Rad
Rabbit IgG Antibody to Human Prostate Specific Antigen (PSA)	Meridian Life Science
SbpA S-layer protein	Purified by author in Chapter 5
SbpA <sub>31-1064</sub> /ZZ S-layer protein	Purified by author in Chapter 5
Sheep anti-Human IgG	Millipore

Table 2.2: Proteins and commercial biological kits used in immunosensing and protein purification.

#### 2.1.1.3 Cell Lines

Cell line	Cell information	Supplier
<i>Lysinibacillus sphaericus</i>	ATCC 4525	Purchased from American Type Culture Collection (ATCC)
<i>Escherichia coli</i>	BL21DE3 containing pBluescript SbpA <sub>31-1068</sub> /ZZ	Genetically modified by Dr Charlotte LeLan

Table 2.3: Cell lines and suppliers that were used for S-layer protein expression and extraction.

#### 2.1.1.4 Self-made Buffers and Solutions

Buffer/Solution	Application	Components
Tin sensitising solution	Electroless Deposition of Gold	SnCl <sub>2</sub> 26 mM Trifluoroacetic Acid 70 mM methanol/water 50/50 (v/v)
Silver activation solution	Electroless Deposition of Gold	AgNO <sub>3</sub> 30 mM

*Materials and General Methods*

Au bath (Alpha)	Electroless Deposition of Gold	Na <sub>3</sub> Au(SO <sub>3</sub> ) <sub>2</sub> Na <sub>2</sub> SO <sub>3</sub> NaHCO <sub>3</sub> pH 8.0, 4°C	79 mM 127 mM 25 mM
Au bath (Beta)	Electroless Deposition of Gold	Na <sub>3</sub> Au(SO <sub>3</sub> ) <sub>2</sub> Na <sub>2</sub> SO <sub>3</sub> NaHCO <sub>3</sub> Formaldehyde pH 8.0, 4°C	79 mM 127 mM 25 mM 625 mM
Carbonate buffer	ELISA	Na <sub>2</sub> CO <sub>3</sub> NaHCO <sub>3</sub> pH 9.6	15 mM 35 mM
Tris-T	General Use	Tween 20 Tris Buffer pH 7.4	0.05% (v/v)
PBS-T	General Use	Tween 20 PBS pH 7.4	0.05% (v/v)
PBS	General Use	NaCl KCl Na <sub>2</sub> HPO <sub>4</sub> KH <sub>2</sub> PO <sub>4</sub> pH 7.4	13.7 mM 2.7 mM 5.3 mM 1.8 mM
Tris buffer	General Use	Tris NaCl MgCl <sub>2</sub> pH 7.4	100 mM 100 mM 2.5 mM
Immunosensing buffer	Immunosensing	BSA PBS or Tris buffer pH 7.4	50 µg/mL
Tris-Saline- Tween (TST)	SbpA-ZZ Purification - IgG Affinity Column	Tris-HCl NaCl Tween 20 pH 7.6	50 mM, 150 mM 0.05% (v/v)
Acetic acid buffer (HAc)	SbpA-ZZ Purification - IgG Affinity Column	CH <sub>3</sub> COOH (HAc) pH 3.4	500 mM

*Materials and General Methods*

Ammonium acetate buffer (NH <sub>4</sub> Ac)	SbpA-ZZ Purification - IgG Affinity Column	NH <sub>4</sub> C <sub>2</sub> H <sub>3</sub> O <sub>2</sub> pH 5.0	5 mM
Separating gel (12%)	SDS-PAGE	Acrylamide Bisacrylamide SDS APS TEMED Tris-HCl pH 6.8	12 % (w/v) 0.1% 0.1% (w/v) 0.1% (w/v) 0.1% (v/v) 125 mM
Stacking gel (4%)	SDS-PAGE	Acrylamide Bisacrylamide SDS APS TEMED Tris-HCl pH 8.8	12% (w/v) 0.32% 0.1% (w/v) 0.1% (w/v) 0.1% (v/v) 375 mM
Running buffer	SDS-PAGE	Tris-base Glycine SDS	25 mM 192 mM 0.1% (w/v)
Protein loading buffer (6x)	SDS-PAGE	Glycerol SDS Bromophenol blue DTT (freshly added) Tris-HCl pH 6.8	30% (w/v) 10% (w/v) 0.1% (w/v) 600 mM 300 mM
SDS-PAGE loading buffer (Lug)	SDS-PAGE	SDS β-mercaptoethanol Glycerol Bromophenol Blue Tris-HCl pH 8.8	3% (w/v) 2% (v/v) 10% (w/v) 0.1% 200 mM
Coomassie blue staining solution	SDS-PAGE	Coomassie Brilliant Blue R-250 Methanol Glacial Acetic Acid H <sub>2</sub> O	1 g/L 50% (v/v) 10% (v/v) 40% (v/v)
Destaining solution	SDS-PAGE	Methanol Glacial Acetic Acid H <sub>2</sub> O	40% (v/v) 10% (v/v) 40% (v/v)

*Materials and General Methods*

Silver contrast enhancing solution	Silver Contrast Enhancement on Gold Modified pSi	Equal volumes of Solution A and Solution B	
Solution A	Silver Contrast Enhancement on Gold Modified pSi	Silver Acetate	12 mM
Solution B	Silver Contrast Enhancement on Gold Modified pSi	Hydroquinone Citrate buffer pH 3.8	44 mM
Enzyme silver contrast enhancing solution	Silver Contrast Enhancement on Gold Modified pSi	Magnesium Acetate Silver Acetate Hydroquinone Diphosphate Citrate buffer pH 7.0	5 mM 6 mM 100 mM (22 mM was also trialled)
Citrate buffer	Silver Contrast Enhancement on Gold modified pSi	Na <sub>3</sub> C <sub>6</sub> H <sub>5</sub> O <sub>7</sub> .H <sub>2</sub> O C <sub>6</sub> H <sub>8</sub> O <sub>7</sub> .H <sub>2</sub> O pH 3.8 or 7.0	80 mM 120 mM
Buffer A	S-layer Protein Purification	Tris-HCl pH 7.2	50 mM
Buffer B	S-layer Protein Purification	Tris-HCl Triton X-100 pH 7.2	50 mM 0.75% (v/v)
Buffer C	S-layer Protein Purification	Tris-HCl Guanidine HCl pH 7.2	50 mM 5 M
N-type Si etching solution	pSi Etching	HF (48%) milliQ H <sub>2</sub> O NCW-1001	25 mL 200 mL 1 mL

Table 2.4: Custom made buffers and solutions used for pSi preparation, immunosensing, cell culture and protein purification.

*2.1.1.5 Cell Culture Media*

Media	Components	
Nutrient Broth (NB)	Beef extract Peptone pH 7.4	3.0 g/L 5.0 g/L
NB Agar Plates	As above with: Agar	1% (w/w)

## Materials and General Methods

Lysogeny Broth (LB)	Yeast extract Tryptone NaCl pH 7.4	5 g/L 10 g/L 10 g/L
LB Agar Plates	As above with: Agar	1% (w/w)
Glycerol Solution	NB or LB Glycerol 80%	0.75 mL 0.75 mL

Table 2.5: Media used for the cell culture of *L. sphaericus* and *E. coli*.

### 2.1.1.6 96 Well ELISA Plates

<b>96-well Microtitre Plate</b>	<b>Supplier</b>
Costar 9018 High Binding	Corning
Costar 9017 Medium Binding	Corning
Costar 3596 Tissue Culture Treated	Corning

Table 2.6: 96 well microtiter plates used in ELISA and protein recrystallisation studies.

## 2.2 General Methods

### 2.2.1 pSi Etching Procedure

#### 2.2.1.1 Silicon Wafer Specifications

Type	Dopant	Resistivity ( $\Omega$ .cm)	Supplier
p <sup>++</sup>	Boron	0.0005 – 0.002	Virginia Semiconductors Inc.
n <sup>+</sup>	Phosphorous	0.008 – 0.02	Siltronix

Table 2.7: Silicon wafer, dopant type and resistivity used for pSi fabrication.

#### 2.2.1.2 Generic Silicon Preparation & Etching

Silicon wafers were scored with a diamond scribe and fractured over a straight edge to create pieces  $\sim 2 \text{ cm}^2$ . Dust and large particles present from the cutting procedure were removed via a strong blast of dry nitrogen. The silicon was then placed into a Teflon etching cell which contained an aluminium foil backing anode and a platinum mesh cathode (Figure 2.1). The wafer was placed upon the aluminium foil and a viton o-ring situated on top. The wafer was then clamped within the Teflon cell to prevent HF leaks. The etching chamber of the cell has a diameter of 1.5 cm and a height of 1.5 cm. The etching cell was washed sequentially with methanol, acetone and DCM to clean the wafer before being dried under a stream of nitrogen. To finalise the assembly, the platinum cathode was placed at a fixed distance, 0.5 cm, from the wafer. HF solution (1 mL) was introduced to the cell and electrochemical etching performed using a galvanostat (Keithley 2425, 100 W source meter) as the current source. Depending on the desired pore size, layer thickness and porosity, the etching conditions were varied. Etching time, or charge, directly relates to the layer thickness, while current density and HF concentration influence the pore size and porosity. Once etching was completed, the HF was decanted and the etched silicon was again rinsed consecutively with methanol, acetone and DCM and dried under a stream of nitrogen. The cell was then disassembled and the pSi sample was removed and rinsed again with DCM and dried under nitrogen. Standard etching conditions and electrolytes used throughout this thesis can be found in Table 2.8.

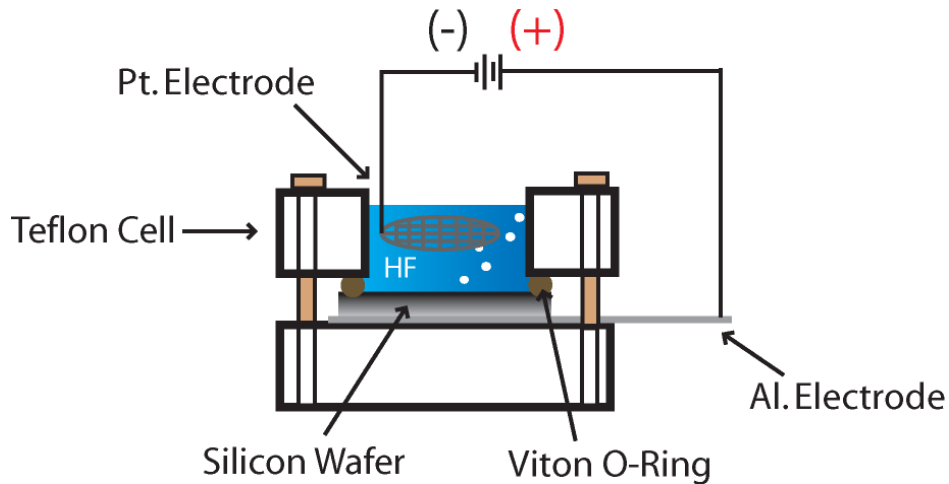


Figure 2.1: Schematic of the Teflon electrochemical etching cell used to fabricate pSi

### 2.2.1.3 Standard Electrochemical Etching Conditions

Type	Resistivity ( $\Omega\cdot\text{cm}$ )	Current Density ( $\text{mA}/\text{cm}^2$ )	Time (sec)	Etching Solution
p <sup>++</sup>	0.0005-0.002	450	10	3:1 HF:Ethanol
n <sup>+</sup>	0.008-0.02	50	45	25 mL HF
n <sup>+</sup>	0.008-0.02	50	50	200 mL milliQ H <sub>2</sub> O 1 mL Wako NCW-1001

Table 2.8: Typical conditions and electrolyte composition used for the electrochemical etching of Si.

## 2.2.2 Surface Modification and Functionalisation

### 2.2.2.1 Ozone Oxidation

Oxidation in ozone gas was performed using an ozone generator (Fischer, Ozone-Generator 500). Freshly etched porous silicon was placed into a clean glass desiccator (modified with a gas inlet and outlet). O<sub>2</sub> gas was purged through a Drierite™ column into the ozone generator for 2 minutes prior to being turned on. The oxygen flow rate was set to 100 L/hr and the power dial set to position 2.8 resulting in a current of 1.25 A and the production of 3.25 g/h of ozone. The desiccator was attached to the generator output and the pSi samples exposed to the gas flow. Depending on the application, oxidation times ranged from 10 –

120 minutes. After oxidation, the samples were removed from the modified desiccator and either used immediately or stored under vacuum.

#### *2.2.2.2 Thermal Oxidation*

Thermal oxidation was performed using a tube furnace (Labec HTF50/12 1200°C Tube Furnace). pSi was placed in a soda glass crucible and inserted in the tube furnace for heat treatment. Depending on the application, samples were heated to between 400 - 600°C for a period of 40 minutes – 2 hours. The samples were then removed and allowed to cool to room temperature. The entire process was performed in ambient atmosphere.

#### *2.2.2.3 Silanisation (Alkoxy Silanes)*

Oxidised pSi samples were introduced to 100 mM silane in anhydrous toluene and mixed on an orbital shaker (Ratek EOM5) for 5 minutes at 25 °C. The samples were then removed from the silane solution, rinsed extensively with toluene before being dried with nitrogen and used immediately or stored under vacuum.

#### *2.2.2.4 Covalent Immobilisation of Biomolecules on pSi*

Oxidised pSi was functionalised with 100 mM 3-isocyanatopropyl triethoxysilane (IPTES) as described in Chapter 2 section 2.2.2.3. The modified sample was then placed into a reaction vessel (Figure 2.2) and exposed to 1 mL of solution containing the relevant biomolecule. Following 2 hours incubation at room temperature on an orbital shaker, the sample was washed 3 times with 2 mL aliquots of PBS-Tween 20 (0.5% v/v) (PBS-T) and 3 times with PBS. Unreacted isocyanate groups were quenched by exposing the treated samples to a solution of 5 mM ethanolamine hydrochloride for 30 minutes at room temperature under gentle agitation on an orbital shaker. The functionalised pSi was rinsed another 3 times with 2 mL aliquots of PBS. The sample was then immersed in PBS and used immediately for immunosensing applications.

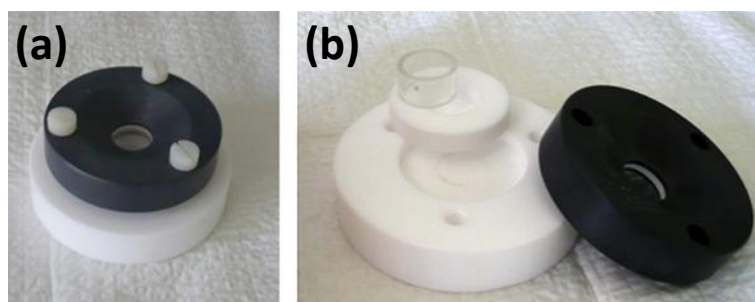


Figure 2.2: pSi biological reaction vessel. (a) Assembled vessel and (b) the disassembled components.

#### 2.2.2.5 Covalent Immobilisation of Biomolecules on flat silicon

Oxidised flat silicon was functionalised with 50 mM 3-isocyanatopropyl triethoxysilane (IPTES) as described in for pSi in Chapter 2 section 2.2.2.3. Biomolecule immobilisation was then performed as described for pSi in Chapter 2 section 2.2.2.4.

#### 2.2.2.6 Gravimetric Determination of Porosity

Clean pieces of cut silicon wafer were weighed on a laboratory balance with a resolution of 10  $\mu\text{g}$  prior to etching ( $m_1$ ). The silicon was then electrochemically etched and oxidised for 10 minutes via ozonolysis as described in Chapter 2 section 2.2.2.1. The resulting pSi was then weighed ( $m_2$ ). The pSi was then placed in a 1 M NaOH solution to dissolve the porous layer. The treated silicon was rinsed with methanol, acetone and DCM and dried under a stream of nitrogen before being weighed a final time ( $m_3$ ). The porosity,  $P$ , is defined as the ratio of the empty pore volume to the total volume and was calculated using the following equation:

$$P = \frac{m_1 - m_2}{m_1 - m_3}$$

Equation 2.1: Gravimetric determination of porosity.

### **2.2.3 Spectroscopy Techniques**

#### *2.2.3.1 Interferometric Reflectance Spectroscopy*

The components of the Interferometric Reflectance Spectroscopy (IRS) system consisted of a bifurcated fibre-optic probe, tungsten halogen light source (Ocean Optics LS-1) and a CCD spectrometer (Ocean Optics USB 2000) capable of recording visible wavelengths between 350 – 1050 nm. All IRS pSi studies were performed using a custom built Perspex flow cell as pictured in Figure 2.3 (b). pSi samples were secured in the flow cell which was then attached to a motorised stage using double sided adhesive tape. The height of the Interferometric Reflectance Spectroscopy's (IRS) lens was adjusted to achieve a focused point of light of approximately 1 mm diameter on the pSi surface. This approach provided the strongest reflectance signal which equated to a high fidelity Fabry-Perot fringe pattern. The design of the flow cell allowed fluid to be flowed over the pSi surface while simultaneously monitoring the reflectance profile. Solutions were flowed through the flow cell over the pSi sample with the help of syringes or peristaltic pump connected via Silastic<sup>®</sup> tubing to the flow cell. The outflowing solution was collected in a waste container. Reflectance spectra of the pSi sample were recorded every minute using a custom designed Labview VI software package. Two techniques were utilised in this thesis to analyse the reflected optical profile of pSi. The first involved the Fast Fourier Transform (FFT) of the Fabry-Perot fringe pattern to calculate an Effective Optical Thickness (EOT) value for the porous layer (Igor Pro software). A shift to the fringe pattern manifested as a change to the EOT of the material with blue shifts corresponding to a decrease and red shifts an increase in EOT. All EOT measurements reported in this thesis have been normalised to the first EOT measurement taken at time 0 min by dividing each EOT measurement (EOT) over time by the initial value (EOT<sub>0</sub>) to achieve EOT/EOT<sub>0</sub>. The second form of analysis involved monitoring changes to the intensity of the reflected fringe pattern at a particular wavelength to recognise the deposition of strongly adsorbing compounds within the porous layer.

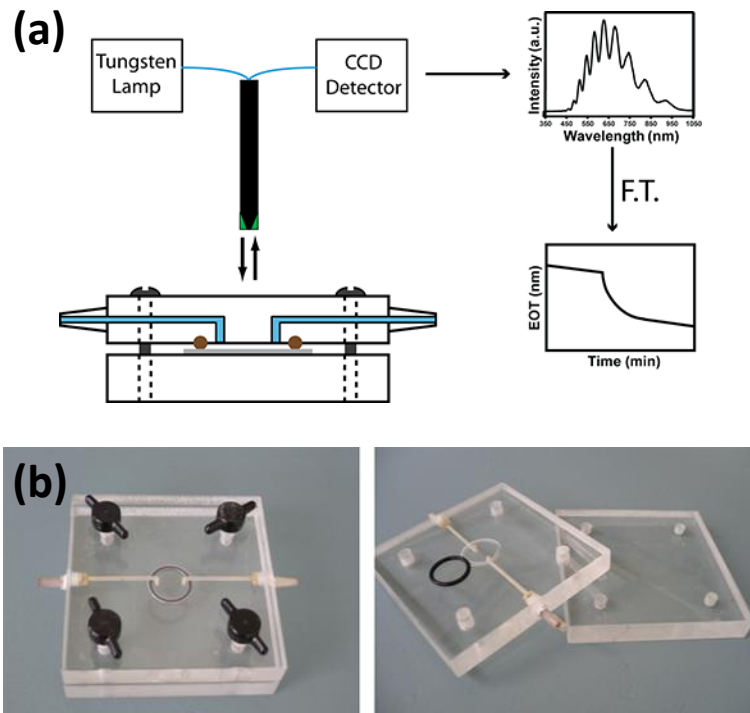


Figure 2.3: Interferometric Reflectance Spectroscopy. (a) Schematic of the IRS components and operation. (b) IRS flow cell used for pSi studies.

### 2.2.3.2 Human IgG Immunosensing Protocol - IRS

The Perspex IRS flow cell was blocked for 18 hours at 4 °C with 2.5% w/v BSA in PBS, pH 7.4, to prevent adsorption of biomolecules during the sensing experiment. Directly prior to the beginning of the immunosensor experiment, the BSA solution was flushed from the flow cell by 3 mL PBS-T, followed by 10 mL PBS. The pSi sample containing immobilised receptor molecule was removed from the reaction vessel and placed into the IRS flow cell, ensuring that the surface remained wet during the process to prevent the degradation of the receptor protein. 10 mL of PBS was injected through the flow cell and the reflected fringe pattern of the porous layer was measured once every 60 seconds for 10 minutes to establish a sensorgram baseline. Preparation of the human IgG analyte involved dilution from stock IntraGAM solution (60 mg/mL of human protein comprising 94% IgG and the remainder IgA and IgM and 100 mg/mL maltose) to the relevant working concentration. Dilutions were prepared in PBS containing 50 µg/mL BSA (immunosensing buffer) to reduce non-specific binding of immunoglobulins on pSi. Following establishment of a baseline, 3 mL of the analyte in PBS immunosensing buffer was injected into the flow cell and

left for twenty minutes to allow binding to the immobilised receptor. Excess analyte was then flushed out of the flow cell with 3 mL Tris-T followed by 10 mL Tris buffer. After five minutes to equilibrate the sensor signal, 3 mL Tris immunosensing buffer containing 1:500 goat  $\alpha$ -human IgG secondary antibody conjugated to alkaline phosphatase was injected into the flow cell and left for 20 minutes. The pSi surface was once again washed with 3 mL Tris-T followed by 10 mL Tris buffer, which was left in the flow cell for five minutes. Finally, 3 mL of the enzyme substrate was injected and incubated with the sample for 10 minutes. The sample was then rinsed with 10 mL Tris buffer and baselined for a further 10 minutes. The data acquisition was then stopped and the sample removed from the flow cell for future characterisation.

This is the standard protocol followed for pSi immunosensing experiments, however incubation times, buffers and substrates were altered depending on the specific application. This is addressed further in each chapter.

Time (min)	Volume	Solution
0 – 10	10 mL	$\alpha$ -human IgG capture antibody immobilised to pSi in PBS, pH 7.4
10 – 30	3 mL	Human IgG
30 – 35	3 mL	Tris-T, pH 7.4
35 – 40	10 mL	Tris, pH 7.4
40 – 60	3 mL	1:500 Goat $\alpha$ -human IgG antibody conjugated to alkaline phosphatase
60 – 65	3 mL	Tris-T, pH 7.4
65 – 70	10 mL	Tris buffer rinse, pH 7.4
70 – 80	3 mL	Enzyme substrate
80 – 90	10 mL	Tris buffer rinse, pH 7.4

Table 2.9: Experimental timeline for human IgG immunosensing on pSi.

### 2.2.3.3 Infrared Spectroscopy

Infrared Spectroscopy (IR) was performed on a Nicolet iN10MX IR-Microscope (Thermo Scientific). Attenuated Total Reflectance (ATR) IR was carried out using a Germanium ATR crystal and a liquid nitrogen cooled MCT detector. ATR IR was performed on pSi samples after each major functionalisation step

including etching, oxidation, silanisation, receptor molecule immobilisation and immunosensing. Spectra were recorded using an aperture size of  $80\ \mu\text{m}^2$  in the range of  $650\text{-}4000\ \text{cm}^{-1}$  at a resolution of  $8\ \text{cm}^{-1}$  and an average of 64 scans. IR data was analysed using OMNIC Picta software (Thermo Scientific). All spectra were blanked against a background of ambient air.

#### *2.2.3.4 Mass Spectroscopy*

Electrospray Mass Spectroscopy (MS) was performed on the synthesised hydroquinone diphosphate enzyme substrate using a Water Synapt HDMS. MS measurements were performed by Flinders Analytical technicians.

#### *2.2.3.5 NMR*

NMR spectra were recorded on a 400 MHz NMR spectrometer (Bruker) using either DMSO or  $\text{D}_2\text{O}$  as a solvent. All  $^1\text{H}$  spectra were recorded using standard parameters with chemical shifts ( $\delta$ ) recorded in ppm, referenced to DMSO and coupling constants in Hz. The following abbreviations were used in  $^1\text{H}$  NMR analysis: s = singlet, J = coupling constant (Hz).

#### *2.2.3.6 Scanning Electron Microscopy (SEM)*

High resolution micrographs were obtained with a number of Scanning Electron Microscopes. The Helios Nanolab 350 Dual Beam (FEI), XL30 Field Emission SEM (Philips) and Quanta 450 Environmental SEM (FEI) were all used to image pSi. All images were obtained at 10 kV via secondary electron detection. Preparation of the pSi samples involved scoring of the surface with a diamond tip pen and the fracturing of the wafer along that line to afford a cross-section of the surface for examination. Samples were sputter coated with platinum to a thickness of 0.5 - 3 nm (Quorumtech K757X Sputter Coater) in order to ensure good sample conductivity during SEM analysis. Micrographs were taken of the surface and cross-section of the sample. From these images, information such as pore diameter, thickness of the porous layer and the direction of pore growth were obtained.

# Chapter 3

---

## 3 Porous Silicon Optical Transducer Design

### **3.1 Abstract**

In this chapter the relationship between the electrochemical anodisation parameters and the observed porous morphology is investigated. Development of a templated 2-step etching process was found to result in unobstructed pore openings at the surface to promote entry and diffusion of immunosensor species into the porous matrix. The effect of current density on pore diameter, porosity and etching rate were determined via SEM analysis. The viability of these characterised structures as a sensor platform was then assessed using IRS to determine sensitivity to refractive index change within the porous matrix. Based on the findings of these combined studies, a current density of  $50 \text{ mA/cm}^2$  was identified to provide a suitable platform for subsequent optical immunosensor studies.

### **3.2 Introduction**

The optical properties of pSi are directly related to the morphology of the material. Pore size and shape, porosity and depth all play a role in the reflected/transmitted optical profile of the material and as such, the morphology of pSi is an important factor in the development of optical biosensors, not only because of the role it plays as a transducer but also because the pore size must be of a sufficient diameter to allow the binding and detection of target biomolecules. In biosensing applications receptors are immobilised to the pore walls and properties such as pore size and porosity can have a large impact on the available surface area and ultimately the sensor signal. For example, the internal surface area of pSi at a certain porosity can differ greatly depending on the size of the pores within the structure. In such cases, as pore size is increased the internal surface area is decreased, limiting the total number of binding sites [157]. Porosity is also a major factor in the sensitivity of optical pSi transducers to refractive index change within the matrix. According to the Bruggeman model discussed in Chapter 1 section 1.2.4.1 monolayer structures of higher porosity are more sensitive to changes to the refractive index of the medium within the pores because of the increased void space and larger surface area [158]. This effect can be monitored via the EOT of the material which will experience a larger change at higher porosities upon alteration to the refractive index of the layer.

Therefore it is important to optimise the physical properties of pSi to suit the specific application. In this thesis, immunosensing via two main approaches is undertaken: (i) detection of IgG via precipitation of an organic compound and (ii) precipitation of a metal within the pores. Both types of sensors utilise immunoassays as their sensing components and optimisation of the platforms involves utilisation of a range of proteins and nanoparticles. To this end it was important to ensure that the pSi layer contained macropores in the range of 100 – 200 nm in diameter to accommodate the sensing species and possessed relatively high porosity to achieve good optical sensitivity.

As discussed in Chapter 1, an established relationship exists between the electrochemical etching conditions and the physical properties of pSi. Briefly, increasing the current density can result in a larger pore size and porosity, while etching time directly relates to the thickness of the layer. Some of the work in

this thesis builds upon previously developed enzyme based pSi IgG sensors [16, 17]. In those studies highly doped p-type pSi was utilised as the sensor platform. Such structures are investigated briefly in this chapter, however macroporous n-type pSi etched in the dark was the focus of the study. Such pSi has been used in microcavity structures as a biosensor to detect the protein Intimin-ECD, rabbit IgG, latex beads and streptavidin/biotin [47, 102]. The large pores and clear, wide openings highlight this type of pSi as an ideal platform for optical biosensing applications. In this chapter the in-depth characterisation of n-type pSi was undertaken to identify a suitable optical immunosensor platform. The effect of electrochemical etching conditions on essential immunosensor parameters such as pore size, porosity and optical sensitivity was assessed to optimise the pSi morphology.

### 3.3 Experimental

#### 3.3.1 Preparation of Porous Silicon

Porous silicon surfaces were prepared following the procedure outlined in Chapter 2 section 2.2.1.2. N-type silicon, 0.008 – 0.02  $\Omega$ .cm, was etched according to a two-step process developed by Ouyang *et al.* [47, 102]. First, a sacrificial etch was performed at high current density, 275 mA/cm<sup>2</sup>, and short time, 1.82 seconds, to template the surface. A secondary etch at a lower current density was then performed to propagate the defects on the silicon surface to form pores. P-type silicon, 0.0005 – 0.002  $\Omega$ .cm was etched by a one step process as described by Jane *et al.* [16]. All etching conditions and electrolyte details can be found in Table 3.1.

Type	Resistivity ( $\Omega$ .cm)	Current Densities (mA/cm <sup>2</sup> )	Time (sec)	Etching Solution
p <sup>++</sup>	0.0005-0.002	450	10	3:1 HF:Ethanol
n <sup>+</sup>	0.008-0.02	275	1.82	25 mL HF
n <sup>+</sup>	0.008-0.02	20, 30, 40, 50, 60, 70	200, 133.33, 100, 80, 66.67, 57.14	200 mL milliQ H <sub>2</sub> O 1 mL NCW-1001

Table 3.1: Electrochemical etching conditions used in the optimisation of the pSi optical immunosensor platform.

#### 3.3.2 Surface Functionalisation and Characterisation

Freshly etched pSi samples were oxidised by ozone oxidation as described in Chapter 2 section 2.2.2.1. All samples were oxidised for 30 minutes.

pSi samples were investigated using SEM as described in Chapter 2 section 2.2.3.6. Pore size and pore to pore distributions were calculated from SEM micrographs using ImageJ software v 1.46r and Image Tool software version 3.0.

Porosity was determined via gravimetric analysis as described in Chapter 2 section 2.2.2.6. Refractive index sensitivity measurements were performed using IRS as described in Chapter 2 section 2.2.3.1. To compare different pSi samples

### *Porous Silicon Optical Transducer Design*

the EOT readings were normalised by dividing each EOT measurement by the initial EOT value at time 0 minutes ( $EOT_0$ ) to achieve  $EOT/EOT_0$ . The magnitude of the normalised EOT change ( $\Delta EOT/EOT_0$ ) upon transition between liquids of different refractive index formed the basis of the sensor readout.

## **3.4 Results**

### **3.4.1 pSi Fabrication Technique**

Traditional 1-step etching protocols typically result in the formation of a thin layer of nano-mesoporous silicon on the surface before larger pores are developed and propagated [47, 159]. This thin layer can act as a size exclusion filter, preventing entry and diffusion of immunosensing species into the pSi matrix. A 2-step n-type etching method developed by Ouyang *et al.* was established to prevent the formation of such layers and to provide large pore openings to facilitate entry and diffusion of large biomolecules and nanoparticles [47, 102]. Fabrication of large defects or ‘pits’ on the surface by application of a high semi electro-polishing current density can be used as nucleation points for the formation and growth of new pores in subsequent etching steps. Ouyang *et al.* formed such defects via a sacrificial etching method whereby a thin porous layer was first etched and then removed via application of a second, high electropolishing current density. The approach used in this work has simplified the method to a single template etching step. In our approach, a high current density approaching electropolishing conditions was applied to silicon for a short period to promote a rough pitted surface without the need to remove a sacrificial porous layer (Figure 3.1 (a)). This rough template was then etched at a lower current density as described by Ouyang *et al.* to grow a porous matrix containing large macropores with wide openings at the surface (Figure 3.1 (b)). Comparison of the template surface and the final porous sample showed an apparent decrease in the surface roughness following the elongation step. While pore seeding and propagation may occur within the pits and defect of the template, the second etch appears to smooth the surface via limited dissolution prior to hole depletion.

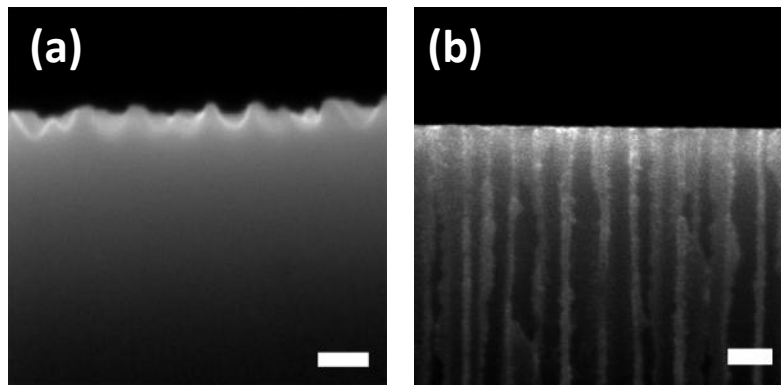


Figure 3.1: SEM analysis of the 2-step n-type template etching protocol. (a) Templated silicon surface after exposure to  $275 \text{ mA/cm}^2$  for 1.82 seconds. (b) Final porous layer after the application of a second, lower current density,  $40 \text{ mA/cm}^2$  for 100 seconds. All scale bars represent 200 nm.

### **3.4.2 N-type and P-type pSi Comparison**

To illustrate the difference in surface structure of templated and non-templated pSi, two pSi samples were fabricated using etching conditions previously reported for pSi sensors. N-type pSi was etched as described by Ouyang *et al.* via the 2-step template approach and p-type silicon etched by a traditional 1-step approach as described by Jane *et al.* [16, 47]. Both structures are relevant to this thesis and are used in Chapter 4 as immunosensing transducers.

Figure 3.2 contains SEM micrographs of the cross-section and surface perspectives of both structures. Both types of pSi samples demonstrated similar average pore diameters ( $113 \text{ nm} \pm 23 \text{ nm}$  for n-type,  $104 \text{ nm} \pm 25 \text{ nm}$  for p-type) in the cross-sectional analysis, with the n-type sample displaying a broader pore size distribution profile (Figure 3.2 (a&c)). The pore-to-pore distance was noticeably smaller for the p-type sample indicating higher porosity. In contrast to these results, the surfaces of the two samples showed marked differences. While the templated n-type pSi exhibited large pore openings corresponding in size and spacing to the underlying porous matrix, Figure 3.2 (b), the p-type sample displayed a flat cracked surface and the absence of ordered macroporous pore openings, Figure 3.2 (d). These two micrographs clearly identify the advantages of incorporating a templating step into the fabrication protocol. The absence of readily accessible pore openings on the surface of the p-type sample has the potential to limit the response of a sensor by inhibiting entry and diffusion

biomolecules into the underlying pores. The large openings at the surface on n-type pSi make this form of pSi highly desirable for many applications including biosensing. Removal of the mesoporous surface layer on p-type pSi would be entirely possible through a template etching process; however the p-type pSi was etched as described by Jane *et al.* and Szili *et al.* to illustrate the drawback of the one step etching approach [16, 17]. The previous successful use of templated n-type pSi in a variety of sensors, coupled with its attractive physical properties led to its choice as the optical transduction platform in this thesis. Characterisation of the effect of etching conditions on n-type pSi morphology was undertaken in following sections to optimise the material as an optical immunosensor.

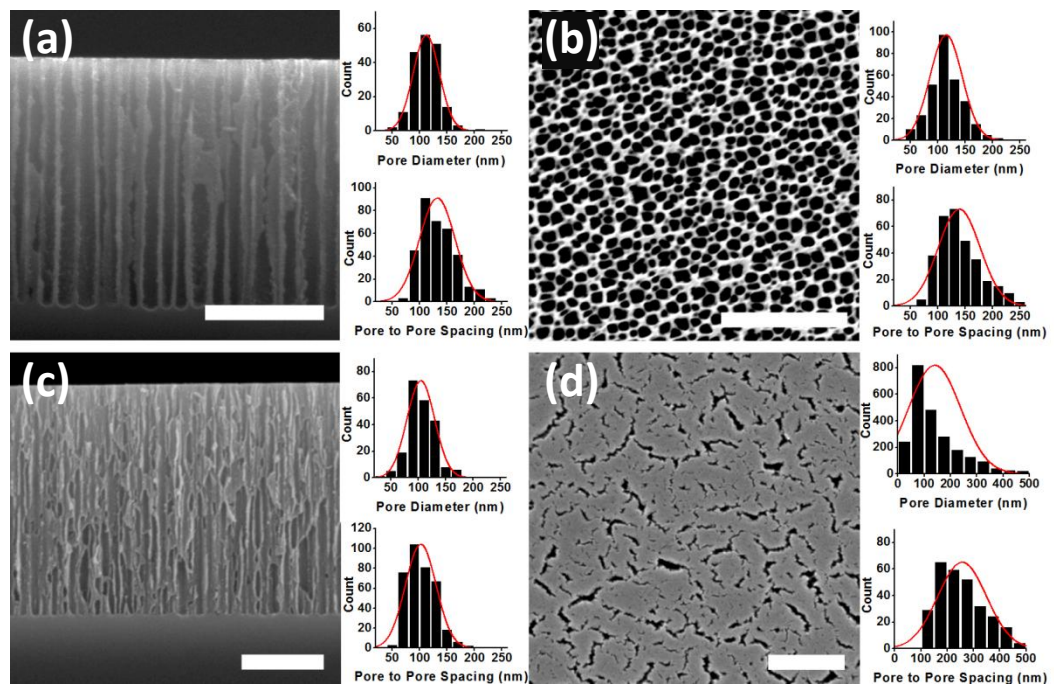


Figure 3.2: Comparison between a templated and non-templated etches on n- and p-type pSi. (a & b) N-type pSi etched at 275 mA/cm<sup>2</sup> for 1.82 seconds followed by 40 mA/cm<sup>2</sup> for 100 seconds. (c & d) P-type pSi etched at 450 mA/cm<sup>2</sup> for 10 seconds. All scale bars depict 1 µm. Both the cross-sectional and surfaces micrographs were analysed to extract pore size and pore to pore distributions which are included next to each image.

### 3.4.3 Effect of Current Density on Pore Diameter

The relationship between current density and physical pore diameter was established using SEM analysis of pSi monolayers fabricated at different current densities. It can be seen in Figure 3.3 that the average pore diameter rapidly increased from 31 nm at 20 mA/cm<sup>2</sup> to 112 nm by 40 mA/cm<sup>2</sup>, after which it remained relatively constant regardless of current density. Porous structures formed by current densities  $\geq 40$  mA/cm<sup>2</sup> fall into the class of macropores and are large enough to accommodate IgG immunocomplexes, which consist of multiple IgG antibodies (typical IgG dimensions, height 14.5 nm, width 8.5 nm, thickness 4.0 nm [160]). The pore size is also sufficient to promote entry of nanoparticles and other larger materials and was considered suitable as a flexible immunosensor transducer.

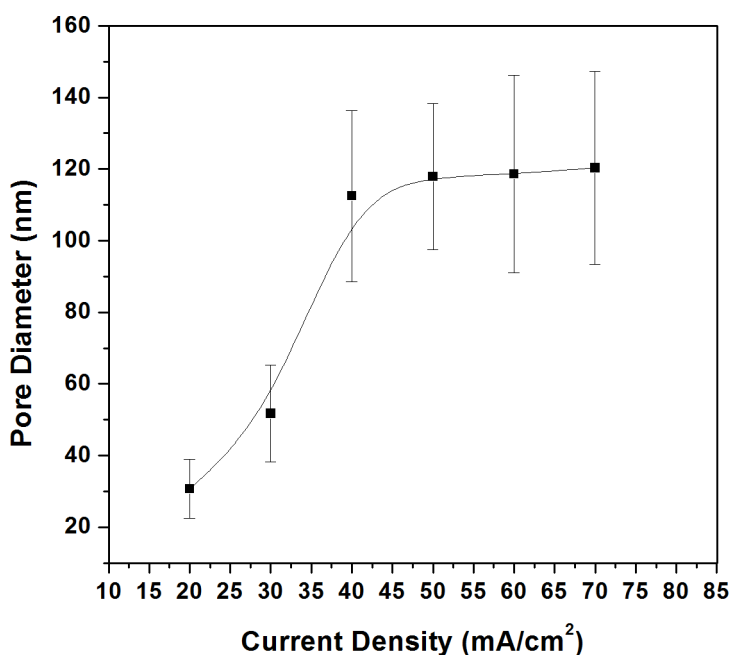


Figure 3.3: Dependence of pore diameter of n-type pSi on current density.

### 3.4.4 Effect of Current Density on Porosity

One of the most important characteristics of a porous silicon layer is its porosity, defined as the percentage of void inside the porous layer. The porosity directly relates to the refractive index of the porous material and impacts on the sensitivity of optical pSi sensors to changes in the refractive index within the pores.

Porosity was determined via gravimetric analysis and Figure 3.4 shows the linear relationship that exists between current density and porosity. While this trend differs from exponential relationships reported for many p-type pSi structures, it corresponds with the findings of Ouyang *et al.* and others who established this n-type etching method [45, 47]. Comparison with the pore diameter study indicated that while the pore size remained constant for samples produced at current densities  $\geq 50$  mA/cm<sup>2</sup>, the porosity continued to increase by reducing the pore to pore distance between the pores. Highly porous structures were achieved using current densities of  $\geq 60$  mA/cm<sup>2</sup>, however samples etched under these conditions demonstrated increased variability and sometimes mild forms of electropolishing. This might be attributed to sample variation or error due to small weight differences in the gravimetric analysis. While extremely porous structures were achieved, the most consistent etching conditions occurred between 40 – 50 mA/cm<sup>2</sup> and the porosity levels of such samples were considered sufficient for sensing applications.

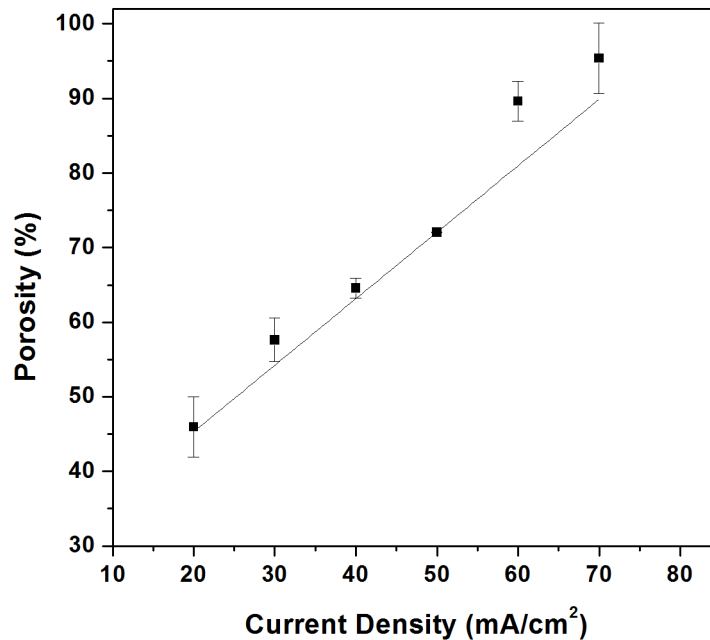


Figure 3.4: The relationship between current density and porosity for n-type pSi.

### **3.4.5 N-type pSi Etching Rate**

The etching rate of the porous layer as a function of current density was also assessed. pSi samples etched at different current densities using the same charge,  $4.0 \text{ C/cm}^2$ , were analysed via SEM and their layer thickness determined. Figure 3.5 shows an exponential relationship between the etch rate and the current density; with higher current densities displaying faster etch rates. This profile is consistent with many previously reported studies [45]. If this trend continues, the high etch rate for current densities  $\geq 50 \text{ mA/cm}^2$  may begin to affect sample – sample variability due a loss of fine control and error associated with the source meter. From these findings, layer depth could be accurately predicted and optimised prior to etching.

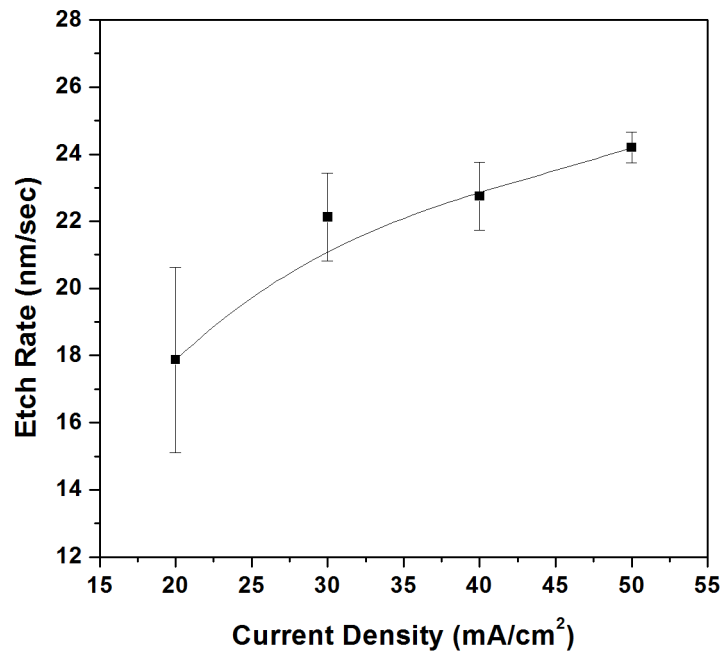


Figure 3.5: The relationship between current density and the rate of the electrochemical etching process for n-type pSi.

### **3.4.6 Current Density – Sensitivity to Refractive Index Change**

Finally, the effect of current density on optical sensor performance was assessed. Oxidised pSi was placed in an IRS flow cell and liquids of various refractive index were introduced to assess the change in EOT of the layer. To compare the different pSi structures, sensitivity was obtained in terms of refractive index unit

(RIU). This calculation was done by dividing the measured change in  $EOT/EOT_0$  ( $\Delta EOT/EOT_0$ ) by the refractive index change. Figure 3.6 (a) shows a sensorgram from pSi etched at  $50 \text{ mA/cm}^2$  exposed to milliQ water, ethanol and isopropanol in sequential order. Figure 3.6 (b) shows the sensitivity of different current densities to a change of 1 refractive index unit (RIU). The  $\Delta EOT/EOT_0$  response for a change of 1 RIU within the pores follows a linear trend, correlating with the relationship observed for layer porosity. From this finding it can be determined that higher porosities, regardless of pore size, provide improved sensitivity for refractive index based optical transducers. However, as pSi biosensing typically relies on changes to the refractive index at the pore wall and not in bulk solution, a minimum pore size is still required to allow entry of biosensing species.

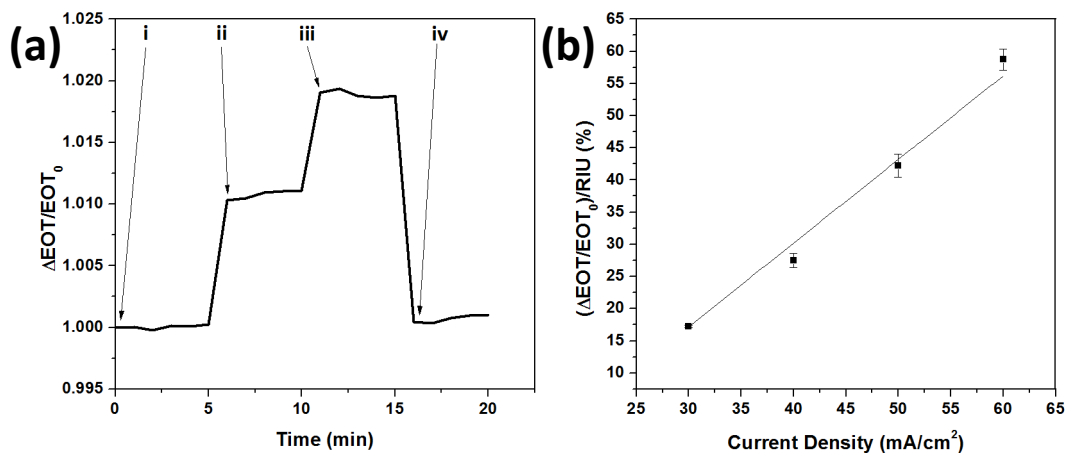


Figure 3.6: Relationship between current density and the sensitivity of the material to refractive index change as assessed by optical interferometry. (a) Response of a  $50 \text{ mA/cm}^2$  pSi sample to: i – milliQ water ( $n = 1.3334$ ), ii – ethanol ( $n = 1.3611$ ), iii – isopropanol ( $n = 1.3776$ ), iv – milliQ water. (b) Combined EOT responses for different current densities normalised to 1 refractive index unit.

### **3.5 Conclusion**

The characterisation of pSi fabrication has been demonstrated by exploring the relationship between the electrochemical etching conditions and the physical characteristics of the porous layers. SEM analysis of 2-step template etching identified improved access to the porous matrix through the removal of the mesoporous surface layer and the formation of large pore openings. The effect of current density on the pore diameter, porosity, etch rate and optical sensitivity was then analysed. It was observed that higher current density applied during the etching cycle led to a general increase in pore size, porosity and etching rate, matching established trends. A relationship was also established between the level of porosity and the sensitivity of pSi optical interferometric transducers to changes in the refractive index of liquids within the pores in accordance with the Bruggeman approximation.

According to these findings, etching parameters were chosen for use in all sensing experiments performed in this thesis. A current density of  $50 \text{ mA/cm}^2$  was identified to provide necessary macropores, good sample to sample consistency, moderately high porosity and good sensitivity to changes to the refractive index within the porous layer. These factors allow the integration of biomolecules, good sensitivity and relatively low variability compared with other conditions investigated. Such a material provided a flexible platform for signal transduction on which the various immunosensors investigated in this thesis are based.

# **Chapter 4**

---

## **4 Detection of Human IgG on Porous Silicon via Enzyme Catalysed Precipitation of BCIP/NBT**

#### **4.1 Abstract**

A new pSi optical immunosensor detection strategy and signal processing technique was demonstrated in this chapter to build upon and improve the sensitivity of existing enzyme based pSi immunosensors. The detection of human IgG on pSi was shown via an immunoassay containing a secondary antibody conjugated to alkaline phosphatase and the precipitation of the enzyme substrate 5-bromo-4-chloro-3-indoyl phosphate (BCIP)/nitro blue tetrazolium (NBT). The intense colour change and strong absorbance of the biocatalysed BCIP/NBT compounds upon analyte detection provided the basis of the new approach. A number of signal processing techniques were also investigated to improve the sensitivity of the device. Adaption of the alkaline phosphatase – BCIP/NBT system to pSi has enabled the formation of a highly sensitive new immunosensor platform that demonstrated satisfactory precision and high specificity.

## **4.2 Introduction**

The ability to detect analytes based on enzyme catalysed changes to the effective optical thickness of pSi films has been demonstrated in the past to detect human IgG and human La protein [16, 17]. Those methods utilised changes to the porous morphology and thus the EOT of the layer as a transduction mechanism. While this approach could successfully detect the presence of an analyte, the sensitivity of the platform was inadequate to compete against pre-existing techniques. A new detection strategy has been explored in this chapter to improve the sensitivity and detection limit of pSi optical immunosensors. To achieve this goal, this chapter builds upon the architecture developed in those immunosensors by incorporating a different enzyme and new detection approach. The testing of different immunoassays and detection strategies is essential in optimising the pSi optical immunosensor technology. Within the new design demonstrated in this chapter, a human IgG specific sandwich immunoassay incorporating an alkaline phosphatase labelled secondary antibody was used in conjunction with 5-bromo-4-chloro-3-indoyl phosphate (BCIP) to improve the signal strength and sensitivity of the sensor.

Traditionally, precipitation of BCIP by alkaline phosphatase has been used for many years in paper ELISA's, immunoblotting (i.e. dot blots and western blots) and for immunohistochemistry (staining cells) [24, 161-164]. Enzymatic dephosphorylation of BCIP forms an indoxyl which subsequently tautomerizes to the ketone. In alkaline conditions, this ketone dimerizes, resulting in the formation of an insoluble 5,5'-dibromo-4,4'-dichloro-indigowhite (BCIP-indigowhite) molecule and a weak blue colour (Figure 4.1) [165].

BCIP is also commonly used in combination with nitro blue tetrazolium (NBT) to generate a stronger detection signal. During dimerization of the catalysed BCIP, the ketone releases  $H^+$  ions, which reduce the NBT to an insoluble purple-coloured NBT-diformazan (formazan dye) (Figure 4.1). Both dyes then mix and precipitate resulting in a dark violet colour and leading to a larger signal than if BCIP was used independently [166]. The combined precipitant absorbs strongly in the region of 400 nm – 700 nm with absorption maxima occurring at 650 nm (BCIP-indigowhite product) and 600 nm (NBT-diformazan), Table 4.1.

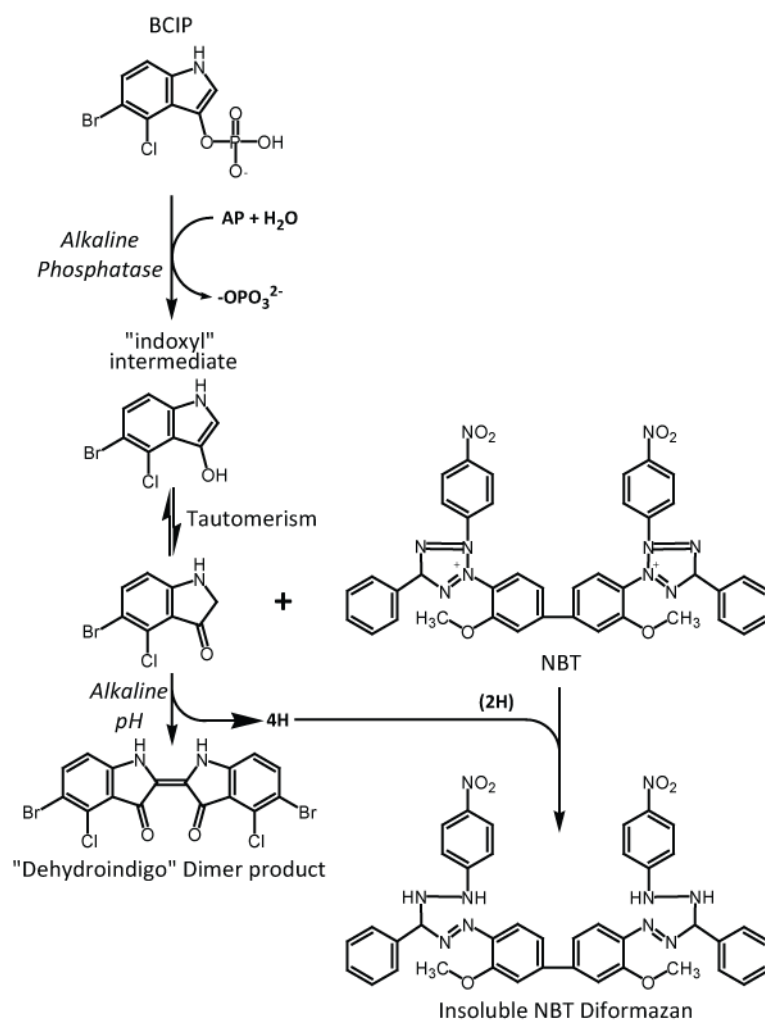


Figure 4.1: Reaction pathway of BCIP/NBT precipitation [165].

Catalysed Substrate	Absorbance maxima	Reference
BCIP-indigo	650 nm	[167, 168]
NBT-diformazan	600 nm	[166]

Table 4.1: The absorbance wavelengths of the biocatalysed alkaline phosphatase substrates, BCIP & NBT.

More recently, the alkaline phosphatase/BCIP system has been adapted for use in a quantitative electrochemical sensor, whereby detection of target DNA elicited precipitation of BCIP, coating a gold electrode and blocking electron transfer [169]. It was also adapted by the same research group for use in a quartz crystal micro balance for the same purpose [169]. Incorporation of such a precipitation

system into the pSi architecture could provide a new method for the amplified detection of proteins and other analytes on pSi. Small amounts of precipitation could alter the refractive index within the porous matrix, while strong precipitation in large quantities could change the structure/depth of the pores, altering the reflected optical profile.

The research work conducted in this chapter demonstrates for the first time the incorporation of alkaline phosphatase, BCIP and/or BCIP/NBT into a pSi sensor architecture for the detection of human IgG. The precipitation of the enzyme substrate is proven to be specific to the presence of the target analyte and the sensitivity of the system is improved via alterations to signal processing. It is demonstrated that in the case of BCIP/NBT precipitation on pSi, processing the reflected intensity of the pSi layer provided a stronger signal than either Fourier transform based EOT or fringe shift methods.

This demonstration of the detection of human IgG with an immunoassay containing alkaline phosphatase and BCIP/NBT improved the response time and detection limit of the sensor compared to what was previously reported by similar pSi optical immunosensors [16, 17]. This opens new opportunities toward the development of rapid point of care sensors that can provide comparable sensitivity to pre-existing laboratory based alternatives. Integration of this approach into an array format may also allow the development of quick, high throughput screening for multiple analytes.

### **4.3 Experimental Method**

#### **4.3.1 Preparation of Porous Silicon**

Porous silicon surfaces were prepared following the procedure outlined in Chapter 3 section 3.3.1. N-type silicon 0.008 – 0.02  $\Omega$ .cm was etched at a current density of 50 mA/cm<sup>2</sup> for 45 seconds.

#### **4.3.2 Formation of the Immunosensing Platform and Functionalisation of Porous Silicon**

Freshly etched pSi samples were first oxidised by 1 of 2 methods, ozone or thermal oxidation as described in Chapter 2 sections 2.2.2.1 and 2.2.2.2. Ozone oxidation was conducted for 20 minutes, while thermal oxidation involved treatment for 1 hour at 400 °C. Once oxidised, silanisation was performed for 5 minutes following the procedure outlined in Chapter 2 section 2.2.2.3 by exposing individual samples to a 10 mL solution of 100 mM 3-isocyanatopropyltriethoxysilane in anhydrous toluene at room temperature.

Following silanisation, immobilisation of sheep anti-human IgG capture antibody was performed following the procedure outlined in Chapter 2 section 2.2.2.4. The surface was exposed to an antibody solution at 68.4  $\mu$ g/mL (1:500 dilution) and incubated for 30 minutes. The sample was then washed with PBS-T, followed by a PBS rinse. Unreacted isocyanate groups were quenched by exposing the treated samples to a 1.5 mL solution of 5 mM ethanolamine hydrochloride. The sample was finally rinsed with PBS and immediately transferred to the immunosensing apparatus for sensing experiments. The functionalisation process is displayed as a schematic in Figure 4.2.

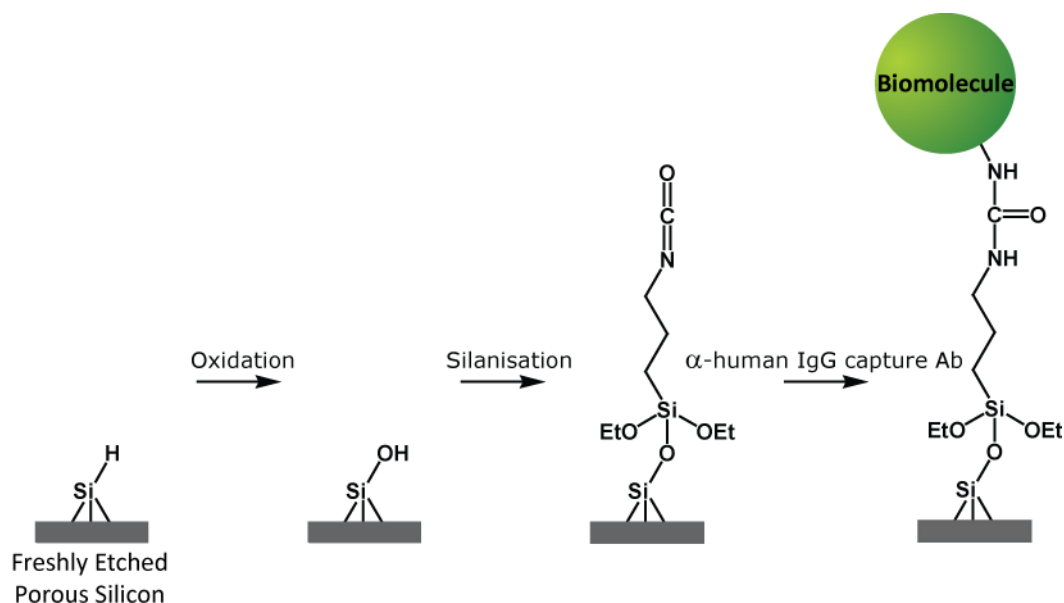


Figure 4.2: Surface functionalisation procedure showing oxidation, silanisation and biomolecule immobilisation.

#### 4.3.3 Immobilisation of Alkaline Phosphatase

Alkaline phosphatase was covalently immobilised on pSi following the protocol outlined in Chapter 2 section 2.2.2.4. Briefly, alkaline phosphatase was attached to pSi via the formation of a urea bond between an isocyanate silane on the pSi surface and an amino group on the enzyme. Relevant control surfaces were not exposed to protein and consisted of isocyanate silane functionalised pSi neutralised with 1.5 mL of 10 mM ethanolamine hydrochloride in a reaction vessel for 30 minutes. Surfaces were then rinsed 3 times with 1.5 mL PBS and used immediately for immunosensing studies.

#### 4.3.4 Immobilisation of α-Human IgG Conjugated to Alkaline Phosphatase

Goat α-human IgG conjugated to alkaline phosphatase was covalently immobilised on pSi following the protocol outlined in Chapter 2 section 2.2.2.4. Briefly, incubation of isocyanate silanised pSi with 1.5 mL 1:500 antibody diluted in PBS resulted in the formation of a urea bond between an isocyanate silane on the pSi surface and an amino group on the antibody.

#### **4.3.5 Functionalisation of Flat Silicon with Alkaline Phosphatase**

Alkaline phosphatase was covalently immobilised on bulk silicon following the protocol outlined in Chapter 2 section 2.2.2.5. Briefly, alkaline phosphatase was attached to flat silicon via the formation of a urea bond between an isocyanate silane on the silicon surface and an amino group on the enzyme. Control surfaces consisted of flat silicon functionalised with neutralised isocyanate silane as outlined in Chapter 4 section 4.3.3.

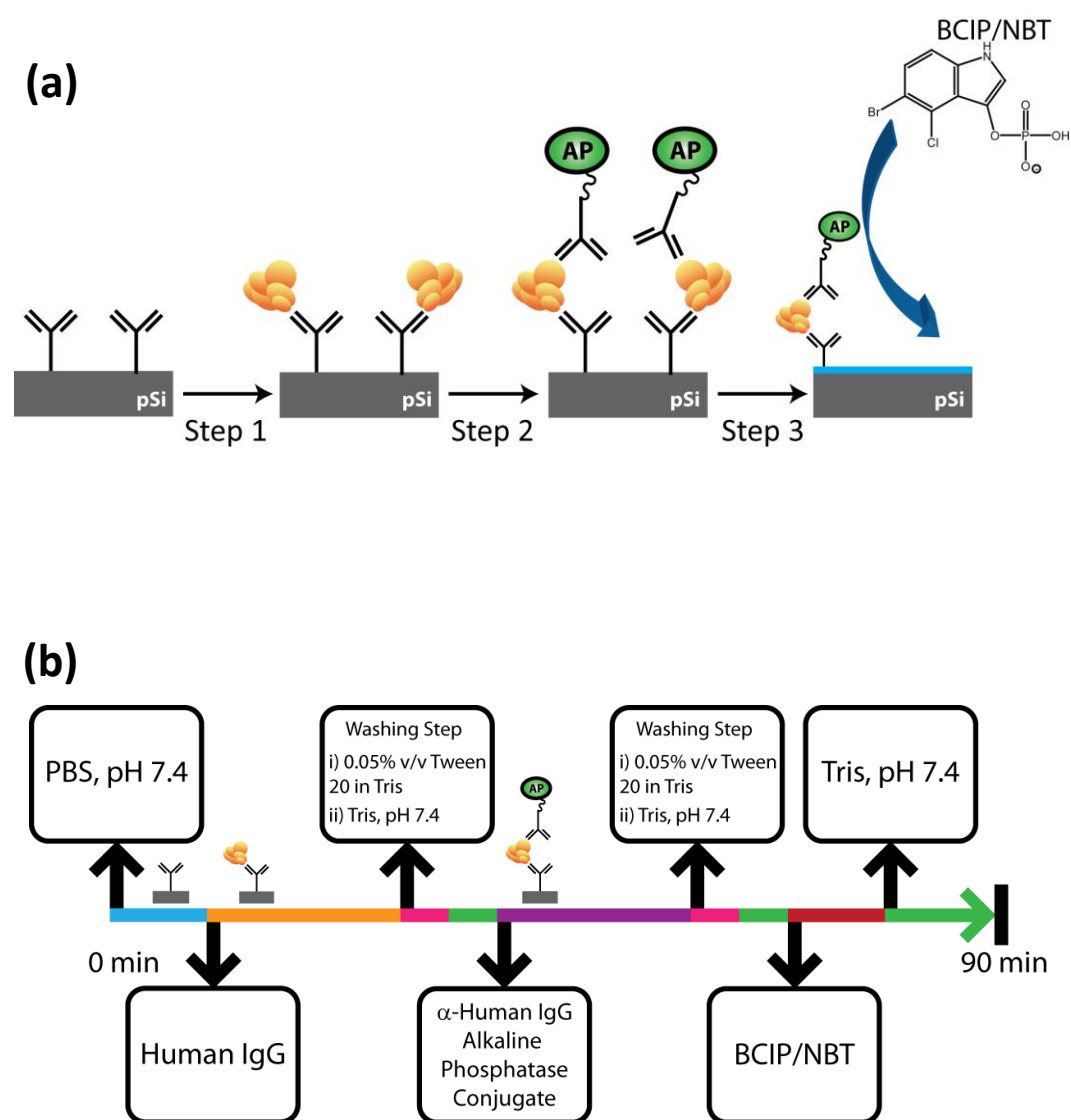
#### **4.3.6 Enzyme Substrate Optimisation**

Surfaces prepared in Chapter 4 sections 4.3.3, 4.3.4 and 4.3.5 were utilised for the integration and optimisation of the alkaline phosphatase and BCIP or BCIP/NBT substrate systems on pSi. Sensing was performed inside a custom built IRS flow cell (Chapter 2 section 2.2.3.1, Figure 2.3) which prior to each sensing experiment was blocked for 12 hours at 4°C with 2.5% w/v BSA in PBS, pH 7.4. The reflected white light optical profile of pSi was acquired with IRS and the sensor readout signal consisted of either EOT, wavelength shift or intensity change at 600 nm depending on the specific experiment. To investigate the response of enzyme catalysed precipitation of BCIP and or BCIP/NBT on pSi, functionalised pSi was placed into the flow cell and 10 mL Tris buffer, pH 7.4, was injected through the cell. The readout signal was baselined for 10 minutes before 3 mL of 3 mM BCIP in Tris buffer or Sigma-Aldrich BCIP/NBT liquid substrate solution was injected and incubated for 10 minutes. After incubation with the enzyme substrate, the cell was flushed with 10 mL Tris buffer to remove un-reacted substrate and the signal baselined for a further 10 minutes. The sensor response was calculated by comparing the final value at 30 minutes against the initial baseline value at 10 minutes to determine the magnitude of the signal change.

#### **4.3.7 Human IgG pSi Immunosensing**

Immunosensing was carried out following the procedure described in Chapter 2 section 2.2.3.2. Monitoring the reflected white light intensity from the porous surface at 600 nm formed the basis of the immunosensor readout signal.

A schematic of the immunosensor approach and experimental timeline appear in Figure 4.3 (a) & (b) respectively. A more detailed timeline also appears in Table 1. Sheep  $\alpha$ -human IgG capture antibody decorated pSi was placed into the flow cell and 10 mL PBS, pH 7.4, was injected through the cell. The signal was baselined for 10 minutes before 3 mL of human IgG in PBS immunosensing buffer was injected and incubated for 20 minutes (Figure 4.3 (a) Step 1). The concentration of the human IgG analyte was varied from 0 – 2000 ng/mL during different experiments to create a standard curve. After incubation of the analyte, the cell was flushed with 3 mL Tris-T solution, pH 7.4 and left for 5 minutes to remove non-specifically bound protein. 10 mL Tris immunosensing buffer was then injected into the cell and the signal baselined for 5 minutes. The change in buffer from PBS to Tris was performed to provide a more suitable environment for the subsequent introduction of the secondary antibody. 1.5 mL of 1:500 goat anti-human IgG secondary antibody conjugated to alkaline phosphatase in Tris immunosensing buffer, pH 7.4, was injected and incubated in the flow cell for 20 minutes (Figure 4.3 (a) Step 2). This polyclonal antibody was specific to the gamma chain of human IgG. The sample was then rinsed as previously. The final step involved the introduction of 1.5 mL of a commercially prepared BCIP/NBT solution (Figure 4.3 (a) Step 3). The sample was then rinsed with 10 mL PBS after 10 minutes exposure to the BCIP/NBT and the new baseline monitored. Control experiments were performed under the same conditions; however 0 ng/mL human IgG or 500 ng/mL of an alternative non-specific rabbit antibody was used. Three separate locations were simultaneously investigated on each porous silicon sample to ensure uniformity and repeatability. An average response was calculated from these locations and used in subsequent analysis.



Time (min)	Volume	Solution
0 - 10	10 mL	PBS, pH 7.4
11 - 30	3 mL	Human IgG
31 - 35	3 mL	Tris-T
35 - 40	10 mL	Tris, pH 7.4
41 - 60	3 mL	1:500 Goat $\alpha$ -human IgG antibody conjugated to alkaline phosphatase
61 - 65	3 mL	Tris-T
66 - 70	10 mL	Tris buffer, pH 7.4
71 - 80	3 mL	BCIP/NBT
81 - 90	10 mL	Tris buffer, pH 7.4

Table 4.2: Experimental timeline of the alkaline phosphatase BCIP/NBT based pSi sensor experiment.

#### ***4.3.8 Cross-Reactivity/Specificity of the pSi Immunosensor***

The specificity of the human IgG pSi immunosensor was tested by exposing the sensor platform to IgG and other protein from alternate animal species. Immunosensor experiments were performed following the procedure detailed in Chapter 4 section 4.3.7, however the human IgG analyte was replaced by either Rabbit IgG or BSA. Positive cross-reactivity was tested by replacing the human IgG analyte with either 500 ng/mL of Rabbit IgG or 50  $\mu$ g/mL BSA. Negative cross-reactivity was performed by spiking Rabbit IgG or BSA fractions with 25 ng/mL human IgG and assessing the effect on the expected immunosensor signal response.

#### ***4.3.9 Fabrication of Immunoassay Patterned pSi for FTIR Mapping***

The procedure for the formation of immunoassay patterned pSi via PDMS masking is shown in Figure 4.4. First,  $\alpha$ -human IgG capture antibody was immobilised on pSi following the procedure outlined in Chapter 4 section 4.3.2. The PDMS mask was prepared from Sylgard 184 Silicon Elastomer Kit by mixing PDMS monomer with a cross-linker at a ratio of 10:1. The liquid PDMS was then poured into plastic cell culture petri dishes to a thickness of  $\sim$ 1.5 mm

and placed under vacuum in a desiccator to degas. The PDMS was cured in an oven at 70 °C for 30 minutes before being peeled from the petri dish and cut to form a straight edge.

The PDMS film was situated on the sample to cover half of the pSi, effectively masking this region due to the native adhesion of the polymer. The masked pSi was placed into a glass petri dish and exposed to 3 mL of the human IgG analyte in immunosensing buffer for 20 minutes (Figure 4.4, Step 1). The surface was then removed from the petri dish and rinsed 3x with Tris-T and 3x with Tris immunosensing buffer. The PDMS mask was peeled off the sample and the patterned pSi was placed into a reaction vessel and exposed to 1 mL of  $\alpha$ -human IgG secondary antibody conjugated to alkaline phosphatase for 20 minutes (Figure 4.4, Step 2, refer to Chapter 2 section 2.2.2.4, Figure 2.2 for more information on this vessel). The sample was then washed as before and incubated with commercially prepared BCIP/NBT for 10 minutes at room temperature (Figure 4.4, Step 3). Finally, the sample was washed 4x with Tris buffer and 4x with milliQ water before being dried under a stream of nitrogen and under vacuum overnight.

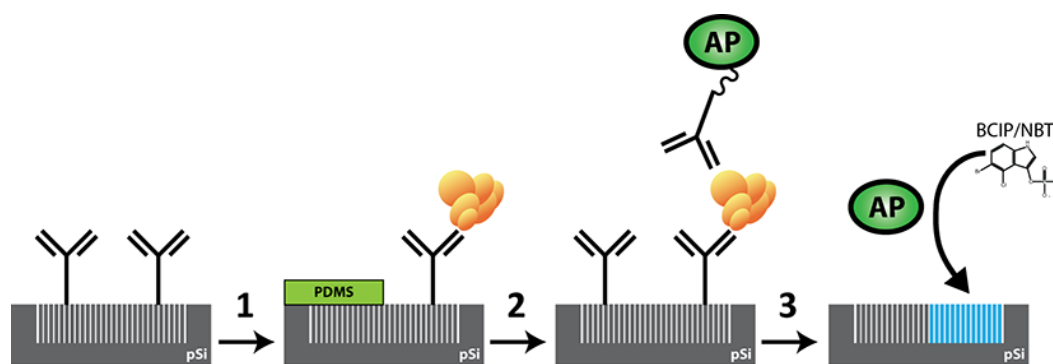


Figure 4.4: Schematic detailing the formation of immunoassay patterned pSi. (1) Capture antibody pSi was masked with a PDMS film and exposed to human IgG analyte (yellow protein). (2) The human IgG patterned pSi was unmasked and exposed to the secondary antibody conjugated to alkaline phosphatase. (3) Incubation with BCIP/NBT caused precipitation to only occur in the unmasked region.

#### **4.3.10 Refractive Index Measurements**

Refractive indices ( $n$ ) of the enzyme-substrate components were determined to within  $\pm 1 \cdot 10^{-5}$  using a digital Abbe refractometer RX-5000 (ATAGO, Tokyo, Japan). Before conducting the measurements, the refractometer was calibrated using milliQ water in accordance with the instrument instructions. The temperature of all solutions was matched via incubation in a water bath at 25 °C for 1 hour. The samples were then directly pipetted from these stock solutions into the sample chamber of the instrument. For samples that required mixing (enzyme/substrate), these liquids were combined and quickly stirred in the sample chamber of the instrument to achieve readings from 0 min.

## **4.4 Results and Discussion**

### **4.4.1 Surface Characterisation**

#### **4.4.1.1 SEM**

pSi was etched from n-type silicon following the procedure outlined in Chapter 3 section 3.3.1. By propagating a pre-etched, templated silicon surface, etching  $n^+$  at  $50 \text{ mA/cm}^2$  for 45 seconds achieved a homogeneous porous structure with large pore openings. The large, straight pores and wide openings promote diffusion of biomolecules which is essential for biosensing. The freshly etched pSi surface, Figure 4.5 (a), and cross section, Figure 4.5 (b), were investigated with SEM to ascertain the pore size and thickness of the pSi film. The resulting pore structure matched those previously fabricated in Chapter 3, displaying a similar pore size distribution and pore depth. The pore walls are linear, free of branches or obstructions and are fully open at the surface. Pore size ranged from  $\sim 50 - 250 \text{ nm}$  in diameter with an average pore diameter of  $118.24 \text{ nm}$  (Figure 4.5 (c)).

The porous matrix was quite shallow, with an average depth of  $1019.44 \text{ nm}$ . This was preferential as samples etched under these conditions saw reduced reflectivity when etched for longer periods. Such samples are not suitable for an optical sensor based on reflected white light and their manufacture was avoided.

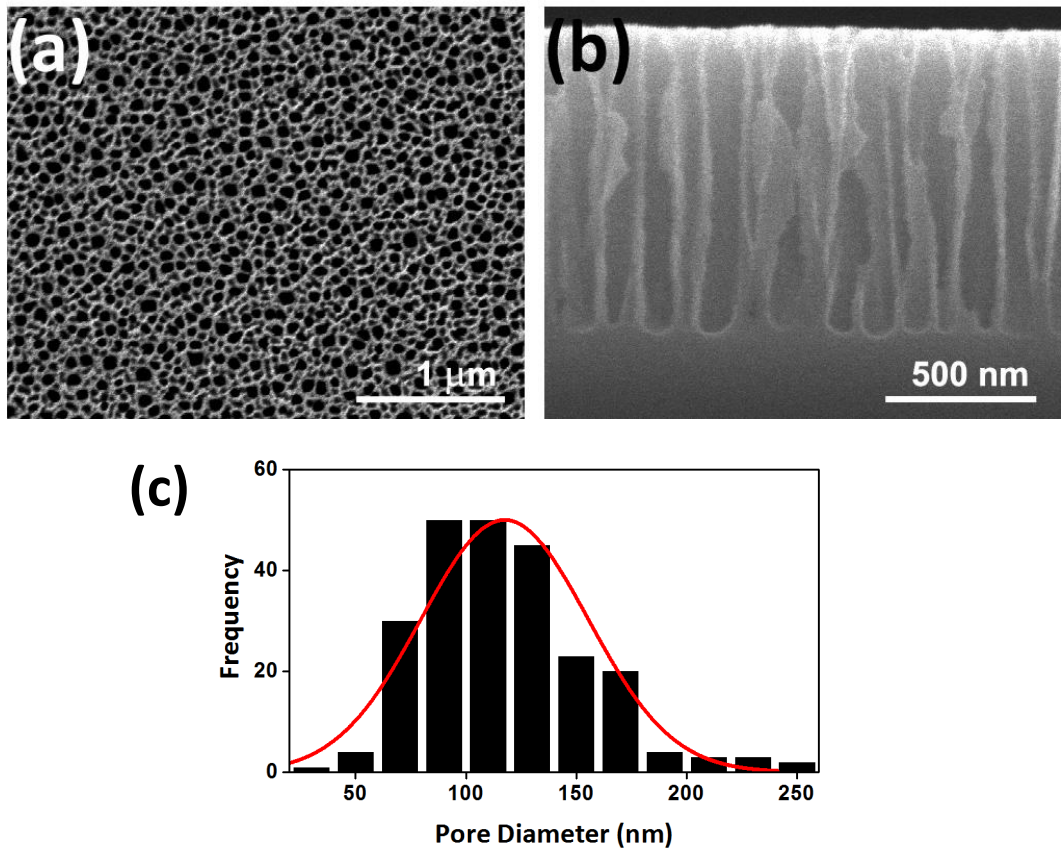


Figure 4.5: SEM micrographs of 0.008-0.02  $\Omega$ .cm n-type pSi etched following a two step process – surface templating: 275  $\text{mA}/\text{cm}^2$  for 1.82 seconds, pore propagation: 50  $\text{mA}/\text{cm}^2$  for 45 seconds. (a) Top down view of the pSi surface. (b) Cross-sectional perspective. (c) Pore size distribution histogram.

#### 4.4.1.2 IR Spectroscopy

Throughout the functionalisation process, the chemistry of the modified pSi surface was analysed using FTIR ATR. Scans were taken of the porous silicon surface immediately after each major step: etching, silanisation and capture antibody immobilisation.

Figure 4.6 (a) shows a series of FTIR spectra corresponding to each step in the surface modification process. The spectra correspond to freshly etched pSi, 3-

isocyanatopropyl-triethoxysilane functionalised pSi and sheep anti-human IgG immobilised pSi. Freshly etched silicon is silicon hydride terminated and provides signature SiH<sub>2</sub> scissoring and SiH stretching peaks at 900 cm<sup>-1</sup> and 2100 cm<sup>-1</sup> respectively [170-172]. Exposure to ozone gas or heat via thermal oxidation, converted the silicon hydride groups to silicon oxide which is clearly evident via the elimination of the hydride peaks and appearance of a broad SiO stretching peak in the region of 1100 cm<sup>-1</sup>. A characteristic broad silanol (SiOH) peak also appeared at 3400 cm<sup>-1</sup> [170-172]. Silanisation of the pSi with 3-isocyanato triethoxysilane was confirmed via a N=C=O stretching peak at 2270 cm<sup>-1</sup> and the CH<sub>2</sub> peaks in the region of 2850 – 3000 cm<sup>-1</sup> [173, 174]. The observation of a broad hump at 3640 cm<sup>-1</sup> is representative of N-H stretching vibrations. Another group of peaks in the region of 1250 cm<sup>-1</sup> – 1700 cm<sup>-1</sup> also indicates the presence of a combination of C-N stretching and N-H bending vibrations (1558 cm<sup>-1</sup>), N-C-N symmetrical stretching (1150 cm<sup>-1</sup>), N-C-N antisymmetric stretching (1342 cm<sup>-1</sup>) and carbonyl stretching vibrations (1628 cm<sup>-1</sup>), all of which are indicative of a urea group [173-175]. This indicates that some of the silane molecules have become cross-linked during silanisation. This phenomenon is possibly due to a reaction between the isocyanate group and residual water in the solvent or due to water vapour in the air during sample handling and characterisation, leading to the formation of carbamates, which then dissociates into carbon dioxide and an amine. The amine then reacts with neighbouring isocyanates leading to a urea cross-link [176].

Following silanisation, the sheep anti-human IgG capture antibody was immobilised within the pores via a reaction between the isocyanate and an amine group within the protein to produce an isourea bond [177]. Any remaining isocyanate groups were then neutralised with ethanolamine hydrochloride to form carbamate bonds (1686 cm<sup>-1</sup>) [173]. Subsequently the peak at 2300 cm<sup>-1</sup> diminished significantly in intensity, indicating that the isocyanate groups had reacted with the protein or had become cross-linked in contact with the aqueous medium. A clear problem associated with IR analysis of isocyanate functionalised pSi, is the overlap of signals. Essential information such as the appearance of a carbonyl peak (1632 cm<sup>-1</sup>) upon protein immobilisation can be

lost due to overlap with the cross-linked silane carbonyl peak or the carbamate peak [173].

For this reason, Figure 4.6 (b) displays an enlarged section of the IR spectra that allows the carbonyl and amide stretching vibrations to be easily visualised. No changes to the peak structure or position was apparent, indicating that there was insufficient IR spectroscopic evidence to identify successful immobilisation of the capture antibody. While this result was inconclusive, the immobilisation technique has been tested and proven to work in literature using XPS [16, 17]. The inability to identify bioconjugation in this study may be as a result of the n-type silicon used in this study requiring a reflective form of IR spectroscopy due to the high dopant levels. Transmission IR characterisation can be performed on silicon containing lower dopant levels and samples a much larger area than ATR more easily identifying new and altered peaks. Further IR analysis in Chapter 4 section 4.4.6.2 provides additional evidence of successful immobilisation of the capture antibody.

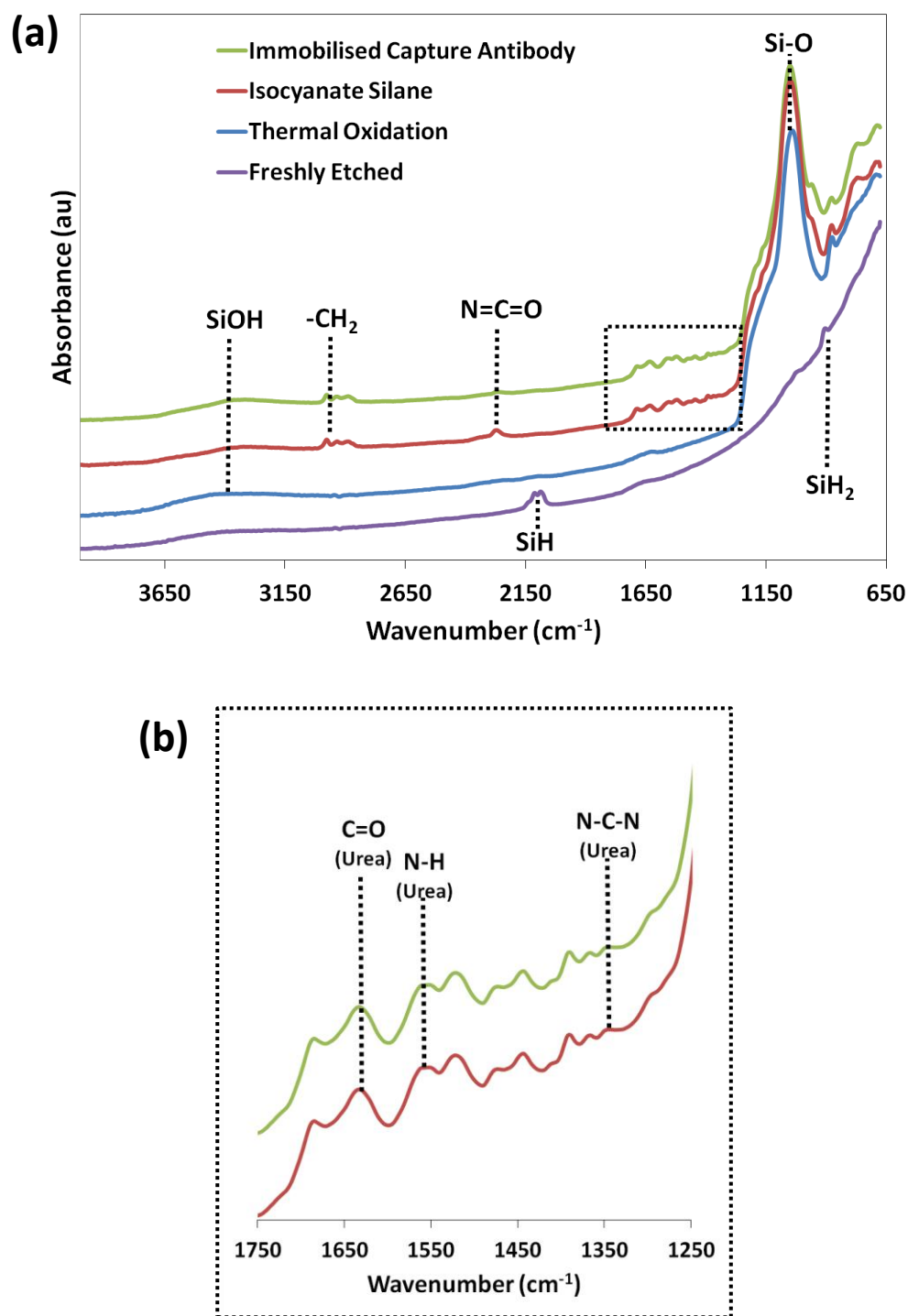


Figure 4.6: IR spectra of sequential pSi surface modifications resulting in the immobilisation of  $\alpha$ -human IgG capture antibody. (a) Freshly etched, thermally oxidised, isocyanate silanised and capture antibody immobilised pSi. (b) Expanded view of the isocyanate silane and capture antibody spectra to highlight the urea vibrations more clearly.

#### **4.4.2 Enzyme Substrate Optimisation**

##### **4.4.2.1 BCIP Enzyme Substrate**

Investigation of the enzyme substrate, 5-bromo-4-chloro-3-indoyl phosphate (BCIP), as an immunosensor detection approach on pSi was undertaken due to its successful use on other sensors where it exhibited strong precipitation and colour change when exposed to alkaline phosphatase [24, 161-164]. In order to test this detection strategy on pSi, 20 U/mL alkaline phosphatase was covalently immobilised on isocyanate coated n-type and p-type pSi to form an active surface. Surfaces were also prepared where alkaline phosphatase was replaced by 10 mM ethanolamine hydrochloride to act as a control. The functionalised pSi was placed into the immunosensing apparatus and monitored via IRS to form an EOT sensorgram. The EOT measurements presented in this chapter have been normalised to the first EOT measurement taken at time 0 min by dividing each EOT measurement (EOT) over the original EOT taken at 0 min ( $EOT_0$ ). This allows direct comparison between samples without the error associated with offsetting data. Figure 4.7 shows the response from the active and control surfaces for (a) n-type pSi and (b) p-type pSi. Introduction of 3 mM BCIP in Tris buffer caused a significant decrease in the EOT on both the active n-type and p-type pSi compared with the initial baseline established in Tris buffer. Washing the sample with Tris buffer after 30 minutes incubation had no major effect on the n-type pSi signal, indicating that the effect was permanent. The p-type sample experienced a further decrease in EOT upon wash, which was probably a result of the inherent instability of ozone oxidised  $p^{++}$  pSi when exposed to aqueous conditions, as previously reported [16]. Comparison of the active and control surfaces from both types of pSi in Figure 4.7 demonstrated that the decrease in EOT only occurred in the presence of the enzyme-substrate combination, as the control surface's baseline trend was not altered. This demonstrates specificity and is essential for the system to be incorporated into an immunosensor. The active p-type sample provided a much larger decrease in EOT (1.10%) than the n-type sample (0.74%) which may be attributed to its high porosity as demonstrated by the smaller pore diameter and pore-to-pore distance in Chapter 3 section 3.4.2. While a stronger response was observed on  $p^{++}$  pSi, the stability of the material and EOT signal was poor, registering a non-specific decrease of 0.29%. This instability may relate to the dissolution of the mesoporous surface layer of p-type

pSi by hydrolytic attack. The template etched n-type pSi did not contain such a structure and experienced considerably less non-specific baseline drift (0.10%). This system presents a new detection pathway for immunosensing within pSi. Optimisation based on BCIP concentration, analyte and immunological components could improve the signal and allow the development of a range of specialised sensors.

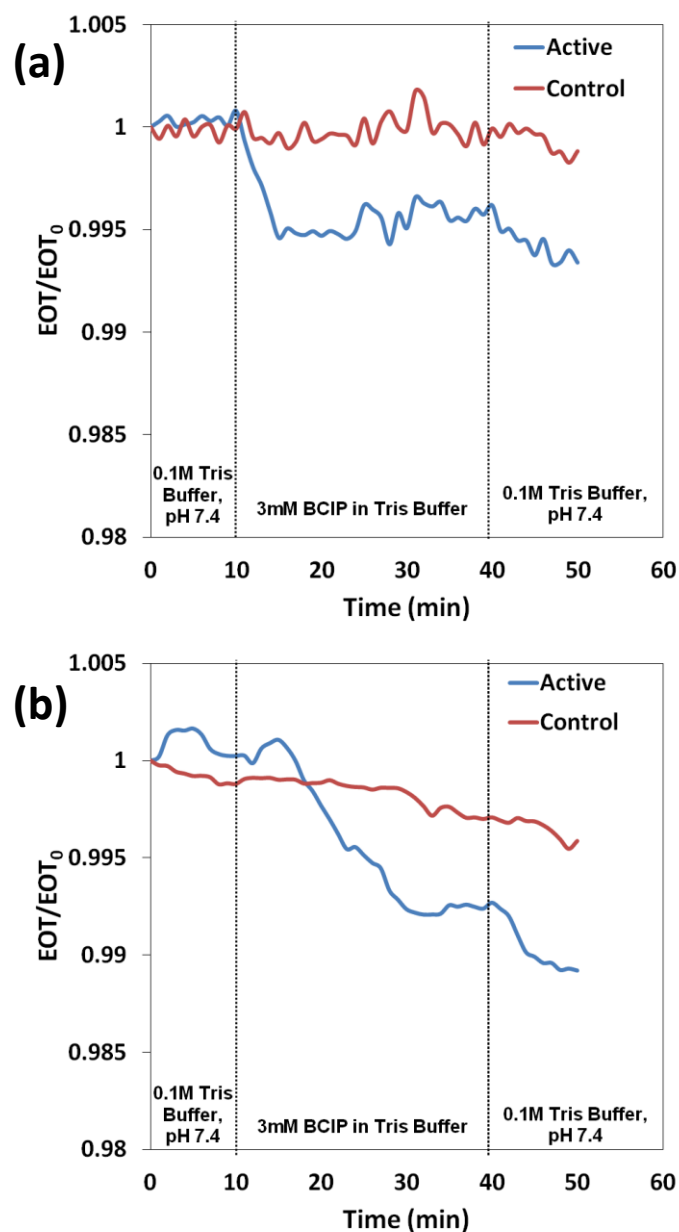


Figure 4.7: Response from de-phosphorylation of BCIP by alkaline phosphatase on pSi. (a) Active and control n-type pSi surfaces. (b) Active and control p-type pSi surfaces.

#### *4.4.2.2 BCIP/NBT Enzyme Substrate*

Detection of human IgG via alkaline phosphatase and BCIP was significant, however the observed signal strength was small. To achieve a greater signal, the BCIP compound was replaced by a BCIP/NBT substrate mixture. When these two compounds are present in the same environment as alkaline phosphatase, dephosphorylation of BCIP also generates a highly insoluble NBT-diformazan product (Figure 4.1). This in turn causes amplified precipitation and colour change, producing a larger EOT signal than using BCIP independently. Due to the instability of the p-type silicon signal observed in Chapter 4 section 4.4.2.1 and the presence of a mesoporous surface layer identified in Chapter 3, n-type pSi was chosen as the sensor scaffold for this study. The same procedure as described in Chapter 4 section 4.4.2.1 was used to form the test sensor with the exception being the replacement of the BCIP substrate solution with a commercially prepared BCIP/NBT liquid substrate solution. Upon introduction of the new substrate mixture to the alkaline phosphatase decorated pSi, a larger decrease in EOT (1.71% decrease) was elicited when compared to the same experiment performed solely with BCIP (0.74% decrease), Figure 4.8. This indicated that the addition of NBT to the substrate solution appeared to enhance the signal. However, it can also be observed in Figure 4.8 that control experiments experienced a large non-specific signal. The initial control consisted of an ozone oxidised pSi sample that was silanised with isocyanate and blocked with ethanolamine. Addition of the BCIP/NBT substrate solution and incubation for 30 minutes yielded a large permanent 1.37% decrease in EOT. This effect was unexpected as the control surface contained no enzyme to catalyse the precipitation of the BCIP/NBT. Due to the non-specific response exhibited by the control, the active surface only yielded a decrease of 0.54%, a poorer sensor response compared to the previous BCIP sensor.

To investigate the cause of this non-specific signal further, a second control experiment was performed in the same manner except that thermal oxidation was applied in place of ozone oxidation. Thermal oxidation forms a thicker oxide layer consisting of more SiO<sub>2</sub> groups than ozone oxidation [45]. This improves the stability of the material in aqueous environments as explained in Chapter 1

section 1.2.3. The thermally oxidised pSi control also experienced a decrease in EOT of 0.95% upon incubation with the substrate solution. The reduction in the EOT decrease experienced by the more passive thermally oxidised surface indicated that the signal could originate from non-specific corrosion of the pSi matrix.

The pH of the commercial BCIP/NBT solution was then analysed and found to be basic (pH 9.8), a level optimal for alkaline phosphatase activity. pSi is unstable in basic conditions, where OH<sup>-</sup> ions convert silicon dioxide to silanol groups, allowing increased nucleophilic attacks from water molecules and accelerated corrosion [178]. To investigate if the alkaline conditions were the cause of the non-specific signal, the pH of the BCIP/NBT solution was adjusted using HCl to pH 7.4 and a thermally oxidised control surface was exposed to this solution to determine if corrosion still occurred. It is clearly evident in Figure 4.8 that the pH altered solution did not trigger a non-specific decrease in EOT upon exposure; displaying an unaltered baseline and a total decrease of 0.22%. This result indicated that the non-specific signal occurred due to the alkalinity of the substrate solution and was not related to the substrate chemicals.

Accounting for the pH related corrosion of pSi, comparison of the active and control surfaces in Figure 4.8 identified discrepancies in the region immediately following injection of the substrate solution. When the enzyme was present, the EOT experienced a large and rapid decrease compared to the small and gradual decrease observed when the enzyme was absent. This is important, as during the initial 5 – 10 minutes exposure the non-specific response remained quite low, while the active surface generated a strong signal. This result indicated that the BCIP/NBT substrate solution could be used to form a pSi immunosensor if exposure time was optimised.

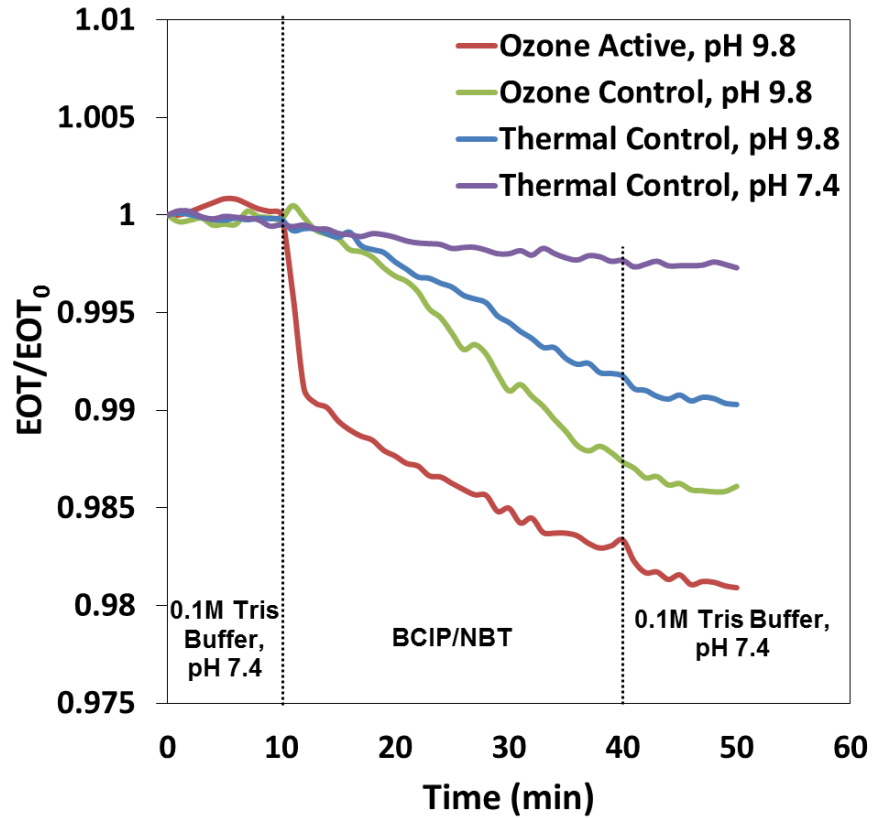


Figure 4.8: Response from precipitation of BCIP/NBT by alkaline phosphatase on n-type pSi as a result of oxidation protocol and pH.

#### 4.4.2.3 Effect of Reduced Exposure Time – Removal of the Non-Specific Corrosion Signal

Removal of the non-specific detection signal was paramount to developing the platform into a working sensor. To achieve this goal, the corrosion effect associated with the alkaline substrate solution was reduced via a combination of thermal surface passivation and reduction to the exposure time that pSi was in contact with the alkaline substrate solution. By varying the exposure length of the BCIP/NBT solution to the alkaline phosphatase enzyme and pSi surface, an optimal time could be identified that demonstrated a compromise between signal strength and the non-specific corrosion signal.

pSi samples were prepared as described in Chapter 4 section 4.3.3 and coated with, 20 U/mL alkaline phosphatase. Control samples were also prepared via the same protocol and contained neutralised isocyanate silane and no enzyme. Both types of surfaces were subjected to decreasing exposure times of: 30, 20, 10 and 5

minutes to monitor the extent and stability of the EOT change. The change in EOT was calculated by subtracting the final EOT reading of the experiment from the EOT value at 10 minutes (the last value in the initial buffer baseline). Figure 4.9 contains the results of the exposure investigation, depicting time resolved EOT data from the active, (a), and control, (b), surfaces. It also shows the total EOT response exhibited by each exposure time in Figure 4.9 (c) and a resulting sensitivity comparison between each exposure time in Figure 4.9 (d). 30 minutes exposure to thermally oxidised n-type pSi yielded a significant decrease in EOT of 1.44% on the active surface and a 0.97% decrease on the control surface. Reduction of the exposure time to 20 minutes saw a slight reduction to the decrease in EOT for the active surface to 1.27%, however the amount of non-specific corrosion on the control surface was dramatically reduced to 0.48%. 10 minutes exposure also saw the trend continue, retaining relative signal strength with an EOT decrease of 0.93% on the active surface, while the control experienced a low level decrease in the background non-specific corrosion of 0.13%. 5 minutes exposure time generated the smallest decrease in EOT compared to the other conditions, 0.66%, but exhibited a similar background signal on the control surface to that observed for the 10 minute sample, 0.11%. Comparison of the 4 exposure times in Figure 4.9 (d) indicated that 10 minutes incubation of the pSi/enzyme/substrate yielded the highest ratio between the active signal and the non-specific background. Using this approach, the non-specificity associated with the corrosion of the pSi transducer was effectively reduced to minimal levels, providing a stable system with which to conduct sensing experiments. This outcome had a secondary benefit, reduction of the detection time associated with the sensor. Generating a fast sensor response time is an important factor to consider when designing a new sensor technology. By lowering the detection time by 10 – 20 minutes compared with previously reported enzyme based pSi optical immunosensors, detection and diagnosis can be made more rapidly, making the device more attractive to health care facilities [16, 17].

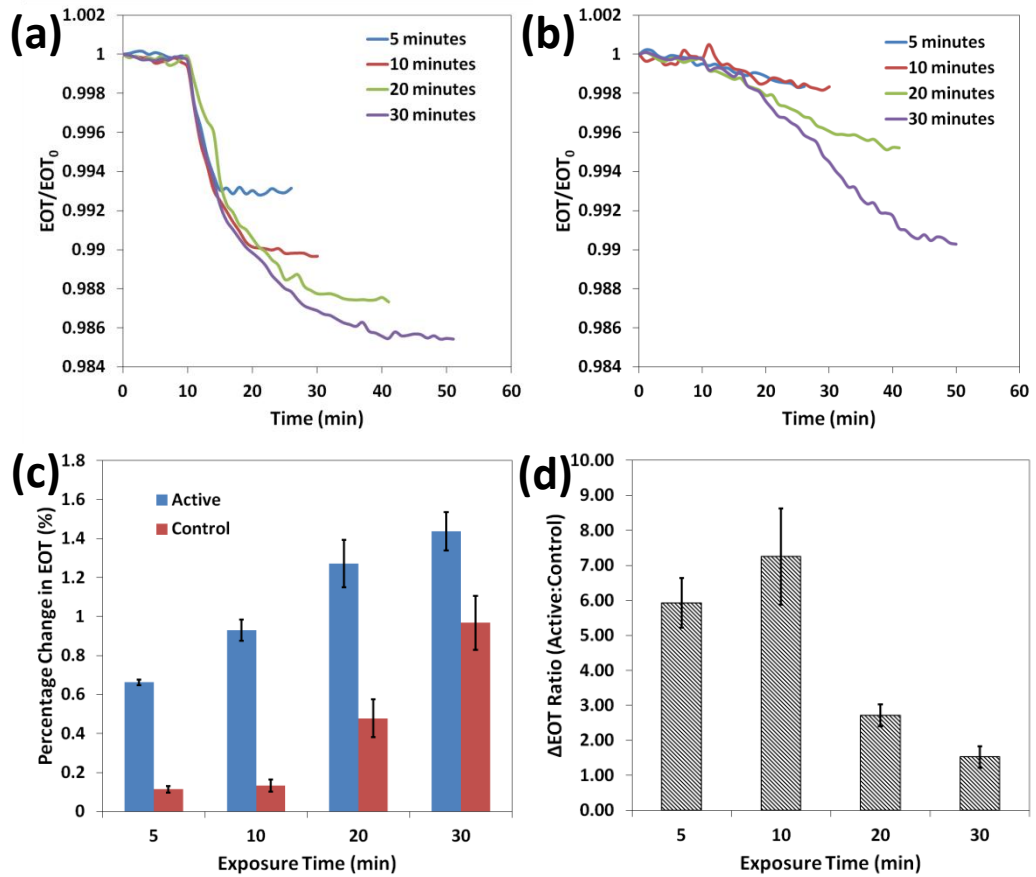


Figure 4.9: Response from precipitation of BCIP/NBT by alkaline phosphatase on n-type pSi as a result of reduced exposure times. (a) Active pSi surfaces containing covalently immobilised alkaline phosphatase. (b) Control pSi surfaces containing no enzyme. (c) Change in EOT experienced by both active and control surfaces. (d) Signal ratio, active:control, for each exposure time investigated.

#### 4.4.3 Signal Processing Optimisation

Optimisation of the detection pathway is only one facet for achieving a sensitive biosensor device. Signal processing can also be a strong factor on the ability to detect low levels of analyte. Many optical pSi biosensors have been developed using interferometry [16, 17, 179-183], which is able to detect analytes via changes in refractive index, resulting in shifts to the reflected fringe pattern or via Fourier transform and changes to the EOT of the material. While a large number of pSi biosensors are based on this technique, the sensing mechanism developed

in this chapter may not be suited towards this approach due to the effect of substrate precipitation on the reflected optical profile.

The EOT change experienced by the n-type pSi when exposed to alkaline phosphatase in the presence of BCIP/NBT is a sharp and rapid decrease as observed in Figure 4.9. According to Equation 4.1, such an effect can only occur if there is a decrease in either the refractive index (n) and/or the depth (d) of the porous layer.

$$EOT = 2.n.d$$

Equation 4.1: Effective Optical Thickness of a porous film.

This observed EOT decrease was investigated by recording the refractive indices of the various components involved in the biocatalysis of BCIP/NBT, Table 4.3. Following the procedure outlined in Chapter 4 section 4.3.10, the refractive index of each native solution associated with the test sensor was measured. 10  $\mu$ L of alkaline phosphatase (AP) was then added to 490  $\mu$ L of the substrate solution and the refractive index recorded at 0, 3 and 5 minutes. Analysis revealed that the refractive indices of the substrate solutions rose slightly after addition of the alkaline phosphatase enzyme.

Solution	Refractive Index (n)
Water	1.33253
Tris Buffer	1.33606
BCIP/NBT	1.33482
Alkaline Phosphatase (AP)	1.33612
AP+BCIP/NBT (0min)	1.33546
AP+BCIP/NBT (3min)	1.33548
AP+BCIP/NBT (5min)	1.33549

Table 4.3: Refractive indices of solutions used in the biocatalysation of BCIP/NBT by alkaline phosphatase

The rise in refractive index of the substrate solution upon addition of the enzyme at 0 minutes can be partially related to the mixing of the two liquids according to the following equation:

$$n = \frac{n_1V_1 + n_2V_2}{V_1 + V_2}$$

Equation 4.2: Refractive index of mixed solutions.

Where  $n$  is the new refractive index of the mixed solution,  $n_1$  and  $V_1$  are the refractive index and volume of liquid 1 and  $n_2$  and  $V_2$  are the refractive index and volume of liquid 2 [184].

According to Equation 4.2, the refractive index of the AP+BCIP/NBT solution at 0 minutes should be 1.33484 compared to the observed value of 1.33546. While the addition of a small amount of enzyme partially contributed to the increase in refractive index of the substrate solution, it did not explain the observed result of 1.33546. The additional increase in refractive index may be attributed to the immediate biocatalysation of the BCIP/NBT substrate upon introduction of the alkaline phosphatase enzyme, leading to the formation of new compounds of higher refractive index. Monitoring the refractive index over a 5 minute incubation period also supported this hypothesis by demonstrating that the enzyme/substrate reaction continued to increase the refractive index.

Comparison of the refractive indices recorded in Table 4.3 against the signal response of the pSi sensor in Figure 4.9 yielded conflicting results. The refractive index of the BCIP/NBT substrate solution, 1.33482, was lower than the Tris buffer, 1.33606. According to Equation 4.1 and assuming a 1019.44 nm thick porous layer (Chapter 4 section 4.4.1.1), a change of 0.00115 to the refractive index should only correspond to a decrease in EOT of 2.34 nm (0.06%) before the EOT begins to rise again in response to the refractive index change from biocatalysation of the substrate solution. This response was not observed when alkaline phosphatase pSi was exposed to BCIP/NBT for 5 minutes; instead a steady and continual decrease of 26.39 nm (0.66%) was generated. The inconsistency between the refractive index measurements and the EOT response of the pSi sensor indicated that the sensor response did not occur primarily as a result of a refractive index change within the pores.

The cause of the inconsistency was investigated by assessing the effect of the biocatalysation event on the reflected optical profile of pSi. The Fabry-Perot fringe pattern became distorted when exposed to a combination of alkaline phosphatase and BCIP/NBT substrate Figure 4.10. A substantial decrease in intensity occurred in the region of ~500 – 700 nm and a slight wavelength shift towards the red was also apparent within the affected area. The Fourier transform and calculation of EOT from this altered fringe pattern resulted in the false decrease in EOT observed in Figures 4.8 and 4.9. The manner in which the fringe pattern is altered proves that the refractive index was not the cause of the EOT change, as a refractive index change should alter the entire optical profile of the material through a wavelength shift [185].

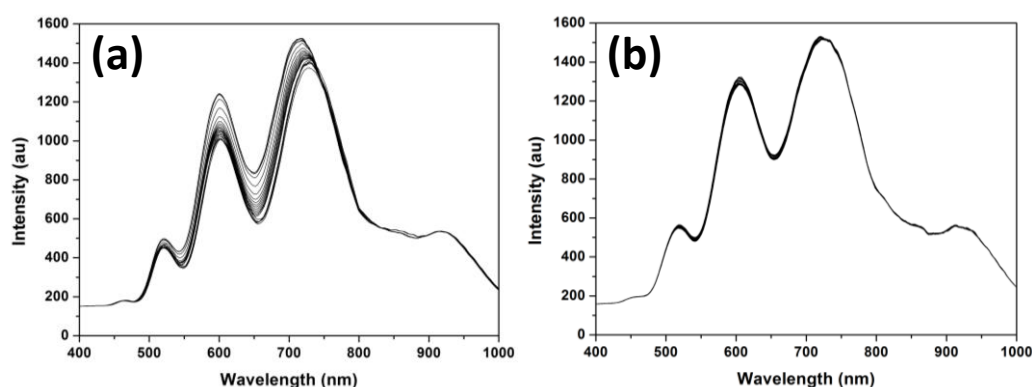


Figure 4.10: Effect of biocatalysed BCIP/NBT precipitation on the fringe pattern of pSi. (a) Active surface containing the alkaline phosphatase enzyme. (b) Control surface containing no enzyme.

The alteration to the fringe pattern upon the biocatalysation of BCIP/NBT is due to the formation and precipitation of the de-phosphorylated BCIP-dimer and NBT-diformazan products. The de-phosphorylation of BCIP and reduction of NBT result in a strong colour change from pale yellow to a dark purple and strong absorption in the region of ~525 nm - 750 nm (absorption maxima at 600 nm [186]). When the pSi surface is coated with this substance, the intensity of the reflected spectrum within the absorbance band is reduced, altering the shape and order of the fringe pattern leading to the ‘decrease’ in EOT observed in Figure 4.9.

Due to the effect of the detection event on the reflected fringe pattern, the detection signal can potentially be processed via 3 main approaches: EOT, fringe shift (wavelength) and intensity. Each approach was subsequently investigated to determine the most sensitive method. Comparison of the 3 signal processing methods was carried out by analysing the response of pSi to an alkaline phosphatase, BCIP/NBT precipitation event. A secondary  $\alpha$ -human IgG antibody conjugated to alkaline phosphatase was diluted at a ratio of 0, 1:5000 and 1:2000 in Tris buffer and immobilised on pSi as outlined in Chapter 4 section 4.3.4. The functionalised surfaces were then exposed to the BCIP/NBT substrate solution and the response in EOT, wavelength shift and intensity was monitored. Each of these three signals could be acquired via post-processing experimental data acquired using IRS while the experimental method remained unchanged.

The EOT was calculated using the conventional method of performing Fourier Transform on the entire pSi fringe pattern as outlined in Chapter 1 section 1.2.4.1. The EOT response was normalised as described in Chapter 4 section 4.4.2.2 and plotted as percentage change vs. time in-order to easily compare the technique's sensitivity against the other forms of signal processing, Figure 4.11 (a). The wavelength shift was determined by fitting an interference peak in the Fabry-Perot fringe pattern at 607 nm and monitoring the position over time. Igor Pro software designed for EOT calculations was adapted for this task. The resulting wavelength shift data was normalised in the same manner and plotted as percentage change vs. time in Figure 4.11 (b). The change in intensity was recorded by monitoring the intensity value of the fringe pattern at 600 nm, the absorbance wavelength of NBT-diformazan, Figure 4.11 (c) [166]. This wavelength is located close to the centre of the absorbance band and is situated near the apex of a peak within the fringe pattern. Once again the intensity data was normalised by dividing all intensity measurements by the initial intensity reading at 0 minutes and plotted as intensity change vs. time. The signal response from each technique was calculated by subtracting the final reading at 30 minutes from the value recorded prior to addition of the substrate at 10 minutes. Data from all 3 techniques is represented in Figure 4.11 (d).

Processing via the wavelength shift method provided the lowest response, registering an overall signal change of 1.23% from baseline levels at a

concentration of 1:2000 secondary antibody. The EOT technique provided the second strongest response at 3.17%, while processing via the intensity approach provided the strongest response by a large margin, registering a signal change of 12.7% at 1:2000. Control surfaces for all techniques only provided marginal changes. It was clearly evident from this result that the intensity change at 600 nm provided the most sensitive approach. As such, this form of signal processing was implemented as the primary technique in subsequent studies.

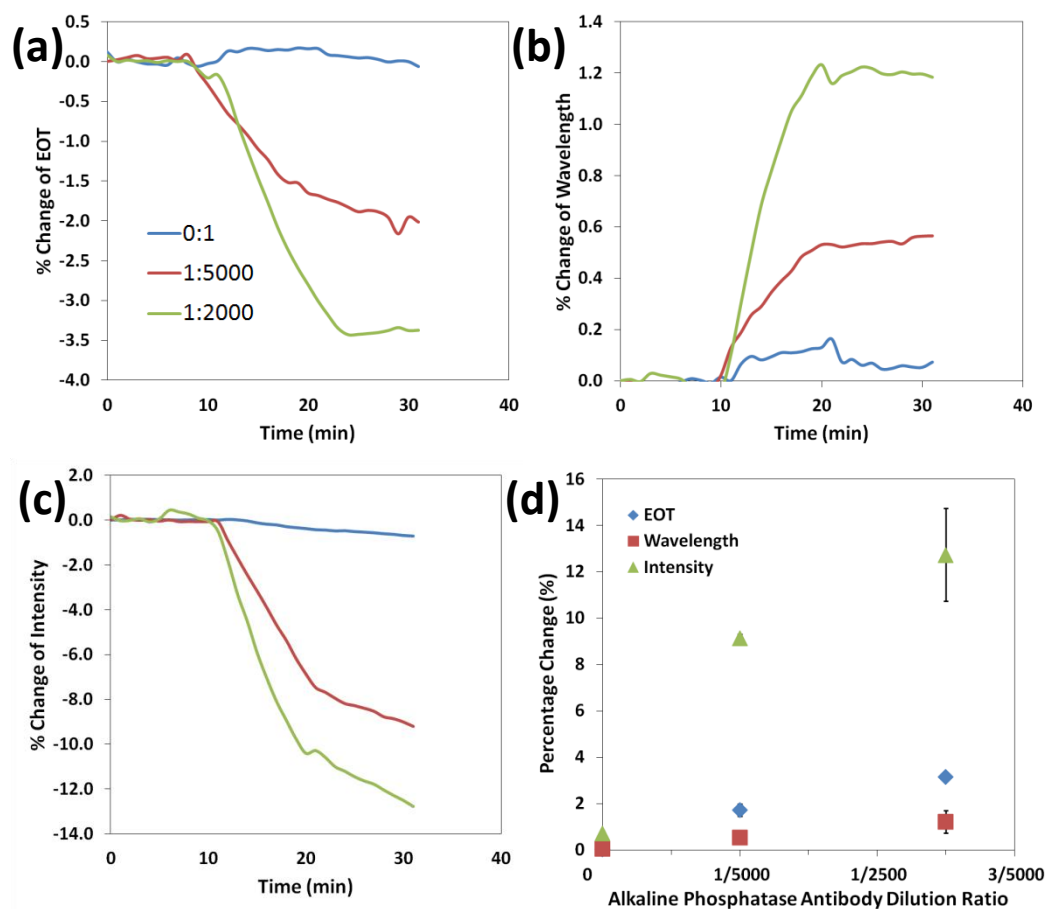


Figure 4.11: Comparison of 3 signal processing techniques. Goat  $\alpha$ -human IgG antibody conjugated to alkaline phosphatase was covalently immobilised pSi at dilutions of 0:1, 1:5000 and 1:2000 antibody:Tris buffer. The modified surfaces were then exposed to BCIP/NBT and the response monitored. (a) Percentage change of EOT. (b) Percentage change of wavelength shift. (c) Percentage change in intensity at 600 nm. (d) Combined data from a, b and c comparing the signal strength from the three approaches.

#### **4.4.4 Intensity Response to BCIP/NBT Precipitation on pSi and Flat Silicon**

The decision to use a change in reflected intensity as a transduction signal brings this pSi immunosensor in line with other techniques such as ELISA that monitor the absorbance of a colour change. The benefit of pSi over techniques that employ wells or flat supports is the porosity of the material and subsequent high surface area that can be utilised to bind additional receptor molecules within the same spatial dimensions. This characteristic has been previously demonstrated using pSi to detect low levels of fluorescently labelled viruses via changes in the fluorescence intensity of the surface [187]. To highlight the benefits of this effect, the intensity response from pSi was compared against the response from bulk silicon (flat silicon). Isocyanate functionalised pSi and flat silicon were incubated with 20 U/mL alkaline phosphatase to form active surfaces. Control surfaces were prepared by neutralising the isocyanate silane with 10 mM ethanolamine. To visualise the response of each surface upon exposure to BCIP/NBT, the samples were placed in a flow cell and monitored via IRS as shown in Figure 4.12. The samples were baselined in Tris buffer, pH 7.4, for 10 minutes, then exposed to BCIP/NBT for 10 minutes before being baselined again in Tris buffer for a further 10 minutes. Figure 4.12 (a) & (b) show the reflected white light optical profile of the respective pSi active and control surfaces, while Figure 4.12 (c) & (d) show the respective flat silicon active and control surfaces. The maximum intensity of all surfaces corresponds to the initial baseline in Tris buffer, prior to the addition of BCIP/NBT. Figure 4.12 clearly demonstrates that the active surfaces for both types of material elicited a marked change in their reflected optical profiles, while the control surfaces only produced minor changes. The reflected intensity of the active surfaces was diminished upon exposure to BCIP/NBT over the range of ~525 nm – 750 nm, although the fringe pattern of the pSi was altered in a different manner to the flat silicon. The pSi experienced the largest decrease in intensity at the apex of the interference peaks and the base of the troughs of the reflected fringe pattern. In addition, a greater decrease in intensity was also observed at lower wavelengths compared to the active flat silicon sample. In contrast, the flat silicon surface's optical profile retained its general shape, simply reducing in intensity over the affected range.

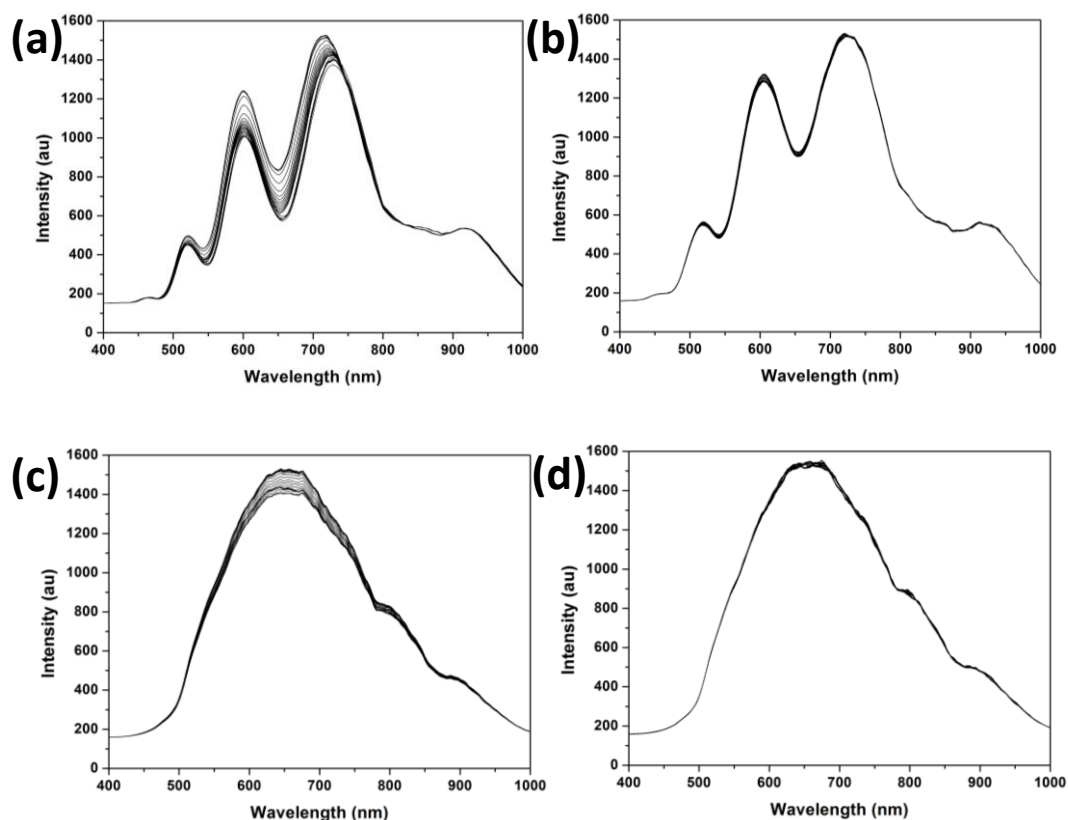


Figure 4.12: Effect on the reflected optical profiles of pSi and flat silicon in response to precipitation of BCIP/NBT. (a) & (b) Active and control pSi surfaces. (c) & (d) Active and control flat silicon surfaces.

Figure 4.13 displays the intensity data for all four surfaces, providing a comparison of their response to BCIP/NBT precipitation. Total intensity change was calculated by subtracting the final reading at 30 minutes from the intensity measurement at 10 minutes. The figure clearly shows that on average, the active pSi yielded a much stronger intensity change at 600 nm (14.65%) compared to its flat silicon counterpart (4.35%). By utilising the high surface area associated with pSi, a 10.30% increase in signal strength was achieved, presumably due to the increased number of receptors in the same spatial region. The control surfaces both experienced small changes in intensity with the pSi generating a change of 1.91% and the flat silicon control a change of 0.90%. The larger signal for the pSi control may be related in part to background corrosion caused by the basic pH of the BCIP/NBT solution, however it is more likely linked to non-specific precipitation over the larger porous surface area. Interestingly, the

washing step at 20 minutes following incubation with BCIP/NBT appears to have washed a large amount of precipitate from the flat silicon surface, while the pSi surface remained unchanged. This indicates that the porous structure trapped the precipitate creating a more permanent and reliable signal. The results of this study demonstrate how the increased surface area of a pSi scaffold can produce a stronger signal than using traditional flat scaffolds.

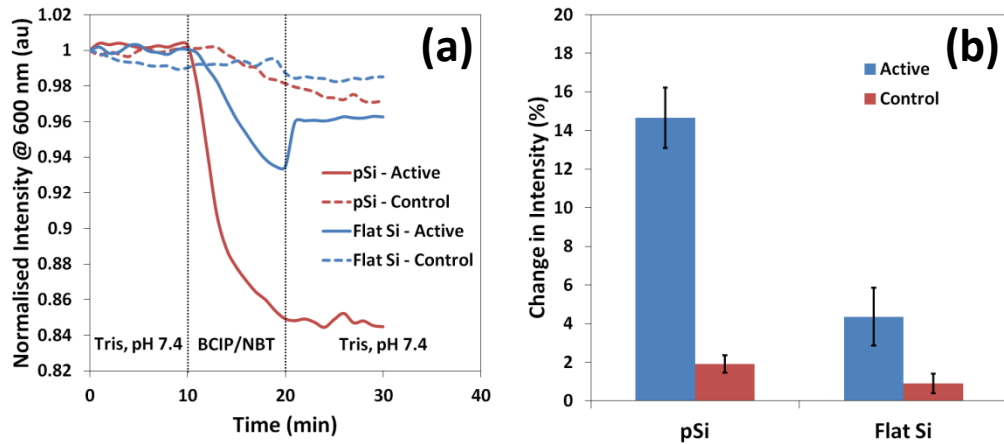


Figure 4.13: Comparison of the change in intensity experienced by pSi and flat silicon upon precipitation of BCIP/NBT. (a) Change in intensity over time experienced by pSi and flat silicon surfaces upon exposure to BCIP/NBT (Active – alkaline phosphatase, Control – no enzyme). (b) Comparison of the total signal response experienced by pSi and flat silicon.

#### **4.4.5 Human IgG Immunosensing**

##### **4.4.5.1 Detection of Human IgG**

Immunosensing involved exposure of receptor coated pSi to an IntraGAM solution consisting of 94% human IgG with the remainder containing human IgA and IgM. This was followed by the introduction of an alkaline phosphatase conjugated secondary antibody to form an IgG specific sandwich assay. The detection event occurred when BCIP/NBT was added and subsequently dephosphorylated by the conjugated enzyme to form a strongly absorbing, insoluble precipitate as depicted in Figure 4.3 (a). The change in reflected intensity of pSi in the region surrounding the absorbance wavelength of NBT, 600 nm, can easily

be observed in Figure 4.14. This figure displays the recorded fringe pattern and corresponding intensity plot for an active pSi surface exposed to 500 ng/mL human IgG. Upon precipitation of BCIP/NBT within the pores, the intensity of the reflected fringe pattern decreased significantly over the region of 500 nm – 750 nm as observed previously. Figure 4.14 (b) shows the corresponding sensorgram for the intensity change at 600 nm plotted against time. Depicted in this manner, the precipitation of BCIP/NBT and subsequent decrease in intensity can clearly be observed. The enzyme substrate is introduced to the flow cell at 70 minutes and immediately elicits a large decrease in intensity. After 10 minutes incubation, the surface was rinsed with Tris buffer to remove un-reacted substrate from the system, quenching the reaction and establishing a final baseline. This step was performed to ensure fast response times as precipitation continued long past 10 minutes especially with higher IgG concentrations. By rinsing the sample, the reaction is stopped but the precipitated compound remains. This allows direct comparison of different analyte concentrations without waiting long periods for the signal to stabilise.

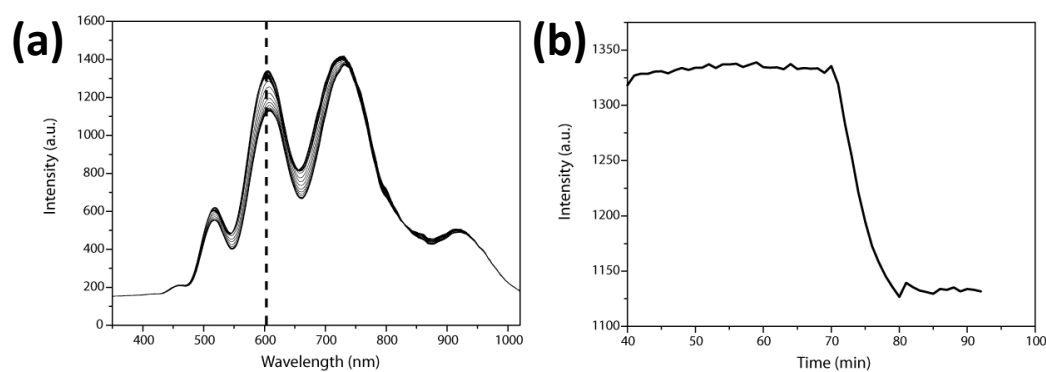


Figure 4.14: Combined porous silicon reflection spectra and corresponding change in intensity at 600 nm for the detection of 500 ng/mL human IgG. (a) Compiled fringe patterns from 0 to 92 minutes depicting a sharp decrease in the intensity of the reflected light upon detection of the human IgG, this effect is particularly strong over the region 500 nm – 750 nm. (b) Change in reflected light intensity over time at 600 nm, the absorbance wavelength of NBT [166].

The change in reflected intensity experienced by pSi was directly related to the concentration of the human IgG in the system. Sensorgrams for a range of human IgG concentrations are shown in Figure 4.15 (a), while Figure 4.15 (b) depicts the relationship more clearly by presenting the intensity change at 600 nm in the form of a standard curve. In the absence of human IgG, only a slight decrease in intensity is observed which might be attributed to non-specific precipitation or corrosion of the pSi due to the basic substrate solution. As the concentration of human IgG was increased, the corresponding intensity change also increased. The intensity change follows linear relationship at analyte levels  $<250$  ng/mL which slowly alters until total signal saturation occurs at analyte levels  $\geq 1000$  ng/mL. It was also observed that larger concentrations of the analyte, 1000 ng/mL and 2000 ng/mL, experienced a rise in intensity following the final buffer rinse at 80 minutes, Figure 4.15 (a). This effect was similar to that experienced by flat silicon in Chapter 4 section 4.4.4 and indicates that some precipitate was removed during the final washing step. It is hypothesized that the presence of more alkaline phosphatase at these analyte concentrations leads to higher levels of precipitation occurring on the pSi surface, top region of the pore walls and in solution. The washing step at 80 minutes is able to more easily dislodge and remove the precipitate from these areas, thus causing the observed increase in intensity. Precipitated BCIP/NBT located deeper in the pores remains trapped and provides the permanent change in intensity observed for all surfaces. This phenomenon appears to be a limiting factor of the sensor, as the intensity change is saturated at levels above 1000 ng/mL even though additional precipitation occurs. While this is not a concern in this study, it may be rectified by etching a deeper porous layer to trap additional amounts of precipitant.

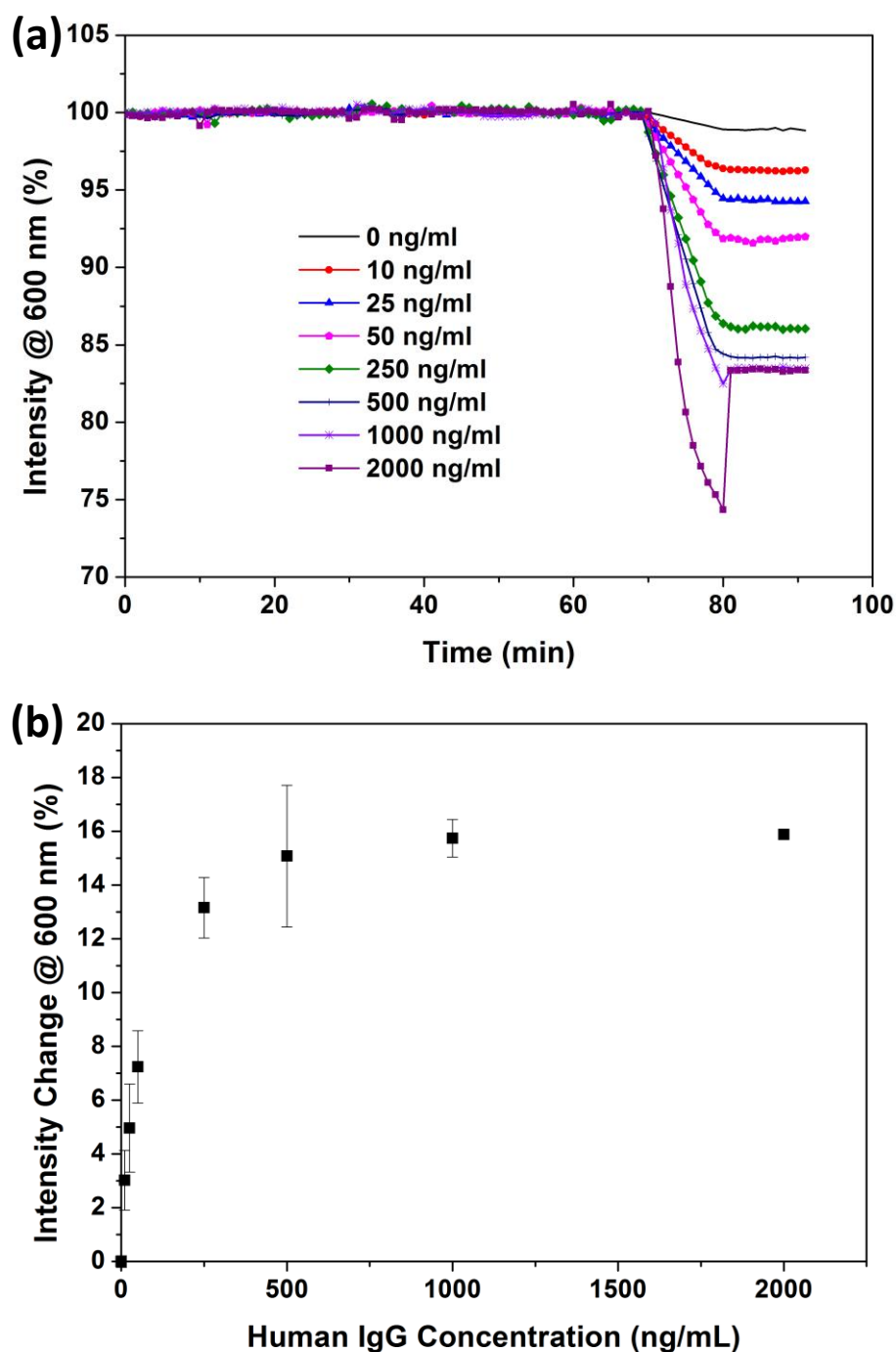


Figure 4.15: Human IgG detection on pSi via alkaline phosphatase catalysed precipitation of BCIP/NBT. (a) Sensorgrams representing the change in reflected intensity at 600 nm for the detection of human IgG. Analyte concentration was varied between 0 ng/mL, and 2000 ng/mL. The detection event occurred at 70 minutes, while the signal step at 80 minutes was a result of a final rinsing step. (b) Background corrected standard curve of human IgG detection on pSi via alkaline phosphatase – BCIP/NBT precipitation.

#### 4.4.5.2 Human IgG pSi Immunosensor Sensitivity

The lowest concentration of human IgG tested was 10 ng/mL, however calculation of the lower limit of detection (LOD) can be achieved via the  $3\sigma$  approach. The LOD is defined as that concentration corresponding to a signal three standard deviations above the mean of the 0 ng/mL human IgG sample. It is derived from the smallest measure that can be detected with reasonable certainty,  $x_{LOD}$ . The value of  $x_{LOD}$  can be calculated by the equation:

$$x_{LOD} = x_{bl} + k \cdot s_{bl}$$

Equation 4.3: Limit of detection (Absorbance) [188].

Where  $x_{bl}$  is the mean of the blank measurements,  $s_{bl}$  is the standard deviation of the blank measures and  $k$  is a numerical factor relating to the confidence level required ( $k = 3$  for  $3\sigma$ ). Figure 4.16 (a) shows the results of 6 separate 0 ng/mL human IgG pSi sensor acquisitions (blank). The mean of the blank measurements is  $x_{bl} = 0.778\%$  and the standard deviation of the 6 measurements is  $s_{bl} = 0.214\%$ . For  $3\sigma$  analysis  $k = 3$  and the LOD is calculated to be  $x_{LOD} = 0.778 + 3(0.214) = 1.420\%$ . This LOD value is indicated by the dashed line in Figure 4.16 (a).

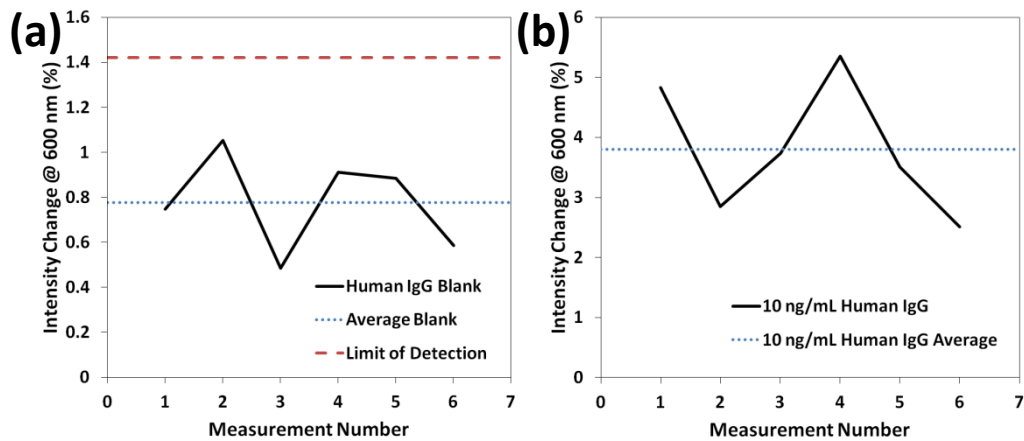


Figure 4.16: Replicate intensity measurements for a pSi immunoassay sensor exposed to (a) 0 ng/mL human IgG analyte; and (b) 10 ng/mL human IgG analyte. The black trace represents intensity measurements; the blue dotted line represents the average value, while the red dashed line represents the limit of detection.

To relate the LOD to concentration, Equation 4.3 can be converted from measurement units to concentration,  $C_{LOD}$ , via inclusion of sensitivity,  $S = \Delta\text{concentration}/\Delta\text{intensity}$ , the slope of the standard curve.

$$C_{LOD} = c_{bl} + k \cdot s_{bl} \cdot S$$

if the concentration of the blank,  $c_{bl}$ , is equal to 0 ng/mL human IgG, this becomes:

$$C_{LOD} = 0 + k \cdot s_{bl} \cdot S$$

$$C_{LOD} = k \cdot s_{bl} \cdot S$$

Equation 4.4: Limit of Detection (Concentration) [188].

Figure 4.16 (b) shows the results of 6 separate pSi sensor acquisitions at 10 ng/mL human IgG (the lowest concentration trialled). The average intensity change that was observed for 10 ng/mL was 3.800 %. As such, the sensitivity of the pSi sensor is  $S = (10 \text{ ng/mL} - 0 \text{ ng/mL}) / (3.800 \% - 0.780 \%) = 3.311 \text{ ng/mL}/\%$ . Thus by using Equation 4.4 and multiplying  $3\sigma$  of the blank and  $S$ , a limit of detection for human IgG on pSi is calculated to be 2.14 ng/mL. This LOD is competitive with leading commercial immunological based techniques such as ELISA which can achieve detection of limit of 0.1 – 1 ng/mL human IgG [189-194]. Total IgG levels within a healthy human adult has been shown to be ~11 mg/mL [195, 196], although subsets of the IgG antibody family specific to certain diseases exist at much lower concentrations applicable to the pSi immunosensor response. As such, the results shown here demonstrate that the immunosensor could be used to detect human IgG in real-world application and clinical human serum samples. In addition to the impressive LOD, the porous silicon immunosensor provided a much shorter detection time when compared with the ELISA method. While the pSi sensor delivered a response within 80 minutes, ELISA systems typically require at least 4 hours before an equivalent result is achieved [193]. The significant detection time, coupled with high sensitivity highlights this alkaline phosphatase - BCIP/NBT based human IgG pSi immunosensor as an important new transduction system. Scaling this technology to an array format also has potential for rapid simultaneous screening of multiple analytes.

#### *4.4.5.3 Human IgG pSi Immunosensor Precision*

Intra-assay precision is measured as a coefficient of variation (CV) from the mean value. It can be calculated from the following equation by dividing the standard deviation, SD, by the mean,  $\bar{x}$ , and multiplying by 100.

$$CV = \%CV = \left( \frac{SD}{\bar{x}} \right) \times 100$$

Equation 4.5: Intra-assay precision [21].

CV was determined from 4 replicates in 3 pools with low (10 ng/mL), medium (250 ng/mL) and high concentrations of human IgG analyte (1000 ng/mL). The results of this investigation appear in Table 4.4 and the precision profile can be found in Figure 4.17. The working range of an assay or sensor can be defined as the range where imprecision is below a preset level such as 20% as shown by the dashed line in Figure 4.17. In accordance with this definition, the pSi silicon sensor developed in this chapter falls within this range for the majority of analyte concentrations tested. Imprecision becomes a factor at concentrations <50 ng/mL human IgG, with the 10 ng/mL sensor runs exhibiting a CV of 29.1%. While imprecision as a function of standard deviation is expected to rise as analyte concentration decreases, such a high level of imprecision was not expected [188]. This result may be attributed to the small number of replicates included in the analysis. In excess of 20 replicates are recommended to achieve reliable precision data [21], however only 4 replicates from each pool were available for this study. Such a small sample number is likely the cause of the imprecise nature of the sensor at low analyte concentrations and could be rectified by performing additional sensing runs in the future. Even with the imprecision at low concentrations, the sensor still demonstrated precise measurements over a large working range, 38 ng/mL – 2000 ng/mL which could potentially be extended to lower analyte concentrations with additional research.

Pool	Intra-assay CV
Low	29.1 %
Medium	8.06 %
High	4.24 %

Table 4.4: Intra-assay precision of the alkaline phosphatase - BCIP/NBT based human IgG pSi immunosensor. The pools listed above correspond to the following concentrations of human IgG analyte, Low – 10 ng/mL, Medium – 250 ng/mL, High – 1000 ng/mL.

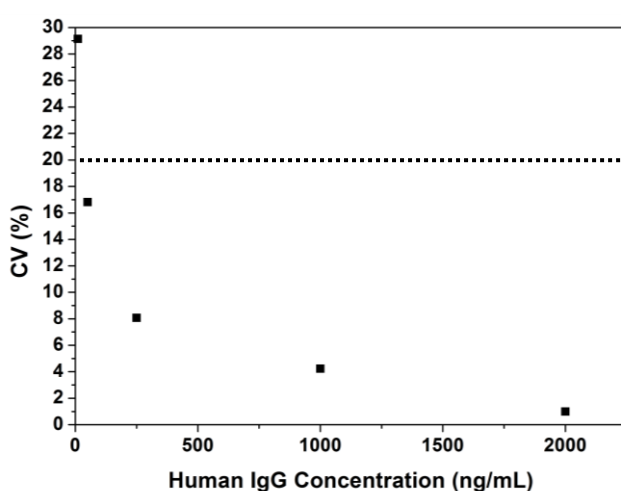


Figure 4.17: Precision profile of the alkaline phosphatase - BCIP/NBT based human IgG pSi immunosensor. The dashed line represents the threshold of the working range of the assay.

#### 4.4.5.4 Human IgG pSi Immunosensor Specificity/Cross-Reactivity

Cross-reactivity is a measurement of antibody response to substances other than the analyte. The effect can manifest as either a false increase in human IgG levels (positive cross-reactivity) or as a false decrease in true human IgG through inhibition of binding sites (negative cross-reactivity). Rabbit IgG at 500 ng/mL and BSA at 50  $\mu$ g/mL were tested for positive cross-reactivity by assaying the sample as an unknown according to the established immunosensor protocol. Negative cross-reactivity was evaluated by spiking Rabbit IgG and BSA fractions with 25 ng/mL human IgG and assessing the signal response with respect to the

standard curve in Figure 4.15. The results of the specificity study appear in Figure 4.18 and Table 4.5. Rabbit IgG and BSA exhibited <1% of either type of cross-reactivity at the tested concentrations. The positive cross-reactivity sensorgrams in Figure 4.18 exhibited intensity changes equivalent to 0 ng/mL human IgG, indicating that these proteins do not generate a false positive signal. The negative cross-reactivity sensorgrams in Figure 4.18 exhibited intensity changes equivalent to 25 ng/mL human IgG, indicating that the presence of either Rabbit IgG or BSA did not significantly interfere with the assay for human IgG. Additional specificity testing is required to ensure cross-reactivity does not occur at other concentrations or with other substances, however this preliminary result indicates that the sensor developed in this chapter is specific for the target human IgG analyte.

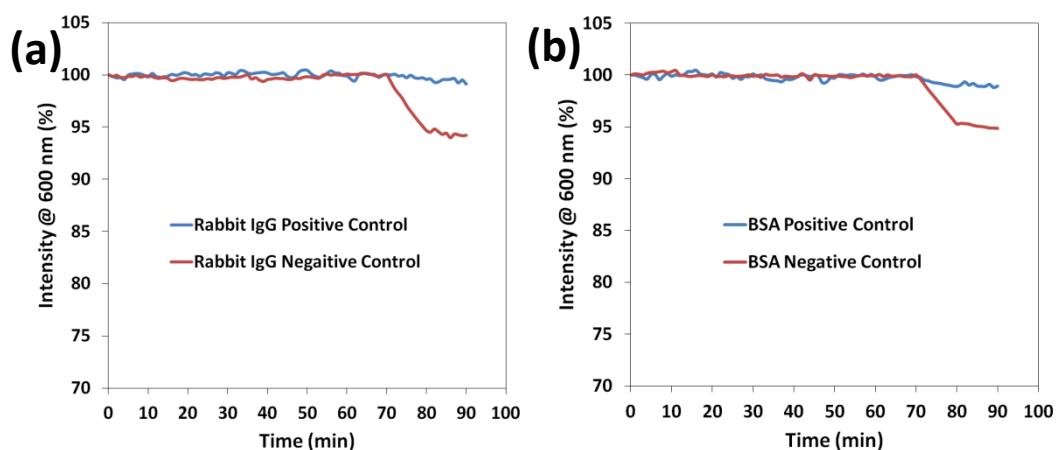


Figure 4.18: Sensorgrams representing cross-reactivity to alternate biomarkers on the alkaline phosphatase - BCIP/NBT based human IgG pSi immunosensor. (a) Positive and negative cross-reactivity controls using Rabbit IgG. (b) Positive and negative cross-reactivity controls using BSA. Note: the negative control for both species was spiked with 25 ng/mL human IgG.

Analyte	(+) Cross-Reactivity	(-) Cross-Reactivity
Rabbit IgG	0.167 %	0.877 %
BSA	0.169 %	0.763 %

Table 4.5: Cross-Reactivity of the alkaline phosphatase - BCIP/NBT based human IgG pSi immunosensor to biomolecules from other animal species.

#### **4.4.6 Surface Characterisation Following Immunosensing**

##### *4.4.6.1 SEM Analysis Following the Detection Event*

The effect of BCIP/NBT precipitation on pSi was investigated using SEM. Upon completion of the immunosensing experiments, a pSi sample exposed to 1000 ng/mL human IgG was rinsed with water and prepared for SEM. A control pSi sample exposed to 0 ng/mL human IgG was also prepared in the same manner. During the preparation it was noted that the active sample had formed a coloured ‘film’ over the surface where the substrate had precipitated. The active pSi sample experienced a slight change in colour from a dark grey to a blue/violet hue, which was more pronounced where the inlet to the flow cell terminated, Figure 4.19 (g). This effect was not apparent on the control pSi. Figure 4.19 displays micrographs of the pSi samples from the top-down and cross sectional perspectives. Figure 4.19 (d), (e) & (f) correspond to the active immunosensor surface, while Figure 4.19 (a), (b) & (c) correspond to the control surface. The cross sectional perspective, Figure 4.19 (d) & (a) depicted empty pores on both the active and control samples indicating that the precipitated compound was either too small to visualise with the microscope or was removed during the cracking of the sample during the preparation procedure. The magnified top down micrographs shown in Figures 6.19 (b) & (e) also showed no discernible change to the standard structure of the active and control surfaces. However, when the surface is analysed with less magnification a clear difference between the active and the control surfaces became apparent. Imaging the pSi region situated directly under the flow cell inlet it can be seen that the active surface displays a darkened circle approximately double the size of the inlet aperture (1 mm), while the control surface displayed no discernible change.

EDAX analysis of the active surface revealed the presence of a carbon signal indicative of organic material, Figure 4.19 (h). The low counts for sodium, magnesium, potassium, calcium and chlorine imply that very little of the buffer salts remain to contribute to the signal. The low phosphorous levels also indicate that the phosphate group cleaved from BCIP during the catalysation reaction has also been removed from the system due to the high solubility of the resulting sodium phosphate salt [197].

The specificity of this effect combined with the colour change and permanent marking of the surface could be important. Using this technique, a basic qualitative sensor could be fabricated relying on a colour change to the pSi surface to diagnose the presence of an analyte. Further investigation may also be able to achieve quantitative detection similar to paper ELISA based on this method.

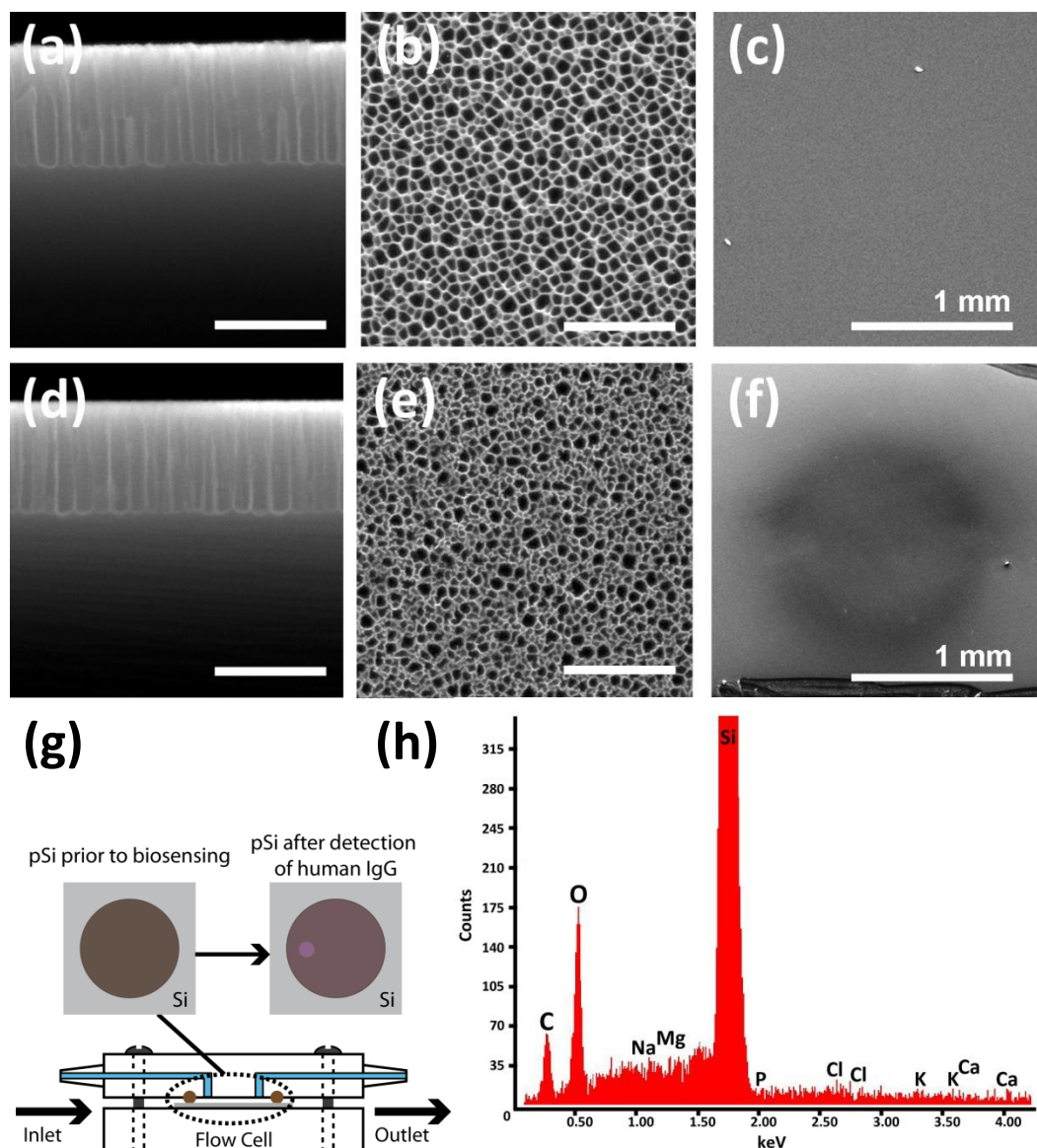


Figure 4.19: Cross-sectional and top down SEM images of pSi following a human IgG immunosensor experiment. (a), (b) & (c) Control pSi surface exposed to 0 ng/mL human IgG (scale bar = 1  $\mu$ m unless otherwise identified). (d), (e) & (f) Active pSi surface exposed to 1000 ng/mL human IgG. (g) Schematic of the flow cell configuration and the location of the strong colour change on active pSi. (h) EDAX analysis of the active pSi surface in (f).

#### *4.4.6.2 IR Spectroscopy Analysis of the Immunosensor Detection Event*

IR spectroscopy and microscopy were used to characterise the alkaline phosphatase catalysed precipitation of BCIP/NBT within pSi to demonstrate precipitation occurs exclusively in the presence of a complete immunoassay complex. Figure 4.20 displays a series of conventional IR spectra and a IR microscopy graph for an immunoassay patterned surface, along with a schematic indicating the relevant surface chemistry. pSi functionalised with sheep  $\alpha$ -human IgG capture antibody was masked, exposed to a solution containing 500 ng/mL human IgG, unmasked and the newly patterned surface exposed to alkaline phosphatase labelled secondary antibody using the procedure outlined in Chapter 4 section 4.3.9. This technique created a patterned pSi surface that contained an assembled human IgG immunoassay on one side and capture Ab functionalised pSi on the remaining side, Figure 4.20 (d).

Figure 4.20 (a) contains IR spectra of capture Ab functionalised pSi prior to masking and the masked and unmasked regions of the pSi surface after exposure to the immunoassay and BCIP/NBT solution. Figure 4.20 (b) provides an enlarged portion of the Figure 4.20 (a) spectra to assist in peak identification, while Figure 4.1 contains a reaction schematic for the de-phosphorylation and precipitation of BCIP/NBT. Covalently immobilised capture antibody displayed peaks indicative of a urea linkage in the region of  $1100 - 1700 \text{ cm}^{-1}$ . Peaks at  $1628 \text{ cm}^{-1}$  (C=O stretching),  $1558 \text{ cm}^{-1}$  (N-H deformation),  $1150 \text{ cm}^{-1}$  (N-C-N symmetrical) and  $1342 \text{ cm}^{-1}$  (N-C-N antisymmetrical stretching) all indicate that the antibody may be bound to the surface [173-175]. However as discussed in Chapter 4 section 4.4.1.2, many of these peaks overlap with peaks found within IR spectra of isocyanate silane functionalised pSi, preventing definitive proof that the antibody was immobilised (Figure 4.6).

To determine if the capture antibody was present, masking and surface patterning was employed. The chemistry of the unmasked pSi was altered upon exposure to the immunoassay and BCIP/NBT solutions. The IR spectrum in Figure 4.20 (a) & (b) corresponding to the unmasked pSi displayed new peaks in the region of  $1300 - 1700 \text{ cm}^{-1}$ . The peak at  $1320 \text{ cm}^{-1}$  denotes the presence of Aryl C-N stretching vibrations present in both the BCIP dehydroindigo dimer product and NBT Diformazan product [198]. The shape of the peak at  $1442 \text{ cm}^{-1}$  has altered

with respect to the capture Ab spectrum and the intensity increased indicating the presence of tetra-substituted aromatic ring stretching in the BCIP product and Azo (-N=N-) stretching in the NBT Diformazan product [199]. Aromatic ring stretching vibrations corresponding to the BCIP product are also evident at 1590  $\text{cm}^{-1}$  where a small side peak appears. Halogen C-Cl stretching within the BCIP product occurs at 771  $\text{cm}^{-1}$  where the peak broadens and intensifies with respect to the capture Ab spectrum [200]. A small ketone (-C-CO-C-) stretching vibrational peak also appeared at 1724  $\text{cm}^{-1}$  originating from the BCIP product. Another small vibrational peak corresponding to antisymmetrical stretching of the nitro group (C-NO<sub>2</sub>) within the NBT product appeared at 1551  $\text{cm}^{-1}$ . There is also a cyclic alkene (C=C) stretching vibration from both the BCIP and NBT products that occurs at 1660  $\text{cm}^{-1}$ . The final IR spectrum displayed in Figure 4.20 (a) & (b) corresponds to the masked pSi region. Comparison of this spectrum against the original capture Ab spectrum identified no change in the chemistry of the pSi surface. The same peaks were present and no shifts were detected.

The detection of peaks associated with the catalysed BCIP and NBT compounds within the unmasked region of pSi confirms the presence of alkaline phosphatase and the successful formation of a human IgG immunoassay on pSi. The lack of a new chemical signature within the masked region indicated that no immunoassay was formed and the surface chemistry remained unaltered upon exposure to the BCIP/NBT solution. This result demonstrates that the capture Ab immobilisation technique was successful and that catalysation and precipitation is specific to the presence of the target analyte.

A three dimensional IR intensity map is displayed in Figure 4.20 (c) of a 10.5  $\mu\text{m}^2$  area of the patterned interface between the masked and unmasked region (see Figure 4.20 (d) for a schematic of the patterned pSi). The IR map shows the correlation intensity of all IR spectra collected within the patterned area, to that of a typical BCIP/NBT vibrational peak located at 1320  $\text{cm}^{-1}$ . It can be seen that the highest peak intensity occurs on the unmasked side of the patterned surface, where alkaline phosphatase was present and precipitation occurred. IR spectra from the masked region shows little to no correlation to the BCIP/NBT peak indicating that the enzyme substrate was not precipitated in the absence of a completed immunoassay. The interface between the masked and unmasked

region is not sharp and displays a gradual decrease in intensity with regards to distance. This could be due to ineffective masking at the interface or diffusion of the biocatalysed products close to the interface. Regardless, this result indicates that the immobilisation of the capture Ab was successful and that BCIP/NBT is only precipitated in the presence of a completed human IgG immunoassay. This result also indicates that the precipitation of BCIP/NBT is closely confined to the region containing alkaline phosphatase, which may be useful if developing a pSi sensor array.

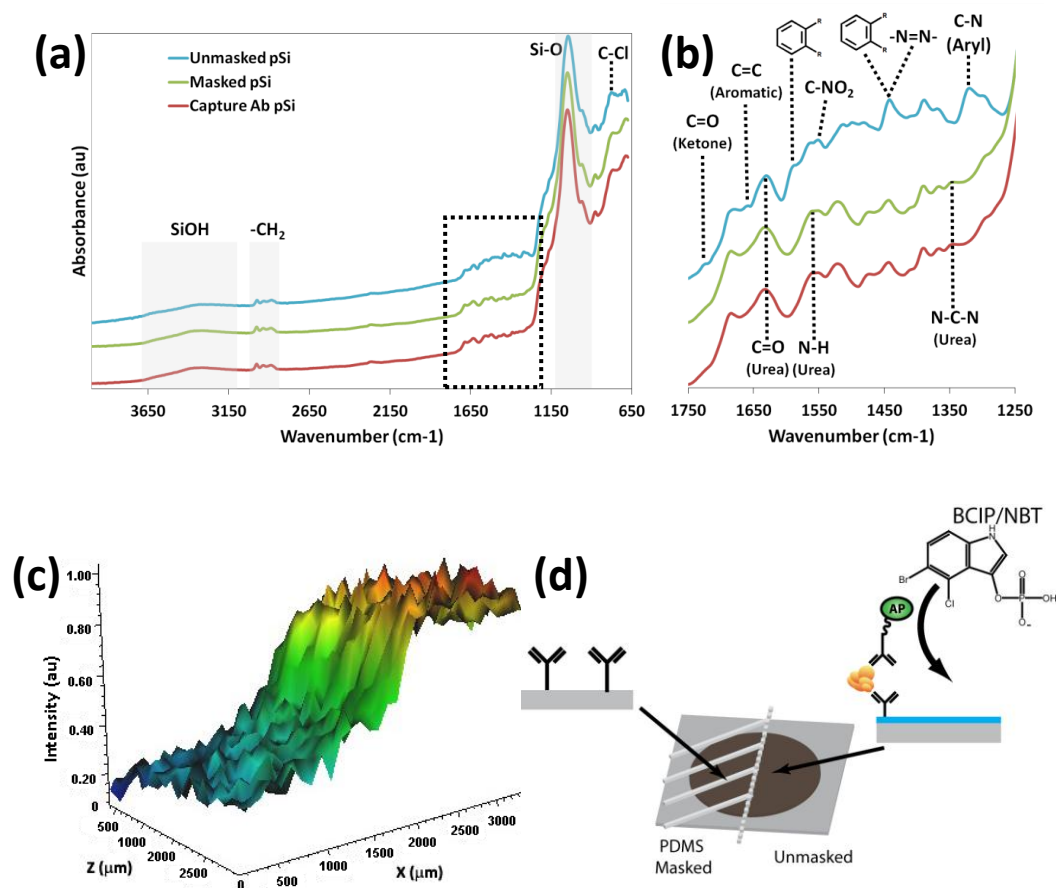


Figure 4.20: IR characterisation of pSi surfaces following a human IgG immunosensor experiment. (a) IR spectra displaying covalently immobilised capture antibody pSi prior to immunosensing, and masked and unmasked patterned pSi following a immunosensor experiment. (b) An expanded section of the IR spectra displaying labelled stretching vibrations of precipitated BCIP/NBT more clearly. (c) IR correlation intensity map of IR spectra matching that of the catalysed BCIP/NBT peak at 1320 cm<sup>-1</sup>. (d) Schematic of the patterned pSi and the resulting immunoassay configuration following the immunosensor experiment. The IR map was obtained from the interface between the PDMS masked and unmasked regions.

#### **4.5 Conclusions and Future Directions**

This work has demonstrated the development of a new pSi optical immunosensor based on the intensity of an IRS Fabry-Perot fringe pattern. pSi was etched to contain large pores with a shallow depth and the surface chemistry modified to permit the incorporation of a new signal transduction pathway resulting in precipitation of an organic compound. Using the technique of IRS, alkaline phosphatase catalysed de-phosphorylation of BCIP resulting in subsequent precipitation of BCIP/NBT within the porous matrix, producing an optical signal in the form of a decrease to the reflected intensity of the Fabry-Perot interference fringe pattern within the region of 600 nm. Monitoring the intensity at 600 nm formed the basis of the immunosensor's readout signal. The immunosensor's detection event consisted of a rapid decrease in intensity upon reaction of the BCIP/NBT substrate with alkaline phosphatase.

The alkaline phosphatase – BCIP/NBT system was incorporated into pSi architecture previously characterised in Chapter 3 and utilised for the detection of human IgG. Optimisation of the substrate formulation was achieved by combining NBT with BCIP to achieve enhanced amplification, while stabilisation of the porous layer was demonstrated via thermal oxidation. Furthermore, investigation of the signal processing and wavelength choice improved the signal strength of the immunosensor compared to other methods such as EOT and wavelength shift. Precipitation of BCIP/NBT within the porous silicon matrix enhanced the immunosensor signal 3.4-fold compared to precipitation on bulk silicon demonstrating the benefits of the material's large surface area. Combining these design features improved the performance of the platform, forming a highly sensitive and stable immunosensor. The immunosensor was used to detect human IgG from a solution of IntraGAM (a mixture of human IgG, IgM and IgA antibodies) with a LOD of 2.14 ng/mL. This sensor was also demonstrated to be specific to the human IgG analyte and achieve acceptable intra sample precision. The response time of the sensor was improved compared to previously reported enzyme based pSi optical immunosensors and is shown to be three-fold faster than the industry standard ELISA. Adaptation of this platform into an array has potential for high through-put, rapid screening of multiple analytes. All of these factors combined with competitive sensitivity highlight this pSi sensor as a potential alternative to traditional commercial techniques such as ELISA.

Future experiments with other biomolecules are required to fully evaluate specificity and additional data is required for a complete precision analysis. The depth of the porous layer should also be optimised to assess if smaller concentrations of human IgG are detectable.

It will be important to assess the viability of the immunosensor for the quantitative analysis of clinical samples. Also of high importance is to investigate the versatility of the immunosensor by incorporating alternative receptor molecules, such as DNA or aptamers and/or immunoassays for the detection of other relevant proteins and biomarkers, such as human IgG antibodies specific to HIV, Sjogren's syndrome or Hepatitis.

# Chapter 5

---

## 5 S-layer Fusion Protein as a Promoter for pSi Immunosensors

## **5.1 Abstract**

The work in this chapter focuses on the formation of an S-layer protein based IgG affinity layer within pSi for the immobilisation of capture antibodies. Expression and isolation of both native and genetically modified fusion S-layer proteins from bacteria were achieved. In vitro self-assembly of the purified native SbpA protein and the IgG binding recombinant rSbpA<sub>31-1068</sub>/ZZ fusion protein was demonstrated by the formation of crystalline protein layers on various planar silicon surface chemistries. IgG binding capacity was shown on rSbpA<sub>31-1068</sub>/ZZ coated ELISA microtiter plates via the immobilisation of capture IgG antibodies and detection of human IgG and human Interleukin-6 analytes.

Recrystallisation of the S-layer fusion protein, rSbpA<sub>31-1068</sub>/ZZ, on pSi was achieved to provide defined IgG binding locations within the porous matrix. Immobilisation of IgG capture antibodies to the S-layer coating allowed the detection of human IgG and the formation of a standard curve. Integration of the rSbpA<sub>31-1068</sub>/ZZ affinity coating within pSi resulted in a general improvement in sensor performance compared to covalent attachment of capture antibodies.

## 5.2 Introduction

As discussed in Chapter 1 section 1.2, the development of sensitive silicon and pSi based sensors is an area of extensive research and many new and exciting advances have recently been made. One of the key steps in designing any form of biosensor is the integration of a biorecognition element with a signal transducer. Many common biosensing and/or immunosensing techniques such as ELISA, SPR and pSi sensors adsorb or covalently immobilise receptor molecules onto the solid phase surface to create stable coatings. Such immobilisation approaches may not result in maximum affinity of the receptors due to the random orientation and steric hindrance of the receptor on the solid phase (Figure 5.1) [129]. It has also been identified that protein based receptors can experience partial denaturation upon interaction with the surface, further reducing binding activity [201]. Therefore a method for the oriented immobilisation of receptors is highly desirable.

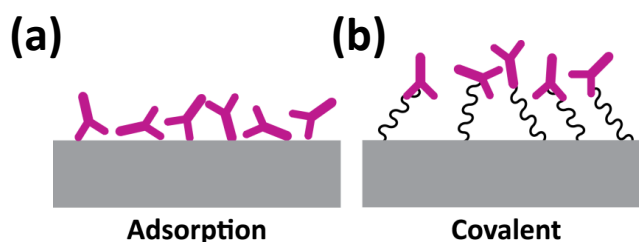


Figure 5.1: Schematic of common receptor immobilisation techniques on biosensing platforms. Binding bio-receptors via (a) adsorption and (b) covalent approaches can lead to the miss-alignment and steric hindrance of molecules such as capture antibodies.

One approach aimed at solving this problem utilises S-layer proteins from common strains of bacteria. As discussed in Chapter 1 section 1.3, S-layer proteins have been demonstrated to self-assemble in vitro on silicon into large crystalline lattices with long range order. Genetic modification of the S-layer protein, SbpA, from *Lysinibacillus sphaericus* has also yielded a fusion protein which combined a S-layer monomeric protein sub-unit with two Z binding domains to form the chimaeric protein rSbpA<sub>31-1068</sub>/ZZ (SbpA-ZZ) [148]. This fusion protein retained the self-assembly properties and order of the native S-

layer protein, while providing periodic binding sites for IgG antibodies at the nanometer scale. The original development of this protein was aimed at purification of IgG from blood samples for autoimmune disease treatment, however since this initial study the SbpA-ZZ fusion protein has been underutilised and has yet to be adapted to new applications. The real benefit of this fusion protein lies in its clever design. As detailed in Chapter 1 section 1.3.5.1, the Z domain is a synthetic analogue of the IgG-binding domain of Protein A from *Staphylococcus aureus* and is capable of binding the Fc chain of all IgG's. Genetic engineering has situated the Fc binding Z-domain at an exposed position on recrystallised S-layer and bound antibodies are aligned such that their antigen binding sites face away from the surface (Figure 5.2). Therefore recrystallisation of SbpA-ZZ or other modified S-layer proteins on solid supports could greatly improve sensor fabrication processes through the oriented immobilisation of proteins and other biomolecules [201]. This would subsequently have a positive impact on the sensitivity of sensing platforms through reduction in receptor inhibition. This approach has vast application potential in a range of sensing and diagnosis fields, particularly as scaffolding in immunosensing devices.

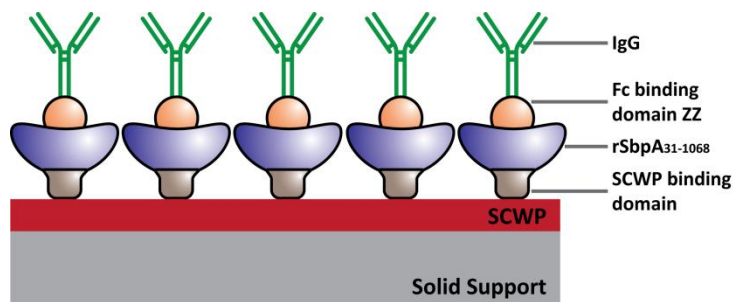


Figure 5.2: Schematic of the genetically modified SbpA-ZZ fusion protein. The N-terminal contains a binding domain for the SCWP while the C-terminal has been modified to contain two Z domains capable of binding the Fc chain of IgG antibodies. The protein architecture aligns the IgG such that the antibodies active sites point away from the solid support. Adapted from [119].

Integration of the SbpA-ZZ S-layer fusion protein into a pSi immunosensor was the main objective of this chapter. Extraction of the native SbpA S-layer protein was achieved and the recrystallisation method, including surface chemistry, was optimised. Successful cloning and expression of the chimaeric S-layer protein was achieved in *Escherichia coli* and the SbpA-ZZ fusion protein was then successfully extracted and recrystallised on different surface chemistries and materials. Recrystallised native and fusion protein were imaged using AFM in a liquid medium and the binding of IgG to the Z domain of SbpA-ZZ was demonstrated in the framework of an ELISA assay. Preliminary sensitivity tests were also conducted using ELISA. Recrystallisation of SbpA-ZZ within a pSi matrix as a self-assembled receptor coating was then examined and assessment of immunosensing on SbpA-ZZ coated pSi was performed using IRS and the human IgG detection system developed in Chapter 4.

## **5.3 Experimental Method**

### **5.3.1 Cell Culture - *Lysinibacillus sphaericus* ATCC 4525**

Culture and expression of the SbpA S-layer protein was achieved via the procedure outlined in [202-205] with some minor changes. 10  $\mu$ L of *L. sphaericus* ATCC 4525 bacterial stock in glycerol was streaked on a nutrient broth (NB) agar plate and incubated for 24 hrs at 30°C. Isolated colonies were selected and transferred to a 1 L conical flask containing NB media (500 mL). This formed the basis of the pre-culture and was incubated for 18 hrs at 30°C and 180 rpm. Once the optical density at 600 nm ( $OD_{600\text{ nm}}$ ) of the culture had reached 0.8 a.u. (Fluostar Omega) it was removed from the incubator. 100 mL of the pre-culture was added to a 2 L flask and the volume made up to 1 L. This was repeated 5 times to achieve a total volume of 5 L. This culture was then incubated for 20 hrs at 30°C and 180 rpm. Once the OD had reached 0.8 a.u. the culture was decanted into 50 mL centrifuge tubes and centrifuged at 4500 rpm for 15 min at 4°C (Sigma 4-16K). The supernatant was discarded and the bacteria pellets resuspended in 50 mL of 50 mM Tris/HCl buffer, pH 7.2 (Buffer A). The individual pellets were recombined and again centrifuged at 4500 rpm for 15 min at 4°C. The supernatant was again discarded and the bacteria pellet re-suspended in 20 mL Buffer A. The bacteria suspension could then be used immediately or stored at -20°C for later use.

### **5.3.2 Extraction and Purification of Native S-layer Protein SbpA**

Isolation of the S-layer protein followed the procedure described in [202, 205] with minor changes. Cell lysis of the *L. sphaericus* bacterial suspension prepared in Chapter 5 section 5.3.1 was achieved via application of high pressure, 30 kpsi, within a French pressure cell press (Constant Systems TS 0.75) to break the cell wall. Separation of the cell wall fragments was achieved via centrifugation at 16,000 g in a Sorvall Superspeed centrifuge for 15 minutes at 4°C. The supernatant was removed and the pellet re-suspended in 10 mL of Tris/HCl 50 mM, pH 7.2, Triton X-100 0.75% (v/v) (Buffer B). This washing step was performed a further 2 times. Purification of the cell wall fragments continued with the suspension being centrifuged at 28,000 g for 10 minutes at 4°C and resuspended in 10 mL of Buffer B. This washing process was repeated a further

2 times to remove unwanted cell components. The S-layer protein could then be extracted from the cell wall fragments by re-suspension of the cell wall pellet in Buffer C (containing 5 M of the chaotropic agent, guanidine hydrochloride (GnHCl)) for 30 minutes at 25°C on a shaking table. Disrupted S-layer protein was isolated via centrifugation at 100,000 g in an Optima L-100 Ultra Beckman Coulter centrifuge for 30 minutes at 4°C. The pellet was discarded and the supernatant was dialysed against 5 L of deionised water using dialysis tubing with a molecular cut off of 4000 – 6000 Da to remove the disrupting agent GnHCl. The water was regularly replaced each hour for 9 hours to ensure complete removal. The dialysed sample was again centrifuged at 100,000 g for 30 minutes at 4°C to end the purification process. The pellet was discarded and the clear supernatant containing purified disassembled S-layer protein subunits was concentrated via centrifugation at 4500 rpm through a 50 kDa cut-off membrane filter (Vivaspin 20, GE) and then adjusted to 1 mg/mL by addition of milliQ water and stored at 4°C for later use.

### **5.3.3 Genetic Modification of S-layer Protein**

Cloning and expression of the pBluescript SbpA<sub>31-1068</sub>/ZZ chimeric gene encoding the S-layer fusion protein rSbpA<sub>31-1068</sub>/ZZ in *E. coli* BL21DE3 bacteria were performed by Dr Charlotte Lelan as described by Vollenkle *et al.* [148].

### **5.3.4 E. Coli Cell Culture and Expression of rSbpA<sub>31-1068</sub>/ZZ**

10 µL of *E. coli* BL21DE3 stock containing pBluescript SbpA<sub>31-1068</sub>/ZZ in glycerol solution was streaked on a lysogeny broth (LB) agar plate and incubated for 24 hrs at 37°C. Isolated colonies were selected and transferred to a 500 mL conical flask containing LB media (200 mL). Selection of transformants harbouring pBluescript was achieved via the addition of ampicillin to the media to a final concentration of 100 µg/mL per flask. This formed the basis of the pre-culture and was incubated for 18 hrs at 37°C and 120 rpm. Once the OD<sub>600 nm</sub> of the culture had reached 2 a.u. it was removed from the incubator. 20 mL of the pre-culture was added to a 500 mL flask containing 200 mL of LB media with 100 µg/mL ampicillin. This was repeated 10 times to achieve a total volume of 2 L. This culture was then incubated at 37°C and 180 rpm. The OD<sub>600 nm</sub> was

monitored every hour and upon reaching 0.4 a.u., expression of the SbpA<sub>31-1068</sub>/ZZ gene was induced by the addition of IPTG to a final concentration of 1 mM. The induced culture was then incubated for 18 hrs at 37°C and 180 rpm. When the OD<sub>600 nm</sub> reached 2 a.u. the culture was decanted into 50 mL centrifuge tubes and centrifuged at 4500 rpm for 15 min at 4°C (Sigma 4-16K). The supernatant was discarded and the bacteria pellets resuspended in 50 mL of Buffer A. The individual pellets were recombined and again centrifuged at 4500 rpm for 15 min. The supernatant was again discarded and the bacteria pellet resuspended in Buffer A to a final volume of 50 mL. The bacteria suspension could then be used immediately or stored at -20°C for later use.

### **5.3.5 Extraction and Purification of rSbpA<sub>31-1068</sub>/ZZ S-layer Fusion Protein**

Cell lysis of the *E. coli* bacterial suspension prepared in Chapter 5 section 5.3.4 was achieved via application of high pressure, 30 kpsi, within a French pressure cell press (Constant Systems TS 0.75) to break the cell wall. Separation of the cell wall fragments was achieved via centrifugation at 16,000 g in a Sorvall Superspeed centrifuge for 15 minutes at 4°C. The supernatant was removed for further treatment and the pellet discarded. The supernatant was then added to a 50 mL centrifuge tube containing 3 mL of IgG Sepharose 6 Fast Flow microbeads (binding capacity 2 mg Protein A/mL) and incubated at 4°C for 1 hour on an orbital shaker (flow through 1). The IgG microbeads were then separated from the supernatant via centrifugation at 4000 rpm at 4°C. The reacted microbeads were placed into a column to act as an affinity matrix and the supernatant passed through the column to ensure maximum protein extraction (flow through 2). The beads were then washed by passing 10 mL of 50 mM Tris buffer, pH 7.6, 150 mM NaCl and 0.05% Tween 20 (TST buffer) through the column (wash 1). The IgG matrix was washed a second time with 3 mL of 5 mM Ammonium Acetate buffer (NH<sub>4</sub>Ac), pH 5 (wash 2). Elution of the bound SbpA-ZZ protein was achieved by lowering the pH and washing the IgG matrix a third time with 0.5 M Acetic Acid buffer (HAc), pH 3.4 (elutant). The pH of the fraction containing the eluted fusion protein was altered to 7.4 via addition of NaOH to stabilise the protein. The fraction containing the eluted protein was then dialysed against 5 litres of deionised water using dialysis tubing with a molecular cut off of 4000 –

6000 Da to remove the acid and salts. The water was regularly replaced each hour for 6 hours to ensure complete removal. The concentration of the dialysed sample containing the purified disassembled rSbpA<sub>31-1068</sub>/ZZ S-layer protein subunits was concentrated via centrifugation at 4,500 rpm through a 50 kDa cut-off membrane filter (Vivaspin 20, GE Healthcare) and then adjusted to 1 mg/mL by addition of milliQ water and stored at 4°C for later use.

### *5.3.5.1 Gel Electrophoresis*

#### *5.3.5.1.1 SDS-Polyacrylamide Gel Electrophoresis (SDS-PAGE)*

Expression and purification of the native and fusion S-layer proteins was monitored using gel electrophoresis. Separation and analysis was performed on polyacrylamide gel in the presence of SDS (SDS-PAGE). Protein gels consisted of a 4% stacking gel and a 12% running gel. Gels were prepared by pouring the gel solution into the assembled glass protein gel chamber and covering with ethanol. Once the gel was set, ~25 minutes, the ethanol was decanted and the stacking gel solution was poured into the chamber on top of the polymerised running gel. A comb was inserted into the liquid gel to form wells and the gel was left for a further 25 minutes to polymerise. The procedure was performed in duplicate to create two sets of gels. The assembled gels were placed into a Mini-PROTEAN Tetra Cell vertical electrophoresis system (Bio-Rad Laboratories Inc.) and filled with 1x Running buffer. Samples were taken from each of the major culture steps for analysis. 1 mL samples were sourced from plated colonies, pre-culture, culture prior to induction, culture after induction and the final bacterial pellet. 1 mL samples were also taken from each of the major purification steps including cell lysis, various pellets and supernatant samples and the final dialysed protein product. Sample preparation involved the mixing of 4 µL of milliQ water, 4 µL of the sample and 7 µL of Lug buffer for pellets and 7 µL of the sample with 7 µL of Lug buffer for supernatant samples. These solutions were then heated at 60°C for 10 minutes. 15 µL of each sample was added to the gel along with 8 µL of the protein marker (Precision Plus Protein Dual Colour Standards #161-0374, Bio-Rad Laboratories Inc.). SDS-PAGE was then performed at 140 V and the progress of the protein front monitored. Completed gels were removed from the apparatus, immersed in Coomassie blue staining

solution and heated in a microwave until the solution began bubbling. The gel was removed and washed with milliQ water, immersed in destaining solution and heated as before. The gel was again removed and washed with milliQ water, then immersed in milliQ water and heated as before. The heated solution was agitated on an orbital shaker for 10 minutes in the presence of absorbent paper towel to ensure a sufficient signal contrast.

#### **5.3.5.2 Protein Concentration Assay**

Protein concentration was determined using a Lowry assay. Bio-Rad Dc Protein Assay was conducted according to the manufacturer's instructions. Different concentrations of BSA were used for the preparation of the standard curve. Measurements were performed on a Fluostar Omega spectrometer at 595 nm.

#### **5.3.6 Growth Measurements**

Growth characteristics of *L. sphaericus* cells and *E. coli* cells expressing S-layer proteins were determined by measuring the optical density in 96-well plates on a Fluostar Omega spectrometer (BMG Labtech). Samples were taken at various stages throughout the pre-culture and culture procedures and the optical density measured at 600 nm (OD<sub>600 nm</sub>). Measurements were conducted on wells containing cell culture samples diluted at a ratio of 1/10 with the respective cell culture medium to achieve a total volume of 250 uL. All measurements were blanked against the respective cell culture medium.

#### **5.3.7 Solid Substrate Preparation**

##### **5.3.7.1 Flat Silicon Substrate**

###### **5.3.7.1.1 Cleaning and Ozone Treatment**

P<sup>++</sup> silicon wafers were cut into pieces ~0.5 cm<sup>2</sup> in size with a diamond cutter. Each piece was rinsed with ethanol, acetone and DCM and dried under a stream of nitrogen. The silicon pieces were then pre-cleaned with piranha solution containing 3:1 sulphuric acid:hydrogen peroxide to remove any organic residue. Silicon pieces were rinsed with milliQ water, immersed in piranha solution and incubated for 10 minutes at room temperature before removing and rinsing with milliQ water and drying under nitrogen. The native silicon oxide layer was

stripped by immersing the pieces in a solution of 1:50 HF to H<sub>2</sub>O for 1 minute. The samples were then rinsed with milliQ water, dried under a stream of nitrogen and placed into a glass desiccator containing a steady flow of ozone gas at a rate of 3.2 g/hr for 30 minutes. The samples were then removed from the desiccator and underwent mild thermal oxidation at 400°C for 10 minutes in ambient conditions (to mimic previous pSi functionalisation, Chapter 4). The modified samples were used immediately, either for further functionalisation (ozone treatment only) or for protein self-assembly studies.

#### 5.3.7.1.2 Thermal Oxidation

Sample preparation and cleaning was performed as described in Chapter 5 section 5.3.7.1.1. However instead of ozone treatment, silicon pieces underwent thermal oxidation in a tube furnace for 1 hour at 400 °C in an ambient atmosphere. The modified samples were then used immediately for protein self-assembly studies.

#### 5.3.7.1.3 Silicon Substrate Silanisation (Alkoxy Silanes)

Freshly oxidised silicon samples prepared in Chapter 5 section 5.3.7.1.1 were silanised according to the procedure described in Chapter 2 section 2.2.2.3 with minor changes. Silanisation involved immersing oxidised silicon pieces in a 10 mL, 50 mM silane solution in anhydrous toluene. The reaction mixture was incubated for 10 minutes at room temperature while shaking. Silicon pieces were removed, washed with anhydrous toluene and dried under a stream of nitrogen, ready for immediate use.

#### 5.3.7.1.4 Silicon Substrate Silanisation (Chloro Silanes)

Freshly oxidised silicon samples prepared in Chapter 5 section 5.3.7.1.1 were covered with a droplet of ~50 µL of neat chloro silane. Surfaces were placed into an oven and incubated for 2 hours at 80°C before being removed and rinsed with toluene, acetone and ethanol and dried under a stream of nitrogen.

#### 5.3.7.1.5 Polyelectrolyte Polymerisation

Adsorption of the polyelectrolyte poly(styrene sulfonate) (PSS) on thermally oxidised flat silicon was accomplished by incubation of silicon pieces in 0.5 mM Potassium Phosphate buffer, pH 5.0, containing 10 mM PSS for 30 minutes at ambient conditions. The coated silicon was then rinsed with buffer and stored in recrystallisation solution (Chapter 5 section 5.3.9) until ready for use.

#### **5.3.7.2 Polystyrene Substrate**

The flat bottom of wells from a Costar 9017 Medium binding 96-well microtiter plate (Corning) were cut from the plate using a hacksaw to provide a native polystyrene surface. After cleaving, the flat supports were rinsed thoroughly with milliQ water and dried under a stream of nitrogen.

#### **5.3.8 Static Contact Angle Analysis**

The surface wettability of modified silicon and native polystyrene surfaces was investigated via sessile drop water contact angle analysis. Contact angle measurements were performed under ambient conditions on a custom built sessile drop apparatus with an Olympus SZ-PT microscope and lens system coupled to a Sony CCD camera. 1  $\mu$ L drops of milliQ water were dispensed on three separate locations on each surface. Angle measurements were taken on both sides of the droplet 40 – 60 seconds after drops were applied to the surface using ImageJ software v 1.46r. Contact angle data reports the average of three drops at difference surface locations.

#### **5.3.9 In vitro Recrystallisation of S-layers on Solid Supports**

The composition of the standard recrystallisation solution (0.1 mg/mL S-layer protein in 0.5 mM Tris-HCl buffer, pH 9, 10 mM CaCl<sub>2</sub>) was prepared using the following method. 100 mM Tris-HCl stock buffer, pH 9.0, was diluted and combined with freshly prepared 11 mM CaCl<sub>2</sub> in milliQ water immediately before use. S-layer stock solution was then diluted by a ratio of 1:10 into this recrystallisation buffer to achieve the working concentration described above. The S-layer recrystallisation solution was then immediately filtered through a 0.22  $\mu$ m nylon syringe filter into a 1.5 mL plastic Eppendorf centrifuge tube to remove any undesired protein aggregates or particulate contaminants. The solid supports used as a platform for S-layer recrystallisation were placed on the inside of the lid with the polished silicon or polystyrene surface facing away from the lid. The tube was then inverted to immerse the support in the S-layer recrystallisation solution and incubated for 18 hours at room temperature. The samples were then removed and imaged via liquid AFM.

### **5.3.10 Atomic Force Microscopy**

Surface morphology was analysed using a Digital Instruments Nanoscope IV with an E-scanner. Standard silicon nitride cantilevers (NP-10, Bruker) with a nominal spring constant of 0.06 N/m were used for imaging. Scanning was carried out in contact mode under fluid with a liquid cell. Solid samples containing recrystallised S-layer were removed from the recrystallisation solution, rinsed with milliQ water and a drop (approximately 50  $\mu$ L) of fresh recrystallisation buffer was pipetted on the S-layer coated solid support before the cell was assembled. The self-assembled lattice structures of native and fusion S-layer proteins were imaged by AFM and the applied force was kept low during scanning to prevent the tip from deforming the sample surface. The scan rate used in this chapter ranged from 0.5 - 6 Hz. Images were plane fitted and dimensions were measured using Nanoscope Analysis v1.20 (Veeco Corporation) or WSxM 5.0 (Nanotech Electronica S.L.)

### **5.3.11 S-layer Based ELISA**

#### **5.3.11.1 ELISA Plate Functionalisation**

Recrystallisation of S-layer proteins within a 96-well ELISA plate was conducted using a similar method to that outlined in Chapter 5 section 5.3.9. 150  $\mu$ L of the recrystallisation solution containing SbpA-ZZ was added to appropriate wells to form a receptor matrix, while 150  $\mu$ L of native SbpA was added to appropriate wells to act as a control. The plate was covered with parafilm and incubated with the recrystallisation solution for 18 hours at room temperature. The wells were then rinsed 5 times with 250  $\mu$ L/well recrystallisation buffer to remove free protein before receiving a final rinse with 250  $\mu$ L/well milliQ water. In the case of Human Interleukin-6 experiments, the wells were blocked with 200  $\mu$ L/well Human IL-6 ELISA Ready-SET-Go! (eBioscience) 1x assay diluent reagent for 1 hour at room temperature. The wells were aspirated and washed five times with 250  $\mu$ L/well Human IL-6 ELISA Ready-SET-Go! wash buffer. Finally 200  $\mu$ L/well of Human IL-6 ELISA Ready-SET-Go! Coating buffer was introduced ready for the ELISA protocol (refer to Chapter 5 section 5.3.11.2). In the case of Human IgG experiments, wells containing recrystallised S-layer protein were

blocked with 200  $\mu\text{L}$ /well 50  $\mu\text{g}/\text{mL}$  BSA in PBS, pH 7.4 for 1 hour at room temperature. The wells were aspirated and washed four times with 250  $\mu\text{L}$ /well of PBS-T. Finally 200  $\mu\text{L}$ /well of PBS was introduced to the wells, ready for the ELISA protocol.

### *5.3.11.2 ELISA Protocol*

#### *5.3.11.2.1 Human IgG Binding Affinity Assay – Z Domain Accessibility Test*

Four columns of a 96-well polystyrene plate were coated with SbpA-ZZ and another four with SbpA S-layer protein as per Chapter 5 section 5.3.11.1. 2  $\mu\text{g}/\text{mL}$  sheep anti-human IgG capture antibody (Millipore, AB7112) in PBS, pH 7.4, was added to all wells (100  $\mu\text{L}$ /well) and the plate then covered with parafilm to prevent evaporation and incubated at 4°C for 12 h. The plate was washed three times with PBS-T (250  $\mu\text{L}$  /well) before being blocked with 2.5% (w/v) BSA in PBS (250  $\mu\text{L}$ /well) and incubated at 37°C for 1 hour. The plate was washed as before with PBS-T. 250 ng/mL Human IgG in PBS immunosensing buffer was added to half of the SbpA-ZZ and SbpA treated wells, while the remaining wells received 0 ng/mL (PBS immunosensing buffer only, 100  $\mu\text{L}$ /well). The plate was again incubated at 37°C for 1 hour before being subjected to six washes with Tris-T. Goat anti-human IgG HRP conjugate (1:500, 100  $\mu\text{L}$ /well) was then added to each well and the plate incubated at 37°C for 1 hour. The plate was then washed four times with Tris-T. The substrate BCIP/NBT (100  $\mu\text{L}$ /well) was introduced to each well, covered with aluminium foil and allowed to develop. The absorbance was then read at 530 nm using a plate reader (Fluostar Omega) at 20 minutes after addition of the substrate.

#### *5.3.11.2.2 Human Interleukin-6 ELISA*

A sandwich ELISA was used to compare the effectiveness of the recrystallised S-layer fusion protein SbpA-ZZ against common 96-well plate surface chemistries. For the purposes of the study Human IL-6 ELISA Ready-SET-Go! (eBioscience) was used as a model assay to detect Human Interleukin-6 (IL-6). The ELISA was performed following the manufacturer's protocol and using the supplied reagents. Briefly, wells were coated with 100  $\mu\text{L}$ /well of  $\alpha$ -human IL-6 capture antibody and incubated at 4°C overnight. The wells were then washed five times with 250  $\mu\text{L}$ /well wash buffer. The wells were blocked with 200  $\mu\text{L}$ /well assay diluent and incubated at room temperature for 1 hour. The wells were then washed as

previously. IL-6 standards were typically prepared at concentrations of 200, 100, 50, 25, 12.5, 6.25, 3.125, 1.56, 0.78125, 0.39063 and 0.01 pg/mL and 100  $\mu$ L/well of each standard was added to the appropriate wells. The plate was covered with parafilm and incubated at room temperature for 2 hours. Following incubation with the standards, the plate was washed as before. 100  $\mu$ L/well of  $\alpha$ -human IL-6 secondary antibody conjugated to biotin was then added to each well, the plate incubated for another hour and the plate washed as before. 100  $\mu$ L/well HRP conjugated to avidin was then added to each well and incubated at room temperature for a further 30 minutes. The wells were then washed as before with the addition of 3 extra washing cycles to ensure removal of unbound HRP. 100  $\mu$ L of Tetramethylbenzidine (TMB) substrate solution was added to each well and the plate incubated for 15 minutes. 50  $\mu$ L of 1 M H<sub>2</sub>SO<sub>4</sub> was added to stop the reaction and the plates were read at 450 nm using a Fluostar Omega spectrometer. Based on the standard curve, the limit of detection (LOD) was calculated as detailed Chapter 4 section 4.4.5.2 and is represented as the mean value of the blank (wells without human IL-6 added) plus three times the standard deviation of the blank. In order to evaluate the consistency and reliability of the results, three to four replicates were completed for each standard concentration and each experiment was repeated in duplicate or triplicate.

### **5.3.12 pSi Preparation**

Porous silicon surfaces were prepared following the procedure outlined in Chapter 3 section 3.3.1. N-type silicon 0.008 – 0.02  $\Omega$ .cm was etched at a current density of 50 mA/cm<sup>2</sup> for 45 seconds.

### **5.3.13 pSi Functionalisation**

#### **5.3.13.1 Oxidation**

Freshly etched pSi samples underwent ozone oxidation by placing the thermally oxidised samples into a glass reaction vessel and exposing them to ozone gas for 1 hour at a flow rate of 3.2 g/hr. Hydroxylated samples were then thermally oxidised at 400°C for 10 minutes in ambient conditions.

### *5.3.13.2 In Vitro Recrystallisation of rSbpA<sub>31-1068</sub>/ZZ S-layer Fusion Protein on pSi*

Recrystallisation of the SbpA-ZZ fusion protein was conducted using a similar method to that outlined in Chapter 5 section 5.3.9. Briefly, an oxidised pSi sample was clamped into a reaction vessel and 1.5 mL of recrystallisation solution pipetted into the reaction chamber. The pSi was incubated for 18 hours at room temperature in the presence of the S-layer solution. The solution was then decanted and the wafer rinsed three times with 1.5 mL milliQ water and immersed in fresh PBS pH 7.4, ready for capture antibody immobilisation.

#### *5.3.13.2.1 IRS Analysis of rSbpA<sub>31-1068</sub>/ZZ Recrystallisation on pSi*

The S-layer recrystallisation process on pSi was monitored using IRS. Oxidised pSi was clamped into a reaction vessel and equilibrated in 1.5 mL of recrystallisation buffer for 4 hours prior to commencement of the study to ensure a stable baseline. The reaction vessel containing the pSi sample was placed under the fibre optic probe of the IRS instrument and parafilm used to seal the space between the probe and vessel to reduce evaporation. The EOT signal was baselined for 1 hour in 1.5 mL recrystallisation buffer before this solution was then removed by pipette and replaced with 1.5 mL of recrystallisation solution containing 0.1 mg/mL SbpA-ZZ. The pSi surface was monitored overnight, under ambient conditions, for 14 hours to ensure maximum surface coverage. The surface was then rinsed three times with 1.5 mL of recrystallisation buffer at 15, 16 and 17 hours to assess the amount of protein desorption.

### *5.3.14 Capture Antibody Immobilisation on SbpA-ZZ modified pSi and Human IgG Immunosensing.*

Following SbpA-ZZ recrystallisation, the reaction vessel containing modified pSi was exposed to Sheep  $\alpha$ -human IgG capture antibody at 68.4  $\mu$ g/mL (1:500 dilution) in 1.5 mL PBS for 30 minutes in accordance with the protocol established in Chapter 4 section 4.3.2. Any remaining IgG binding sites were blocked by the addition of 1.5 mL of 5  $\mu$ g/mL non-specific rabbit IgG and incubation for 1 hour. Bare silicon that might be exposed through patches in the S-layer lattice was blocked via 1 hour incubation of the sample with 1.5 mL of 2.5% w/v BSA in PBS. Following each of these steps the pSi was washed three times with PBS-T and three times with PBS to remove any unbound protein. In

contrast to the study performed in Chapter 4, formation of the human IgG immunocomplex was performed in the reaction vessel, rather than the IRS flow cell. The experimental timeline remained consistent with earlier studies, Chapter 4 section 4.3.7, whereby the pSi sample was incubated with 1.5 mL of the human IgG analyte and secondary antibody as detailed in Table 5.1. Following formation of the immunocomplex, the pSi sample was removed from the reaction vessel and clamped into an IRS flow cell to monitor the detection event. After establishing a baseline in Tris buffer for 10 minutes, the detection of human IgG was achieved as outlined in Chapter 4 section 4.3.7. Based on the standard curve, the limit of detection (LOD) was calculated as detailed Chapter 4 section 4.4.5.2 and is represented as the mean value of the blank (wells without human IL-6 added) plus three times the standard deviation of the blank. Sensor precision was determined from the coefficient of variation as described in the same section of Chapter 4.

Time (min)	Solution
Reaction Vessel	
0	$\alpha$ -human IgG capture antibody coated pSi in PBS, pH 7.4
0 - 20	Human IgG
21 - 25	PBS-T
26 - 30	PBS, pH 7.4
31 - 50	1:500 Goat $\alpha$ -human IgG antibody conjugated to alkaline phosphatase
51 - 55	Tris-T
56	Tris buffer rinse, pH 7.4
IRS Flow Cell	
0 - 10	Tris buffer, pH 7.4
11 - 20	BCIP/NBT
21 - 30	Tris buffer, pH 7.4

Table 5.1: Experimental timeline of the SbpA-ZZ-pSi human IgG immunosensor experiment.

## 5.4 Results and Discussion

### 5.4.1 Expression and Extraction of SbpA S-layer Protein from *L. Sphaericus* ATCC 4525

Native SbpA S-layer protein was used a model system to investigate the self-assembly, recrystallisation and structure of S-layer lattices formed on various surface chemistries to optimise conditions for later SbpA fusion protein experiments. In order to perform these experiments SbpA was expressed and then extracted from the bacteria *L. sphaericus* and the process characterised with SDS-PAGE analysis. Figure 5.3 shows two scanned SDS-PAGE gels detailing the expression, isolation and purification steps involved in the extraction of SbpA. Studies have shown that the SbpA protein has a theoretical molecular mass of 132,062 Da [206] which can easily be identified throughout the gel by a strong band in this region. S-layer protein is one of the most abundant cellular proteins in *L. sphaericus* and its presence is evident in the bacterial culture via the large band at ~110 – 150 kDa in Lane C. Following cell lysis via application of pressure, centrifugation was used to remove unwanted cell components. Throughout the washing and separation process, the SbpA protein remained in the pellet fraction P1 – P4, while lighter cell fragments remained in the supernatant (S1 – S4) and were totally removed by the final wash at S4. The unfolding of SbpA via the addition of GnHCl affected the staining process masking proteins in this lane. Removal of GnHCl by dialysis against milliQ water and ultracentrifugation yielded a single protein band at ~ 130 kDa in the S5 lane while the pellet fraction contained a large mix of cellular fragments. The protein band in S5 matches the molecular weight of SbpA observed in previous studies indicating successful purification [206]. The purification was not completely efficient as a strong S-layer band remained in the pellet (P5). However the purified sample contained a sufficient amount of protein for the subsequent experiments as Lowry assays determined a concentration of 0.27 mg/mL, which was then adjusted to a stock concentration of 1 mg/mL via centrifugation through a membrane.

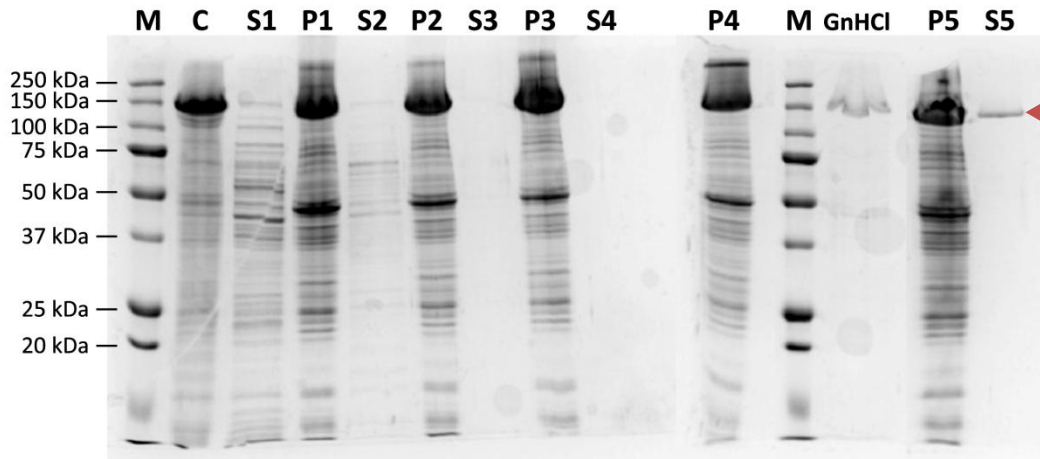


Figure 5.3: SDS-polyacrylamide gel electrophoresis of whole cell extract and purification of SbpA from *L. sphaericus* ATCC 4525. Lanes: M = Protein marker; C = Pellet of *L. sphaericus* bacterial culture; S1–S4 & P1–P4 = Supernatant and pellet fractions following cell lysis and subsequent centrifugation and washing steps; GnHCl = S-layer unfolding step with guanidine hydrochloride; P5 & S5 = Pellet and supernatant fractions following dialysis and centrifugation. The single band in the S5 lane has a molecular weight of approximately 130 kDa.

#### **5.4.2 Optimisation of S-layer Recrystallisation on Silicon**

Optimisation of S-layer recrystallisation conditions was undertaken using native SbpA protein on flat silicon and polystyrene supports. Flat supports were used in preference to pSi in this study primarily due to the difficulty imaging recrystallised protein structures on porous surfaces. The pSi used in this chapter exhibits a rough surface architecture (Figure 5.4), a result of the template etching procedure, rendering it extremely difficult to discern protein on the porous surface. SbpA protein was investigated because the SbpA-ZZ fusion protein was still being genetically engineered at the time of this study and can still offer important information regarding recrystallisation properties. Modification of the silicon surface chemistry was performed to achieve a range of hydrophobicity and surface charge as it has been previously demonstrated that these conditions play an important role in the self-assembly of S-layer lattice structures [134, 139].

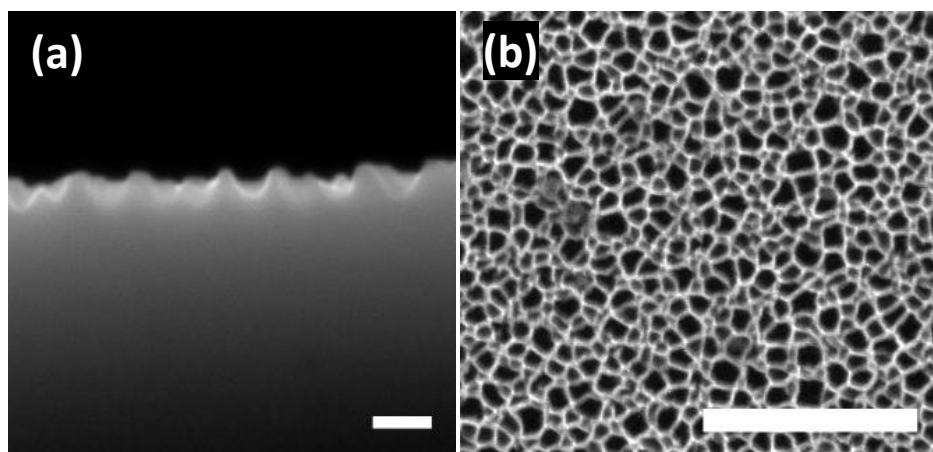


Figure 5.4: SEM micrographs of n-type pSi scaffolds for S-layer recrystallisation. (a) Cross-sectional micrograph of an initial template etch demonstrating the roughness of the surface. Scale bar 200 nm. The porous silicon matrix is propagated from this surface template. (b) Top-down micrograph of pSi surface following pore propagation. Scale bar 1  $\mu\text{m}$ .

#### 5.4.2.1 Surface Wettability

To analyse the effect of surface chemistry on the recrystallisation of S-layer proteins, a number of hydrophilic and hydrophobic silanes, a polyelectrolyte and polystyrene were investigated. Surface charge and wettability are key factors in mediating the level of protein adsorption on solid supports [207, 208] and the solid-liquid interface is essential in identifying the wettability (hydrophobicity/hydrophilicity) of a surface and subsequent interactions between that surface and components in the liquid contacting the surface. On flat surfaces, the major contributor to wettability is surface chemistry and surface energies. As surface energy is lowered, the hydrophobicity and thus the water contact angle of a surface are increased [209].

In this study the wettability of various silicon wafer surface chemistries was determined using static water contact angles as described in Chapter 5 section 5.3.8. Silicon surface chemistries investigated included ozone treated silicon, thermally oxidised silicon, (3-aminopropyl)triethoxysilane (APTES), poly(styrene sulfonate) (PSS), n-(triethoxysilylpropyl)-o-polyethylene oxide urethane (PEG Silane), Pentafluorophenyl dimethylchlorosilane (PFCS), and Tridecafluoro-1,1,2,2-tetrahydrooctyl-dimethylchlorosilane (TDFCS). Untreated

polystyrene from an ELISA plate was also investigated. Figure 5.5 shows a digital photograph of a 1  $\mu$ L droplet of water on freshly ozone treated silicon. The low contact angle demonstrates relatively high wetting, indicating the surface is hydrophilic. The results of the full contact angle analysis can be found in Table 5.2. PSS and ozone treated silicon demonstrated low contact angles, 27° and 32° respectively, indicating high wetting and hydrophilic surfaces. APTES and PEG silane chemistries generated contact angles in the region of 45° indicating moderate wettability. The thermal treatment of silicon yielded a moderately hydrophobic surface as did polystyrene, while the fluorinated surfaces PFCS and TDFCS demonstrated the high contact angles indicating low wetting and highly hydrophobic surfaces. Interestingly, the low contact angle achieved on ozone treated silicon indicates that some silanol functionality must remain on the surface following subsequent thermal treatment. The presence of such groups is known to instil hydrophilic properties on silicon surfaces and the contrast in contact angle measurements between silicon treated with ozone/thermal oxidation and silicon treated with thermal oxidation supports this. Optimisation of the sensor surface chemistry is an essential step in the formation of a pSi immunosensor and the range of surface hydrophobicity achieved here was fundamental in the subsequent S-layer recrystallisation investigations for attaining good surface coverage, crystal structure and protein orientation.

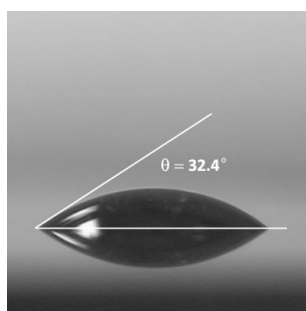


Figure 5.5: Digital photograph of a static water contact angle measurement performed on freshly ozone treated silicon.

Surface Chemistry	Static Contact Angle	Structure
PSS	$27^\circ \pm 2$	
Ozone Treated Silicon	$32^\circ \pm 2$	SiOH & SiO <sub>2</sub>
APTES	$43^\circ \pm 2$	
PEG Silane	$45^\circ \pm 2$	
Thermal SiO <sub>2</sub>	$60^\circ \pm 3$	SiO <sub>2</sub>
Polystyrene (96-well)	$79^\circ \pm 3$	
PFCS	$95^\circ \pm 4$	
TDFCS	$107^\circ \pm 3$	

Table 5.2: Static water contact angle measurements as a function of surface chemistry.

#### 5.4.2.2 Recrystallisation of Native SbpA Protein on Modified Silicon

Silicon modified with the hydrophilic/hydrophobic coatings prepared in Chapter 5 section 5.4.2.1 were used as solid supports for S-layer recrystallisation and the ensuing protein structures assessed via liquid AFM. Figure 5.6 shows 2 sets of height images taken at  $10 \mu\text{m} \times 10 \mu\text{m}$  and  $400 \text{nm} \times 400 \text{nm}$  for all surface chemistries investigated: PSS, ozone treated silicon, APTES, PEG silane, thermally oxidised silicon, polystyrene, PFCS and TDFCS. SbpA was shown to recrystallise with relatively good coverage on all modified surfaces, regardless of the surface wettability, indicating that dehydration of the solid support was not a crucial factor in the recrystallisation process [139]. The hydrophobicity of the

surface did however influence the consistency of the polycrystalline layer, causing a reduction in the size and an increase in the number of individual domains (protein ‘sheets’ or ‘islands’) on more highly hydrophobic surfaces (TDFCS & PFCS). Hydrophilic surfaces PSS and ozone treated silicon demonstrated much larger domain diameters in the order of 300 – 400 nm, while the moderately hydrophilic surfaces APTES and PSS and the moderately hydrophobic thermal SiO<sub>2</sub> and polystyrene exhibited reducing domain diameters in the region of 200 – 100 nm (Table 5.3). The highly hydrophobic surfaces, PFCS and TDFCS both showed much smaller domain diameters, 72 and 44 nm respectively. It was also noted that all modified surfaces displayed several recrystallisation directions in neighbouring domains, regardless of the surface properties. The smaller size and greater number of the S-layer domains on hydrophobic surfaces is indicative of a higher number of nucleation sites and can be attributed to a higher affinity of hydrophobic surfaces to adsorb proteins, leading to the nucleation of crystal growth at more locations and faster S-layer formation than on hydrophilic counterparts [134, 139].

Comparison of recrystallisation on the silicon modified surfaces and the polystyrene surface indicates the latter has a less uniform coverage. Roughness analysis of 800 nm<sup>2</sup> AFM images of thermally oxidised silicon and polystyrene saw an increase in the surface roughness on polystyrene (RMS = 1.24 nm and 1.91 nm respectively). The differences in S-layer coverage and uniformity on polystyrene suggest that the underlying support is rougher and the untreated, uncleaned surface may contain small defects or contaminants compared with the cleaned silicon counterpart.

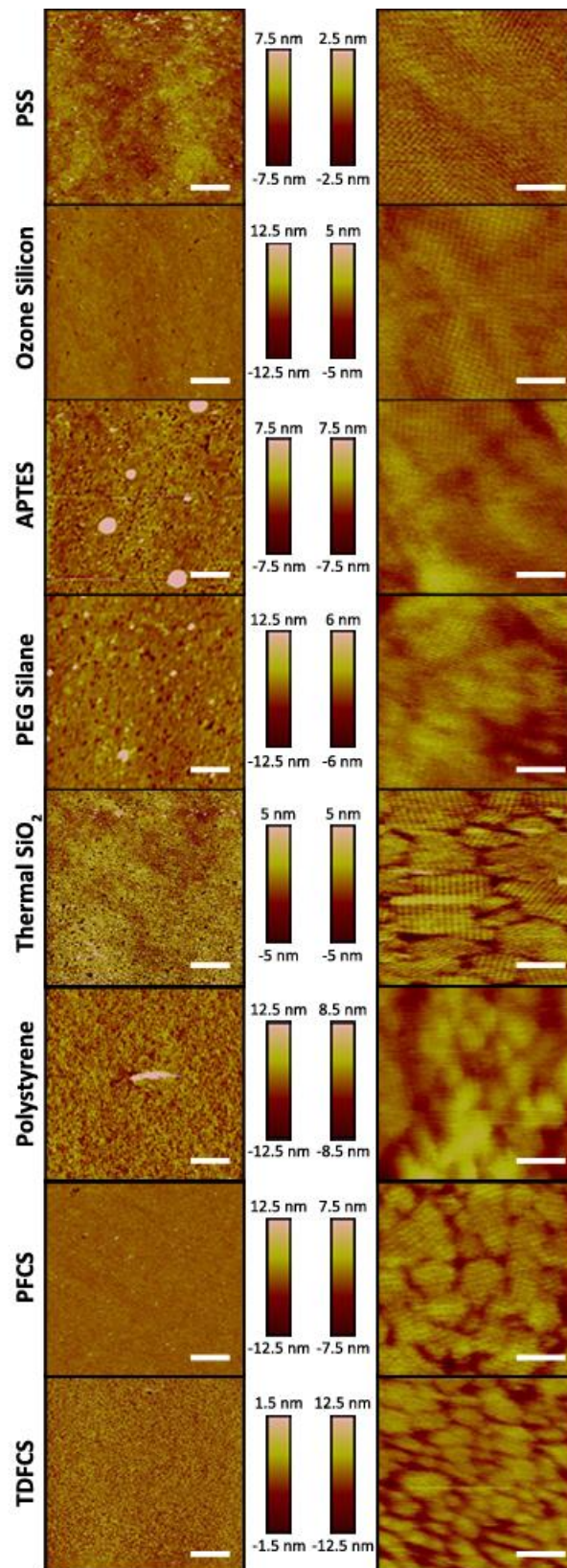


Figure 5.6: Liquid AFM images of recrystallised SbpA protein on various surface chemistries. Images are ranked in order of increasing surface hydrophobicity. The left column shows 10 μm<sup>2</sup> height images and the scale bars correspond to 2 μm. The right column shows 400 nm<sup>2</sup> height images and the scale bars correspond to 100 nm.

Surface Chemistry	CtC (nm)	Domain Ø (nm)	SbpA D (nm)	Mass (ng/cm <sup>2</sup> )
PSS	13.04 ± 1.03	415.62 ± 106.84	14.89 ± 0.75	1,032
Ozone Silicon	13.11 ± 1.45	288.64 ± 97.05	15.32 ± 0.92	1,021
APTES	13.20 ± 1.47	181.09 ± 49.63	14.84 ± 0.96	1,009
PEG Silane	12.98 ± 1.42	157.49 ± 63.25	12.78 ± 1.73	1,041
Thermal SiO <sub>2</sub>	13.08 ± 1.07	179.85 ± 63.45	9.53 ± 0.17	513
Polystyrene	13.59 ± 1.37	115.58 ± 28.50	9.30 ± 0.41	475
PDCS	13.63 ± 1.34	71.76 ± 26.46	9.13 ± 1.03	472
TDFCS	13.42 ± 0.96	44.50 ± 18.07	9.18 ± 1.20	487

Table 5.3: SbpA lattice properties extracted from AFM analysis of in vitro protein recrystallisation on hydrophilic and hydrophobic surfaces. CtC – Centre-to-Centre distance between morphological units; SbpA D – S-layer thickness; Domain Ø – Diameter of S-layer crystalline domains; Mass – Theoretical mass of recrystallised protein on the surface.

Crystallinity of the S-layer lattice was found to be independent of the domain size and surface properties. The self-assembled proteins formed a square lattice of p4 symmetry with a centre to centre spacing of ~ 13 nm as expected for crystalline SbpA S-layer (Figure 5.7 (a), Table 5.3) [134]. This value was relatively constant across all samples, with a very small increase in centre-to-centre (CtC) distance occurring on hydrophobic surfaces [210]. This finding supports the hypothesis that surface hydrophobicity does not overly affect the inter-molecular interactions between the monomeric protein subunits required for self-assembly. The thickness of the protein layer (SbpA D) was also investigated and it was found that the hydrophilic surface chemistries, PSS, ozone treated silicon, APTES and PEG exhibited layer thicknesses of ~15 nm, while all hydrophobic surfaces demonstrated a layer thickness of ~9 nm (Figure 5.7, Table 5.3). It has previously been reported that a crystalline monolayer of SbpA protein is ~9 nm thick [211] which corresponds to the thickness observed on the hydrophobic supports, while SbpA bilayers ~15 nm thick have been observed on hydrophilic supports [134, 139]. Hydrophobic surfaces are known to exclusively form SbpA protein monolayers due to the presence of charged domains within the protein.

The positively charged inner surface of the SbpA orients toward the hydrophobic support, while the outer more hydrophilic surface faces the aqueous medium (Figure 5.7 (e)) [134, 212]. This conformation is similar to the native orientation of SbpA on *L. sphaericus*, where inner surface of the protein interacts with the underlying negatively charged secondary cell wall polymer (SCWP), orienting the C-terminal towards the aqueous phase [139, 213]. The formation of the bilayer on hydrophilic surfaces was due to hydrophilic-hydrophilic interactions from the protein and surface [134, 212]. This results in the positive inner surface facing the aqueous medium allowing a second layer to form on top of the first in the same fashion as on hydrophobic surfaces. Similar crystalline SbpA topography and structure on hydrophilic and hydrophobic surfaces in Figure 5.6 indicates that the protein orientation within monolayers and top layer of bilayers is the same. Comparison of the hydrophilic and hydrophobic layer thicknesses found that the bilayer was ~ 1.5 times the thickness of the SbpA monolayer, rather than double the monolayer thickness, which may be due to the two layers conforming to one another like cogs in a gear, as depicted in Figure 5.7 (e) [139]. Comparison of the surface charge of the solid support against the formation of mono- and bilayer SbpA lattices suggests that it may also play a major role in the self-assembly process. Figure 5.7 (e) contains a simplified schematic of the SbpA structure identifying charged regions within the protein. Electrostatic interactions between these charged domains and surface charge could form the structures observed in this study and has already been reported to influence protein orientation and recrystallisation kinetics [134, 139, 210, 214]. However, the hydrophilic properties of APTES appear to prevail over electrostatic interactions, as this surface formed a bilayer structure rather than the possible monolayer which could form from interactions between the positive amino groups on the surface and the negative N-terminal of the SbpA. This contradicts earlier S-layer studies with APTES, where protein monolayers and small domains were observed, however the surface prepared in that study was much more hydrophobic, exhibiting a contact angle of 67°, which would complement the effect of the surface charge [210].

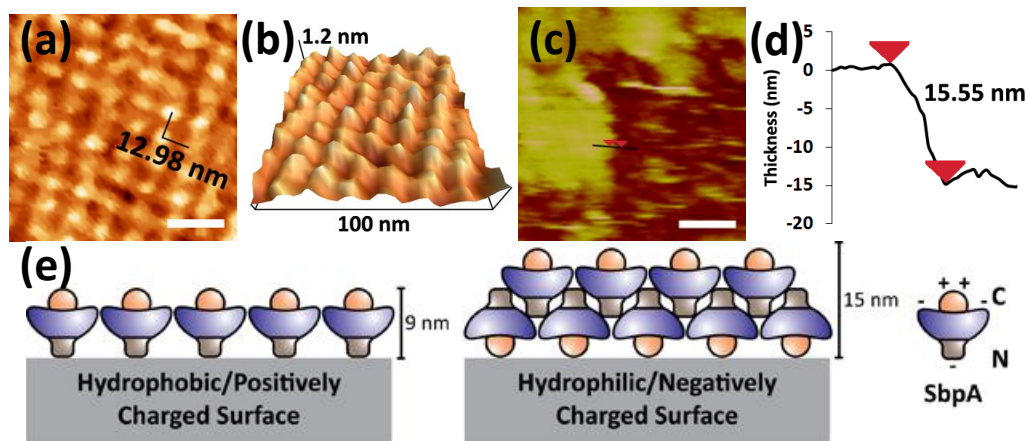


Figure 5.7: AFM analysis of recrystallised SbpA protein on ozone treated silicon. (a) AFM height image indicating the average centre-to-centre distance (CtC) between monomeric protein subunits. Scale bar 25 nm, Z-range 1.2 nm (b) 3D representation of the SbpA protein layer (c) AFM height image indicating the sectional height analysis of a SbpA protein layer on ozone treated silicon. The protein layer was removed from the underlying silicon surface through increased tip force. Scale bar 100 nm, Z-range 30 nm. (d) Line profile showing the height of the SbpA layer formed. (e) Schematic representation of SbpA protein structures formed on hydrophobic and hydrophilic surface chemistries. Adapted from [134, 139].

The theoretical mass of recrystallised S-layer protein can be calculated by means of the molecular weight of SbpA, 132,062 Da, the square lattice symmetry, and CtC spacing of the morphological units (Table 5.3) [215]. This method is a rough approximation and assumes complete surface coverage with no surface defects and does not replace experimental analysis. However, this approximation is still valuable as it could be used to help optimise S-layer concentration in recrystallisation solutions or provide an indication of the number of potential binding sites that exist on a recrystallised fusion protein surface. The calculated mass of protein on the surface of hydrophilic samples ( $\sim 1,000 \text{ ng/cm}^2$ ) and hydrophobic surfaces ( $\sim 500 \text{ ng/cm}^2$ ) were somewhat lower than experimentally derived values previously reported [210, 215-217]. This is probably due to the fact that the simplified theoretical calculation does not take into account patches of multilayers, the presence of protein aggregates or complex conformations associated with bilayer structure. As such this approach is used as a conservative

estimate of the protein surface density and the values displayed in Table 5.3 are representative of this.

The results of this study highlight the versatility and unique structures formed by the SbpA S-layer protein on hydrophilic and hydrophobic surfaces. The ability to adapt to surfaces of different wettability and charge through the formation of mono- or bilayers is important for future adaptation to various sensing techniques. Of the surfaces investigated, ozone treated silicon was considered the optimal surface for use with the SbpA-ZZ fusion protein. Factors, such as strong protein surface coverage, hydrophilic properties and low amounts of sample processing highlight this functionality as a model surface to assess the recrystallisation of SbpA-ZZ and for integration into a pSi sensor.

#### **5.4.3 Expression and Purification of the S-layer Fusion protein SbpA-ZZ**

SbpA-ZZ was expressed and extracted from the bacteria *E. coli* BL21DE3 containing pBluescript SbpA<sub>31-1068</sub>/ZZ and the process characterised with SDS-PAGE analysis. Figure 5.8 shows three scanned SDS-PAGE gels detailing the expression, isolation and purification steps involved in the extraction of SbpA-ZZ. Induction of the expression of SbpA-ZZ via the addition of IPTG (Lane d), saw the appearance of a new protein band at ~123 kDa in the *E. coli* bacterial culture, compared with prior to induction (Lanes b & c). The molecular mass of the band corresponds to the theoretical mass of the protein, 123,057 Da, and suggests successful transfection [148]. Isolation of this protein from the host cells was achieved through cell lysis via application of pressure. Centrifugation of the lysis product saw the retention of the fusion protein in both the supernatant and pellet fractions (Lanes h & i respectively). Isolation of the S-layer fusion protein from the soluble phase (supernatant fraction) was achieved by passing the solution through an IgG affinity column (Lanes j – r) which separated much of the unwanted cell fragments from the IgG specific S-layer fusion protein. Bound SbpA-ZZ was eluted from the column by lowering the pH, Lane o, however the isolated SbpA-ZZ was difficult to visualise due to the effect of the acidic conditions on the protein staining process. Dialysis against milliQ water to remove the buffer yielded a single protein band at 123 kDa suggesting successful isolation of SbpA-ZZ (Lane s). A by-product of the dialysis process was

manifested in the form of a white precipitate at the bottom of the tubing. This precipitate contained cell components that had remained in the elution fraction of the purification process and were then denatured by the removal of the buffer (Lane t). These components were likely bound/attracted to the S-layer protein and remained throughout the purification protocol because a chaotropic agent such as GnHCl was not employed to unfold and disassociate the S-layer. The results in Figure 5.8 indicate that GnHCl is not necessarily required as part of this particular protocol, as the change in pH and removal of buffering salts via dialysis were sufficient to purify the chimeric S-layer protein SbpA-ZZ from any remaining contaminants. Lowry protein assay determined a final SbpA-ZZ concentration of 0.45 mg/mL, which was then adjusted to a stock concentration of 1 mg/mL via centrifugation through a membrane.

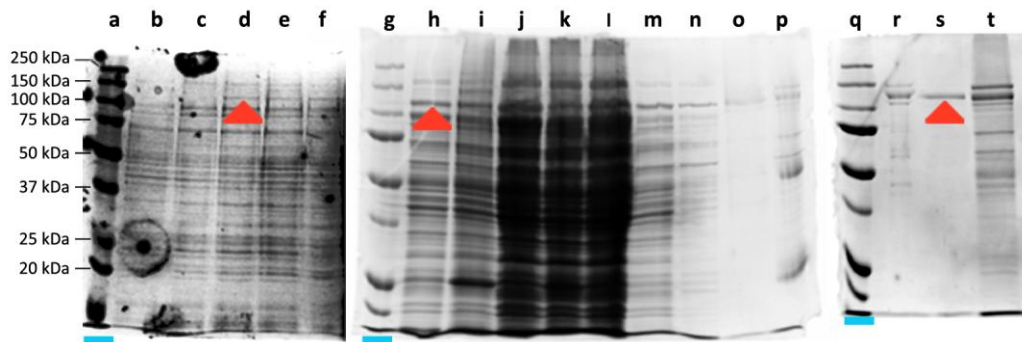


Figure 5.8: SDS-polyacrylamide gel electrophoresis detailing the purification of the fusion protein rSbpA31-1068/ZZ (SbpA-ZZ) from *E. coli* BL21DE3. Lanes: (a), (g) & (q) Protein marker – these lanes are highlighted by a blue line; (b) *E. coli* pre-culture; (c) *E. coli* culture prior to induction; (d) *E. coli* culture after induction and expression of SbpA-ZZ; (e)&(f) *E. coli* culture 2 and 4 hours after induction; (h) Cell lysis supernatant; (i) Cell lysis pellet; (j) IgG column – Flow through 1; (k) IgG column – IgG micro bead matrix; (l) IgG column – Flow through 2; (m) IgG column – wash 1; (n) IgG column – wash 2; (o) IgG column – elutant; (p) IgG column – IgG matrix; (r) IgG column – wash 4; (s) IgG elutant following dialysis containing purified SbpA-ZZ; (t) Precipitate formed during dialysis.

#### **5.4.4 Recrystallisation of SbpA-ZZ Fusion Protein on Solid Supports**

Successful integration of the SbpA-ZZ fusion protein in a pSi sensor device requires retention of the self-assembly properties of the SbpA precursor, while incorporating the essential IgG binding Z domains. Following the results of the SbpA recrystallisation study in Chapter 5 section 5.4.2.2, ozone treated silicon was chosen as the primary silicon support for this investigation due to the desirable wettability and surface charge, optimal protein coverage and structure of the resulting S-layer lattice. Polystyrene supports were also investigated in preparation for subsequent ELISA experiments.

Figure 5.9 shows AFM height images taken at a large perspective,  $10\ \mu\text{m}^2$ , and close perspective,  $400\ \text{nm}^2$ , of recrystallised SbpA-ZZ protein on ozone treated silicon and polystyrene. The fusion protein achieved surface coverage similar to that observed for the native SbpA protein on the same surface functionality. SbpA-ZZ displayed excellent coverage on ozone treated silicon, with only small, scattered imperfections in the protein lattice (Figure 5.9 (a)), while polystyrene produced a less uniform, rougher coverage (Figure 5.9 (c)). Close analysis of the S-layer structures shows that the protein layer on silicon exhibited crystalline domains with diameters in the order of 235 nm and contained several recrystallisation directions (Figure 5.9 (b)), while polystyrene exhibited domain diameters in the region of 114 nm (Table 5.4). Both of these parameters correlate with the properties of the native SbpA protein on the same surface chemistry (Chapter 5 section 5.4.2.2).

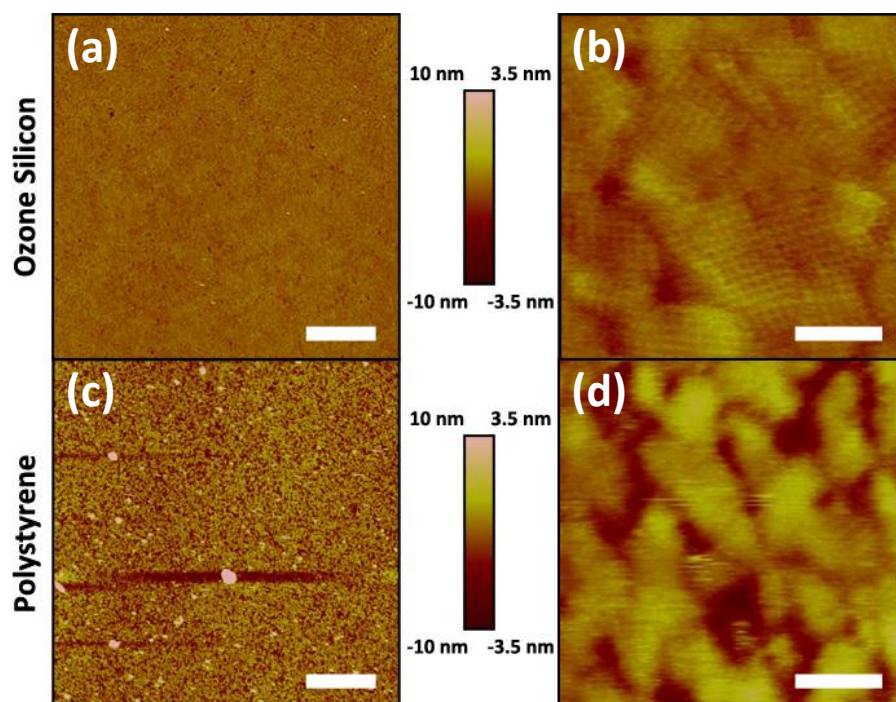


Figure 5.9: Liquid AFM images of recrystallised SbpA-ZZ protein on ozone oxidised silicon and polystyrene. (a)&(c) Height image of a  $10 \mu\text{m}^2$  area, scale bar  $2 \mu\text{m}$ . (b)&(d) Height image of a  $400 \text{nm}^2$  area, scale bar  $100 \text{nm}$ .

Surface Chemistry	CtC (nm)	Domain $\emptyset$ (nm)	SbpA-ZZ D (nm)	Mass (ng/cm <sup>2</sup> )
Ozone Silicon	$13.15 \pm 0.89$	$235 \pm 33.91$	$5.80 \pm 0.83$	946
Polystyrene	$13.58 \pm 1.52$	$114.55 \pm 35.84$	$8.95 \pm 0.83$	443

Table 5.4: SbpA-ZZ lattice properties extracted from AFM analysis of in vitro protein recrystallisation. CtC – Centre-to-Centre distance between morphological units; SbpA-ZZ D – S-layer Thickness; Domain  $\emptyset$  – Diameter of S-layer Crystalline domains; Mass – Theoretical mass of recrystallised protein on the surface.

The crystallinity of recrystallised SbpA-ZZ fusion protein was also found to be in agreement with native SbpA properties, forming a square lattice structure of p4 symmetry with a centre to centre spacing between the morphological units of  $13.15 \text{ nm}$  on the silicon sample. The poor quality of the polystyrene height images made acquisition of this information difficult, however the CtC spacing was able to be determined from corresponding deflection images (not shown) and

was found to be 13.58 nm and display the same lattice structure. Analysis of the height images identified that the fusion protein formed a 8.95 nm thick monolayer on the polystyrene (Table 5.4) but the images acquired of recrystallised SbpA-ZZ on silicon did not include the layer edge, therefore, layer thickness was measured at defects in the layer structure and found to be 5.80 nm, a value which corresponded to neither a SbpA monolayer, 9 nm, nor a bilayer, 15 nm (Figure 5.10 (c)). As the thickness measurement was too small to indicate the formation of a monolayer, it suggests that a bilayer structure had formed in accordance with SbpA behaviour on hydrophilic surfaces and that the AFM measured the underlying SbpA-ZZ monolayer at the investigated surface defects. Due to the proposed bilayer model, Figure 5.7 (e), removal of the top portion of the bilayer and exposure of the underlying layer would result in a decrease in layer thickness of ~6 nm, matching the thickness measurements observed here. From this model and previous SbpA fusion protein studies from literature, it can be assumed that the total layer thickness is ~15 nm. Assuming full surface coverage and accounting for the formation of a bilayer, shape of the lattice, spacing between protein subunits and molecular mass of SbpA-ZZ, the estimated protein surface mass density on silicon was calculated to be 945.7 ng/cm<sup>2</sup> and 443 ng/cm<sup>2</sup> for polystyrene using the approach detailed in Chapter 5 section 5.4.2.2. The lower mass density of the fusion protein compared to the native SbpA was expected due to the reduction in molecular mass (from ~132 kDa to 123 kDa) that occurred as part of the truncation and genetic engineering process. Accounting for the formation of a bilayer on silicon, these value match theoretical and experimental protein densities reported in literature for monolayers of this chimaeric protein [148]. Using the same method, the density of morphological protein units on silicon was also calculated to be 2.3x10<sup>12</sup> morphological units/cm<sup>2</sup> and assuming that each unit contains two Z domains capable of binding IgG, it can be estimated that approximately 4.6x10<sup>12</sup> Z domains/cm<sup>2</sup> exists on a recrystallised SbpA-ZZ silicon surface. The same analysis of the polystyrene sample yielded a potential binding site density of 4.34x10<sup>12</sup> Z domains/cm<sup>2</sup>. Such a high density of receptor sites coupled with the ability to self-assemble into monolayers with good surface coverage makes this protein an ideal coating for immunosensor devices.

The successful recrystallisation of the S-layer fusion protein with good adherence to established SbpA properties suggests that incorporation of the two Z domains at the C-terminal does not affect self-assembly of the SbpA fragment. Furthermore the ability to recrystallise with extremely good coverage on ozone treated silicon is an important step towards integration into pSi architecture for sensing applications.

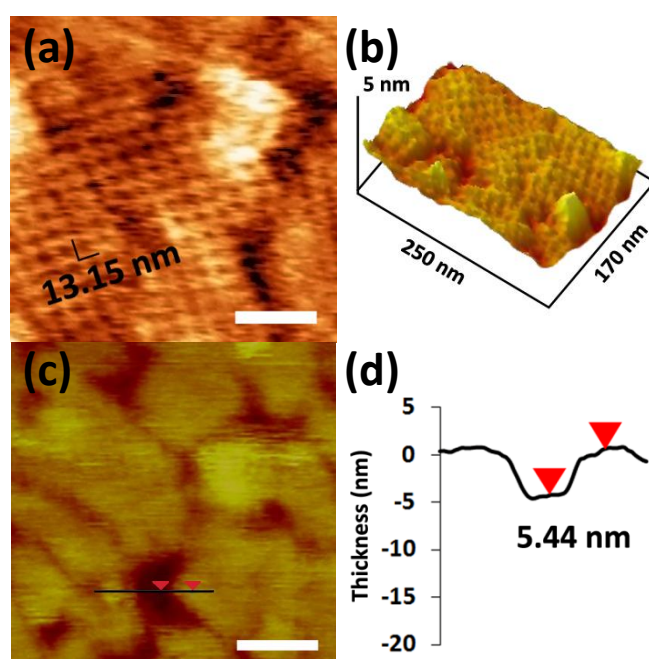


Figure 5.10: AFM analysis of recrystallised SbpA-ZZ protein on ozone treated silicon. (a) AFM height image indicating the average CtC distance between monomeric protein subunits. Scale bar 50 nm, Z-range 1.5 nm. (b) 3D representation of the SbpA-ZZ protein layer (c) AFM height image indicating the sectional height analysis of a SbpA-ZZ protein layer on oxidised silicon. Scale bar 100 nm, Z-range 10 nm. (d) Line profile showing the height of the SbpA-ZZ layer.

#### **5.4.5 Accessibility of Fused ZZ Domains - Human IgG Assay**

Following successful recrystallisation of the fusion protein on ozone treated silicon and polystyrene surfaces, the accessibility of the fused Z domains on the recrystallised product was investigated. Protein folding, protein-protein interactions, recrystallisation and orientation are all factors that may inhibit the accessibility of the Z domains within the fusion protein. According to the recrystallisation model proposed in Chapter 5 section 5.4.2.2, the C-terminal containing the fused Z domains should be unobstructed and orient towards the aqueous phase regardless of the formation of a monolayer or bilayer structure. To assess the accessibility of these domains, a human IgG immunoassay was performed on recrystallised SbpA-ZZ and SbpA within a 96-well polystyrene microtiter plate. Immobilisation of a  $\alpha$ -human IgG capture antibody to the SbpA-ZZ surface formed a receptor matrix and detection of bound human IgG was achieved via an alkaline phosphatase conjugated secondary antibody and precipitation of BCIP/NBT. This technique yielded an absorbance reading directly related to the concentration of the analyte, the results of which appear in Figure 5.11. It can clearly be observed that SbpA-ZZ treated wells successfully detected the presence of human IgG, demonstrating a 6-fold increase in signal intensity compared to SbpA-ZZ control surfaces and a 12-fold signal increase compared to SbpA control surfaces. Moreover, the low absorbance measurements for SbpA treated control surfaces indicate minimal non-specificity, signifying that IgG specifically binds to surfaces containing the Z domain. This result suggests that SbpA-ZZ has successfully bound the IgG capture Ab, demonstrating that accessibility of the Z domains was not affected by the self-assembly and recrystallisation process. Successful binding also indicates correct protein orientation within the monolayer in accordance with the proposed model, as incorrect orientation could result in inhibition of the binding sites.

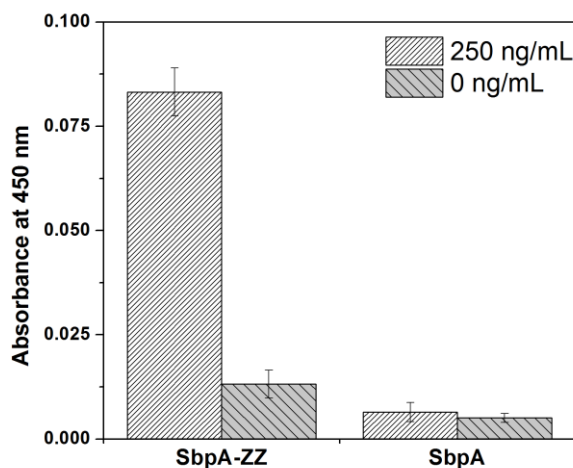


Figure 5.11: Assessment of the binding affinity of SbpA-ZZ to IgG antibodies via sandwich immunoassay to human IgG on a 96-well untreated polystyrene plate. Recrystallised SbpA-ZZ and SbpA surfaces were exposed to sheep  $\alpha$ -human IgG which selectively bound to the Z domains on SbpA-ZZ. Exposure to 250 ng/mL of the target analyte, human IgG, and formation of an immunocomplex containing a goat  $\alpha$ -human IgG secondary antibody conjugated to alkaline phosphatase caused a colour change upon de-phosphorylation of the enzyme substrate BCIP/NBT which was monitored at 530 nm.

#### **5.4.6 Assessment of SbpA-ZZ performance (ELISA Studies)**

Following successful immobilisation of IgG on recrystallised SbpA-ZZ, the capacity for integration into pre-existing immunosensor architectures was assessed. The fusion protein was adapted to enzyme-linked immunosorbent assay (ELISA), a common technique that provides a sensitive, specific and accurate method for the detection of analytes at very low levels, including ng/mL and even pg/mL. The quantitative sandwich-type ELISA employs a direct relationship between the signal (y-axis, in units of absorbance) and the analyte concentration (x-axis), which means the greater the signal, the greater the concentration of bound analyte. The effectiveness of ELISA depends on many critical components and factors including the binding and alignment of a receptor coating on the sensor surface. This approach typically utilises 96-well microtiter plates constructed from polystyrene to carry out immunological interactions. A range of commercial ELISA plates are available offering ‘low-bind’ through to ‘high-bind’ surfaces which alter the protein adsorption properties through changes to

the surface potential and wettability [218]. Recrystallisation of S-layer on these surfaces and comparison of the resulting sensor response against untreated surfaces can assist in identifying the suitability of SbpA-ZZ for adaption to a range of sensors including pSi. For the purposes of this study a commercial sandwich ELISA kit for the detection of Human Interleukin-6 (IL-6) was used to compare the sensor response of S-layer coatings against common plate surface chemistries (untreated) to ascertain if the sensitivity of the approach could be improved via the inclusion of SbpA-ZZ. Three plate types were selected as part of this investigation, High protein binding (High bind), Medium protein binding (Medium bind) and low protein binding (Tissue Culture).

Standard curves from human IL-6 ELISAs performed on the three plate types are shown in Figure 5.12. All ELISAs had a relatively low background indicating minimal non-specific adsorption. Recrystallised SbpA-ZZ fusion protein on high bind and medium bind plates displayed similar absorbance readings to the respective untreated surfaces, with the untreated high bind surface consistently providing a slightly more intense absorbance signal at higher analyte concentrations compared to SbpA-ZZ treated wells (Figure 5.12 (a)), although this trend was reversed on the medium bind surface, which saw SbpA-ZZ treated wells outperform its untreated counterpart (Figure 5.12 (b)). High bind plates are primarily hydrophobic but also have a negative surface charge via irradiation of polystyrene which ‘opens’ the benzene ring forming carboxyl groups. Proteins can therefore adsorb via hydrophobic and ionic interactions achieving a higher protein density compared to medium bind plates that possess an uncharged, hydrophobic polystyrene surface [218]. AFM analysis was not conducted on high bind surfaces, although the S-layer structure can potentially be estimated from the surface properties. This surface could potentially form either a S-layer protein monolayer (hydrophobic) or bilayer (negative surfaces) structure or a mixture of both, however due to the surface charge density and the outcome of the study in section 5.4.2.2, a monolayer similar to that observed on medium bind plates (polystyrene) is more likely.

The similarities in absorbance measurements and calculated limits of detection (LOD) suggest that that amount of viable capture antibodies is similar between these different surface types, with SbpA-ZZ treated medium bind wells showing a

slight improvement over the sensitivity of the high bind surface (Figure 5.12 (a & b), Table 5.5). While this result is encouraging, the irregular SbpA-ZZ protein surface coverage observed on medium bind polystyrene (Chapter 5 section 5.4.4) may negatively impact the achievable sensitivity by limiting the possible number of IgG receptor sites within a well. Polystyrene exposed at gaps in the S-layer structure would be filled by non-specific protein in subsequent blocking steps, preventing non-specific adsorption of antibodies and ensuring a low background. Consequently, there may exist the possibility of improved sensor response with additional surface coverage optimisation. The consistently lower absorbance readings for SbpA-ZZ recrystallised on High bind plates suggests poorer SbpA-ZZ coverage (less receptor sites) which could be caused by the surface properties of the high bind plate and could also benefit from optimisation.

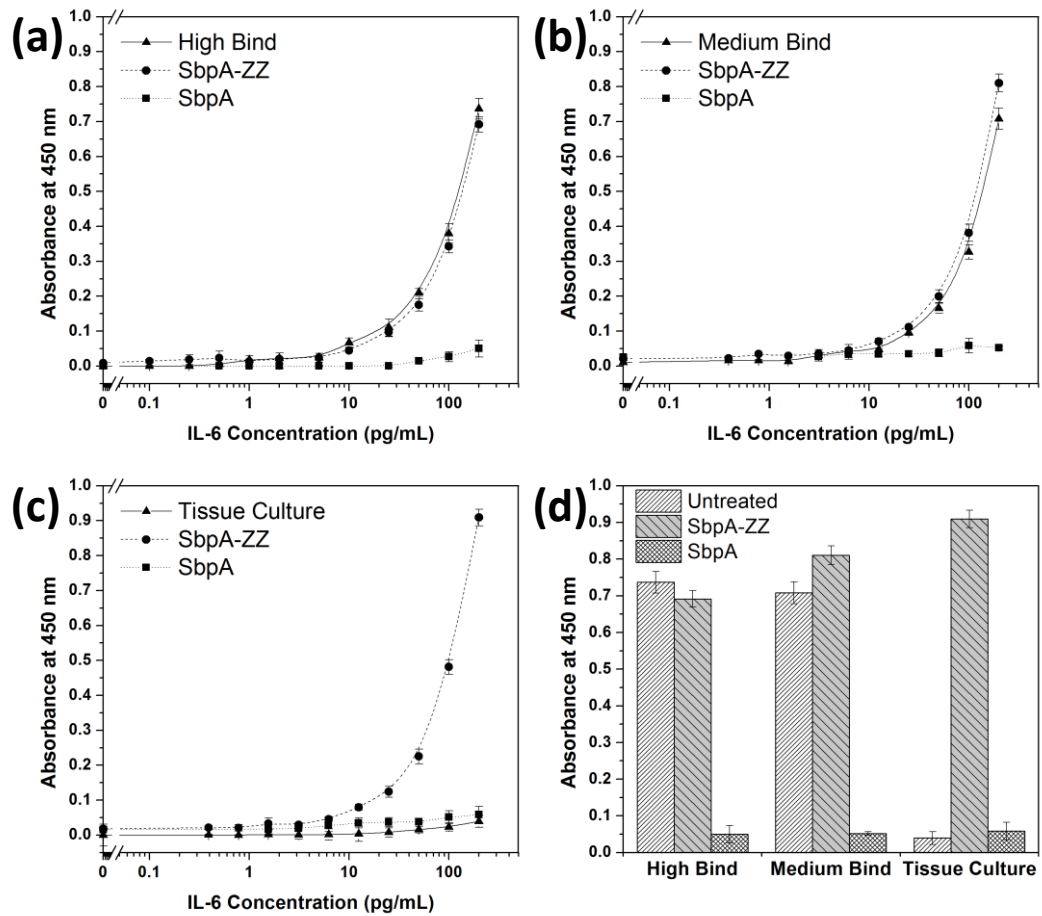


Figure 5.12: Human IL-6 sandwich ELISA standard curves performed on High Bind, Medium Bind, Tissue Culture, SbpA-ZZ and SbpA surfaces. Native SbpA and SbpA-ZZ fusion protein were recrystallised on each type of 96-well microtiter plate and the response compared against untreated wells. (a) ELISA response on Costar 9018 High Binding 96-well microtiter plate. (b) Response on Costar 9017 Medium Binding 96-well microtiter plate. (c) Response on Costar 3596 Tissue Culture Treated 96-well microtiter plate (d) Comparison of the ELISA signal observed on the tested surfaces for an analyte concentration of 200 pg/mL Human IL-6.

In contrast to the high and medium bind surfaces, the low binding tissue culture surface provided a stark difference between the SbpA-ZZ and untreated wells. SbpA-ZZ treated wells generated a strong detection response, while untreated wells merely demonstrated a low background response. Tissue culture plates are modified with oxygen plasma and exhibit hydrophilic properties and a negative charge to reduce protein adsorption and maximise cell attachment and spreading [219, 220]. This type of surface was also not investigated with AFM, however such properties should promote the formation of a SbpA-ZZ bilayer on the surface of a well, while other soluble proteins would typically be repelled by the surface [134, 139]. Due to this property the  $\alpha$ -human IL-6 capture antibody and other proteins were unable to adsorb to the untreated surface preventing the formation of an immunocomplex and detection signal. This resulted in SbpA-ZZ treated surface manifested a 23-fold increase in signal intensity over untreated wells at 200 pg/mL (Figure 5.12 (c)) and highlights the potential of S-layers for improving antibody binding on protein repellent surfaces. Furthermore, and most importantly, SbpA-ZZ response on tissue culture plates demonstrated a general increase in signal intensity and an improved limit of detection over the untreated and SbpA-ZZ treated high and medium bind plates (Figure 5.12 (e)), Table 5.5). This suggests that additional IgG capture antibody was bound within the SbpA-ZZ coated tissue culture wells compared with the other surfaces, implying improved S-layer coverage over other plate types. AFM studies on hydrophilic silicon surfaces support this theory, as larger crystalline domains are formed in S-layer bilayers, reducing defects in the layer structure and increasing potential receptor sites [134, 139, 216]. This preliminary finding indicates that adaptation of SbpA-ZZ to ELISA has the ability to slightly improve the sensitivity of the approach and investigation of the S-layer surface coverage with AFM and optimisation of the underlying polystyrene may provide a route to furthering this improvement in the future.

Surface Treatment	Limit of Detection
High Bind	5.88 pg/mL
High Bind\SbpA-ZZ	6.63 pg/mL
Medium Bind	6.00 pg/mL
Medium Bind\SbpA-ZZ	4.26 pg/mL
Tissue Culture	-
Tissue Culture\SbpA-ZZ	3.63 pg/mL

Table 5.5: Limits of detection of Human Interleukin-6 on commercial and SbpA-ZZ treated 96 well plate surfaces. SbpA treated surfaces exhibited a low background signal and were not included in this comparison.

All wells treated with native SbpA, regardless of surface type, produced minimal signal levels (Figure 5.12 (a-d)). This finding is consistent with background levels of non-specific adsorption and correlates with the earlier human IgG study (Chapter 5 section 5.4.5) indicating low reactivity towards IgG and interleukin biomolecules. The response demonstrated by SbpA at higher concentrations, >50 pg/mL, became larger than corresponding blanks on untreated surfaces indicating increased amounts of non-specific adsorption probably due to protein-protein interactions. This effect may impact on the performance and specificity of SbpA-ZZ based ELISAs at much higher analyte concentrations and in the presence of complex serums, however it was not investigated as part of this study.

The results of this preliminary study into the integration of SbpA-ZZ into ELISA demonstrated an improvement in sensitivity of the approach compared with traditional plate surface chemistries. Optimisation of the surface chemistry and protein coverage has the potential to further improve this finding and coating stability may also benefit from S-layer cross-linking. The demonstrated ability of SbpA-ZZ to recrystallise and detect IgG on low protein binding surfaces may provide a new approach to constructing microarrays and other patterned techniques for the selective attachment of proteins on protein repellent surfaces. Importantly these findings identify that integration of this protein layer within pSi has the potential to improve the sensitivity of the immunosensor.

#### **5.4.7 S-layer Integration into pSi Immunosensor Architecture**

The successful development of a human IgG pSi immunosensor in Chapter 4 combined with the recrystallisation of SbpA-ZZ and successful sensing of IgG and interleukin using ELISA provided a strong basis for the integration and formation of a SbpA-ZZ coated pSi immunosensor. Using the self-assembly properties inherent in the S-layer fusion protein and the findings of the effect of surface properties on lattice structure, a pSi immunosensor was designed utilising SbpA-ZZ as a capture antibody affinity coating on pSi.

##### **5.4.7.1 SEM Surface Characterisation of pSi**

The pSi matrix used for immunosensor development in Chapter 4 was again utilised as the immunosensing transducer in this study. The large pore diameter, 118 nm, and clear pore openings associated with this material are essential for the incorporation of SbpA-ZZ into a pSi sensor (Figure 5.13). According to the results of the AFM studies in Chapter 5 sections 5.4.2.1 and 5.4.4, ozone treatment of the pSi imparts hydrophilic surface properties which should prompt the formation of a ~15 nm S-layer protein bilayer. Self-assembly of these protein layers on the surface of pore walls would effectively reduce pore diameter to ~88 nm while still leaving sufficient room for subsequent immunological reactions (typical IgG dimensions, height 14.5 nm, width 8.5 nm, thickness 4.0 nm [160]). pSi with smaller pore diameters might inhibit diffusion and the formation of immunocomplexes required for immunosensing or even prevent recrystallisation of SbpA-ZZ within the pores due to insufficient space.

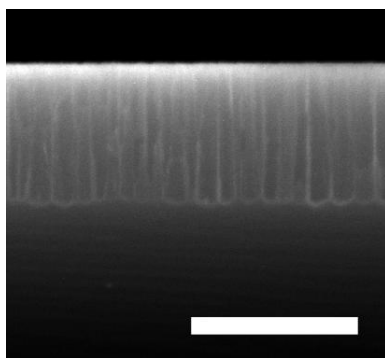


Figure 5.13: Cross-sectional SEM micrograph of n-type pSi used as a scaffold for SbpA-ZZ recrystallisation and sensing experiments. Scale bar 1  $\mu\text{m}$ . For the relevant SEM top-down perspective, refer to Figure 5.4

#### *5.4.7.2 Recrystallisation of SbpA-ZZ within pSi*

Formation of an IgG affinity coating was achieved via self-assembly of SbpA-ZZ protein lattices within pSi. Visual confirmation of recrystallised S-layer within pSi via AFM was not achieved as the surface was too rough and the cross-section of the material could not be imaged. Instead, optical interferometry was used to monitor the self-assembly process on pSi. Figure 5.14 shows the effective optical thickness (EOT) of ozone treated pSi as a function of time, measured by IRS. Once the SbpA-ZZ solution was added to the reaction vessel the EOT increased due to the change of refractive index at the pore interface (transition from buffer,  $n \approx 1.33$ , to protein,  $n \approx 1.45$ ). This effect is related to Equation 4.1, where an increase in refractive index will result in a net increase to the overall EOT of the system. The process began with a rapid increase followed by a gradual slowing of the trend until no further change is observed and recrystallisation was assumed to have completed (12 – 14 hours). After this period the pSi was rinsed with fresh recrystallisation buffer to remove excess protein. Following the initial two washing steps a limited amount of desorption was observed, however by the third rinse the sensorgram stabilised indicating removal of all unbound protein. The profile is indicative of protein adsorption within the pores and suggests successful recrystallisation of SbpA-ZZ within the matrix. As a result of this study all pSi samples used in subsequent immunosensing experiments were incubated with SbpA-ZZ for 18 hours (overnight) to ensure maximum recrystallisation and surface coverage.

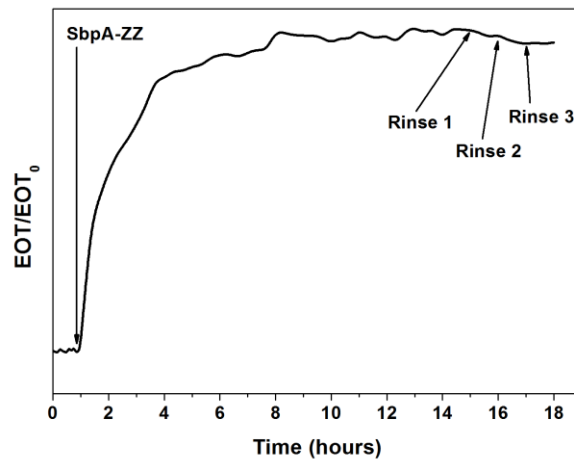


Figure 5.14: EOT sensorgram as a function of time of SbpA-ZZ recrystallisation on pSi. The fusion protein was added at a concentration of 0.1 mg/mL.

#### *5.4.7.3 Detection of Human IgG with SbpA-ZZ Coated pSi Immunosensor*

Confirmation of the recrystallisation/adsorption of SbpA-ZZ on pSi provided a porous platform capable of high density binding of IgG molecules with defined orientation. Formation of the receptor layer was achieved through exposure of the modified pSi to sheep  $\alpha$ -human IgG capture antibody at high concentration, 68.4  $\mu\text{g/mL}$ , in an attempt to saturate the available binding sites (Z domains). Any remaining binding sites and bare pSi was blocked via addition of a non-specific rabbit IgG and 500  $\mu\text{g/mL}$  BSA in separate steps. Immunosensing involved exposure of receptor coated pSi to human IgG antibody, followed by the introduction of an alkaline phosphatase conjugated secondary antibody to form a sandwich assay. Detection of human IgG was achieved via changes to the reflected intensity of the pSi at 600 nm which became reduced upon dephosphorylation of BCIP/NBT in the presence of alkaline phosphatase as described in Chapter 4 section 4.4.5.1.

Figure 5.15 shows a standard curve created from difference concentrations of human IgG on the SbpA-ZZ pSi sensor. As expected, the change in intensity was directly related to the concentration of the human IgG in the system. Samples

containing 0 ng/mL human IgG exhibited small background signals and were considered blanks. The blank measurements were slightly higher than observed on the original pSi immunosensor in Chapter 4, 0.19% difference, which could occur due to increased protein-protein interactions with the S-layer or unsuccessful saturation of the Z domains with capture antibody leading to non-specifically bound analyte. Regardless, the blank levels were still very low and well within acceptable levels for this sensor. As the concentration of human IgG was increased, the corresponding intensity change also increased as expected. Human IgG concentrations between 0 - 500 ng/mL were trialed on this platform and saturation of the sensor was not observed. The S-layer modified pSi only produced a small background signal in the absence of the human IgG analyte (0 ng/mL) indicating low non-specific protein adsorption and no cross-reactivity with the BCIP/NBT enzyme substrate.

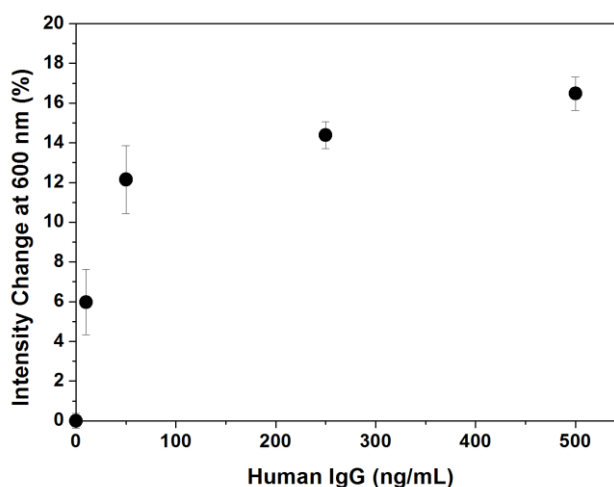


Figure 5.15: Background corrected human IgG standard curve on a SbpA-ZZ modified pSi optical immunosensor platform.

5.4.7.3.1 Comparison of Receptor Immobilisation Techniques and the Effect on Performance

Replacement of the covalent immobilisation of capture antibodies used in Chapter 4 with a self-assembled SbpA-ZZ protein layer resulted in changes to the performance of the human IgG pSi immunosensor technique. Figure 5.16 shows comparison plots of the standard curves and precision profiles, while Table 5.6 contains data on the sensitivity and precision pools of pSi immunosensors prepared using the covalent and SbpA-ZZ approaches. Assessment of the standard curves shows a similar trend in signal response between the two approaches, however, the SbpA-ZZ modified pSi consistently provided a stronger signal over the covalent approach, especially at lower concentrations of the human IgG analyte. This effect was similar to the trend observed in the ELISA experiments (Chapter 5 section 5.4.6) and is indicative of the presence of additional viable capture antibodies on the SbpA-ZZ modified surface. The increase in signal response on SbpA-ZZ pSi had a direct effect on the sensitivity of the sensor, reducing the LOD to 1.24 ng/mL compared with the previous LOD of 2.14 ng/mL achieved on covalently modified pSi. The precision of the sensor was also improved by the incorporation of SbpA-ZZ, demonstrating lower CV values and a much larger working range compared with the original sensor architecture.

These results indicate a general improvement in sensor performance of the SbpA-ZZ modified pSi immunosensor over the previous covalent based approach. This finding may be related to less inhibition of bound capture antibodies on the SbpA-ZZ samples through the selective attachment and orientation of IgG compared with the non-specific covalent attachment which occurred in the previous approach. The theorised uniform orientation of IgG on SbpA-ZZ may have also provided a higher density of capture antibodies within the pores compared with un-aligned covalent attachment (Figures 5.1 and 5.2). Specificity of the SbpA-ZZ pSi immunosensor was not assessed and could not be compared in this section.

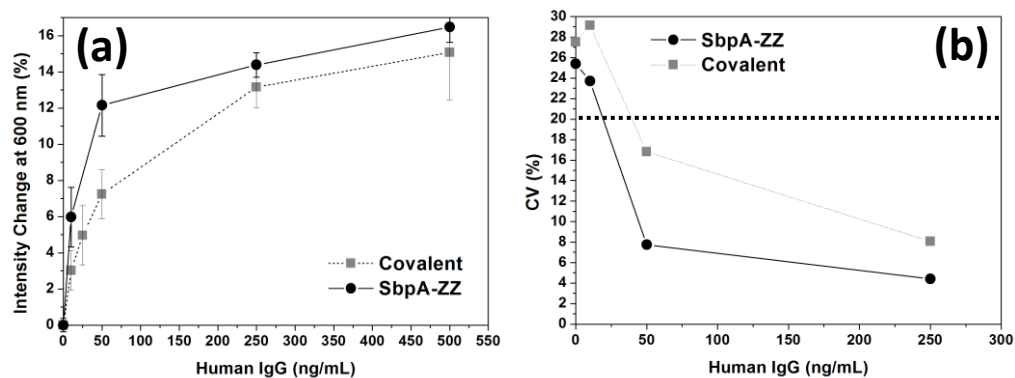


Figure 5.16: Comparison of the human IgG pSi immunosensor prepared using covalent and SbpA-ZZ functionalisation methods. (a) Standard curves for human IgG detection. (b) Precision profiles of the two sensors. The dashed line represents the threshold of the working range of the assay.

Functionalisation	Limit of Detection	Intra-Assay Precision (CV)		
		Low	Medium	High
Covalent	2.14 ng/mL	29.10 %	8.06 %	4.24 %
SbpA-ZZ	1.24 ng/mL	23.71 %	4.40 %	4.83 %

Table 5.6: Comparison of human IgG pSi immunosensor parameters as a function of surface functionalisation. The table contains sensitivity (LOD) and precision (CV) data for human IgG pSi immunosensors prepared using covalent and SbpA-ZZ functionalisation methods. The limit of detection was calculated using the  $3\sigma$  technique and the intra-assay pools correspond to the following concentrations of human IgG analyte, Low – 10 ng/mL, Medium – 250 ng/mL, High – Covalent: 1000 ng/mL, SbpA-ZZ: 500 ng/mL.

## **5.5 Conclusions and Future Directions**

Isolation and purification of the S-layer protein, SbpA, from the bacteria *L. sphaericus* was carried out and the effect of surface conditions on the recrystallisation process has been investigated. Regardless of the surface properties, SbpA was found to successfully recrystallise on solid supports forming crystalline lattices of long-range order with morphological units displaying square, p4 symmetry. Surfaces containing hydrophobic chemical layers resulted in good surface coverage through the formation of protein monolayers with numerous small crystalline domains. Hydrophilic surfaces also saw good surface coverage presumably due to the formation of protein bilayers which displayed the same crystal structure but contained larger crystalline domains. Successful expression and purification of the S-layer fusion protein, rSbpA<sub>31-1068</sub>/ZZ (SbpA-ZZ) from genetically modified *E. coli* was then demonstrated. Successful recrystallisation of SbpA-ZZ was achieved on modified silicon and polystyrene surfaces with the resulting lattice properties correlating with earlier SbpA studies on matching surfaces. The ability of the recrystallised S-layer fusion protein to capture IgG molecules was observed indicating that the fused Z domains were still accessible. Implementation of SbpA-ZZ as an IgG affinity coating was achieved in the ELISA technique where SbpA-ZZ treated surfaces outperformed commercial high protein binding surfaces resulting in improved sensitivity in the detection of human IL-6.

Successful adaptation of SbpA-ZZ as an IgG affinity coating to the pSi immunosensor developed in Chapter 4 has been demonstrated via detection of human IgG. pSi immunosensor performance was enhanced on samples modified with SbpA-ZZ compared to the covalent functionalisation technique previously utilised in Chapter 4. Improvements to sensitivity, precision and working range has provided a more attractive sensor platform capable of detecting low levels of analyte. The results of the ELISA and pSi sensing studies highlight the viability of SbpA-ZZ as a promoter coating for immobilisation of IgG on immunosensing platforms and a range of other applications.

Investigation into and optimisation of the recrystallisation process of SbpA-ZZ on pSi could be considered in future experiments. The use of pSi with larger pores may facilitate a stronger sensor response through improved diffusion and

additional room to perform immunological reactions. The cross-linking of the S-layer structure within pores and/or ELISA microtiter wells may also improve sensor response by preventing desorption of the affinity coating. Adaptation of the SbpA-ZZ fusion protein to other applications may also be considered. Properties such as the ability to recrystallise on low protein binding surfaces like PEG layers or surfaces with hydrophilic properties could form the basis of such applications as patterned IgG microarrays.



# Chapter 6

---

## **6 Enzyme Mediated Signal Enhancement by Silver Reduction on Gold Modified pSi: Towards a New Optical Immunosensor Detection Strategy**

## **6.1 Abstract**

In this chapter the development of a new pSi optical immunosensor detection strategy is presented. Refractive index contrast enhancement by silver deposition on gold treated porous silicon, using silver acetate and hydroquinone, was found to result in a significant decrease to the EOT. Using the magnitude of the EOT change as the sensor readout, the silver contrast enhancement process was optimised on both gold nanoparticle modified pSi and electrolessly gold plated pSi.

Development of enzyme mediated contrast enhancement by silver deposition on gold was then investigated for use with future immunosensors. The synthesis and application of hydroquinone diphosphate (HQDP) as an alkaline phosphatase enzyme substrate was demonstrated. The synthesised HQDP compound was shown to be un-reactive towards silver acetate in its phosphorylated form, but reacted strongly, reducing the silver upon hydrolysis to hydroquinone in the presence of alkaline phosphatase.

Enzyme mediated contrast enhancement by silver deposition on gold plated pSi was then demonstrated and optimised. Finally, adaptation of this system to a pSi optical immunosensor was demonstrated via the detection of human IgG.

## 6.2 Introduction

Silver enhancement of gold has been employed for many years for targeted visualisation of bioconjugated gold nanoparticles (AuNP's) in histochemical microscopy studies [221, 222]. This approach utilises gold promoted deposition of silver metal from a solution of silver ions and a reducing agent such as hydroquinone [221-223]. In these staining applications, gold nanoparticle cores are coated with silver, increasing the size of the particle to micrometer dimensions for easy visualisation with a microscope or the naked eye (Figure 6.1). This ability to enhance or amplify weak signals has led to the adaptation of this system to immunosensing applications such as scanometric assays [224, 225], dot-blot immunoassays [226, 227], immunochromatographic assays [29, 228, 229] and some electrochemical and optical sensors [224, 230].

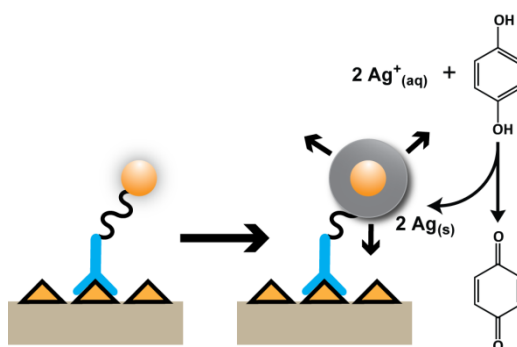


Figure 6.1: Silver enhancement of immunogold. Gold labelled biomolecules target specific analytes and the reduction of silver ions to bulk silver by hydroquinone results in the coating and growth of the gold nanoparticles. In this manner the detection event is amplified improving the sensitivity compared to the use of gold alone.

Silver enhancement of gold within porous silicon could pose an IRS mechanism for the detection of pathogens or other antigens. The material's large surface area coupled with sensitive interferometry reflectance spectroscopy could offer a pathway for the formation of a gold labelled immunological based biosensor. As discussed in Chapter 1 section 1.2, many porous silicon biosensors are based on the interference profile of reflected white light from the material's surface and a

calculated effective optical thickness (EOT). This approach relies on changes to the refractive index within the matrix or changes to the porous structure through degradation or elongation of the pores to provide a sensor response [16, 17, 183]. In the past, label-free detection has been mainly achieved through changes to the refractive index via the addition of biomolecules and the formation of complexes at the pore surface [66, 84]. These systems have demonstrated acceptable results, however amplification of such signals via silver enhancement has the potential to vastly improve the sensitivity of this technique. This is due to the enhancement of refractive index change associated with the biosensing species. Biomolecules such as antibodies and other proteins typically possess a refractive index in the order of  $n \approx 1.45$  and their adsorption/immobilisation within pSi results in the exclusion of buffer or water ( $n \approx 1.33$ ) at the pore interface. This causes an effective refractive index change of  $n \approx 0.1$  within the porous matrix. In contrast, metallic gold and silver possess much lower refractive indices,  $n = 0.45$  and  $0.18$  respectively, and their selective deposition with pSi could result in a much larger change to the refractive index and consequently an increased EOT response (Figure 6.2). The refractive index ‘contrast enhancement’ approach also has the capacity for qualitative analysis through changes to the colour and appearance of the pSi material.

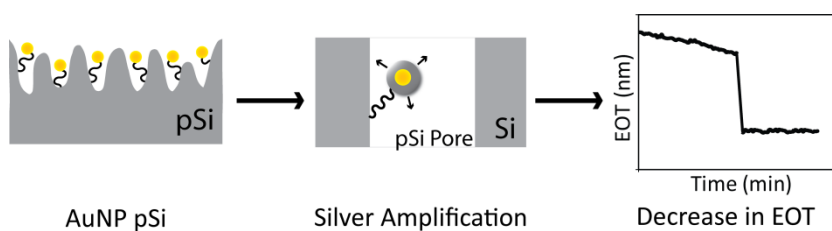


Figure 6.2: Proposed silver enhancement of gold transduction on pSi.

Refractive index contrast enhancement by silver deposition on gold modified porous silicon (silver contrast enhancement) was first achieved via enhancement of immobilised AuNP's within pSi with commercial silver staining reagents. Optimisation of self-made reagents then followed and saw improved EOT response from the enhancement process.

Rather than adapting a gold labelled immunoassay for silver contrast enhancement on pSi, development of a new enzyme mediated enhancement reaction was then undertaken through the use of alkaline phosphatase and the synthesis of the enzyme substrate hydroquinone diphosphate (HQDP). This substrate has been previously reported in literature but it has not been used with porous silicon or for the purpose of silver enhancement [231-234]. Hydrolysis and dephosphorylation of the substrate in the presence of alkaline phosphatase led to the formation of hydroquinone and the subsequent reduction of silver. Specificity of the substrate as a reducing agent was tested and found to only reduce silver in the presence of the enzyme.

Fabrication of electrolessly gold plated pSi was then investigated to act as a promoter surface for the enzyme mediated system. Refractive index contrast enhancement via silver deposition was demonstrated on this surface using alkaline phosphatase catalysed dephosphorylation of HQDP. Finally, detection of human IgG by silver contrast enhancement on gold plated pSi was then demonstrated utilising the HQDP substrate and a sandwich assay containing an alkaline phosphatase conjugated secondary antibody.

## **6.3 Experimental**

### **6.3.1 Preparation of porous silicon**

Porous silicon surfaces were prepared following the procedure outlined in Chapter 3 section 3.3.1. N-type silicon 0.008 – 0.02  $\Omega$ .cm was etched at a current density of 50 mA/cm<sup>2</sup> for 50 seconds.

### **6.3.2 Surface Functionalisation**

#### **6.3.2.1 Oxidation**

Freshly etched pSi samples were oxidised by 1 of 2 methods, ozone or thermal oxidation. The oxidation protocol is described in Chapter 2 sections 2.2.2.1 and 2.2.2.2. Ozone oxidation was extended compared with the general approach and freshly etched pSi received 2 hours exposure to the ozone gas to promote a thicker hydroxyl terminated oxide layer [235, 236].

#### **6.3.2.2 Covalent Immobilisation of Gold Nanoparticles**

##### **6.3.2.2.1 Solution Based Nanoparticle Immobilisation (Method 1)**

Freshly oxidised pSi samples prepared in Chapter 6 section 6.3.2.1 were subjected to silanisation with 50 mM APTES according to the method described in Chapter 2 section 2.2.2.3. A stock solution containing 16 nm AuNP's coated with a monolayer of 11-mercaptoundecanoic acid (MUA) was diluted 1:10 in milliQ water and 0.5 mL added to the pSi sample in a reaction vessel. Following 1 hour incubation, 0.5 mL of 0.4 M EDC + 0.4 M Sulfo-NHS was added to the solution and allowed to react for a further 3 hours. The gold modified sample was rinsed thoroughly with milliQ water and dried under nitrogen ready for use.

##### **6.3.2.2.2 Surface Based Nanoparticle Immobilisation (Method 2)**

Freshly oxidised pSi samples prepared in Chapter 6 section 6.3.2.1 were subjected to silanisation with 50 mM APTES according to the method described in Chapter 2 section 2.2.2.3. 200  $\mu$ L of concentrated AuNP's coated with a monolayer of MUA in milliQ water was pipetted onto the functionalised pSi and left for 1 hour at room temperature. The sample was then placed in an oven for 1 hour at 80°C to ensure drying of the sample to draw the AuNP's into the pores

through capillary actions. The dried sample was then covered with 300  $\mu\text{L}$  of 0.4 M EDC + 0.4 M Sulfo-NHS in milliQ water and incubated at room temperature for 16 hours. The gold modified sample was rinsed thoroughly with milliQ water and dried under nitrogen ready for use.

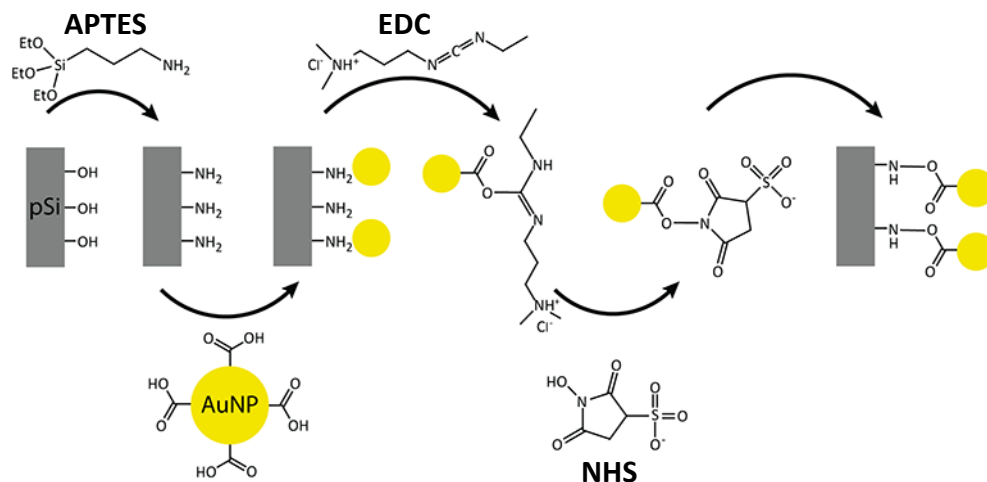


Figure 6.3: Reaction scheme for the covalent attachment of AuNP's on pSi. Oxidised pSi is first silanised with APTES and the sample then exposed to AuNP's and cross-linked to the surface via addition of EDC/NHS.

### 6.3.2.3 Electroless Deposition of Gold within pSi

Electroless deposition of gold within pSi was performed according to Menon *et al.* and Velleman *et al.* with minor changes for adaptation to porous silicon [237, 238]. Freshly ozone oxidised pSi samples were immersed in methanol for 30 minutes to wet the surface. The pSi was then immersed in solution containing 0.026 M  $\text{SnCl}_2$ , 0.07 M trifluoroacetic acid in 50/50 methanol/water for 45 minutes to sensitise the surface. The sample was then removed and washed twice in methanol for a total of 5 minutes. The pSi was then immersed in an aqueous solution of 0.029 M  $\text{AgNO}_3$  for 30 minutes to activate the surface and then rinsed with milliQ water at 4°C for 5 minutes. The silver coated sample was submersed in pre-cooled gold deposition solution, 4°C, pH 8, formulated with 0.079 M  $\text{Na}_3\text{Au}(\text{SO}_3)_2$ , 0.127 M  $\text{Na}_2\text{SO}_3$  and 0.025 M  $\text{NaHCO}_3$  (Au Bath (Alpha)). After seeding gold on pSi the sample was transferred to a new deposition bath which consisted of the same composition with in addition to 0.625 M formaldehyde (Au Bath (Beta)). Deposition times were varied from 30 minutes to 17 hours to optimise the thickness of the gold coating and prevent clogging of the pores. The

gold coated pSi was removed from the solution and rinsed thoroughly with milliQ water. To remove any remaining traces of silver, the pSi was then immersed into a 25% nitric acid solution for 10 minutes. Finally the pSi then received a wash with water, followed by EtOH and was then dried under a stream of nitrogen.

#### 6.3.2.4 Covalent Immobilisation of Biomolecules on Gold Coated pSi

pSi electrolessly plated with gold in Chapter 6 section 6.3.2.3 was immersed in 10 mM MUA in ethanol for 24 hours to promote the formation of a self assembled monolayer (SAM) on the gold surface. Activation of the surface was achieved by immersion of the sample in a solution containing 0.2 M EDC and 0.2 M NHS for 1 hour. The activated surface was rinsed with milliQ water and then immersed in Tris buffer, pH 7.4 containing 10 U/mL alkaline phosphatase (AP) for 2.5 hours to covalently immobilise the enzyme. The surface was then rinsed with Tris buffer and exposed to 10 mM ethanolamine in the same buffer. This step was performed to neutralise any unreacted NHS esters. Bare patches of pSi were blocked through physical adsorption via incubation with 500  $\mu\text{g/mL}$  BSA in the same buffer. Finally the functionalised pSi was immersed in Tris buffer ready for immediate use. Control surfaces only underwent functionalisation with MUA.

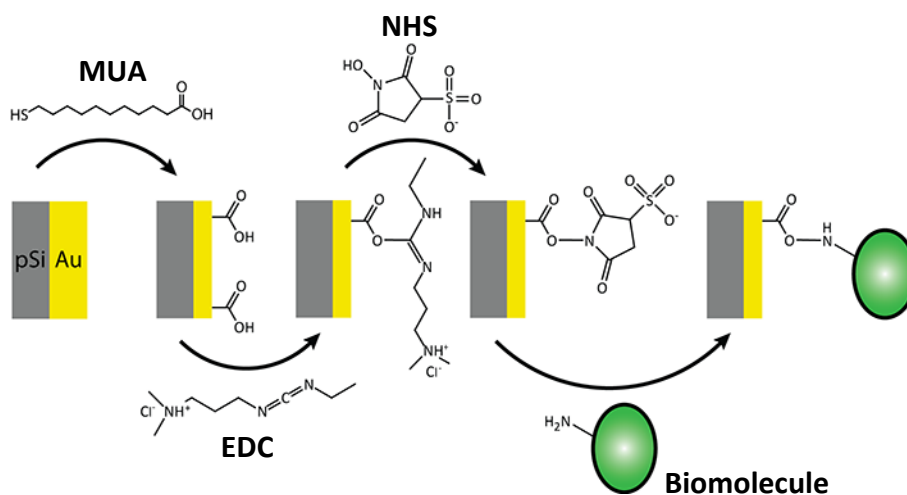


Figure 6.4: Immobilisation of biomolecules to gold plated pSi. Gold deposits are first treated with MUA to form a carboxylic acid terminated SAM. The surface is then activated with EDC/NHS to facilitate covalent immobilisation of enzymes and antibodies.

### **6.3.3 Surface Characterisation**

#### **6.3.3.1 SEM**

Sample preparation and SEM of modified pSi samples was performed as detailed in Chapter 2 section 2.2.3.6.

### **6.3.4 Silver Enhancement of Gold**

#### **6.3.4.1 Silver Contrast Enhancement with a Commercial Enhancing Kit**

Silver enhancement was performed on AuNP modified pSi in an IRS flow cell using Nanoprobes LI Silver Enhancement Kit in accordance with the manufacturer's instructions. An EOT baseline was first established by injecting 10 mL of milliQ water through the IRS flow cell containing the pSi sample and monitoring the surface for 10 minutes. Silver enhancement involved mixing equal volumes of the Nanoprobes enhancer and initiator solutions of which 1.5 mL was then injected through the flow cell and incubated for 10 minutes. During this period the flow cell was shielded from the intense light of the IRS to prevent non-specific reduction of silver. Following enhancement, the flow cell was rinsed with 10 mL milliQ water and the IRS signal reacquired. All EOT measurements reported in this chapter have been normalised to the first EOT measurement taken at time 0 min by dividing each EOT measurement (EOT) over time by the initial value (EOT<sub>0</sub>) to achieve EOT/EOT<sub>0</sub>. The magnitude of the normalised EOT change ( $\Delta\text{EOT}/\text{EOT}_0$ ) upon silver enhancement formed the basis of the sensor readout.

#### **6.3.4.2 Silver Contrast Enhancement with Optimised Reagents**

The customised silver enhancing solution consisted of silver acetate and hydroquinone in citrate buffer, pH 3.8. Separate solutions (A and B) were prepared fresh before each experiment. Solution A consisted of 12 mM silver in milliQ water, while Solution B contained 44 mM of hydroquinone in citrate buffer pH 3.8. Solution A and solution B were then mixed with an equal volume and used immediately to achieve working concentrations of 6 mM silver acetate and 22 mM hydroquinone. IRS analysis of the enhancement process was

performed as described in Chapter 6 section 6.3.4.1, however citrate buffer was used in preference to milliQ water.

### *6.3.4.3 Enzyme Mediated Silver Contrast Enhancement*

#### *6.3.4.3.1 Solution Based*

The silver enhancement solution utilised for solution based enzyme studies consisted of 6 mM silver acetate, 200 mM HQDP and 5 mM magnesium acetate in citrate buffer pH 7.0. To assess the specificity of the HQDP compound, the development approach followed the protocol in Chapter 6 section 6.3.4.2, where separate SA and HQDP solutions were prepared and then mixed together in equal volumes to achieve the working solution. The solution was visually monitored for 30 minutes to assess any physical changes to the properties.

To assess the viability of HQDP as an enzyme substrate for the reduction of silver, 0.375 mL of 10 U/mL AP was added to 1.125 mL of the enzyme silver enhancement solution and the effects visually monitored for 30 minutes. Prior to use, 1 mL of 40 U/mL alkaline phosphatase was dialysed against 1L of citrate buffer, pH 7.0, containing 5 mM magnesium acetate at 4°C to remove the chloride and sulphate salts present in the aqueous enzyme stock. The buffer was changed every hour for 8 hours and left overnight.

#### *6.3.4.3.2 Porous Silicon Based*

The silver contrast enhancement solution utilised for pSi based enzyme studies and immunosensing consisted of 6 mM silver acetate, 100 mM HQDP (22 mM was also trialled briefly) and 5 mM magnesium acetate in citrate buffer pH 7.0. Preparation of separate solutions was not required due to the low reactivity between the silver acetate and HQDP. The solution was therefore freshly prepared before each experiment as one batch in citrate buffer.

Silver contrast enhancement of electrolessly gold plated pSi containing immobilised AP enzyme was performed in an IRS flow cell and firstly involved injection of 10 mL of citrate buffer, pH 7.0 through the flow cell and establishment of an EOT baseline 10 minutes. 3 mL of the enzyme silver contrast enhancing solution was then passed through the cell and incubated with the pSi sample for a further 10 minutes. During this period the flow cell was shielded

from the intense light of the IRS to prevent non-specific reduction of silver. Following enhancement, the flow cell was rinsed with citrate buffer, pH 7.0 and the IRS signal reacquired. The same readout signal,  $\Delta\text{EOT}/\text{EOT}_0$ , as described in Chapter 6 section 6.3.4.1 was used to measure the enhancement response.

### **6.3.5 Organic Synthesis of Hydroquinone Diphosphate**

Hydroquinone diphosphate (HQDP) was prepared following the procedure established by Wilson *et al.* [234]. Hydroquinone (22.71 mmol, 2.5 g) and KCl (1.68 mmol, 125 mg) were added to excess phosphorus oxychloride (268.23 mmol, 25 mL) and the mixture refluxed under nitrogen for 18 hrs. Excess phosphorous oxychloride was removed under vacuum leaving bis(phosphorodichloridate) as an oily residue. The bis(phosphorodichloridate) was hydrolysed to the diphosphate variant by spreading the residue in a glass petri dish and incubating for 72 h in a partially evacuated desiccator containing aqueous sodium hydroxide. The residue was then dissolved in water and the solution adjusted to pH 8.5 by addition of cyclohexylamine. Acetone was then added to initiate crystallization of hydroquinone diphosphate cyclohexylamine salt, which was then converted to the sodium salt by precipitation from methanol using sodium methoxide. The salt was dried at 40 °C in a nitrogen atmosphere for 24 hrs. The resulting salt had an off-white colour and fine consistency. The compound was stored under nitrogen in the dark. NMR and MS analysis were performed as described in Chapter 2 sections 2.2.3.5 and 2.2.3.4.  $^1\text{H}$  NMR (D<sub>2</sub>O)  $\delta$  = 6.9 (s, aromatic), MS 159, 269, 291 m/z. Yield 6.18 g (76% from hydroquinone).

### **6.3.6 Detection of Human IgG by Enzyme Mediated Silver Contrast Enhancement of Gold**

#### **6.3.6.1 Fabrication and Functionalisation of the pSi Sensor Platform**

pSi electrolessly plated with gold for 1 hour was functionalised with MUA and activated with EDC/NHS as described in Chapter 6 section 6.3.2.4. The modified surface was then exposed to Sheep  $\alpha$ -human IgG capture antibody at 68.4  $\mu\text{g}/\text{mL}$  (1:500 dilution) in 1.5 mL PBS for 2 hours. Excess antibody was removed via the washing protocol described in Chapter 4 section 4.3.2 and any remaining

EDC\NHS groups neutralised with 1.5 mL 10 mM ethanolamine in PBS for 30 minutes and bare patches of pSi blocked with BSA as described in Chapter 6 section 6.3.2.4.

#### *6.3.6.2 Human IgG Immunosensor Protocol*

The immunosensing experiment was carried out in an IRS flow cell as described in Chapter 4 section 4.3.7. Slight modifications to the immunosensor timeline and procedure were made to accommodate the inclusion of silver contrast enhancement. The immunosensor protocol followed the timeline detailed in Table 6.1, whereby a sandwich assay was formed on the pSi surface with human IgG and an alkaline phosphatase labelled secondary antibody. Following formation of the immunocomplex, detection of human IgG was achieved by the enzyme mediated silver contrast enhancement on gold plated pSi as described in Chapter 6 section 6.3.4.3.2. The active sensing surface was exposed to 10 µg/mL human IgG, while the control surface was exposed to 0 µg/mL human IgG. Comparison of the overall decrease in EOT/EOT<sub>0</sub> ( $\Delta\text{EOT}/\text{EOT}_0$ ) caused by silver deposition within the pores formed the basis of the sensor readout signal.

Care was taken to ensure the removal of chloride and sulphate salts associated with the PBS and Tris buffers before silver contrast enhancement by flowing 40 mL of citrate buffer through the flow cell in 10 mL aliquots over a 5 minute period. Retention of these salts has the capacity to interfere with the specificity of the enhancement reaction.

Time (min)	Volume	Solution
0 – 10	10 mL	$\alpha$ -human IgG capture antibody immobilised to electrolessly gold plated pSi in PBS, pH 7.4
10 – 30	3 mL	Human IgG
30 – 35	5 mL	Tris-T
35 – 40	10 mL	Tris, pH 7.4
40 – 60	3 mL	1:500 Goat $\alpha$ -human IgG antibody conjugated to alkaline phosphatase
60 – 65	5 mL	0.05% Tween 20 in Citrate buffer, pH 7.0
65 – 70	40 mL	Citrate buffer rinse, pH 7.0
70 – 90	3 mL	Enzyme silver contrast enhancing solution (flow cell shielded from light)
90 – 100	10 mL	Citrate buffer rinse, pH 7.0

Table 6.1: Experimental timeline for the detection of human IgG by enzyme mediated contrast enhancement of gold plated pSi.

## **6.4 Results**

### **6.4.1 Silver Contrast Enhancement on Gold Nanoparticle (AuNP) Modified pSi**

#### *6.4.1.1 Immobilisation of AuNP's on pSi*

Two approaches were implemented for the covalent immobilisation of 11-mecaptoundecanoic acid (MUA) coated 16 nm AuNP's to pSi, a solution based (method 1) and a drying approach (method 2) (Figure 6.5 (g & h)). Method 1 involved incubation of the AuNP solution with pSi to promote diffusion of the particles into the porous matrix, followed by the addition of the cross-linking agents EDC/NHS. Covalent bonding of the carboxylated AuNP's to APTES functionalised pSi via EDC/NHS linkage was expected to immobilise the diffused particles to the pore walls creating a gold decorated porous layer. SEM analysis of treated samples indicated very little diffusion into the porous layer and the presence of large aggregates (Figure 6.5 (a – c)), which suggested that addition of EDC/NHS prompted the aggregation of AuNP's within solution and size exclusion from the pSi. Aggregation may occur due to NHS esterification of the terminal AuNP carboxyl groups which can disrupt carboxyl ionization and cause charge neutralization on the nanoparticle surface. This process then allows colloidal particle aggregation [239]. These structures were not favourable for pSi sensing as the blockage of the pore openings by the large aggregates would interfere with the reflected optical profile of the material and the low surface coverage would ultimately limit the achievable EOT response of the material.

Following this result, an alternate immobilisation approach was developed. Similar to method 1, method 2 involved 1 hour incubation of AuNP solution with APTES pSi to allow diffusion, however following this step the pSi sample was placed into an oven to evaporate the water medium and promote AuNP entry into the pores via capillary actions. Once dried the sample was then exposed to a small volume of concentrated EDC/NHS to cross-link the AuNP's to the surface. Figure 6.5 (d – f) shows the successful integration of AuNP's within the porous layer using this approach. The majority of the porous surface exhibited uniform coverage of NP's as depicted in Figure 6.5 (e) with minimal aggregates observed. Good pore penetration was also achieved, with NP's observed along the entire pore length. The relative uniformity of the AuNP coverage provided a suitable

platform for subsequent silver enhancement studies. It should be noted that the cross-sectional perspective in Figure 6.5 (f) is not indicative of the typical porous structure utilised in this Chapter and was etched at a lower current density, 35 mA/cm<sup>2</sup>, which resulted in high branching. It was included in this figure only to demonstrate the penetration of AuNP's within pSi.

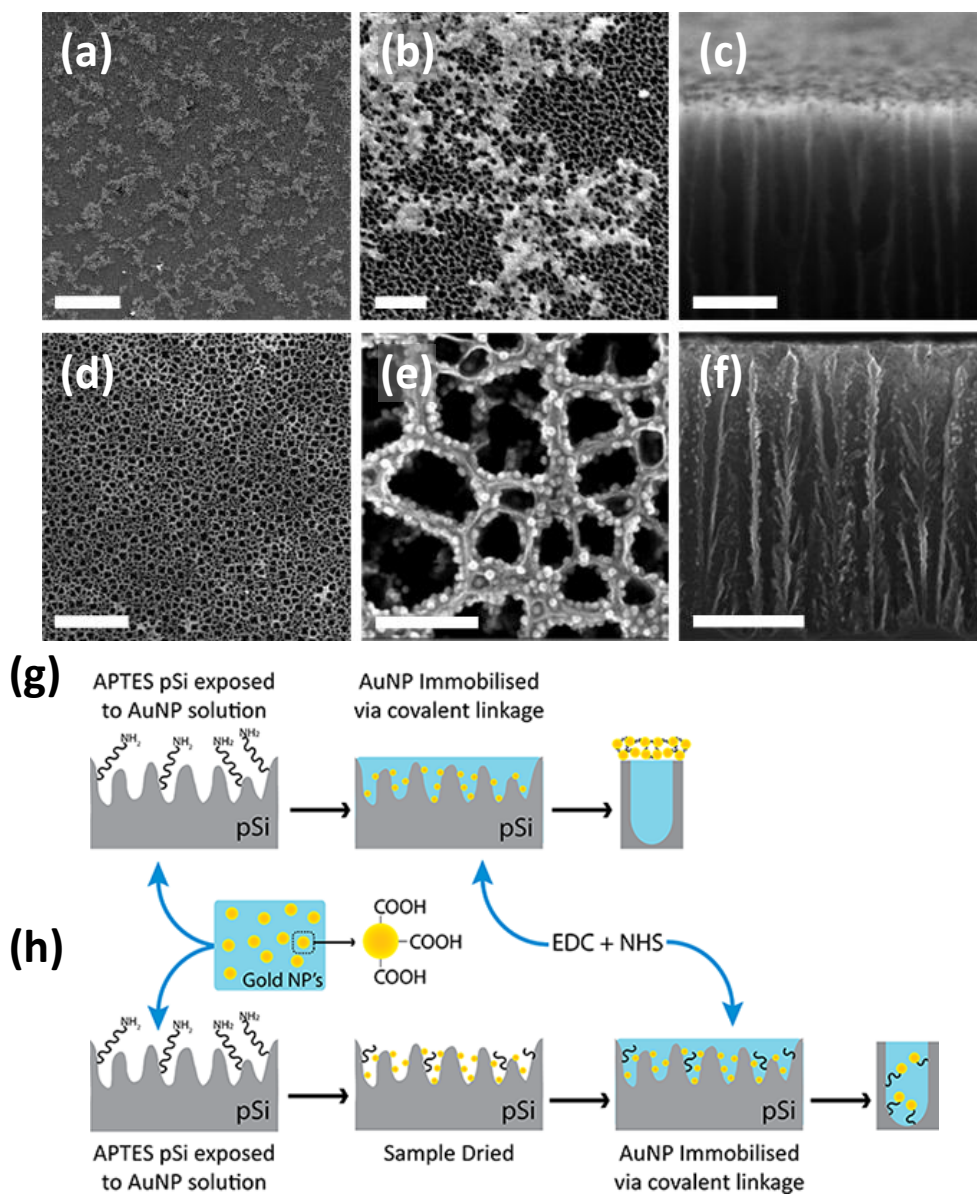


Figure 6.5: SEM micrographs of covalently immobilised gold nanoparticles on pSi. (a),(b)&(c) Solution immobilisation approach (Method 1). Respective scale bars 25 μm, 500 nm, 250 nm. (d),(e)&(f) Drying immobilisation approach (Method 2). Respective scale bars 2μm, 200 nm and 500 nm. The sample in (f) was not indicative of the normal porous structure and was etched at 35 mA/cm<sup>2</sup>. Its presence is merely to demonstrate propagation of AuNP's within the pores. (g) Schematic representation of method 1 protocol and (h) method 2.

#### *6.4.1.2 Silver Enhancement of AuNP pSi*

##### *6.4.1.2.1 Enhancement of AuNP pSi with Commercial Silver Enhancing Solution*

In order to demonstrate silver enhancement of gold on pSi, AuNP modified pSi was exposed to a commercial silver enhancing solution designed for use in histochemical studies. The effect of the enhancement process on the EOT of the porous layer was monitored over time using IRS as shown in Figure 6.6. The IRS readout signal was normalised by dividing the EOT over time by the initial EOT at time 0 minutes to achieve  $EOT/EOT_0$ . During the silver enhancement process, the surface was not monitored, as the IRS probe was blocked and the flow cell covered with thick material to prevent non-specific deposition of silver from exposure to intense light. As such, the effect of silver enhancement on EOT was determined by comparing the EOT baseline prior to and following exposure to the enhancing solution. Figure 6.6 shows the response of silver contrast enhancement of AuNP's on pSi prepared using both method 1 & 2. Both types of surfaces demonstrated a decrease in EOT indicative of a reduction to the refractive index within pSi from the deposition of silver. Comparison of the two immobilisation protocols identified a larger decrease on the surface functionalised via method 2. This was expected as AuNP coverage was more comprehensive in comparison with pSi samples prepared using method 1, facilitating a greater change in refractive index within the porous matrix. This theory is supported by electron microscopy which identified silver deposition throughout the pores and at the surface on method 2 samples, while samples prepared under method 1 only demonstrated silver deposition outside the pores (Figure 6.7). Analysis of the SEM micrographs implies that silver deposition is seeded by the gold and grows from a spherical shape into larger amorphous structures. Silver growth on gold aggregates shown in Figure 6.7 (a)&(b), demonstrated increased deposition and larger silver particles for the same exposure time. This may be due to the increased number of nucleation sites on AuNP aggregates compared to the individual nanoparticles within pSi samples prepared using method 2.

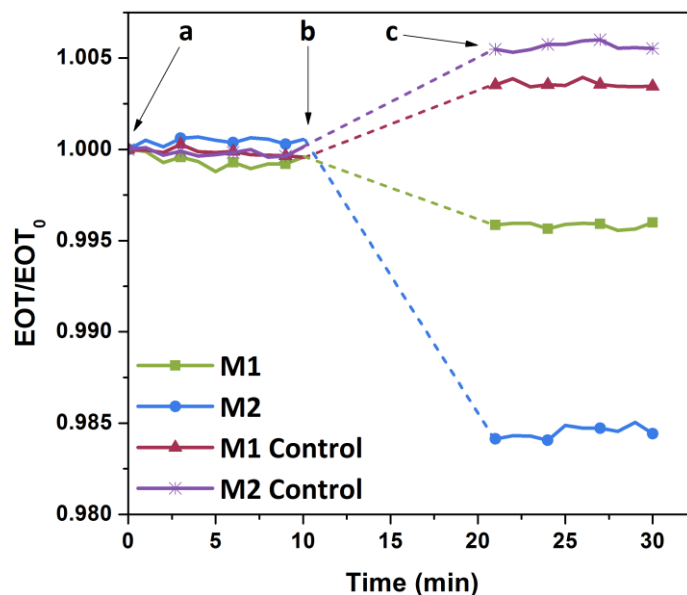


Figure 6.6: Silver enhancement of AuNP pSi prepared under method 1 (M1) and method 2 (M2) using commercial reagents. (a) pSi baselined in milliQ water. (b) Sample shielded from light and “Nanoprobes LI” silver enhancement solution injected into the flow cell. (c) MilliQ water rinse and reacquisition of the sample.

Control surfaces consisting of APTES functionalised pSi did not experience a decrease in EOT upon exposure to the silver enhancing solution but instead generated a positive increase (Figure 6.6). This suggested that silver was not deposited within the pSi; instead, the positive trend indicates the retention of a substance with a refractive index higher than water. This may be explained by the presence of compounds such as gum arabic ( $n = 1.476$ ) which is found in many silver autometallography protocols to increase stability and specificity of the developer solution [221, 240, 241]. While the exact composition of the proprietary ‘LI Silver’ solution is not known, such viscous compounds possessing a higher refractive index than milliQ water may remain in the system after the rinsing step at 20 minutes, thus providing an increase in the overall EOT signal. This effect would occur on the active surfaces as well, but has been overwhelmed by the deposition of silver.

The strength of the EOT signal observed on pSi samples prepared under method 2, coupled with SEM observations, suggested that this approach achieved a more sensitive platform compared with pSi prepared using method 1. As a result

method 2 was used as the default functionalisation approach in subsequent investigations.

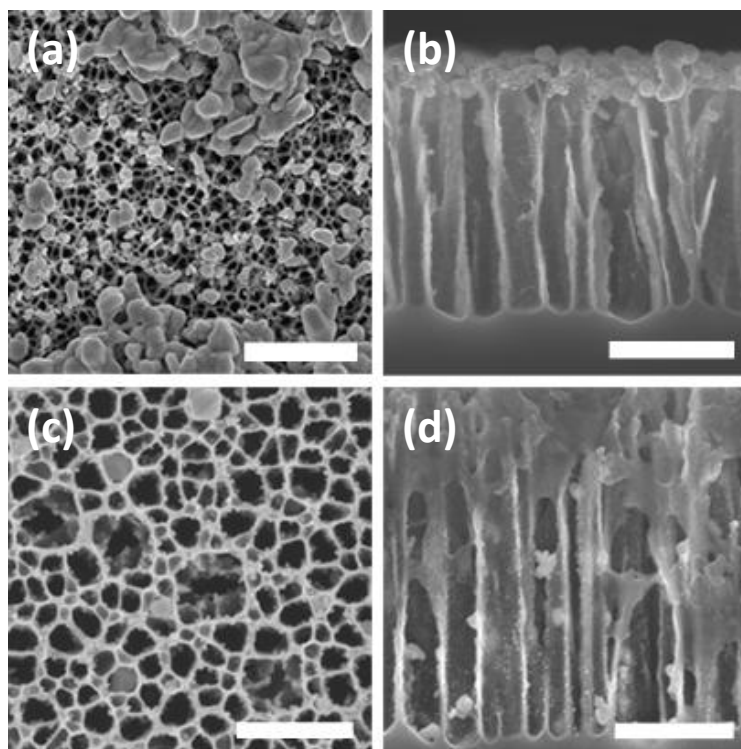


Figure 6.7: SEM micrographs of silver contrast enhancement on gold nanoparticle decorated pSi. (a)&(b) AuNP's immobilised via method 1. Respective scale bars 1  $\mu$ m and 250 nm. (c)&(d) AuNP's immobilised via method 2. Scale bars both represent 500 nm.

#### 6.4.1.2.2 Enhancement of AuNP pSi with Silver Acetate and Hydroquinone

Removal of the non-specific positive EOT change observed on APTES pSi control surfaces was investigated through the preparation and optimisation of custom silver enhancing solutions. Many sources in literature reported good enhancement of gold with either silver lactate or silver acetate in the presence of a hydroquinone reducing agent at low pH [221, 240]. Silver acetate was chosen proceeding forward as it is the least light sensitive of the two compounds, reducing the potential for non-specific responses [221]. Concentrations of 6 mM silver acetate and 22 mM hydroquinone were used in the enhancing solution as many histochemical staining studies have demonstrated controlled silver growth

and improved specificity compared against high concentrations [221]. Subsequent silver enhancement was conducted on AuNP modified pSi prepared using method 2 in citrate buffer, pH 3.8, the results of which appear in Figure 6.8 (a). The EOT sensorgram depicts a larger decrease ( $\Delta EOT/EOT_0 = 0.019$ ) from silver enhancement performed with custom reagents compared to the commercial Nanoprobes reagents used previously ( $\Delta EOT/EOT_0 = 0.004$ ). Importantly, it was also apparent that the APTES functionalised pSi control surface no longer experienced an increase in EOT. Instead, a decrease in EOT was observed, suggesting a small amount of non-specific adsorption of silver to the pSi surface. This finding indicates that the increase in EOT observed for the commercial silver enhancing solution was due to the presence of gum arabic or a similar compound as its removal through the preparation of custom silver enhancing solutions nullified the positive non-specific signal.

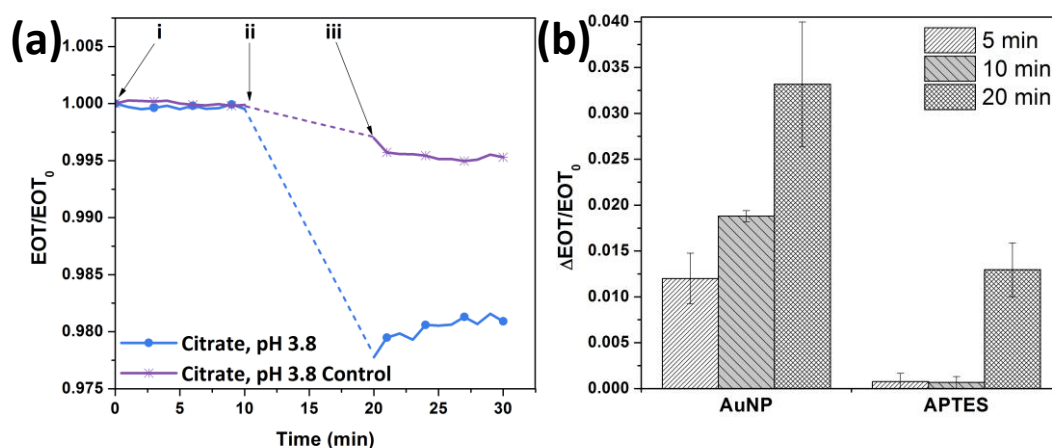


Figure 6.8: Silver enhancement of AuNP's on pSi with 6 mM silver acetate and 22 mM hydroquinone in citrate buffer, pH 3.8. (a) EOT sensorgram of silver enhancement on AuNP modified pSi and APTES pSi. (i) AuNP modified pSi baselined in citrate buffer, pH 3.8. (ii) Sample shielded from light and silver enhancement solution injected into the flow cell. (iii) Surface rinse and reacquisition of the sample. (b) Effect of the silver contrast enhancing solution exposure time on the EOT response of AuNP modified pSi.

Following the successful enhancement of AuNP's on pSi with silver acetate and hydroquinone, the effect of exposure time on EOT was investigated. Silver acetate/hydroquinone (SA/HQ) was exposed to AuNP surfaces prepared with method 2 for 5, 10 and 20 minutes and the change in EOT monitored (Figure 6.8 (b)). As expected, the results showed that as exposure time was increased, the overall EOT response on AuNP surfaces increased via additional deposition of silver metal within the pores. However, analysis of the APTES pSi control surfaces showed a dramatic increase in the non-specific signal at 20 minutes compared against the 5 and 10 minutes counterparts. This event at 20 minutes marks the point at which the system no longer requires gold nucleation to generate an EOT signal and deposition of silver solely due to the SA/HQ reaction takes precedence. Subsequently, following experiments utilised 10 minutes exposure to the SA/HQ enhancing solution to ensure a specific signal from enhancement of gold and a good S/N ratio between the active and control surfaces. The successful enhancement of AuNP's on pSi and ability to register a change in the EOT of the material via interferometric optical transduction was promising. This technique has potential to act as a new sensor platform for the enhancement/amplification of gold labelled biomolecules for the detection of various analytes.

#### **6.4.2 Enzyme Mediated Silver Deposition on Gold Coated pSi**

The strong EOT response achieved through the silver enhancement of AuNP modified pSi has identified a potential new method of biological sensing. Development of this system with traditional gold labelled immunoassays certainly has merit and should be investigated long-term. However, other more novel approaches may be available. Development of enzyme mediated silver deposition was therefore investigated as a new form of analyte detection. Such a system could potentially be more versatile than the gold labelled approach and could find application in many different fields. In order to achieve this goal, synthesis of a phosphorylated variant of the silver reducing agent hydroquinone can provide a pathway for the catalysed reduction of silver by phosphatase enzymes. Wilson *et al.* have shown that hydroquinone diphosphate (HQDP) can be readily synthesised and used as a substrate for the enzyme alkaline

phosphatase in electrochemical sensors, however this compound has yet to be utilised on pSi or in silver deposition applications. Integration of this compound can provide the basis for an immunoassay sensor which utilises an alkaline phosphatase conjugated secondary antibody as a specific detection event.

#### *6.4.2.1 Electroless deposition of Gold on pSi*

Electroless deposition of metals, particularly gold, has been demonstrated on porous substrates, such as porous alumina, to form gold nanotubes and rods for various applications [238, 242, 243]. Here, for the first time, the process has been successfully adapted to pSi for silver contrast enhancement purposes. The proposed HQDP enzyme based silver deposition system does not require traditional gold labelled biomolecules for enhancement and can instead use pre-gold plated sensing platforms as a promoter surface. Electroless deposition of gold within pSi was investigated to form such a coating as this approach has advantages over electrolytic approaches due to the slower deposition rate and ability to coat low-conductivity materials [237, 238, 242, 243]. Improved coverage and increased amounts of gold within the pores via electroless deposition has the potential to promote additional silver growth and a stronger signal response in comparison to the AuNP surfaces previously investigated in Chapter 6 section 6.4.1.2.2.

Initial investigation into the electroless deposition of gold on pSi involved variation to the deposition time in Au bath (beta) to optimise gold coverage. The pSi utilised for this study was oxidised under ozone gas to achieve a Hydroxylated surface, a functionality which has been identified as a promoter of gold deposition through enhanced electrostatic interactions with tin ions involved in sensitisation (Figure 6.9) [238, 242].

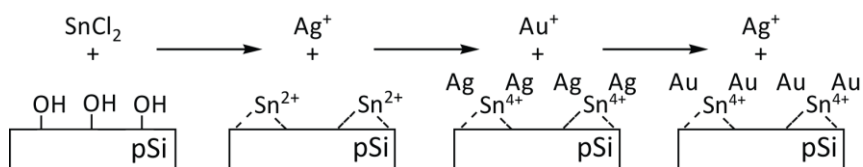


Figure 6.9: Electroless deposition of gold reaction scheme. The electroless deposition process described in Chapter 6 section 6.3.2.3 first involves the sensitisation of the porous silicon surface with tin cations through electrostatic interactions. The sensitised porous layer is then ‘activated’ with silver nitrate which causes a redox reaction in which  $\text{Sn}^{2+}$  is oxidised to  $\text{Sn}^{4+}$  and aqueous  $\text{Ag}^+$  ions are reduced to bulk silver, coating the porous surface with silver particles. Gold deposition then occurs in solution through the galvanic replacement of the silver particles by the more noble metal and growth of these particles into a coating or film is achieved by the concurrent reduction of  $\text{Au}^+$  to bulk gold by formaldehyde. Variation to the deposition time is used to achieve gold coatings of different coverage and thickness [238, 242, 243].

Figure 6.10 shows SEM micrographs of electroless deposition of gold on ozone oxidised pSi. Exposure times of 0 hours (a – b), 0.5 hours (c – d), 5 hours (e – f) and 17 hours (g – h) to Au bath (beta) were investigated. SEM cross-sectional analysis identified the presence of very small sparsely separated nanoparticles throughout the pSi samples at 0 hours which should consist of silver or gold growths deposited during the activation or preliminary gold deposition step in Au bath (alpha). Following 30 minutes exposure to Au bath (beta) many of the nanoparticles had begun to grow in size, forming large particles within the pores. Surface coverage of these particles may actually be greater than shown in the micrographs, as the fracturing process required to achieve cross-sectional analysis may have dislodged some of the gold material from the pores. However, after 5 hours of gold deposition the particles had clearly multiplied and merged to coat the majority of the pore surfaces forming gold nanotube-like structures and by 17 hours the gold had formed into solid nano-rods. Top-down analysis identified a restricting of the pore openings with nanoparticle growth until an almost solid layer is formed by 17 hours deposition. The gold coverage within the pores was considerably improved in comparison to the previous nanoparticle approaches in Chapter 6 section 6.4.1.1, with better pore penetration and larger deposits of gold occurring after just 30 minutes deposition time.

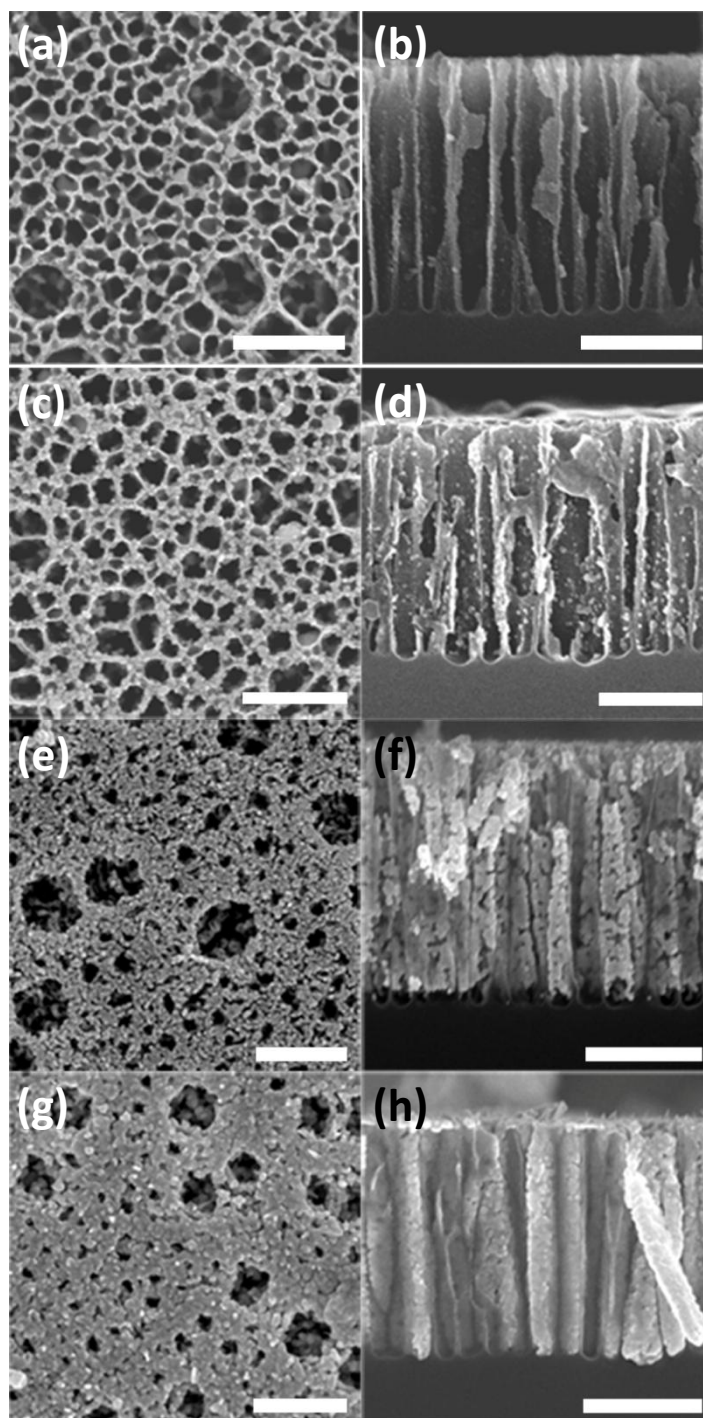


Figure 6.10: SEM micrographs detailing the extent of gold deposition within the porous matrix as a function of exposure time to Au bath (beta). The left column represents a top down perspective of the porous surface, while the right column displays the corresponding cross-sectional view. All surfaces were exposed to Au bath (Alpha) for 2 hours before immersion in Au bath (beta) for: (a)&(b) 0 hours, (c)&(d) 30 minutes, (e)&(f) 5 hours and (g)&(h) 17 hours. All scale bars represent 500 nm.

Study into the impact of gold deposition time on the reflected fringe pattern and EOT of pSi was also investigated (Figure 6.11). As exposure time to the gold solution increased, the fringe pattern began to lose coherency and completely disappeared after 2 hours. The cause of this phenomenon can be attributed to the growth of the rough surface layer and disruptive deposits of metal within the pores observed in the SEM analysis. These rough structures contribute to a degraded optical signature by reflecting and/or scattering the incident light, preventing nominal white light interference from the pSi. This theory was supported by the darkening of gold treated pSi with time which is indicative of increased light scattering similar to anti-reflective coatings. Taking into account sample-sample variability, EOT of the gold coated pSi showed a general decrease over time, in accordance with gold's lower refractive index. Due to the detrimental effect of longer deposition times on the reflected profile of pSi, only treatment times of  $\leq 1.5$  hours were deemed viable as potential sensor platforms.

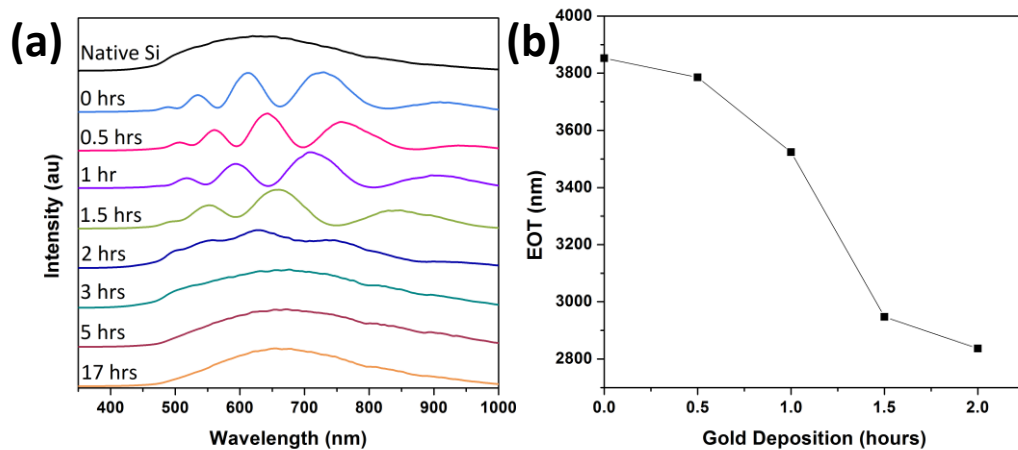


Figure 6.11: Effect of electroless deposition of gold on the optical properties of pSi. (a) Change experienced by the reflected fringe pattern as a function of deposition time. (b) Change to the calculated EOT of the porous layer as a function of deposition time.

*6.4.2.2 Silver Contrast Enhancement of Electrolessly Deposited Gold on pSi with SA/HQ*

Silver contrast enhancement of electrolessly plated Au/pSi with SA/HQ was carried out on samples subjected to 0, 0.5 and 1 hour gold deposition, the results of which appear in Figure 6.12 (a). By monitoring the EOT of the porous layer over time it was observed that all samples experienced a decrease in EOT commonly associated with silver contrast enhancement. As expected the 0 hour sample registered the smallest change,  $\Delta\text{EOT}/\text{EOT}_0 = 0.00619$ , due the low levels of gold at the surface. The extent of the EOT change then increased with respect to Au plating time, with the 1 hour sample registering the largest response,  $\Delta\text{EOT}/\text{EOT}_0 = 0.0396$ . The signal response from these surfaces suggests that the presence of additional gold within the pores promotes faster and/or greater deposition of silver within the pores due to the larger surface area and increased nucleation [223]. pSi samples subjected to 1.5 and 2 hours gold deposition were also trialled, yet following silver enhancement, the fringe patterns began to lose coherency until the reflected profile resembled bulk silicon (Figure 6.12 (b)). As a result, the EOT calculations were inaccurate and these surfaces were considered unviable at 10 minutes exposure. This effect on the fringe pattern may be attributed to increased silver growth blocking the pores, disrupting the interference effect and causing increased reflection. Using the 1.5 hours Au/pSi sample with a shorter silver exposure time, i.e. 5 minutes, may have potential as a sensor platform, however it was not investigated as part of this study.

The ability to tailor the amount of gold within the porous matrix by controlling deposition time provided a method to optimise the platform's signal. The subsequent findings of this study identified that pSi coated with electrolessly deposited gold can achieve a stronger enhancement signal than the previous AuNP system and is suitable for incorporation into an enzyme based silver contrast enhancement system.

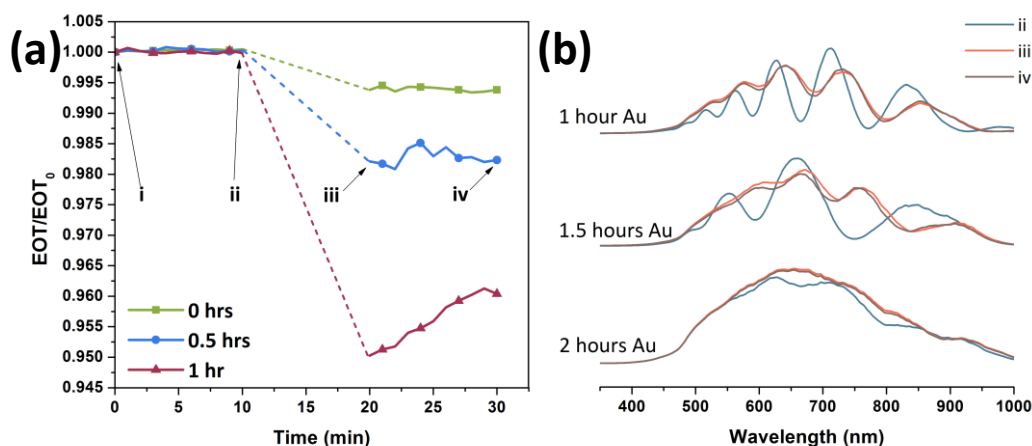


Figure 6.12: Silver contrast enhancement of electrolessly deposited gold on pSi with silver acetate and hydroquinone. (a) EOT sensorgram of silver contrast enhancement on pSi subjected to varying degrees of gold deposition. (i) Gold plated pSi baselined in citrate buffer, pH 3.8. (ii) Sample shielded from light and silver contrast enhancement solution injected into the flow cell. (iii) Surface rinse with citrate buffer and reacquisition of the sample. (iv) Final point in the acquisition. (b) Effect of silver contrast enhancement of gold on the reflected fringe pattern of pSi.

#### 6.4.2.3 Organic Synthesis

Hydroquinone Diphosphate, HQDP, was synthesised as a alkaline phosphatase enzyme substrate. This compound was created to allow the selective deposition of silver on gold plated pSi surfaces for the detection of analytes via optical transduction. The substrate was synthesised through the esterification of hydroquinone with phosphorus oxychloride as shown by the reaction scheme in Figure 6.13 (a). The product, bis(phosphorodichloridate), was separated from excess phosphorus oxychloride under vacuum and hydrolysed to the HQDP phosphate form in the presence of water vapour. Preparation of an aqueous solution of the HQPD in the presence of cyclohexylamine formed the subsequent salt which was then isolated via crystallisation in the presence of acetone. Conversion to the sodium salt was achieved via precipitation from methanol containing sodium methoxide. NMR and Electrospray Mass Spectroscopy (MS)

analysis showed that the product had been successfully produced, although MS also identified the presence of a hypodiphosphoric acid bi-product (Figure 6.13 b & c). There is potential for competitive inhibition of alkaline phosphatase by the inorganic phosphate bi-product [244, 245], however the contaminant was not removed from the final product as previous investigations in literature employing this synthesis/purification method have successfully utilised the resulting HQDP product as an alkaline phosphatase substrate without further purification [234].

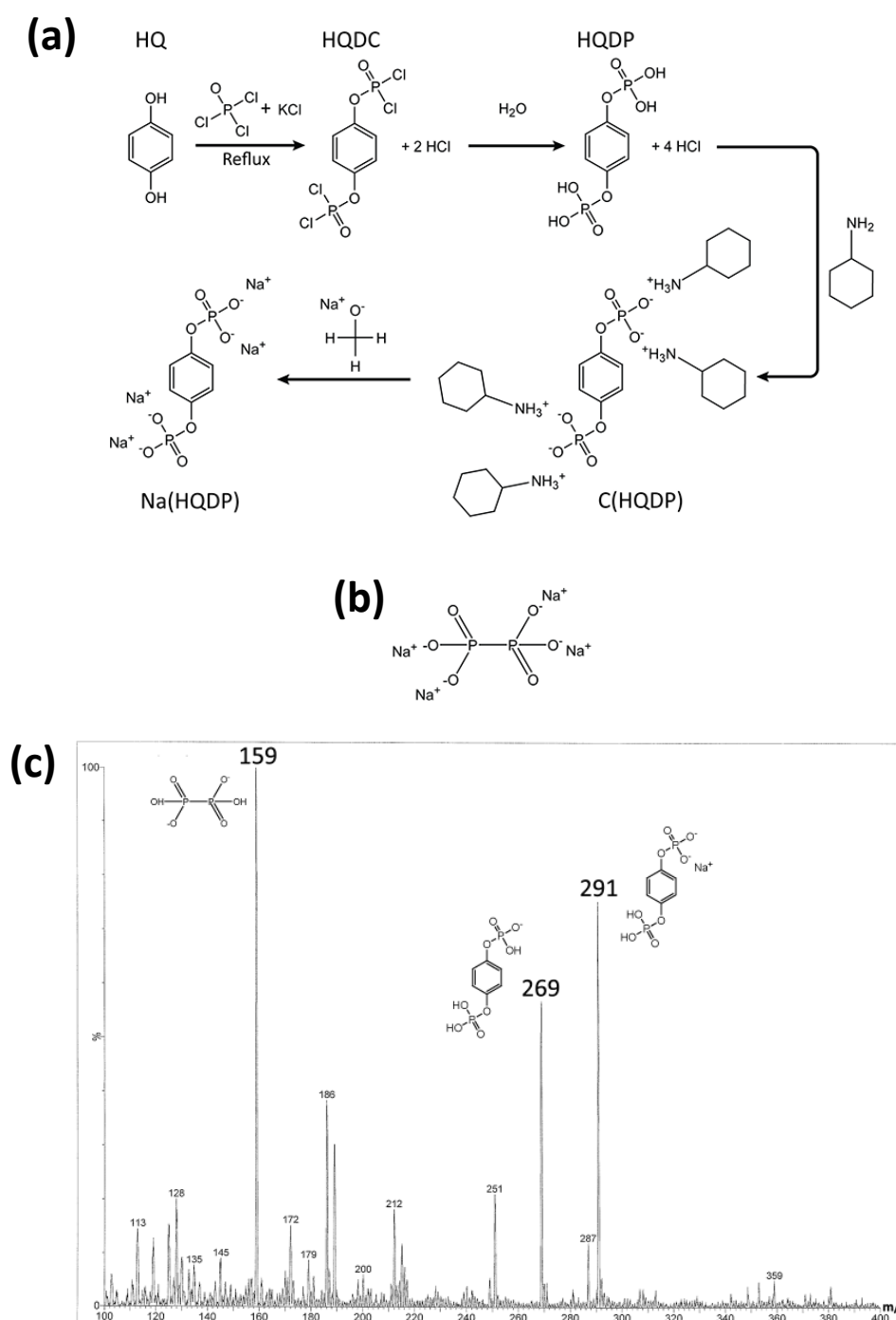


Figure 6.13: (a) Organic synthesis of hydroquinone diphosphate (HQDP). HQ – Hydroquinone; HQDC – bis(phosphorodichloridate); HQDP – Hydroquinone diphosphate; C(HQDP) – Cyclohexylamine salt; Na(HQDP) – Sodium salt. (b) Hypodiphosphoric acid sodium salt bi-product. (c) Electrospray Mass Spectroscopy spectrum of aqueous Na(HQDP) solution. The major peaks at 269 and 291  $m/z$  relate to the HQDP compound, while the other major peak at 159  $m/z$  represents the presence of a bi-product.

#### 6.4.2.4 Silver Contrast Enhancement on Gold pSi with Alkaline Phosphatase, SA and HQDP

The successful enhancement of electrolessly gold plated pSi provided a suitable platform on which to assess the viability of the synthesised enzyme substrate HQDP. The proposed enzyme catalysis pathway is represented in Figure 6.14 and shows the dephosphorylation of HQDP by alkaline phosphatase resulting in the formation of hydroquinone which is then able to reduce silver acetate to bulk silver.

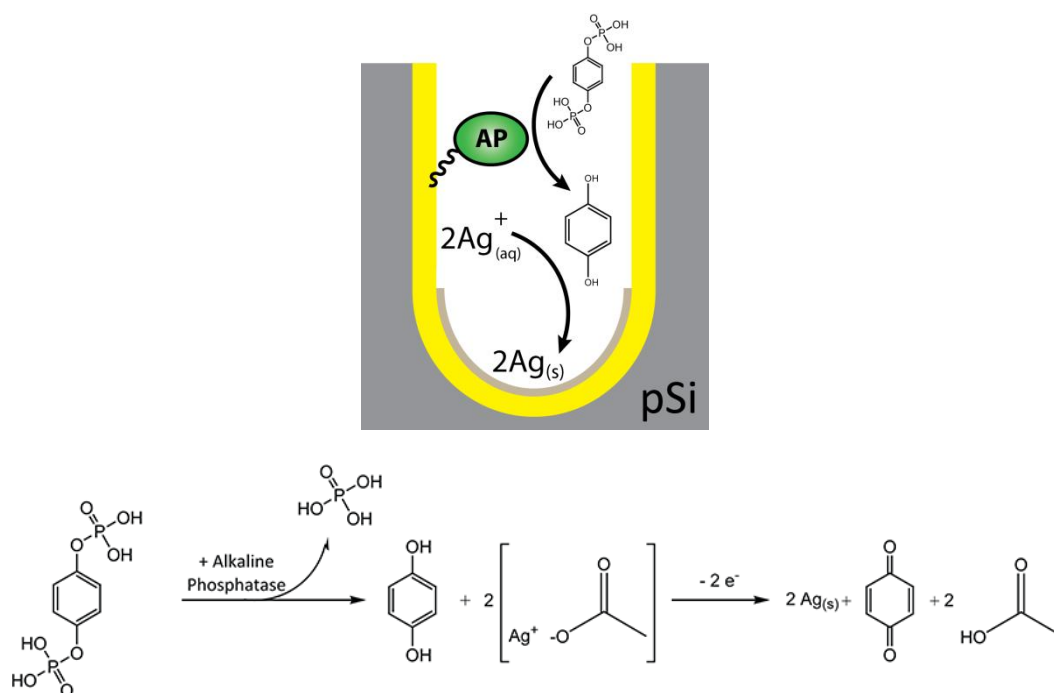


Figure 6.14: Schematic and scheme of the proposed reaction pathway for enzyme mediated reduction of silver on gold plated pSi.

Adaptation of the silver deposition process to a complex enzyme based immunological system introduced many complications compared with the model SA/HQ system demonstrated in Chapter 6 section 6.4.2.2. The presence of salts in buffers used to stabilise and facilitate immunological reactions can negatively impact the specificity and efficiency of silver reduction and acidic pH levels can affect protein-protein binding between antibodies [246, 247]. Silver enhancement is possible at neutral pH and has been demonstrated to achieve well-controlled and specific development of AuNP's with less biological impact compared with enhancement at pH 3.8 [241, 247]. As a result, buffers were formulated without

chloride and sulphate salts and mild pH levels were investigated. The isoelectric point,  $pI = 5$ , of the enzyme, bovine intestinal alkaline phosphatase, made it an acceptable choice in this preliminary investigation as it can function over the pH range of  $\sim 5.5 - 10$ , although it exhibits substantially lower activity in acidic conditions and ultimately inhibition below pH 6 [248-250].

The reactivity of the synthesised HQDP towards silver acetate (SA) was first assessed by diluting the substrate in citrate buffer, pH 7.0, containing SA. The appearance of the solution was not altered after 30 minutes incubation, indicating that the phosphorylated variant of HQ was no longer capable of reducing silver (Figure 6.15). Addition of alkaline phosphatase initiated the formation of a grey compound which subsequently darkened and precipitated overtime. Reaction of HQ with SA under the same conditions produced the same effect, although the formation of the precipitate and colour change occurred much faster (image not recorded). This initial result indicated the synthesised HQDP substrate was not reactive towards silver acetate and suggested successful hydrolysis of the HQDP molecule by alkaline phosphatase to catalyse the reduction of silver.

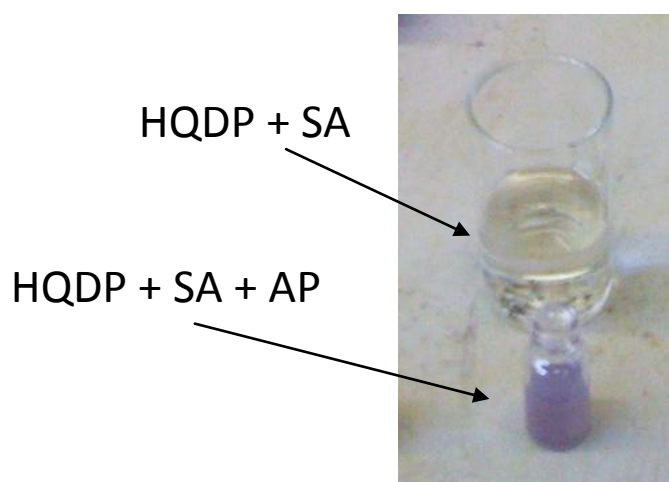


Figure 6.15: Reactivity of hydroquinone diphosphate (HQDP) to silver acetate (SA) and the reduction of SA by alkaline phosphatase (AP) mediated hydrolysis of HQDP to hydroquinone in solution.

Silver contrast enhancement of gold plated pSi containing immobilised alkaline phosphatase was then investigated and the results appear in Figure 6.16 (a). Enzyme mediated silver contrast enhancement was successfully demonstrated at pH 7.0 with a noticeable contrast between the surface containing AP and the MUA control surface. However the EOT signal was much lower than previously achieved with the acidic SA/HQ system and contained a far greater background signal, decreasing the signal to noise ratio of the system from 6.4 to 1.7 (Table 6.2). Enhancement of gold plated pSi with SA/HQ at pH 7.0 yielded a much improved response ( $\Delta EOT/EOT_0 = 0.047$ ) compared to the enzyme based approach ( $\Delta EOT/EOT_0 = 0.009$ ), which was limited by enzyme kinetics and the formation of HQ. This large response from SA/HQ indicated that the platform was capable of achieving a stronger silver contrast enhancement signal in 10 minutes exposure at neutral pH compared against acidic conditions. The improved effect is caused by faster silver deposition at neutral conditions which has been observed in previous histochemical silver staining studies [221, 241, 247].

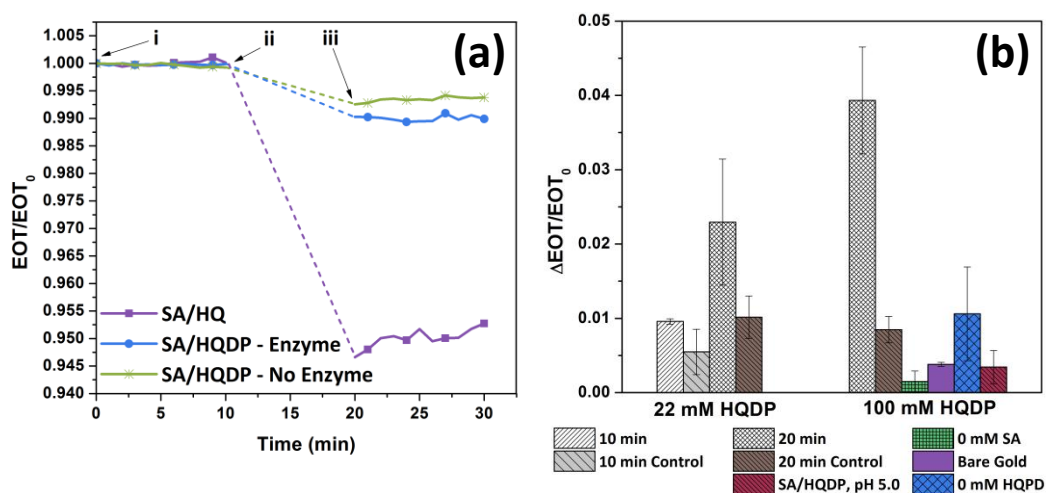


Figure 6.16: Alkaline phosphatase mediated silver contrast enhancement of electrolessly gold plated pSi. (a) EOT sensorgram of silver contrast enhancement in citrate buffer, pH 7.0. The plot represents both enzyme based (6 mM SA, 22 mM HQDP) and SA/HQ (6 mM SA, 22 mM HQ) enhancement. i – Citrate buffer, pH 7.0, ii – Enzyme silver contrast enhancing solution, iii – Citrate buffer, pH 7.0. (b) Combined sensor responses for the optimisation of the enzyme based system and relevant controls.

The low response observed for the AP based system was therefore considered to relate to the enzyme, substrate, reaction time or a combination of all three factors. AP is known to demonstrate much less activity at pH 7.0 compared to its optimal pH range 8 – 10 and as such exhibits slower reaction kinetics [249]. To compensate for this factor the length of the silver contrast enhancing step was extended to 20 minutes to promote additional formation of the HQ reducing agent. The response from this experiment appears in Figure 6.16 (b). As expected, the extended reaction time led to an increase in the magnitude of the EOT change by a factor of 2.3 compared with the previous 10 minute exposure. The background signal on the control sample was also affected by the prolonged exposure, doubling in magnitude in accordance with non-specific adsorption behaviour which will be discussed later.

The concentration of the substrate was then assessed as a cause of the low signal response. The HQDP substrate had been applied at 22 mM in accordance with the HQ concentration utilised in the earlier model SA/HQ studies. However it was identified from MS analysis that the purified HQDP contained a diphosphoric acid bi-product which impacted the molecular weight of the final product (Chapter 6 section 6.4.2.3). As such there was less HQDP present in the silver contrast enhancing solution than the calculated 22 mM. In addition, inorganic phosphorous is known to act as a competitive inhibitor in AP mediated hydrolysis reactions, and the presence of the diphosphoric acid bi-product in the purified HQDP compound would cause an inherent level of inhibition [244, 245]. To counteract these factors, the concentration of the substrate was increased to 100 mM. Figure 6.16 (b) shows a much larger EOT response ( $\Delta\text{EOT}/\text{EOT}_0 = 0.039$ ) compared with the same experiments performed at 22 mM HQDP ( $\Delta\text{EOT}/\text{EOT}_0 = 0.022$ ), while the background levels generated by the control surfaces remained relatively constant ( $\Delta\text{EOT}/\text{EOT}_0 \approx 0.01$ ). This indicated that the increased concentration of HQDP promoted additional formation of the HQ reducing agent and as a result the S/N of the enzyme based platform was considerably improved (Table 6.2).

Surface and Enhancing Conditions	Enhancement Period	Signal to Noise Ratio (Active/Control)
AuNP pSi Method 2 (SA/HQ, pH 3.8)	10 min	4.1
ED (SA/HQ, pH 3.8)	10 min	6.4
ED (SA/22 mM HQDP/AP, pH 7.0)	10 min	1.7
ED (SA/22 mM HQDP/AP, pH 7.0)	20 min	2.3
ED (SA/100 mM HQDP/AP, pH 7.0)	20 min	4.6

Table 6.2: Effect of surface and silver contrast enhancement conditions on the signal to noise ratio of the pSi platform. S/N was calculated from  $\Delta EOT/EOT_0$  values for active and control surfaces from each study. ED = 1hour Electroless Deposition of gold on pSi, SA = 6 mM silver acetate, HQ = 22 mM hydroquinone, AP = 10 U/mL covalently immobilised alkaline phosphatase.

The consistency in the responses of the control surfaces between the 20 minute, 22 mM and 100 mM HQDP experiments suggests that the enzyme substrate is not associated with this signal. Removal of SA from the enzyme silver contrast enhancing solution led to a large reduction in the non-specific signal on control surfaces (Figure 6.16 (b)). This suggests that the presence of the high background signal can be attributed to the non-specific adsorption of silver to the control surfaces. Silver developers, silver acetate in this study, have been shown to be more unstable at neutral conditions, causing non-specific staining in histology samples at increased rates compared with acidic conditions [221, 241]. The instability of the developer is then compounded by the surface charge of the control surfaces which contain a self-assembled monolayer of MUA on electrolessly plated gold. The pKa of MUA is 6.5 which will result in the carboxyl terminated acid group being partially deprotonated at pH 7.0. This will result in a negative surface charge and promotion of non-specific adsorption of positive silver ions [251]. Additional control experiments involving exposure of SA/HQDP to MUA modified gold plated pSi at pH 5 saw a reduced level of non-specific signal indicating an increase in the stability of silver acetate and protonation of MUA at lower pH. Controls on un-modified gold (bare gold) at pH 7.0 also reduced the non-specific signal through the removal of the negative

surface charge (Figure 6.16 (b)). No action was taken to reduce this signal as future immunoassay sensing platforms do not include MUA control surfaces and the S/N between the 100 mM active and control samples was large enough to achieve a preliminary sensor.

This study has demonstrated the selective reduction of silver using the enzyme alkaline phosphatase and the synthesised hydroquinone diphosphate substrate. Enhancement of electrolessly gold plated pSi was shown and then optimised to achieve a sufficient contrast between active and control surfaces for subsequent sensing experiments.

#### **6.4.3 Detection of Human IgG by Silver Contrast Enhancement on Gold Plated pSi**

Adaptation of enzyme mediated enhancement to an optical immunosensor platform was demonstrated via the detection of human IgG by silver contrast enhancement on gold plated pSi. The same immunological components and basic protocol utilised in Chapters 4 and 5 were again implemented here. Immunosensing involved exposure of gold plated pSi containing covalently immobilised receptor antibodies to the human IgG analyte, followed by the introduction of an alkaline phosphatase conjugated secondary antibody to form a sandwich assay (Figure 6.17 a – f). Detection of human IgG was achieved by the hydrolysis of HQDP by alkaline phosphatase and the subsequent reduction of silver deposition on gold. Figure 6.17 shows EOT sensorgrams for the detection of 10 µg/mL human IgG and a control sample that was not exposed to human IgG (0 µg/mL). Introduction of the silver contrast enhancing solution at 70 minutes and reacquisition of the signal at 90 minutes yielded a large decrease in EOT on the surface containing human IgG ( $\Delta\text{EOT}/\text{EOT}_0 = 0.038$ ), while the control surface generated a much smaller response consistent with non-specific reduction of silver acetate observed previously ( $\Delta\text{EOT}/\text{EOT}_0 = 0.006$ ). The large contrast in EOT response between the active and control surfaces clearly identified the presence of human IgG at high concentrations. The non-specific response on the control surface may occur from interaction between SA and biomolecules, non-specifically adsorbed secondary antibody or un-reacted MUA and will have to be investigated further in the future. As this study was a preliminary examination of

the silver contrast enhancement detection approach, other human IgG concentrations were not investigated. However, this initial result is promising and demonstrates potential as a new form of optical immunosensor.

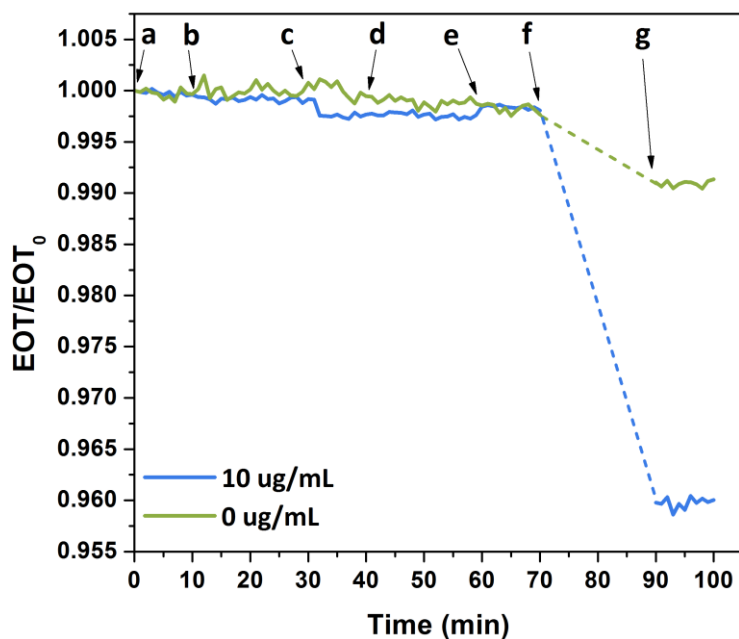


Figure 6.17: Detection of 10  $\mu\text{g/mL}$  human IgG via alkaline phosphatase mediated silver contrast enhancement of gold on pSi. (a) Electrolessly gold plated pSi containing immobilised sheep  $\alpha$ -human IgG antibody in PBS, pH 7.4. (b) 10  $\mu\text{g/mL}$  human IgG in immunosensing buffer (Control, 0  $\mu\text{g/mL}$ ). (c) Washing step and baseline in Tris buffer, pH 7.4. (d) 1:250 goat  $\alpha$ -human IgG secondary antibody conjugated to alkaline phosphatase in immunosensing buffer. (e) Washing step and baseline in citrate buffer, pH 7.0. (f) Enzyme silver contrast enhancement solution – the flow cell was shielded from light to prevent non-specific reduction of silver. (g) Wash with citrate buffer, pH 7.0.

## **6.5 Conclusions and Future Directions**

The effect of signal enhancement via triggered silver reduction onto gold treated pSi was evaluated as a detection strategy for pSi optical immunosensing. Optical contrast enhancement by silver deposition on gold was first achieved on AuNP modified pSi using silver acetate and a hydroquinone reducing agent at pH 3.8. The growth of silver within the porous layers containing AuNP's was confirmed by SEM and was shown to decrease the EOT of the pSi due to the material's lower effective refractive index. Optimisation of the silver contrast enhancing solutions also achieved an improved signal response compared to commercially available reagents.

Electroless deposition of gold on porous silicon to act as a promoter surface for enzyme mediated silver contrast enhancement was verified using SEM and IRS. Refractive index contrast enhancement by silver deposition on this material with SA/HQ achieved stronger EOT responses compared with AuNP pSi due to increased levels of gold within the pSi.

The synthesis of a phosphorylated form of hydroquinone, HQDP, was performed and verified using NMR and MS and successfully applied as an AP substrate. Catalytic dephosphorylation of the substrate was demonstrated by the selective reduction of silver in the presence of AP. Enzyme mediated contrast enhancement by silver deposition on gold plated pSi was then successfully observed and optimised at neutral pH. Finally, enzyme mediated silver contrast enhancement on gold plated pSi was successfully used in a pSi optical immunosensor to detect the presence of 10 µg/mL human IgG.

This new enzymatic detection method may pose an attractive alternative to existing immunosensing approaches based both on pSi and traditional platforms. The large contrast between the optical density of silicon, gold, silver and buffer provides an optical transduction approach potentially capable of highly sensitive detection of analytes on pSi.

Investigation of lower human IgG concentrations and formation of a standard curve should be investigated to determine the sensitivity of the sensor. In addition to this, many components of the system require optimisation to improve the sensor response, including concentrations of the silver developer and enzyme substrate as well as further optimisation of the gold coverage within the pores. Alterations should be made to the HQDP purification process to facilitate the removal of the inorganic phosphorous bi-product to reduce the amount of competitive enzyme inhibition observed. The pH range of the silver contrast enhancement process should also receive attention as replacement of alkaline phosphatase with acid phosphatase may provide an alternate strategy and additional control over the reduction of silver at lower pH levels.



# Chapter 7

---

## 7 Conclusions and Future Perspectives

## *Conclusions and Future Perspectives*

This thesis has explored new detection approaches and receptor immobilisation methods for porous silicon optical immunosensors. The unique properties associated with pSi have led to a growing interest and extensive research into its potential as transduction platform. The application of this technology is still, however in its infancy and much work remains to be done. The aim of this thesis was to improve fabrication techniques, design and sensitivity of current pSi based optical immunosensors to advance sensor design and flexibility. pSi as an optical transduction material was introduced in Chapter 3 and investigated with respect to the relationship between the electrochemical etching conditions and the porous morphology. Higher current density applied during the etching cycle led to larger pore diameters and increased porosity; and assessment of these structures via IRS identified that samples exhibiting high porosity, >70%, provided improved sensitivity to refractive index change within the porous matrix. Results from this initial study yielded a sensitive optical transducer platform exhibiting physical characteristics advantageous for immunosensing. The outcome of this investigation determined the best performing pSi morphology which was used in subsequent immunosensing chapters.

This optimised pSi architecture was then used in the design of an optical immunosensor targeting human IgG. Chapter 4 saw the incorporation of a sandwich immunoassay containing a secondary antibody labelled with alkaline phosphatase which provided the foundation for a new absorbance based pSi optical sensing technique. Enzyme catalysed hydrolysis and precipitation of the organic substrate BCIP/NBT was shown to reduce the intensity of the reflected optical profile of pSi in the region of 600 nm due to strong absorbance. Comparison of different signal processing methods was used to enhance signal strength. The magnitude of the decrease in the intensity of the reflected fringe pattern was directly proportional to analyte concentration and formed the basis of the sensor readout signal. This new pSi immunosensing approach yielded excellent sensitivity and demonstrates potential as an immunosensor technique. Optimisation of the immunoassay parameters, including the concentration of the secondary antibody, substrate concentration and porous morphology, may provide a route to increase sensitivity further. Alternate immunoassays could be incorporated to detect different analytes and increase the capabilities of the

AP/BCIP/NBT/pSi platform. Clinical trials may also be undertaken with both serum and blood based samples to ascertain the viability of the sensor in a practical setting.

In Chapter 5, the sensor architecture was then expanded and improved through the incorporation of a special protein based IgG affinity coating for receptor immobilisation. A genetically modified S-layer fusion protein, rSbpA<sub>31-1064</sub>/ZZ, (SbpA-ZZ) containing twin IgG binding domains and previously reported in application for blood purification was investigated as a self-assembling protein layer capable of immobilising  $\alpha$ -human IgG receptor antibodies with defined orientation. The effect of specific chemical species and surface wettability of planar supports on the recrystallised protein surface coverage and structure were explored. The results from this investigation revealed the formation of an ordered S-layer monolayer on hydrophobic surfaces and the apparent formation of bilayers on hydrophilic surfaces. Recrystallisation of SbpA-ZZ within ELISA plates was used to demonstrate the immobilisation of IgG capture antibodies and the detection of human IgG and human IL-6 analytes. Recrystallisation on various ELISA plate chemistries resulted in improvements to assay sensitivity compared against some of the traditional protein affinity treatments, especially hydrophilic tissue culture surfaces. Recrystallisation of SbpA-ZZ within pSi was also shown to improve characteristics of the previously developed pSi immunosensor by lowering the limit of detection and improving intra-assay precision. The results from this study indicate that the genetically modified S-layer fusion protein, SbpA-ZZ, has the capacity to act as an efficient immunosensor coating by promoting better accessibility and increasing the number of available binding sites compared to traditional covalent and adsorption immobilisation techniques. The results also highlight the potential of genetically engineering proteins tailored for specific applications. By combining desirable properties from multiple biomolecules into a single protein, chimaeric proteins such as SbpA-ZZ could be used in many applications. SbpA-ZZ shows great promise as an IgG receptor affinity coating for all types of immunosensors and should not be limited to optical approaches.

Finally, a new pSi optical interferometric immunosensing method was explored based on the refractive index contrast enhancement of silver deposition on gold

## *Conclusions and Future Perspectives*

modified pSi. In Chapter 6, pSi treated with either AuNP's or chemically plated gold acted as a promoter surface, seeding the chemical reduction of aqueous silver ions and the growth of silver deposits within the pores. This resulted in the displacement of buffer from the pores and an overall decrease in the refractive index of the porous layer. Monitoring the process using IRS saw a decrease in the EOT, the magnitude of which formed the basis of the sensor readout signal. Following these promising results, biomediated reduction of silver was investigated as a new pSi immunosensing detection approach. This strategy involved the organic synthesis of hydroquinone diphosphate (HQDP), a phosphorylated variant of a common silver reducing agent, and alkaline phosphatase. Alkaline phosphatase mediated silver reduction occurred by a cascade pathway, whereby hydrolysis of HQDP by the enzyme resulted in HQ which subsequently reduced silver acetate to metallic silver in the presence of gold. Adaptation of this system to an immunosensor architecture was then achieved through the use of a human IgG specific sandwich assay containing an alkaline phosphatase labelled secondary antibody. Preliminary studies into the use of silver contrast enhancement as an optical immunosensor signal amplification strategy yielded positive results with the successful detection of human IgG analyte. Further investigation is required for establishing a quantitative system. More thorough characterisation involving optimisation of the enzyme substrate purification protocol and the working concentration may provide greater control, sensitivity and speed by minimising competitive inhibition of the enzyme. In addition, the sensitivity, specificity and precision of the technique should be assessed to determine the viability of the sensor.

The optical sensing and receptor immobilisation techniques presented in this thesis provide the basis for new sensitive alternatives to existing analytical tools. The presented sensing enhancement strategies successfully detected low levels of analyte and the effectiveness of the SbpA-ZZ protein as a receptor affinity coating was demonstrated. The unique properties of pSi may ultimately allow the formation of competitive optical sensors based on these techniques rivalling existing techniques in sensitivity, speed, portability, ease of use and accuracy.



## References

1. Lippa, P.B., *et al.* (2001) Immunosensors-principles and applications to clinical chemistry. *Clin Chim Acta* 314, 1-26.
2. Lequin, R.M. (2005) Enzyme immunoassay (EIA)/enzyme-linked immunosorbent assay (ELISA). *Clin Chem* 51, 2415-2418.
3. Yalow, R.S. and Berson, S.A. (1959) Assay of Plasma Insulin in Human Subjects by Immunological Methods. *Nature* 184, 1648-1649.
4. Yalow, R.S. and Berson, S.A. (1960) Immunoassay of endogenous plasma insulin in man. *J Clin Invest* 39, 1157-1175.
5. Wood, W.G. (2008) Immunoassays & co.: past, present, future? - A review and outlook from personal experience and involvement over the past 35 years. *Clin Lab* 54, 423-438.
6. Janeway, J., C.A., *et al.* (2001) *Immunobiology: The Immune System in Health and Disease*. Taylor & Francis Group.
7. de la Escosura-Muniz, A., *et al.* (2010) Immunosensing using nanoparticles. *Materials Today* 13, 24-34.
8. Moina, C. and Ybarra, G. (2012) *Fundamentals and Applications of Immunosensors, Advances in Immunoassay Technology*. InTech.
9. Zourob, M. and Lakhtakia, A. (2009) *Optical Guided-wave Chemical and Biosensors I*. Springer.
10. Leung, A., *et al.* (2007) A review of fiber-optic biosensors. *Sensors and Actuators B: Chemical* 125, 688-703.
11. Marazuela, D. and Moreno-Bondi, M.C. (2002) Fiber-optic biosensors - an overview. *Anal Bioanal Chem* 372, 664-682.
12. Kanwal, S., *et al.* (2010) Polystyrene microspheres based sandwich immunosensor using CdTe nanoparticles amplification and ultrasensitive flow-injection chemiluminescence detection. *Colloids Surf B Biointerfaces* 81, 549-554.
13. Pei, X., *et al.* (2013) Sandwich-type immunosensors and immunoassays exploiting nanostructure labels: A review. *Anal Chim Acta* 758, 1-18.
14. Akkoyun, A. and Bilitewski, U. (2002) Optimisation of glass surfaces for optical immunosensors. *Biosens Bioelectron* 17, 655-664.
15. Cullen, D.C., *et al.* (1987) Detection of immuno-complex formation via surface plasmon resonance on gold-coated diffraction gratings. *Biosensors* 3, 211-225.
16. Jane, A.O., *et al.* (2007) Porous silicon biosensor for the detection of autoimmune diseases. *Proceedings of SPIE - The International Society for Optical Engineering* 6799, 679908.
17. Szili, E.J., *et al.* (2008) Enzymatically activated corrosion of porous silicon could be used for the development of interferometric biosensors. *Manuscript in preparation*
18. Krick, L.J. and Wild, D. (2001) *The Immunoassay Handbook*. Nature Publishing Group.
19. Engvall, E. and Perlmann, P. (1971) Enzyme-linked immunosorbent assay (ELISA) quantitative assay of immunoglobulin G. *Immunochemistry* 8, 871-874.

## References

20. Van Weemen, B.K. and Schuurs, A.H. (1971) Immunoassay using antigen-enzyme conjugates. *FEBS Lett* 15, 232-236.
21. Crowther, J.R. (2000) *The ELISA Guidebook*. Humana Press Inc.
22. Bange, A., *et al.* (2005) Microfluidic immunosensor systems. *Biosensors and Bioelectronics* 20, 2488-2503.
23. Liu, Y., *et al.* (2001) Rapid detection of Salmonella typhimurium using immunomagnetic separation and immuno-optical sensing method. *Sensors and Actuators B: Chemical* 72, 214-218.
24. Cheng, C.-M., *et al.* (2010) Paper-Based ELISA. *Angewandte Chemie International Edition* 49, 4771-4774.
25. Gao, Z., *et al.* (2013) Enhanced Colorimetric Immunoassay Accompanying with Enzyme Cascade Amplification Strategy for Ultrasensitive Detection of Low-Abundance Protein. *Sci. Rep.* 4
26. Mirkin, C.A., *et al.* (1996) A DNA-based method for rationally assembling nanoparticles into macroscopic materials. *Nature* 382, 607-609.
27. Ambrosi, A., *et al.* (2009) Enhanced gold nanoparticle based ELISA for a breast cancer biomarker. *Analytical Chemistry* 82, 1151-1156.
28. Nagatani, N., *et al.* (2006) Gold nanoparticle-based novel enhancement method for the development of highly sensitive immunochromatographic test strips. *Science and Technology of Advanced Materials* 7, 270-275.
29. Yang, W., *et al.* (2011) A colloidal gold probe-based silver enhancement immunochromatographic assay for the rapid detection of abrin-a. *Biosens Bioelectron* 26, 3710-3713.
30. Baac, H., *et al.* (2006) Antibody-based surface plasmon resonance detection of intact viral pathogen. *Biotechnol Bioeng* 94, 815-819.
31. Long, F., *et al.* (2009) Portable optical immunosensor for highly sensitive detection of microcystin-LR in water samples. *Biosensors and Bioelectronics* 24, 2346-2351.
32. Schaible, P. (1969) Thin-film maximum thermometer. *Thin Solid Films* 3, 277.
33. Peterson, K.E. (1980) Integrated silicon micromechanics for sensors and transducers. *Comptes Rendus des Journees d'Electronique*, 139-149.
34. Maiti, C. (1980) Semiconductor diodes as cryogenic temperature sensors. *Indian journal of cryogenics* 5, 52.
35. Gieles, A. (1973) Miniature pressure transducers with a silicon diaphragm. *Philips technical review* 33, 14.
36. Bachner, F.J. (1974) A hybrid integrated silicon diode array for visible earth-horizon sensing. *Proceedings - Electronic Components Conference* 24, 262.
37. Kimura, J. (1984) One-chip biosensors using sapphire-based boards. *Denshi Zairyo* 23, 60.
38. Kuriyama, T. (1985) A single chip biosensor. *NEC Research and Development* 78, 1.
39. Parce, J. (1989) Detection of cell-affecting agents with a silicon biosensor. *Science* 246, 243-247.
40. Canham, L.T. (1990) Silicon quantum wire array fabrication by electrochemical and chemical dissolution. *Applied Physics Letters* 57, 1046.
41. Uhler, A. (1956) *Bell Systems Technology Journal* 35, 333-347.

## References

42. Canham, L.T. and Cullis, A.G. (1991) Visible light emission due to quantum size effects in highly porous crystalline silicon. *Nature* 353, 335-338.
43. O'Mara, W.C., Herring, R.B., Hunt, L.P. (1990) *Handbook of semiconductor silicon technology*. Noyes Publications.
44. Lehmann, V. and Gosele, U. (1991) Porous silicon formation: A quantum wire effect. *Applied Physics Letters* 58, 856-859.
45. Canham, L.T. (1997) *Properties of porous silicon*. The Institute of Electrical Engineers.
46. Archer, R.J. (1960) Stain films on silicon. *Journal of Physics and Chemistry of Solids* 14, 104-110.
47. Ouyang, H., *et al.* (2005) Macroporous silicon microcavities for macromolecule detection. *Advanced Functional Materials* 15, 1851-1859.
48. Bonanno, L.M., DeLouise, L. A. (2007) Whole blood optical sensor *Biosensors & Bioelectronics* 23, 444.
49. Berger, M.G., *et al.* (1994) Porous superlattices: a new class of Si heterostructures. *Journal of Physics D, Applied Physics* 27, 1333-1336.
50. Pavesi, L. (1997) Random porous silicon multilayers: Application to distributed bragg reflectors and interferential fabry-perot filters. *Semiconductor Science and Technology* 12, 570-575.
51. Guillermain, E.E., *et al.* (2007) Bragg surface wave device based on porous silicon and its application for sensing. *Applied Physics Letters* 90, 241116.
52. Berger, M.G., *et al.* (1997) Dielectric filters made of PS: advanced performance by oxidation and new layer structures. *Thin Solid Films* 297, 237.
53. Thonissen, M., *et al.* (1997) *Materials Research Society Symposium Proceedings* 45, 643.
54. Pavesi, L. (1997) Porous silicon dielectric multilayers and microcavities. *Rivista del Nuovo Cimento* 20, 1-76.
55. Heinrich, J.L., *et al.* (1992) Luminescent colloidal silicon suspensions from porous silicon *Science* 255, 66-68.
56. Sailor, M.J. and Link, J.R. (2005) "Smart dust": nanostructured devices in a grain of sand. *Chemical Communications*, 1375-1383.
57. Pacholski, C., *et al.* (2005) Biosensing using porous silicon double-layer interferometers: Reflective interferometric Fourier transform spectroscopy. *Journal of the American Chemical Society* 127, 11636-11645.
58. Qian, M., *et al.* (2006) Structural tailoring of multilayer porous silicon for photonic crystal application. *Journal of Crystal Growth* 292, 347-350.
59. DeLouise, L.A., *et al.* (2005) Cross-correlation of optical microcavity biosensor response with immobilized enzyme activity. Insights into biosensor sensitivity. *Analytical Chemistry* 77, 3222-3230.
60. Allongue, P. (1993) Etching of silicon in NaOH solutions: Electrochemical studies of n-Si(111) and n-Si(100) and the mechanism of the dissolution. *Journal of the Electrochemical Society* 140, 1018-1026.
61. Petrova-Koch, V., *et al.* (1992) Rapid-thermal-oxidized porous Si - The superior photoluminescent Si. *Applied Physics Letters* 61, 943-945.
62. Salonen, J., *et al.* (1997) Thermal oxidation of free-standing porous silicon films. *Applied Physics Letters* 70, 637-639.

## References

63. Chen, H., *et al.* (1996) Passivation of porous silicon by wet thermal oxidation. *Journal of Applied Physics* 79, 3282-3285.
64. Chen, Z. and Bosman, G. (1994) Porous silicon photoluminescence enhancement and saturation resulting from thermal annealing in nitrogen gas. *Physica Status Solidi (B)* 184, 283-290.
65. Song, H. (1997) Microsecond photoluminescence decay and oxidation of porous silicon. *Solid State Communications* 102, 813-816.
66. Janshoff, A., *et al.* (1998) Macroporous p-type silicon fabry-perot layers. Fabrication, characterization, and applications in biosensing. *Journal of the American Chemical Society* 120, 12108-12116.
67. Lauerhass, J.M. and Sailor, M.J. (1993) Chemical modification of the photoluminescence quenching of porous silicon. *Science* 261, 1567-1568.
68. Lauerhass, J.M. and Sailor, M.J. (1993) The effects of halogen exposure on the photoluminescence of porous silicon. *Materials Research Society Symposium Proceedings* 298, 259-263.
69. Schwartz, M.P., Buriak, J.M. (2000) Chemical and biological applications of porous silicon applications. *Advanced Materials* 12, 859-869.
70. Tinsley-Bown, A.M., *et al.* (2000) Tuning the pore size and surface chemistry of porous silicon for immunoassays. *Physica Status Solidi. A, Applied Research* 182, 547-553.
71. Geobaldo, F. (2004) A new route to the functionalisation of porous silicon. *Sensors and Actuators B - Chemical* 100, 29-32.
72. Buriak, J.M. (1999) Silicon carbon bonds on porous silicon surfaces: One step closer to device applications. *Advanced Materials* 11, 265-268.
73. Stewart, M.P., Buriak, J.M. (1998) Photopatterned Hydrosilylation on Porous Silicon. *Angewandte Chemie International Edition* 37, 3257-3260.
74. Buriak, J.M. and Allen, M.J. (1999) Photoluminescence of porous silicon surfaces stabilized through lewis acid mediated hydrosilylation. *Journal of Luminescence* 80, 29-35.
75. Robins, E.G., Stewart, M.P., Buriak, J.M. (1999) Anodic and cathodic electrografting of alkynes on porous silicon. *Journal of Chemical Society, Chemical Communications*, 2479-2480.
76. Stewart, M.P., Buriak, J.M. (2001) Exciton mediated hydrosilylation on nanocrystalline silicon surfaces. *Journal of the American Chemical Society* 123, 7821-7830.
77. Buriak, J.M., Stewart, M.J., Geders, T.W., Allen, M.J., Choi, H.C., Smith, J., Raftery, M.D., Canham, L.T. (1999) Lewis acid mediated hydrosilylation on porous silicon surfaces. *Journal of the American Chemical Society* 121, 11491-11502.
78. Buriak, J.M., *et al.* (1999) Metal mediated reactions on porous silicon surfaces. *Journal of Solid State Chemistry* 147, 251-258.
79. Salonen, J., *et al.* (2002) Thermal carbonization of porous silicon surface by acetylene. *Journal of Applied Physics* 91, 456-461.
80. Salonen, J. and Lehto, V.-P. (2008) Fabrication and chemical surface modification of mesoporous silicon for biomedical applications. *Chemical Engineering Journal* 137, 162-172.
81. Salonen, J., *et al.* (2008) Mesoporous silicon in drug delivery applications. *Journal of Pharmaceutical Sciences* 97, 632-653.
82. De Stefano, L., *et al.* (2008) Protein-Modified Porous Silicon Nanostructures. *Advanced Materials* 20, 1529-1533.

## References

83. De Stefano, L., *et al.* (2009) Biological passivation of porous silicon by a self-assembled nanometric biofilm of proteins. *Journal of Nanophotonics* 3, 031985-031985-031986.
84. Lin, V.S.-Y., *et al.* (1997) A porous silicon-based optical interferometric biosensor. *Science* 278, 840-843.
85. Schwartz, M.P., *et al.* (2007) Using an oxidized porous silicon interferometer for determination of relative protein binding affinity through non-covalent capture probe immobilization. *Physica Status Solidi. A, Applied Research* 204, 1444.
86. Miller, B.L. (2007) Porous silicon in biosensing applications. In *Smart Biosensor Technology* (Knopf, G.K., Bassi, A. S., ed), 271-290, CRC Press.
87. Theiss, W. (1997) Optical properties of porous silicon. *Surface Science Reports* 29, 95-192.
88. Dancil, K.P., *et al.* (1999) A porous silicon optical biosensor: Detection of reversible binding of IgG to a protein A-modified surface. *Journal of the American Chemical Society* 121, 7925-7930.
89. Reis, K.J., *et al.* (1984) Streptococcal Fc receptors. II. Comparison of the reactivity of a receptor from a group C streptococcus with staphylococcal protein A. *Journal of Immunology* 132, 3098-3102.
90. Richman, D.D., *et al.* (1982) Binding of staphylococcal protein A by the sera of different animal species. *Journal of Immunology* 128, 2300-2305.
91. Steinem, C., *et al.* (2004) DNA hybridization-enhanced porous silicon corrosion: mechanistic investigations and prospect for optical interferometric biosensing. *Tetrahedron* 60, 11259-11267.
92. Voelcker, N.H., *et al.* (2008) Catalyzed oxidative corrosion of porous silicon used as an optical transducer for ligand-receptor interactions. *ChemBiochem* 9, 1776-1786.
93. Massad-Ivanir, N., *et al.* (2014) Trap and track: designing self-reporting porous Si photonic crystals for rapid bacteria detection. *Analyst* 139, 3885-3894.
94. Mirsky, Y., *et al.* (2013) Optical biosensing of bacteria and cells using porous silicon based, photonic lamellar gratings. *Applied physics letters* 103, 033702.
95. Orosco, M., *et al.* (2006) Protein-coated porous-silicon photonic crystals for amplified optical detection of protease activity. *Advanced Materials* 18, 1393.
96. Kilian, K., *et al.* (2007) Peptide-modified optical filters for detecting protease activity. *ACS nano* 1, 355.
97. Alvarez, S., *et al.* (2007) Using a porous silicon photonic crystal for bacterial cell-based biosensing. *Physica Status Solidi. A, Applied Research* 204, 1439-1443.
98. Schwartz, M.P., *et al.* (2006) The smart petri dish: A nanostructured photonic crystal for real-time monitoring of living cells. *Langmuir* 22, 7084-7090.
99. Martín-Palma, R., *et al.* (2004) Porous silicon multilayer stacks for optical biosensing applications. *Microelectronics Journal* 35, 45.
100. DeLouise, L.A., *et al.* (2005) Cross correlation of optical microcavity biosensor response with immobilised enzyme activity. Insights into biosensor sensitivity. *Analytical Chemistry* 77, 322-3230.

## References

101. Chan, S., *et al.* (2001) Identification of gram negative bacteria using nanoscale silicon microcavities. *Journal of the American Chemical Society* 123, 11797-11798.
102. Ouyang, H., *et al.* (2007) Label-free quantitative detection of protein using macroporous silicon photonic bandgap biosensors. *Analytical Chemistry* 79, 1502-1506.
103. Ouyang, H., *et al.* (2005) Biosensing using porous silicon photonic bandgap structures. *Proceedings of SPIE - The international society for optical engineering* 6005, 600508.
104. Cunin, F., *et al.* (2002) Biomolecular screening with encoded porous-silicon photonic crystals. *Nature Materials* 1, 39-41.
105. Canham, L.T., *et al.* (2000) Derivatized porous silicon mirrors: Implantable optical components with slow resorbability. *Physica Status Solidi. A, Applied Research* 182, 521.
106. Hardman, R. (2006) A toxicologic review of quantum dots: Toxicity depends on physicochemical and environmental factors. *Environmental Health Perspectives* 114, 165-172.
107. Starodub, N.F., *et al.* (1996) Use of the silicon crystals photoluminescence to control immunocomplex formation. *Sensors and Actuators B - Chemical* 35-36, 44-47.
108. Starodub, V.M., *et al.* (1999) Control of myoglobin level in a solution by an immune sensor based on the photoluminescence of porous silicon. *Sensors and Actuators B: Chemical* 58, 409-414.
109. Di Francia, G., *et al.* (2005) Towards a label-free optical porous silicon DNA sensor. *Biosensors and Bioelectronics* 21, 661-665.
110. Mathew, F.P. and Alocilia, E.C. (2005) Porous silicon-based biosensor for pathogen detection. *Biosensors and Bioelectronics* 20, 1656-1661.
111. Yamaguchi, R.-T., *et al.* (2007) DNA hybridization detection by porous silicon-based DNA microarray in conjugation with infrared microspectroscopy. *Journal of Applied Physics* 102, 014303-014307.
112. Song, M., *et al.* (2007) Electrochemical biosensor array for liver diagnosis using silanization technique on nanoporous silicon electrode. *Journal of Bioscience and Bioengineering* 103, 32.
113. Wang, H. and Mu, S. (1999) Bioelectrochemical characteristics of cholesterol oxidase immobilised in a polyaniline film. *Sensors and Actuators B - Chemical* 56, 22-30.
114. Setzu, S., *et al.* (2007) Porous silicon-based potentiometric biosensor for triglycerides. *Physica Status Solidi. A, Applied Research* 204, 1434.
115. Archer, M., *et al.* (2004) Macroporous silicon electrical sensor for DNA hybridization detection. *Biomedical Microdevices* 6, 203-211.
116. Sleytr, U.B., *et al.* (1999) Crystalline bacterial cell surface layers (S-layers): From supramolecular cell structure to biomimetics and nanotechnology. *Angewandte Chemie International Edition* 38, 1034-1054.
117. Houwink, A.L. (1953) A macromolecular mono-layer in the cell wall of *Spirillum spec.* *Biochimica et Biophysica Acta* 10, 360-366.
118. Smarda, J., *et al.* (2002) S-layers on cell walls of cyanobacteria. *Micron* 33, 257-277.
119. Egelseer, E.M., *et al.* (2009) S-Layers, Microbial, Biotechnological Applications. In *Encyclopedia of Industrial Biotechnology*, John Wiley & Sons, Inc.

## References

120. Messner, P. and Sleytr, U.B. (1992) Crystalline bacterial cell-surface layers. *Adv. Microb. Physiol.* 33, 213-275.
121. Ilk, N., *et al.* (2011) S-layer fusion proteins - construction principles and applications. *Current Opinion in Biotechnology* 22, 824-831.
122. Sleytr, U.B., *et al.* (2010) Nanobiotechnological applications of S-layers. In *Prokaryotic Cell Wall Compounds - Structure and Biochemistry* (Konig, H., *et al.*, eds), 459-481, Springer.
123. Sleytr, U.B., *et al.* (2001) Characterization and use of crystalline bacterial cell surface layers. *Progress in Surface Science* 68, 231-278.
124. Sleytr, U.B., *et al.* (2001) Molecular nanotechnology and nanobiotechnology with two-dimensional protein crystals (S-layers). In *Nano-Surface Science Chemistry* (Rosoff, M., ed), 333-389, Marcel Dekker Inc.
125. Sleytr, U.B., *et al.* (2002) Self-assembly protein systems: microbial S-layers. In *Polyamides and Complex Proteinaceous Materials I* (Steinbuchel, A. and Fahnestock, S.R., eds), 285-338, Wiley-VCH.
126. Pum, D. and Sleytr, U.B. (1999) The application of bacterial S-layers in molecular nanotechnology. *Trends in biotechnology* 17, 8-12.
127. Sleytr, U.B., *et al.* (2007) S-layers as a tool kit for nanobiotechnological applications. *FEMS Microbiol Lett* 267, 131-144.
128. Sleytr, U.B., *et al.* (2003) Crystallization of S-layer protein lattices on surfaces and interfaces. *Progress in Organic Coatings* 47, 279-287.
129. Habibi, N., *et al.* (2010) Self-assembly and recrystallization of bacterial S-layer proteins of *Bacillus sphaericus* and *Bacillus thuringiensis* on silicone, mica and quartz crystal supports. *Conf Proc IEEE Eng Med Biol Soc* 2010, 3739-3742.
130. Sara, M. and Sleytr, U.B. (2000) S-Layer Proteins. *J. Bacteriol.* 182, 859-868.
131. Koval, S.F. and Murray, R.G.E. (1986) The superficial protein arrays on bacteria. *Microbiological Sciences* 3, 357-362.
132. Sleytr, U.B. (1978) Regular arrays of macromolecules on bacterial cell walls: structure, chemistry, assembly and function. *International Review of Cytology* 53, 1-64.
133. Engelhardt, H. and Peters, J. (1998) Structural research on surface layers: a focus on stability, surface layer homology domains, and surface layer-cell wall interactions. *Journal of Structural Biology* 124, 276-302.
134. Györfvay, E.S., *et al.* (2003) Self-assembly and recrystallization of bacterial S-layer proteins at silicon supports imaged in real time by atomic force microscopy. *Journal of Microscopy* 212, 300-306.
135. Teixeira, L.M., *et al.* (2010) Entropically driven self-assembly of *Lysinibacillus sphaericus* S-layer proteins analyzed under various environmental conditions. *Macromol Biosci* 10, 147-155.
136. Jarosch, M., *et al.* (2001) Analysis of the structure-function relationship of the S-layer protein SbsC of *Bacillus stearothermophilus* ATCC 12980 by producing truncated forms. *Microbiology* 147, 1353-1363.
137. Pum, D. and Sleytr, U.B. (1995) Anisotropic crystal growth of the S-layer of *Bacillus sphaericus* CCM 2177 at the air/water interface. *Colloids and Surfaces* 102, 99-104.
138. Kiipci, S., *et al.* (1996) Two-dimensional paracrystalline glycoprotein S-layers as a novel matrix for the immobilization of human IgG and their

## References

- use as microparticles in immunoassays. *Journal of Immunological Methods* 196, 73-84.
139. Toca-Herrera, J.L., *et al.* (2005) Recrystallization of bacterial S-layers on flat polyelectrolyte surfaces and hollow polyelectrolyte capsules. *Small* 1, 339-348.
  140. Mader, C., *et al.* (2000) S-layer-coated liposomes as a versatile system for entrapping and binding target molecules. *Biochimica et Biophysica Acta* 1463, 142-150.
  141. Kupcu, S., *et al.* (1995) Liposomes coated with crystalline bacterial cells surface protein (S-layer) as immobilization structures for macromolecules. *Biochim Biophys Acta* 1235, 263-269.
  142. Mader, C., *et al.* (1999) Stabilizing effect of an S-layer on liposomes towards thermal or mechanical stress. *Biochim Biophys Acta* 1418, 106-116.
  143. Nomellini, J.F., *et al.* (1997) Factors controlling in vitro recrystallization of the *Caulobacter crescentus* paracrystalline S-layer. *J Bacteriol* 179, 6349-6354.
  144. Sara, M. and Sleytr, U.B. (1996) Crystalline bacterial cell surface layers (S-layers): from cell structure to biomimetics. *Prog Biophys Mol Biol* 65, 83-111.
  145. Sara, M. and Sleytr, U.B. (1996) Biotechnology and biomimetic with crystalline bacterial cell surface layers (S-layers). *Micron* 27, 141-156.
  146. Sleytr, U.B. and Sara, M. (1997) Bacterial and archaeal S-layer proteins: structure-function relationships and their biotechnological applications. *Trends Biotechnol* 15, 20-26.
  147. Sara, M., *et al.* (2005) S-layers as patterning elements for application in nanobiotechnology. *J Nanosci Nanotechnol* 5, 1939-1953.
  148. Vollenkle, C., *et al.* (2004) Construction of a functional S-layer fusion protein comprising an immunoglobulin G-binding domain for development of specific adsorbents for extracorporeal blood purification. *Appl Environ Microbiol* 70, 1514-1521.
  149. Sleytr, U.B., *et al.* (2007) S-Layers as a basic building block in a molecular construction kit. *FEBS Journal* 274, 323-334.
  150. Huber, C., *et al.* (2006) S-layer-streptavidin fusion proteins and S-layer-specific heteropolysaccharides as part of a biomolecular construction kit for application in nanobiotechnology. *Microelectronic Engineering* 83, 1589-1593.
  151. Huber, C., *et al.* (2006) Heterotetramers formed by an S-layer-streptavidin fusion protein and core-streptavidin as a nanoarrayed template for biochip development. *Small* 2, 142-150.
  152. Moll, D., *et al.* (2002) S-layer-streptavidin fusion proteins as template for nanopatterned molecular arrays. *Proceedings of the National Academy of Sciences* 99, 14646-14651.
  153. Pleschberger, M., *et al.* (2004) An S-layer heavy chain camel antibody fusion protein for generation of a nanopatterned sensing layer to detect the prostate-specific antigen by surface plasmon resonance technology. *Bioconjug Chem* 15, 664-671.
  154. Pleschberger, M., *et al.* (2003) Generation of a functional monomolecular protein lattice consisting of an s-layer fusion protein comprising the variable domain of a camel heavy chain antibody. *Bioconjug Chem* 14, 440-448.

## References

155. Pum, D., *et al.* (2013) S-Layer Protein Self-Assembly. *International Journal of Molecular Sciences* 14, 2484-2501.
156. Armarego, W.L.F. and Perrin, D.D. (1996) *Purification of laboratory chemicals*. Butterworth-Heinemann.
157. Koshida, N. (2008) *Device Applications of Silicon Nanocrystals and Nanostructures*. Springer Science.
158. Sailor, M.J. (2011) *Porous Silicon in Practice: Preparation, Characterization and Applications*. Wiley-VCH.
159. Lehmann, V. and Foll, H. (1990) Formation Mechanism and Properties of Electrochemically Etched Trenches in n<sup>+</sup>-Type Silicon. *Journal of the Electrochemical Society* 137, 653-659.
160. Lee, K.B., *et al.* (2002) Protein nanoarrays generated by dip-pen nanolithography. *Science* 295, 1702-1705.
161. Barger, A., *et al.* (2005) Use of Alkaline Phosphatase Staining to Differentiate Canine Osteosarcoma from Other Vimentin-positive Tumors. *Veterinary Pathology* 42, 161-165.
162. Christodoulides, N., *et al.* (1995) Vascular Smooth Muscle Cell Heme Oxygenases Generate Guanylyl Cyclase-Stimulatory Carbon Monoxide. *Circulation* 91, 2306-2309.
163. Sandén, B., *et al.* (1998) An amperometric enzyme-linked immunosensor for Nitrobacter. *Applied Microbiology and Biotechnology* 50, 710-716.
164. Sperhake, R.D., *et al.* (2004) Detection of Mycobacterium tuberculosis by a polymerase chain reaction colorimetric dot-blot assay. *The International Journal of Tuberculosis and Lung Disease* 8, 312-317.
165. McGadey, J. (1970) A tetrazolium method for non-specific alkaline phosphatase. *Histochemie* 23, 180-184.
166. Eun, H.-M. (1996) *Enzymology Primer for Recombinant DNA Technology*. Academic Press Inc.
167. Witmer, M.R., *et al.* (1991) U-3'-BCIP: a chromogenic substrate for the detection of RNase A in recombinant DNA expression systems. *Nucleic Acids Res* 19, 1-4.
168. Cox Gad, S. (2007) *Handbook of Pharmaceutical Biotechnology*. John Wiley & Sons, Inc.
169. Patolsky, F., *et al.* (2003) Highly sensitive amplified electronic detection of DNA by biocatalyzed precipitation of an insoluble product onto electrodes. *Chemistry – A European Journal* 9, 1137-1145.
170. Borghesi, A., Sassella, A., Pivac, B., Pavesi, L. (1993) Characterization of porous silicon inhomogeneities by high spatial resolution infrared spectroscopy. *Solid State Communications* 87, 1-4.
171. Borghesi, A., Guizzetti, G., Sassella, A., Bisi, O., Pavesi, L. (1994) Induction-model analysis of Si-H stretching mode in porous silicon. *Solid State Communications* 89, 615-618.
172. Bisi, O., Ossicini, S., Pavesi, L. (2000) Porous silicon: a quantum sponge structure for silicon based optoelectronics. *Surface Science Reports*, 1-126.
173. Katti, A., *et al.* (2005) Chemical, physical, and mechanical characterization of isocyanate cross-linked amine-modified silica aerogels. *Chemistry of Materials* 18, 285-296.
174. Hwang, Y.J., *et al.* (2006) Preparation and characterization of PEG-grafted silica particles using emulsion. *J. Ind. Eng. Chem.* 12, 380-386.

## References

175. Yilgor, E., *et al.* (2000) Comparison of hydrogen bonding in polydimethylsiloxane and polyether based urethane and urea copolymers. *Polymer* 41, 849-857.
176. Clayden, J., *et al.* (2001) *Organic Chemistry*. Oxford University Press.
177. Hermanson, G.T. (2008) *Bioconjugate Techniques*. Academic Press.
178. Ziemia, P. (1995) Effects of surface treatment on porous silicon photoluminescence. *Physica Status Solidi A* 149, K47-K49.
179. Murguia, J.S., *et al.* (2013) Two-dimensional wavelet transform feature extraction for porous silicon chemical sensors. *Analytica Chimica Acta* 785, 1-15.
180. Mora, M.B.D.L., *et al.* (2013) *Porous Silicon Biosensors*. Intech.
181. Gupta, B., *et al.* (2013) Functionalised porous silicon as a biosensor: emphasis on monitoring cells in vivo and in vitro. *Analyst* 138, 3593-3615.
182. Dhanekar, S. and Jain, S. (2013) Porous silicon biosensor: Current status. *Biosensors and Bioelectronics* 41, 54-64.
183. Jane, A., *et al.* (2009) Porous silicon biosensors on the advance. *Trends in biotechnology* 27, 230-239.
184. Rinkevichyus, B.S., *et al.* (2010) *Laser Refractography*. Springer
185. Weiss, S.M. (2009) *Biological Applications of Silicon Nanostructures*. Pan Stanford Publishing.
186. Eun, H.-M. (1996) 5 - Phosphatases and Polynucleotide Kinase. In *Enzymology Primer for Recombinant DNA Technology*, 307-344, Academic Press.
187. Rossi, A.M., Wang, L., Reipa, V., Murphy, T. E. (2007) Porous silicon biosensor for detection of viruses. *Biosensors & bioelectronics* 23, 741-745.
188. Thomsen, V., *et al.* (2003) Limits of detection in spectroscopy. *Spectroscopy* 18, 112-114.
189. Eum, J.Y., *et al.* (2014) A highly sensitive immunoassay using antibody-conjugated spherical mesoporous silica with immobilized enzymes. *Chemical Communications*
190. Fu, Z.Z.H., *et al.* (2013) Highly sensitive fluorescent immunoassay of human immunoglobulin G based on PbS nanoparticles and DNAzyme. *Anal. Sci.* 29, 499-504.
191. Chuag, S.-H., *et al.* (2013) Accelerated colorimetric immunosensing using surface-modified porous monoliths and gold nanoparticles. *Science and Technology of Advanced Materials* 14
192. Liu, X., *et al.* (2012) Antibody-biotemplated HgS nanoparticles: Extremely sensitive labels for atomic fluorescence spectrometric immunoassay. *Analyst* 137, 1473-1480.
193. Yang, J., *et al.* (2008) Quantitative determination of humanized monoclonal antibody rhuMAb2H7 in cynomolgus monkey serum using a Generic Immunoglobulin Pharmacokinetic (GRIP) assay. *Journal of Immunological Methods* 335, 8-20.
194. Beyzavi, K., *et al.* (1987) Comparison of horseradish-peroxidase and alkaline phosphatase-labelled antibodies in enzyme immunoassays. *Ann. Clin. Biochem.* 24, 145-152.
195. Stoop, J.W., *et al.* (1969) Serum immunoglobulin levels in healthy children and adults. *Clinical & Experimental Immunology* 4, 101-112.

## References

196. Gonzalez-Quintela, A., *et al.* (2008) Serum levels of immunoglobulins (IgG, IgA, IgM) in a general adult population and their relationship with alcohol consumption, smoking and common metabolic abnormalities. *Clinical & Experimental Immunology* 151, 42-50.
197. Lide, D.R. (2007) *CRC Handbook of Chemistry and Physics*. CRC Press.
198. DeBari, V.A., *et al.* (1975) Direct spectrophotometric observation of intracellular nitro-blue tetrazolium and its formazan by multiple internal reflectance infrared spectroscopy. *Histochemistry* 45, 83-88.
199. Lin-Vien, D. (1991) *The Handbook of infrared and raman characteristic frequencies of organic molecules*. Academic Press.
200. Patel, N.B., *et al.* (2010) Sulfonamides of 2-[(2,6-dichlorophenyl)amino]phenyl acetoxyacetic acid and their antibacterial studies. *Acta Pol Pharm* 67, 351-359.
201. Ikeda, T., *et al.* (2009) Oriented immobilization of antibodies on a silicon wafer using Si-tagged protein A. *Analytical Biochemistry* 385, 132-137.
202. Gobel, C., *et al.* (2010) S-layer templated bioinspired synthesis of silica. *Colloids Surf B Biointerfaces* 75, 565-572.
203. Sleytr, U.B., *et al.* (1986) Structural and chemical characterization of S-layers of selected strains of *Bacillus stearothermophilus* and *Desulfotomaculum nigrificans*. *Arch Microbiol* 146, 19-24.
204. Ilk, N., *et al.* (1999) Structural and functional analyses of the secondary cell wall polymer of *Bacillus sphaericus* CCM 2177 that serves as an S-layer-specific anchor. *J Bacteriol* 181, 7643-7646.
205. Sleytr, U.B. and Glauert, A.M. (1976) Ultrastructure of the cell walls of two closely related clostridia that possess different regular arrays of surface subunits. *J Bacteriol* 126, 869-882.
206. Ilk, N., *et al.* (2002) Molecular characterization of the S-layer gene, *sbpA*, of *Bacillus sphaericus* CCM 2177 and production of a functional S-layer fusion protein with the ability to recrystallize in a defined orientation while presenting the fused allergen. *Appl Environ Microbiol* 68, 3251-3260.
207. Fang, F. and Szleifer, I. (2002) Effect of molecular structure on the adsorption of protein on surfaces with grafted polymers. *Langmuir* 18, 5497-5510.
208. Nath, N., *et al.* (2004) Surface engineering strategies for control of protein and cell interactions. *Surface Science* 570, 98-110.
209. Nakajima, A., *et al.* (2001) Recent studies on super-hydrophobic films. *Monatshefte fur Chemie* 132, 31-41.
210. Lopez, A.E., *et al.* (2010) Surface dependence of protein nanocrystal formation. *Small* 6, 396-403.
211. Weygand, M., *et al.* (1999) Bacterial S-layer protein coupling to lipids: x-ray reflectivity and grazing incidence diffraction studies. *Biophys J* 76, 458-468.
212. Gyoryvary, E., *et al.* (2004) Formation of nanoparticle arrays on S-layer protein lattices. *J Nanosci Nanotechnol* 4, 115-120.
213. Sara, M. (2001) Conserved anchoring mechanisms between crystalline cell surface S-layer proteins and secondary cell wall polymers in Gram-positive bacteria? *Trends in Microbiology* 9, 47-49.
214. Lopez, A.E., *et al.* (2011) Influence of surface chemistry and protein concentration on the adsorption rate and S-layer crystal formation. *Physical Chemistry Chemical Physics* 13, 11905-11913.

## References

215. Schuster, B. and Sleytr, U.B. (2009) Tailor-made crystalline structures of truncated S-layer proteins on heteropolysaccharides. *Soft Matter* 5, 334-341.
216. Delcea, M., *et al.* (2008) Thermal stability, mechanical properties and water content of bacterial protein layers recrystallized on polyelectrolyte multilayers. *Soft Matter* 4, 1414-1421.
217. Schuster, B., *et al.* (2008) S-layer stabilized lipid membranes (Review). *Biointerphases* 3, FA3.
218. Khan, M.N. and Findlay, J.W. (2009) *Ligand-Binding Assays: Development, Validation, and Implementation in the Drug Development Arena*. Wiley.
219. Amstein, C.F. and Hartman, P.A. (1975) Adaptation of plastic surfaces for tissue culture by glow discharge. *Journal of Clinical Microbiology* 2, 46-54.
220. Andrade, J.D. (1985) *Surface and interfacial aspects of biomedical polymers*. Plenum Press.
221. Hayat, M.A. (1995) *Immunogold-Silver Staining: Principles, Methods, and Applications*. CRC Press Inc.
222. Holgate, C.S., *et al.* (1983) Immunogold-silver staining: new method of immunostaining with enhanced sensitivity. *J Histochem Cytochem* 31, 938-944.
223. Zhang, Z., *et al.* (2009) A simple and sensitive biosensor based on silver enhancement of aptamer-gold nanoparticle aggregation. *Electroanalysis* 21, 1316-1320.
224. Lee, J.-S. and Mirkin, C.A. (2008) Chip-based scanometric detection of mercuric ion using DNA-functionalized gold nanoparticles. *Analytical chemistry* 80, 6805-6808.
225. Taton, T.A., *et al.* (2000) Scanometric DNA array detection with nanoparticle probes. *Science* 289, 1757-1760.
226. Hou, S.Y., *et al.* (2007) Development of zeptomole and attomolar detection sensitivity of biotin-peptide using a dot-blot gold nanoparticle immunoassay. *Anal Chem* 79, 980-985.
227. Wang, Y., *et al.* (2008) Ultrasensitive colorimetric detection of protein by aptamer-Au nanoparticles conjugates based on a dot-blot assay. *Chemical Communications*, 2520-2522.
228. Mitamura, K., *et al.* (2013) Clinical evaluation of highly sensitive silver amplification immunochromatography systems for rapid diagnosis of influenza. *Journal of Virological Methods* 194, 123-128.
229. Shyu, R.-H., *et al.* (2002) Colloidal gold-based immunochromatographic assay for detection of ricin. *Toxicon* 40, 255-258.
230. Yeh, C.-H., *et al.* (2009) An immunoassay using antibody-gold nanoparticle conjugate, silver enhancement and flatbed scanner. *Microfluidics and Nanofluidics* 6, 85-91.
231. Akanda, M.R., *et al.* (2013) Hydroquinone diphosphate as a phosphatase substrate in enzymatic amplification combined with electrochemical-chemical-chemical redox cycling for the detection of E. coli O157:H7. *Anal Chem* 85, 1631-1636.
232. Freeman, H.F. and Colver, C.W. (1938) Synthesis of disodium phenyl phosphate. *Journal of the American Chemical Society* 60, 750-751.
233. Friedman, O.M. and Seligman, A.M. (1950) Preparation of naphthyl acid phosphates. *Journal of the American Chemical Society* 72, 624-625.

## References

234. Wilson, M.S. and Rauh, R.D. (2004) Hydroquinone diphosphate: an alkaline phosphatase substrate that does not produce electrode fouling in electrochemical immunoassays. *Biosens Bioelectron* 20, 276-283.
235. Christian, K.F., *et al.* (2009) Silicon oxidation by ozone. *Journal of Physics: Condensed Matter* 21, 183001.
236. Cui, Z. and Takoudis, C.G. (2003) Initial oxidation of H-terminated Si(100) in O<sub>3</sub> (950 ppm)/O<sub>2</sub> and pure O<sub>2</sub>. *Journal of the Electrochemical Society* 150, G694-G701.
237. Menon, V.P. and Martin, C.R. (1995) Fabrication and Evaluation of Nanoelectrode Ensembles. *Analytical Chemistry* 67, 1920-1928.
238. Velleman, L., *et al.* (2011) Raman spectroscopy probing of self-assembled monolayers inside the pores of gold nanotube membranes. *Phys Chem Chem Phys* 13, 19587-19593.
239. Li, D., *et al.* (2007) Immobilization of glucose oxidase onto gold nanoparticles with enhanced thermostability. *Biochem Biophys Res Commun* 355, 488-493.
240. Hacker, G.W., *et al.* (1988) Silver acetate autometallography: an alternative enhancement technique for immunogold-silver staining (IGSS) and silver amplification of gold, silver, mercury and zinc in tissues. *Journal of Histochemistry* 11, 213-221.
241. Lah, J.J., *et al.* (1990) A neutral pH silver development method for the visualization of 1-nanometer gold particles in pre-embedding electron microscopic immunocytochemistry. *J Histochem Cytochem* 38, 503-508.
242. Velleman, L., *et al.* (2008) Engineered gold nanotube membranes for molecular separations *International Conference on Nanoscience and Nanotechnology, 2008.*, 86 - 89.
243. Zhang, Z., *et al.* (2002) Synthesis of ordered metallic nanowires inside ordered mesoporous materials through electroless deposition. *Chemistry of materials* 14, 965-968.
244. Hogarth, D., *et al.* (2002) A decrease in the bovine intestinal mucosa alkaline phosphatase activity in the presence of inorganic phosphate. *Journal of Experimental Microbiology and Immunology* 2, 6-12.
245. Kim, E.E. and Wyckoff, H.W. (1991) Reaction mechanism of alkaline phosphatase based on crystal structures. Two-metal ion catalysis. *J Mol Biol* 218, 449-464.
246. Liu, H.F., *et al.* (2010) Recovery and purification process development for monoclonal antibody production. *MAbs* 2, 480-499.
247. Burry, R.W., *et al.* (1992) Silver enhancement of gold antibody probes in pre-embedding electron microscopic immunocytochemistry. *J Histochem Cytochem* 40, 1849-1856.
248. Fernley, H.N. and Walker, P.G. (1965) Kinetic behaviour of calf-intestinal alkaline phosphatase with 4-methylumbelliferyl phosphate. *Biochem J* 97, 95-103.
249. Flynn, A., *et al.* (2002) The effects of pH on Type VII-NA bovine intestinal mucosal alkaline phosphatase activity *Journal of Experimental Microbiology and Immunology* 2, 50-56.
250. Prasad, N.K. (2011) *Enzyme Technology - Pacemaker of Biotechnology*. PHI Learning Pvt. Ltd.
251. Pishko, M., *et al.* (2002) Mass transfer in amperometric biosensors based on nanocomposite thin films of redox polymers and oxidoreductases. *Sensors* 2, 79-90.